Reaction Chemistry & Engineering

PAPER

Highlighting diffusional coupling effects in zeolite catalyzed reactions by combining the Maxwell–Stefan and Langmuir–Hinshelwood formulations†

Rajamani Krishna,* Richard Baur‡ and Jasper M. van Baten§

The combined phenomena of intra-crystalline adsorption, diffusion and reversible chemical reactions inside microporous crystalline zeolite catalyst particles are described by combining the Langmuir–Hinshelwood kinetics with the Maxwell–Stefan (M–S) diffusion formulation. Simulations of transient diffusion and reaction inside catalyst crystallites are performed for a variety of reactions including: alkane isomerization, xylene isomerization, ethylation of benzene and dehydrogenation of ethane. For all reaction systems, the transient diffusion/reaction process exhibits overshoots in the loading of the more mobile guest molecules within the zeolite pores; such overshoots imply the attainment of supra-equilibrium conversions for a limited time span. The origin of the transient overshoots is traceable to the use of chemical potential gradients as the proper driving forces in the M–S formulation; this leads to coupling effects induced by mixture adsorption thermodynamics. Use of the simplified Fick's law for intra-crystalline diffusion, ignoring thermodynamic coupling, does not result in overshoots. Simulations of fixed zeolite bed reactors are performed to demonstrate the significant differences in the productivity predicted by the M–S and Fick models for intra-crystalline diffusion.

1. Introduction

Zeolites are microporous crystalline aluminosilicates with pore dimensions in the range of 0.3 nm to 1 nm. The crystallographic structures of approximately 230 zeolites are listed in the database of the International Zeolite Association (IZA), using their three-letter IZA code names.[1] Of these, only a handful, MFI, MOR, MTW, FER, FAU, MWW, TON, LTL, CHA, and BEA, find applications as catalysts in processes such as alkane isomerization, xylene isomerization, toluene disproportionation, aromatization, transalkylation of C9+ aromatics, olefin oligomerization, cumene synthesis, and linear alkylbenzene synthesis.[2–10] Most commonly, extra-framework

Van 't Hoff Institute for Molecular Sciences, University of Amsterdam, Science Park 904, 1098 XH Amsterdam, The Netherlands.
E-mail: r.krishna@contact.uva.nl

protons (H^+) form a bond with the negatively charged oxygen anions of the zeolite; this results in Brønsted OH acid sites that have high reactivity.

Intra-crystalline diffusion of reactants and products invariably exert a strong influence on the conversion and selectivity of zeolite-catalyzed reactions;[11–14] such influences are stronger and have a different character than the diffusion influences in amorphous meso-porous and macro-porous catalysts, that are commonly addressed in standard textbooks on chemical reaction engineering.[15–18] The intra-crystalline zeolite diffusivities may vary by several orders of magnitude, depending on molecular size, shape, configuration.[13,14,19–24] For example, in MFI zeolite, that has intersecting 0.55 nm sized channels, *p*-xylene can locate anywhere along the channels; see Fig. 1a. The isomers *o*-xylene, and *m*-xylene are more strongly constrained in the channels and prefer to locate at the channel intersections, that offers more "leg-room". Due to subtle configurational differences, the diffusivity of *p*-xylene in MFI zeolite is about 2–3 orders of magnitude higher than that of *o*-xylene and *m*-xylene.[2,25] In the xylene isomerization reaction, *p*-xylene can diffuse into and out of the catalyst much more easily and this enhanced mobility has a strong influence on reaction selectivity. There is also a wide variety of other non-linear phenomena, such as the window effect, associated with diffusion and reaction in zeolite catalysts.[12–14]
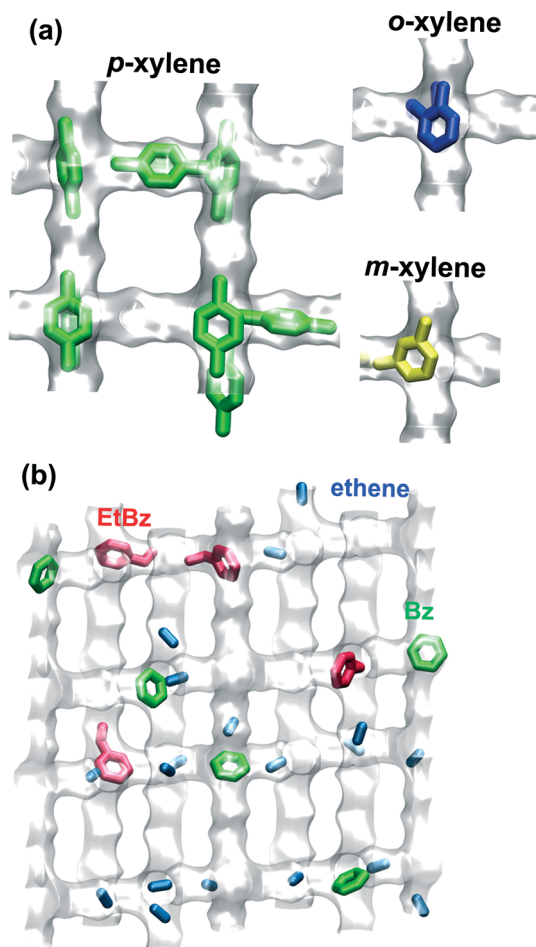
Fig. 1 (a) Snapshots showing the location of p-xylene, o-xylene, and m-xylene within the intersecting channel topology of MFI zeolite. (b) Snapshot showing the location of reactants and products in the alkylation of benzene with ethene to produce ethylbenzene using H-ZSM-5 catalyst.

For the ethylation of benzene using H-ZSM-5 catalyst to produce ethylbenzene, both benzene (reactant) and ethylbenzene (product) are preferentially located at the channel intersections; see Fig. 1b. The blocking of intersections by the aromatic guest molecules causes the effective diffusivity of reactant ethene inside the catalyst to reduce five-fold as the total mixture loading approaches 2 molecules per unit cell.[26]

Within the zeolite micropores, the guest molecules are in the adsorbed state; broadly speaking, the stronger the binding energy, the lower is the guest molecule mobility within the zeolite framework.[27,28] Mixture adsorption thermodynamics has a strong and direct influence on the transport fluxes; the chemical potential gradients are the proper driving forces for intra-crystalline species transport. It is now generally recognized that the Maxwell–Stefan (M–S) formulation, that has its roots in irreversible thermodynamics, affords a proper description of intra-crystalline diffusion.[19,20,26,29–32] For n-component diffusion, the fluxes N_i, relative to the zeolite pore walls, are related to the chemical potential gradients by

$$-\rho \frac{q_i}{RT} \frac{\partial \mu_i}{\partial r} = \sum_{\substack{j=1 \\ j \neq i}}^{n} \left(\frac{x_j N_i - x_i N_j}{Đ_{ij}} \right) + \frac{N_i}{Đ_i}; \quad i = 1, 2 \ldots n \quad (1)$$

where ρ is the framework density with units of kg m^{-3}; q_i is the molar loading of component i in the adsorbed phase with units moles per kg of framework; μ_i is the molar chemical potential of component i. The x_i represent the component mole fractions in the adsorbed phase within the pores

$$x_i = q_i/q_t; \quad q_t = \sum_{i=1}^{n} q_i; \quad i = 1, 2, \ldots n.$$

The M–S diffusivity $Đ_i$, with the units m^2 s^{-1}, is to be interpreted as an inverse drag coefficient between the adsorbate and the surface. For meso-porous, and macro-porous materials, for example, the $Đ_i$ is relatable to the Knudsen diffusivity.[33]

The $Đ_{ij}$ may be interpreted as the inverse drag coefficient between species i and species j. At the molecular level, the $Đ_{ij}$ reflect how the facility for transport of species i correlates with that of species j; they are also termed exchange coefficients. The Onsager reciprocal relations demand the symmetry constraint $Đ_{ij} = Đ_{ji}; i,j = 1, 2, \ldots n$. For all of the examples treated in this article, i–j correlations are considered to be negligible, i.e. $Đ_i/Đ_{ij} \ll 1$, and eqn (1) simplifies to yield

$$N_i = -\rho Đ_i \frac{q_i}{RT} \frac{\partial \mu_i}{\partial r}; \quad i = 1, 2 \ldots n \quad (2)$$

The chemical potential gradients $\partial \mu_i/\partial r$ can be related to the gradients of the molar loadings, q_i, by defining thermodynamic correction factors Γ_{ij}

$$\frac{q_i}{RT} \frac{\partial \mu_i}{\partial r} = \sum_{j=1}^{n} \Gamma_{ij} \frac{\partial q_j}{\partial r}; \quad \Gamma_{ij} = \frac{q_i}{p_i} \frac{\partial p_i}{\partial q_j}; \quad i, j = 1, \ldots n \quad (3)$$

Consider the special case in which each of the pure component adsorption isotherms is described by a single-site Langmuir isotherm model $q = q_{sat} \frac{bp}{1+b}$; $\theta = \frac{bp}{1+bp}$; $bp = \frac{\theta}{1-\theta}$ where p is the bulk gas pressure and we define the fractional occupancy of the adsorbate molecules, $\theta = q/q_{sat}$. The single-site Langmuir isotherm can be derived by equating the rate of adsorption with the rate of desorption. The rate of adsorption is proportional to the total number of vacant sites, Rate$_{ads} = k_{ads} p n_{sites} \theta_V = k_{ads} n_{sites} p(1 - \theta)$. The rate of desorption is proportional to the number of occupied sites, Rate$_{des} = k_{des} n_{sites} \theta$. At adsorption equilibrium, we have $k_{ads} p n_{sites}(1 - \theta) = k_{des} N_{sites} \theta$ and so, $\frac{k_{ads} p}{k_{des}} = bp = \frac{\theta}{(1-\theta)}$. The Langmuir adsorption constant, is

simply the ratio of the adsorption rate constant to the desorption rate constant, $b \equiv \dfrac{k_{ads}}{k_{des}}$.

The mixed gas Langmuir model for calculation of the component loadings in the adsorbed phase is

$$q_i = \frac{q_{i,sat} b_i p_i}{1 + b_1 p_1 + b_2 p_2 + \dots + b_n p_n}; \quad i = 1, 2 \dots n \qquad (4)$$

where p_i is the partial pressure of component i in the bulk gas phase. The elements of the matrix of thermodynamic correction factors can be determined by analytic differentiation of eqn (4); the resulting expression is[34]

$$\Gamma_{ij} = \delta_{ij} + \left(\frac{q_{i,sat}}{q_{j,sat}} \right) \left(\frac{\theta_i}{\theta_V} \right); \quad i, j = 1, 2 \dots n \qquad (5)$$

In eqn (5), we define the fractional occupancies

$$\theta_i = \frac{q_i}{q_{i,sat}}; \quad i = 1, 2, \dots n \qquad (6)$$

and the fractional vacancy θ_V

$$\theta_V = 1 - \theta_1 - \theta_2 \dots - \theta_n = \frac{1}{1 + b_1 p_1 + b_2 p_2 + \dots + b_n p_n} \qquad (7)$$

Eqn (2) can be combined with eqn (3) to yield

$$N_i = -\rho Đ_i \sum_{j=1}^{n} \Gamma_{ij} \frac{\partial q_j}{\partial r}; \quad i = 1, 2 \dots n \qquad (8)$$

For detailed discussions on the applicability of the simplified M–S eqn (8), the reader is referred to earlier works.[19,20,35,36] An important persuasive advantage of the M–S equations is that the $Đ_i$ for mixture diffusion often retains the same magnitude and loading dependence as for unary diffusion.[19,20,35] Molecular dynamics (MD) data[19,20,27–29,37–40] on the M–S diffusivities of a wide variety of guest/zeolite combinations show that the loading dependence can be divided into two broad categories: (1) "weak confinement" scenario which $Đ_i$ are practically loading independent, and (2) "strong confinement" scenario for the M–S diffusivity is proportional to the factional vacancy, $Đ_i = Đ_i(0)\theta_V$, where $Đ(0)$ is the zero-loading diffusivity. Fig. S25–S29† illustrate the applicability of the two scenarios for two common zeolite catalysts, MFI and MOR.

Fig. 2 presents calculations of Γ_{ij}, as a function of total mixture occupancy, $\theta_1 + \theta_2 = 1 - \theta_V$, for adsorption of 1:1 mixtures of 2-methylpentane (2MP) and 2,2 dimethyl-butane (22DMB) in MFI zeolite. The off-diagonal elements Γ_{12}, and
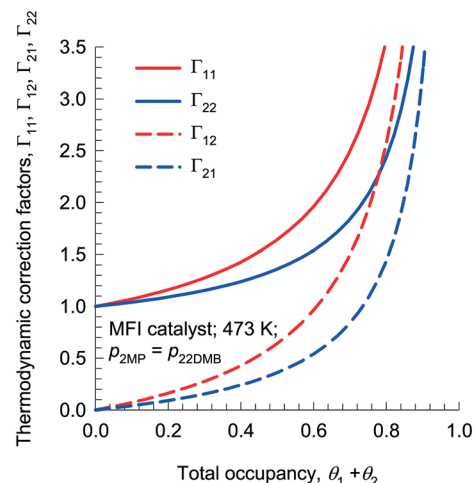

Fig. 2 Elements of the matrix of thermodynamic correction factors Γ_{ij} as a function of total mixture occupancy, $\theta_1 + \theta_2 = 1 - \theta_V$, calculated using the mixed-gas Langmuir model for binary 2MP(1)/22DMB(2) mixture adsorption in MFI zeolite at 473 K. The ratio of partial pressures in the gas phase is 1:1. In these calculations the total gas pressure, p_t, was varied from 0 to 1 MPa.

Γ_{21} become increasingly important with increased mixture occupancy, $\theta_1 + \theta_2$. In particular, it is noteworthy that the off-diagonal elements Γ_{12} and Γ_{21} get progressively closer to diagonal elements Γ_{11} and Γ_{22} as $\theta_1 + \theta_2 \rightarrow 1$. Due to finite magnitudes of Γ_{12}, and Γ_{21}, an important characteristic of diffusion in zeolites is that the flux of any component may be engendered by the gradients in the molar loadings of all the n species in the mixture. Such coupling effects have their origins in mixture adsorption thermodynamics; we shall use the term "thermodynamic coupling" to characterize these.

In the Henry regime of adsorption, when the fractional occupancies are vanishingly small, we have the special case that the matrix of thermodynamic factors reduces to the identity matrix $\Gamma_{ij} \rightarrow \delta_{ij}$, and we obtain the uncoupled form of the flux equations

$$N_i = -\rho Đ_i \frac{\partial q_i}{\partial r}; \quad i = 1, 2 \dots n \qquad (9)$$

Eqn (9) may be considered to be representative of the Fick's law of diffusion for intra-crystalline transport; this flux expression is commonly employed for calculation of effectiveness factors in meso-porous and macro-porous catalysts.[15–17] While implementing the Fickian eqn (9), we commonly assume that the M–S diffusivity is independent of loading.

The primary objective of this communication is to highlight the important consequences of thermodynamic coupling on the performance of a number of zeolite catalyzed reactions, including alkane isomerization, xylene isomerization, ethylation of benzene and dehydrogenation of ethane. We aim to demonstrate the possibility of transient overshoots and uphill transport in zeolite catalysts; such phenomena are not anticipated by use of simple *uncoupled*

326 | *React. Chem. Eng.*, 2017, **2**, 324–336

This journal is © The Royal Society of Chemistry 2017

Fickian eqn (9). Simulations of fixed zeolite bed reactors will be used to demonstrate the strong influence of thermodynamic coupling effects on the selectivity and productivity. For all calculations and simulations presented in this article, we compare the results obtained by the use of three different scenarios for flux calculations.

(1) M–S model eqn (8) with "weak" confinement scenario; thermodynamic coupling effects are duly accounted for using the appropriate model to describe mixture adsorption equilibrium.

(2) M–S model eqn (8) with strong confinement scenario $Đ_i = Đ_i(0)θ_V$ and inclusion of thermodynamic coupling effects.

(3) Fick model eqn (9) in which the M–S diffusivities are independent of loading, and thermodynamic coupling effects are ignored, i.e. $Γ_{ij} = δ_{ij}$.

The ESI† accompanying this publication provides (a) structural data on commonly used zeolite catalysts, (b) detailed derivations of the Maxwell–Stefan (M–S) equations for intra-crystalline diffusion, (c) background information on the loading dependence of M–S diffusivities, (d) computational modelling of transient uptake within single crystals, and (e) computational modeling of transient breakthroughs in fixed bed reactors. The input data on isotherms, M–S diffusivities, and reaction rate constants in the variety of illustrative examples used in this article are provided in Tables 4–11 of the ESI.†

2. Catalyst effectiveness factor

Consider the reversible reaction of 2-methylpentane (2MP) and 2,2 dimethyl-butane (22DMB), 2MP(1) ⇌ 22DMB(2), that is important in the context of increasing the octane number of gasoline. The rate of chemical reaction, expressed as mol kg catalyst^{-1} s^{-1}, R_{kg}, may written as

$$R_{kg} = k_1 q_1 - k_2 q_2 \tag{10}$$

The component loadings q_i may be described by the mixed-gas Langmuir model (eqn (4)), and therefore we derive the familiar Langmuir–Hinshelwood expression

$$R_{kg} = \frac{k_1 q_{1,sat} b_1 p_1 - k_2 q_{2,sat} b_2 p_2}{1 + b_1 p_1 + b_2 p_2} \tag{11}$$

The radial distribution of molar loadings, q_i, within a spherical zeolite crystallite, of radius r_c, is obtained from a solution of a set of differential equations

$$ρ \frac{∂q_i(r,t)}{∂t} = -\frac{1}{r^2} \frac{∂}{∂r}(r^2 N_i) + ρν_i R_{kg} \tag{12}$$

where $ν_i$ is the reaction stoichiometric coefficient; $ν_1 = -1$ for reactant 2MP; $ν_2 = 1$ for product 22DMB. Under steady-state conditions we have

$$\frac{1}{r^2} \frac{∂}{∂r}(r^2 N_i) = ρν_i R_{kg} \tag{13}$$

After insertion of the appropriate rate expressions for the chemical reaction rate, R_{kg}, the flux equations for N_i, the eqn (13) can be solved to obtain the steady-state distribution of the loadings of the components along the crystal radius, r. The effectiveness factor, $η$, is

$$η = \frac{\int_0^1 R_{kg} ξ^2 dξ}{R_{kg}|_{r=r_c} \int_0^1 ξ^2 dξ} \tag{14}$$

where $ξ = r/r_c$ is the dimensionless radial coordinate. The chemical reaction rate R_{kg} varies with loading and is $ξ$-dependent. In the absence of any diffusional limitations, $η = 1$, and the chemical reaction rate can be calculated using the loadings at the external surface, $R_{kg}|_{r=r_c}$.

For the Fickian model in which thermodynamic coupling effects are ignored, $Γ_{ij} → δ_{ij}$, and the $Đ_i$ are considered to be loading independent, the effectiveness factor is given by

$$η = \frac{1}{φ}\left(\frac{1}{\tanh(3φ)} - \frac{1}{3φ}\right) \tag{15}$$

where the classic Thiele modulus is defined as

$$φ ≡ \frac{r_c}{3}\sqrt{\frac{k_1}{Đ_1(0)} + \frac{k_2}{Đ_2(0)}} \tag{16}$$

Baur and Krishna[41,42] have presented analytic solutions to eqn (1) and (13) for two different descriptions of the loading-dependence of the M–S diffusivities $Đ_i$; see details in the ESI.† In the "weak confinement" scenario the M–S diffusivity is loading independent, i.e. $Đ_i = Đ_i(0)$, the value at zero-loading. In the "strong confinement" scenario the M–S diffusivity is taken as being proportional to the fractional vacancy: $Đ_i = Đ_i(0)θ_V$.

Fig. 3a presents calculations of the effectiveness factor, $η$, for uptake inside MFI catalyst exposed to a gas phase 2MP(1)/22DMB(2) mixture at 473 K; the partial pressures of the components in the bulk gas phase are $p_1 = p_2 = 10$ kPa. The x-axis in Fig. 3a is the Thiele modulus, calculated using eqn (16). From configurational considerations, the di-branched isomer 22DMB has a diffusivity that is 80 times lower than the diffusivity of the mono-branched isomer 2MP, i.e. $Đ_1(0)/Đ_2(0) = 80$. The highest effectiveness factors are obtained with Fickian model that assumes $Γ_{ij} = δ_{ij}$. As is to be expected, diffusional influences are strongest for the scenario in which the M–S diffusivities are linearly related to the vacancy, $Đ_i = Đ_i(0)θ_V$.

The most important feature of the M–S formulation is the proper accounting of thermodynamic coupling influences. In order to stress the direct influence of adsorption
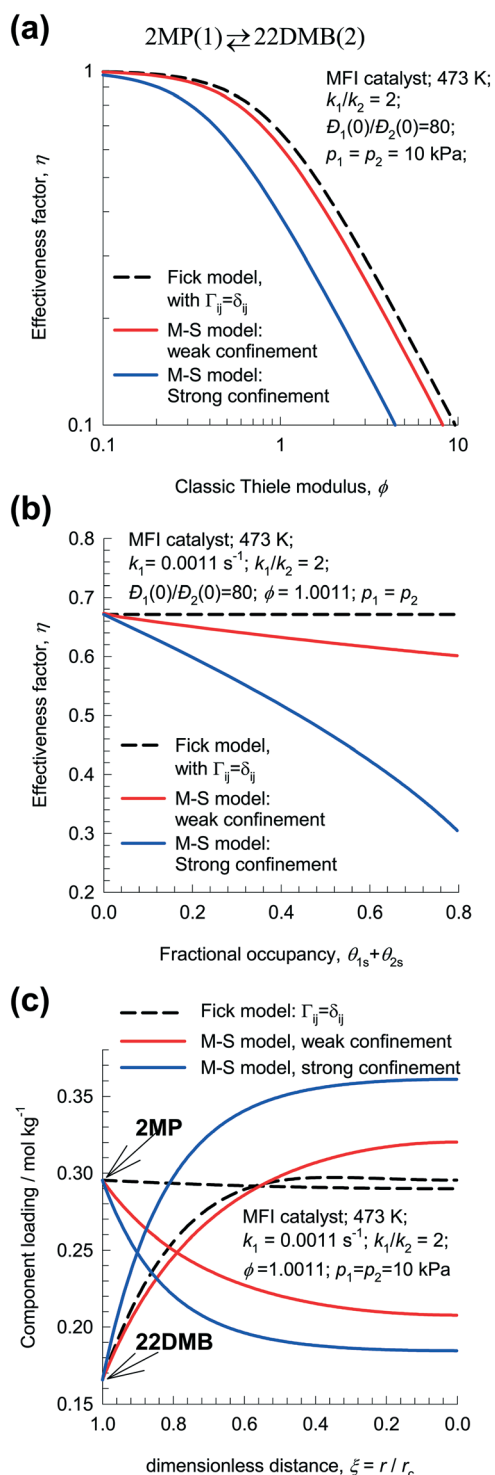
This journal is © The Royal Society of Chemistry 2017

React. Chem. Eng., 2017, **2**, 324–336 | **327**

(a)

$$2MP(1) \rightleftarrows 22DMB(2)$$

MFI catalyst; 473 K;
$k_1/k_2 = 2$;
$Đ_1(0)/Đ_2(0) = 80$;
$p_1 = p_2 = 10$ kPa;

- - - Fick model,
with $\Gamma_{ij} = \delta_{ij}$
—— M-S model:
weak confinement
—— M-S model:
Strong confinement

(b)

MFI catalyst; 473 K;
$k_1 = 0.0011$ s^{-1}; $k_1/k_2 = 2$;
$Đ_1(0)/Đ_2(0) = 80$; $\phi = 1.0011$; $p_1 = p_2$

- - - Fick model,
with $\Gamma_{ij} = \delta_{ij}$
—— M-S model:
weak confinement
—— M-S model:
Strong confinement

(c)

- - - Fick model: $\Gamma_{ij} = \delta_{ij}$
—— M-S model, weak confinement
—— M-S model, strong confinement

2MP

22DMB

MFI catalyst; 473 K;
$k_1 = 0.0011$ s^{-1}; $k_1/k_2 = 2$;
$\phi = 1.0011$; $p_1 = p_2 = 10$ kPa

Fig. 3 Calculation of the effectiveness factor, η, for MFI catalyst carrying out the 2MP(1) $\rightleftarrows$ 22DMB(2) reaction at 473 K. In (a), the partial pressures of the components in the bulk gas phase are $p_1 = p_2 = 10$ kPa. The ratio of rate constants $k_1/k_2 = 2$; the values of the rate constant k_1 are varied. In (b) the constant parameters are $k_1 = 0.0011$ s^{-1}; $k_1/k_2 = 2$; $\phi = 1.0011$. The partial pressures of the components in the bulk gas phase are $p_1 = p_2$; the total pressure $p_1 + p_2$ is varied in the range 0 to 40 kPa. The x-axis is the fractional occupancy at the catalyst surface, $\theta_{1s} + \theta_{2s}$. (c) Radial profile of component loadings for the specific case $p_1 = p_2 = 10$ kPa, $k_1 = 0.0011$ s^{-1}; $k_1/k_2 = 2$; $\phi = 1.0011$. All calculation details and data inputs are provided in the ESI.†

thermodynamics, Fig. 3b presents calculations of the effectiveness factor, η, for a MFI catalyst that is exposed to an equimolar gas 2MP/22DMB gas mixture; the total pressure $p_1 + p_2$ is varied in the range 0 to 40 kPa. Increasing the bulk gas pressure increases the fractional occupancy at the catalyst surface, $\theta_{1s} + \theta_{2s}$. The classical effectiveness factor, calculated from eqn (15), is a constant, independent of $\theta_{1s} + \theta_{2s}$. By proper accounting of the mixture adsorption thermodynamics, we note that the effectiveness factor for M–S model (weak, and strong confinement) decrease when $\theta_{1s} + \theta_{2s}$ increases.

Fig. 3c shows the steady-state radial distribution of component loadings for partial pressures $p_1 = p_2 = 10$ kPa in the bulk gas mixture. The M–S and Fick models yield significantly different radial profiles of the molar loadings; such differences may have consequences in complex reaction schemes.

3. Transient overshoots inside zeolite catalyst

The differences between the M–S and Fick models become much more significant when monitoring the transient approach to equilibrium within the zeolite catalyst. The analysis of transient adsorption, diffusion, and reaction in zeolites is of relevance in the proper interpretation of data obtained in TEOM (tapered element oscillating microbalance), and TAP (temporal analysis of products) experimental investigations.[43–45]

Consider the transient uptake with chemical reaction within MFI catalyst exposed to a gas phase 2MP/22DMB mixture at 473 K with the partial pressures of the components in the bulk gas phase are $p_1 = p_2 = 10$ kPa. The partial differential eqn (12) need to be solved numerically to obtain the spatio-temporal loadings within the catalyst; numerical details are provided in the ESI.† The spatial-averaged component loading within the crystallites of radius r_c is calculated using

$$\bar{q}_i(t) = \frac{3}{r_c^3} \int_0^{r_c} q_i(r,t) r^2 dr \qquad (17)$$

Fig. 4 plots the equilibration trajectories in ternary occupancy space, with coordinates, θ_1 (2MP), θ_2 (22DMB), θ_V (MFI zeolite vacancy); in the inset, $\bar{q}_i(t)$ is plotted as a function of $\sqrt{t}$. Both the M–S model implementations (weak and strong confinement) predict an overshoot in the spatial-averaged loading of the more mobile component 2MP. The Fickian model, that assumes $\Gamma_{ij} \rightarrow \delta_{ij}$, does not anticipate any overshoots in 2MP uptake and the equilibration trajectory in ternary occupancy space has a completely different, monotonous, character. There is a wide variety of experimental data on transient uptake of binary mixtures in zeolites, under non-reacting conditions, that show transient overshoots of
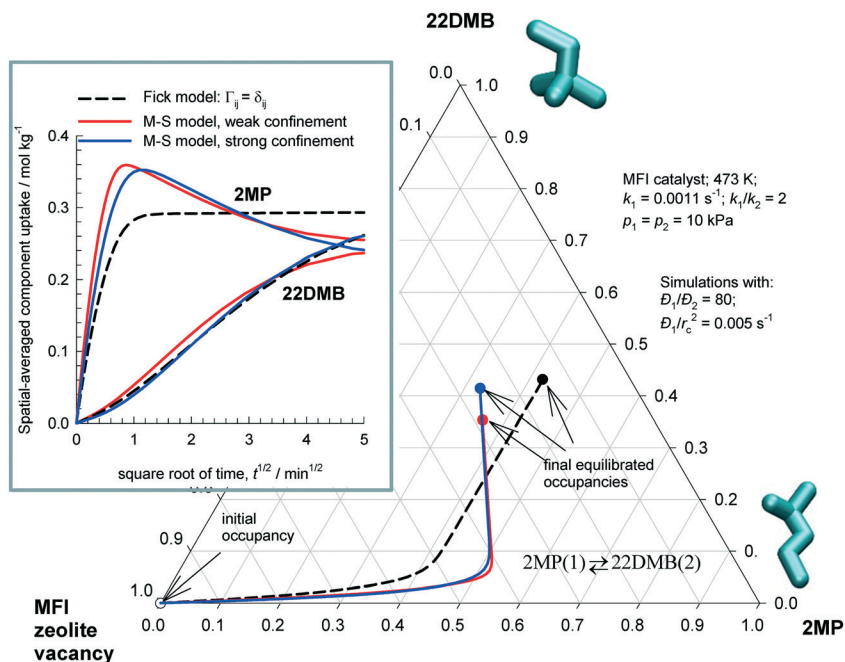
Fig. 4 Transient uptake inside MFI catalyst carrying out 2MP(1) ⇌ 22DMB(2) reaction. The equilibration trajectories are plotted in ternary occupancy space, with coordinates, θ_1 (2MP), θ_2 (22DMB), θ_V (MFI zeolite vacancy). The inset shows $\bar{q}_i(t)$ plotted as a function of $\sqrt{t}$. The continuous solid lines represent uptake simulations include thermodynamic coupling using eqn (8). The dashed lines represent uptake simulations ignoring thermodynamic coupling and use uncoupled flux eqn (9). All calculation details and data inputs are provided in the ESI.† Video animations of the spatio-temporal variations of the component loadings within the catalyst are available as ESI.†
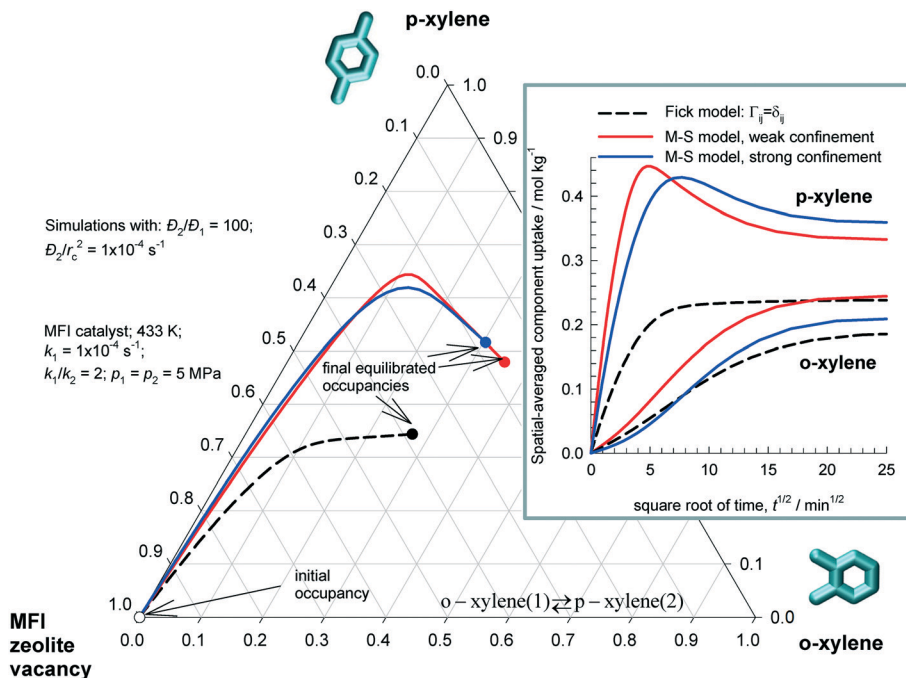
Fig. 5 Transient uptake inside MFI catalyst o-xylene(1) ⇌ p-xylene(2) reaction. The equilibration trajectory is plotted in ternary occupancy space, with coordinates, θ_1 (o-xylene), θ_2 (p-xylene), θ_V (MFI zeolite vacancy). The inset shows $\bar{q}_i(t)$ plotted as a function of $\sqrt{t}$. The continuous solid lines represent uptake simulations include thermodynamic coupling using eqn (8). The dashed lines represent uptake simulations ignoring thermodynamic coupling and use uncoupled flux eqn (9). All calculation details and data inputs are provided in the ESI.† Video animations of the spatio-temporal variations of the component loadings within the catalyst are available as ESI.†

the more mobile species, signifying uphill diffusion phenomena; a detailed analysis of the experimental data[30,46,47] leads to the conclusion that the origin of the overshoots can be traced to thermodynamic coupling effects, i.e. the non-

This journal is © The Royal Society of Chemistry 2017

React. Chem. Eng., 2017, **2**, 324–336 | **329**

diagonal elements of Γ_{ij}. The results in Fig. 4 also lead to the same conclusion; *i.e.* that the origin of transient overshoots in *reacting* systems is traceable to thermodynamic coupling, *i.e.* the off-diagonal elements of Γ_{ij}. Furthermore, the final equilibrated loadings are dependent on the scenario used to calculate the intra-crystalline fluxes. On the basis of the re-analysis of transient 2MP/22DMB breakthrough experiments of Jolimaître *et al.*[48,49] it has been established that the proper model to describe intra-crystalline diffusion is the M–S model with the weak confinement scenario for M–S diffusivities.[29,30]

Analogous results are obtained *o*-xylene(1) $\rightleftharpoons$ *p*-xylene(2) for reaction with MFI catalyst. Fig. 5 plots the equilibration trajectories in ternary occupancy space, with coordinates, θ_1 (*o*-xylene), θ_2 (*p*-xylene), θ_V (MFI zeolite vacancy); in the inset, $\bar{q}_i(t)$ is plotted as a function of $\sqrt{t}$. *Para*-Xylene has a signifi-cantly higher diffusivity than *o*-xylene due to configurational considerations; following the work of Mirth *et al.*[25] we as-sume that the diffusivity of *p*-xylene is 100 times that of *o*-xylene *i.e.* $Đ_1(0)/Đ_2(0) = 100$. Both the M–S model implementations (weak and strong confinement) predict an overshoot in the loading of the more mobile component *p*-xylene. Since *p*-xylene is the desired reaction product, the overshoot signifies the attainment of supra-equilibrium con-versions within the catalyst for a limited duration during the initial transience. Available experimental data[28,50,51] indicate that the M–S model with strong confinement scenario pro-vides an appropriate description of diffusivity of xylene iso-mers in MFI zeolite.

Consider transient uptake within MFI catalyst carrying out the isomerization of *n*-hexane (nC6) to produce mono-branched 3-methylpentane (3MP) and di-branched 2,2 di-methylbutane (22DMB). We restrict our analysis to the sim-plified reaction scheme[52]

$$nC6(1) \rightleftharpoons 3MP(2) \rightleftharpoons 22DMB(3) \tag{18}$$

where the Langmuir–Hinshelwood (L–H) reaction rate expres-sions for the two constituent reversible reactions, expressed as mol kg catalyst^{-1} s^{-1} are

$$R_{kg,1} = (k_{f1}q_1 - k_{b1}q_2) \quad R_{kg,2} = (k_{f2}q_2 - k_{b2}q_3) \tag{19}$$

The subscripts f and b refer to the forward and reverse re-actions, and the subscripts 1 and 2 refer to the first and sec-ond isomerization reaction steps in eqn (18). For total pres-sures exceeding about 100 Pa, the hierarchy of adsorption strengths is nC6 > 3MP > 22DMB due to subtle configura-tional entropy effects arising out of the preferential location of the branched isomers at the channel intersections; the lin-ear nC6 can locate anywhere along the intersecting channel network. For a quantitative description of entropy effects, the mixture adsorption equilibrium is determined using the Ideal Adsorbed Solution Theory (IAST); see Fig. S30–S33 of the ESI.†

Fig. 6a presents simulations of transient uptake inside MFI catalyst exposed to a gas phase nC6(1)/3MP(2)/22DMB(3)

mixture at 362 K; the partial pressures of the components in the bulk gas phase are $p_1 = 1000$ Pa; $p_2 = 1$ Pa, $p_3 = 1$ Pa. The zero-loading M–S diffusivities are $Đ_1(0)/r_c^2 = 2 \times 10^{-4}$ s^{-1}; $Đ_2(0)/r_c^2 = 2 \times 10^{-5}$ s^{-1}; $Đ_3(0)/r_c^2 = 1 \times 10^{-5}$ s^{-1}; the choice of these diffusivities is based on earlier works.[29,30,36,53] The con-tinuous solid lines represent uptake simulations with the M–S eqn (8). We note that the most mobile nC6 displays an overshoot during transient uptake. 3-Methylpentane (3MP), with intermediate mobility, also exhibits a slight overshoot. The dashed lines represent uptake simulations with uncoupled Fickian flux eqn (9); in this scenario, all three components approach equilibrium in a monotonous manner. In the transient uptake experiments of Titze *et al.*,[36] the M–S model, with the weak confinement scenario, has been established to be a good representation of the uptake of *n*-hexane/2-methylpentane mixtures in MFI zeolite.

Fig. 6b presents the corresponding results for transient up-take during the *n*-hexane isomerization reaction nC6(1) $\rightleftharpoons$ 2MP(2) $\rightleftharpoons$ 22DMB(3) using MOR catalyst. For total pressures exceeding 10 kPa, the adsorption hierarchy in this cases is nC6 < 2MP < 22DMB; this is dictated by the fact that most com-pact 22DMB molecules can be most efficiently packed within the 12-ring channels of MOR;[40] see Fig. S34 and S35 of the ESI.† The M–S model calculations, with either weak or strong confinement, display overshoots for the more mobile nC6, and 2MP. No such overshoots are anticipated by the Fick model that ignores thermodynamic coupling; in this scenario all three guest molecules equilibrate monotonously. From the MD simu-lation data of van Baten and Krishna[40] for hexane isomers in MOR, it can be established that the M–S model with the strong confinement scenario is the appropriate one to use.

H-ZSM-5, which has the MFI topology, is used as a catalyst for carrying out the ethylation of benzene to produce ethyl-benzene ethene(1) + benzene(2) $\rightleftharpoons$ ethylbenzene(3); for back-ground on the process and reaction kinetics, see Hansen *et al.*[26,54] In our simulations we use the Langmuir–Hinshel-wood rate expression

$$R_{kg} = k_f q_1 q_2 - k_b q_3 \tag{20}$$

Fig. 7a presents the simulation results for transient uptake inside MFI catalyst exposed to a gas phase ethene(1)/benzene(2)/ethylbenzene(3) mixture at 653 K; the partial pres-sures of the components in the bulk gas phase are $p_1 = 0.6$ MPa; $p_2 = 0.4$ MPa; $p_3 = 0$ MPa. Based on MD simulation data,[26] the zero-loading M–S diffusivities are taken to be $Đ_1(0)/r_c^2 = 1 \times 10^{-3}$ s^{-1}, $Đ_2(0)/r_c^2 = 2 \times 10^{-5}$ s^{-1}; $Đ_3(0)/r_c^2 = 1 \times 10^{-5}$ s^{-1}. Both the M–S model implementations, with weak and strong confinement, predict ethene loading overshoots. The Fickian approach, assuming $\Gamma_{ij} = \delta_{ij}$, anticipates monoto-nous equilibration of all three guest molecules. The MD sim-ulation data of Hansen *et al.*[26] indicate that the M–S model with strong confinement is the appropriate model to use for ethylation of benzene.

Hansen *et al.*[54] describe the use of MFI catalyst for the de-hydrogenation of ethane to produce ethene: ethane(1) $\rightleftharpoons$
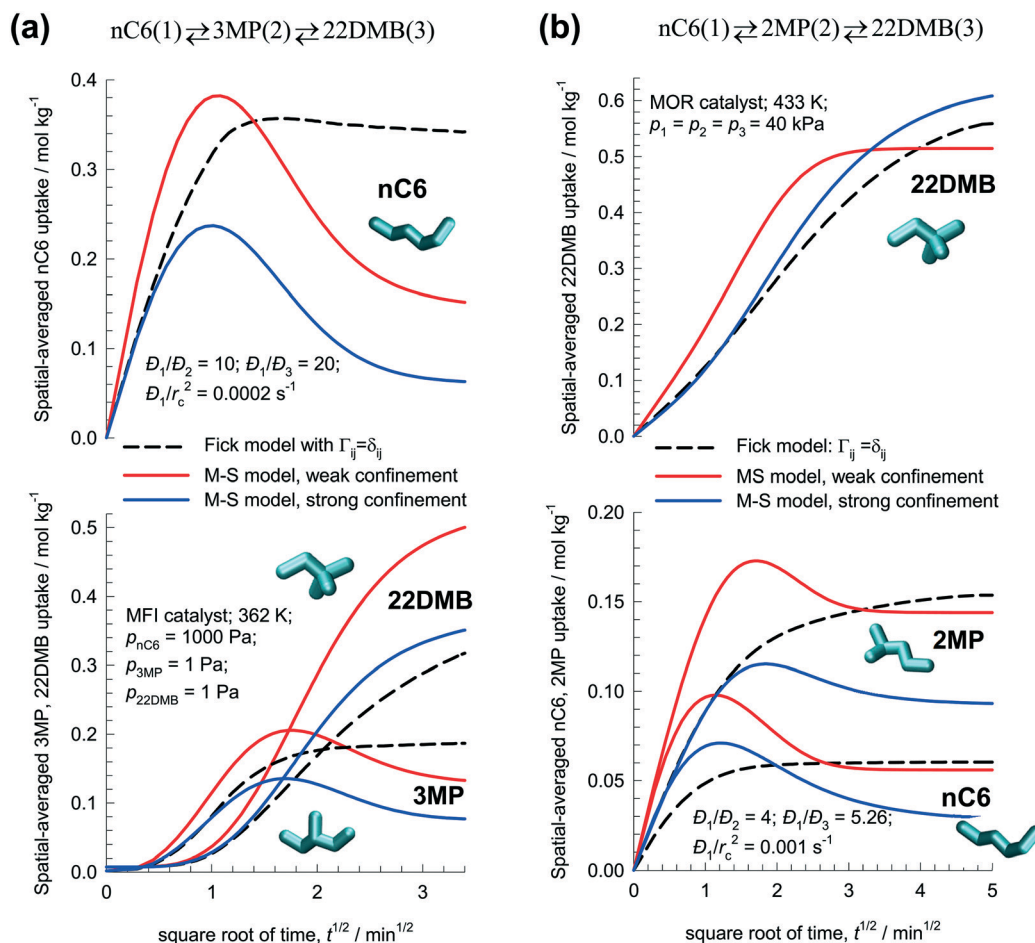
330 | *React. Chem. Eng.*, 2017, **2**, 324–336

This journal is © The Royal Society of Chemistry 2017

Fig. 6 Transient uptake inside zeolite catalysts for the *n*-hexane isomerization reactions: (a) MFI nC6(1) ⇌ 3MP(2) ⇌ 22DMB(3) with MFI catalyst, and (b) nC6(1) ⇌ 2MP(2) ⇌ 22DMB(3) with MOR catalyst. The spatial-averaged loadings are calculated using eqn (17). The continuous solid lines represent uptake simulations include thermodynamic coupling using eqn (8). The dashed lines represent uptake simulations ignoring thermodynamic coupling and use uncoupled flux eqn (9). All calculation details and data inputs are provided in the ESI.† Video animations of the spatiotemporal variations of the component loadings within the catalyst are available as ESI.†

ethene(2) + hydrogen(3). The reaction rate R_{kg} expressed as mol kg catalyst^{-1} s^{-1} is

$$R_{kg} = k_f q_1 - k_b q_2 q_3 \quad (21)$$

Fig. 7b presents the simulation results for transient uptake inside MFI catalyst exposed to a gas phase ethane(1)/ethene(2)/hydrogen(3) mixture at 653 K. The partial pressures of the components in the bulk gas phase are p_1 = 1.0 MPa; p_2 = 2 MPa, p_3 = 3 MPa. Both the M–S model implementations (with weak and strong confinement) predict overshoots in the spatial-averaged loading of the most mobile H$_2$. The Fick model anticipates monotonous equilibration for all guest species.

4. Fick *vs.* Maxwell–Stefan models for fixed bed reactors

We now examine how thermodynamic coupling effects influence the performance of fixed and moving bed reactors; such effects are commonly ignored in reactor models that are used

in practice.[16,55] Simulated moving bed (SMB) reactors are commonly operated in transient mode. Assuming plug flow of an *n*-component gas mixture through a fixed bed maintained under isothermal conditions, the partial pressures in the gas phase at any position and instant of time are obtained by solving the following set of partial differential equations for each of the species *i* in the gas mixture

$$\frac{1}{RT}\frac{\partial p_i(t,z)}{\partial t}$$
$$= -\frac{1}{RT}\frac{\partial(v(t,z)p_i(t,z))}{\partial z} - \frac{(1-\varepsilon)}{\varepsilon}\frac{3}{r_c}\left(N_i\big|_{r=r_c}\right); \quad i = 1, 2, \ldots n \quad (22)$$

In eqn (22), *t* is the time, *z* is the distance along the reactor, ρ is the framework density, ε is the bed voidage, *v* is the interstitial gas velocity, and $N_i\big|_{r=r_c}$ is the molar flux loading at the position $r = r_c$, monitored at position *z*, and at time *t*, determined by use of eqn (8) or eqn (9), as appropriate. Robust
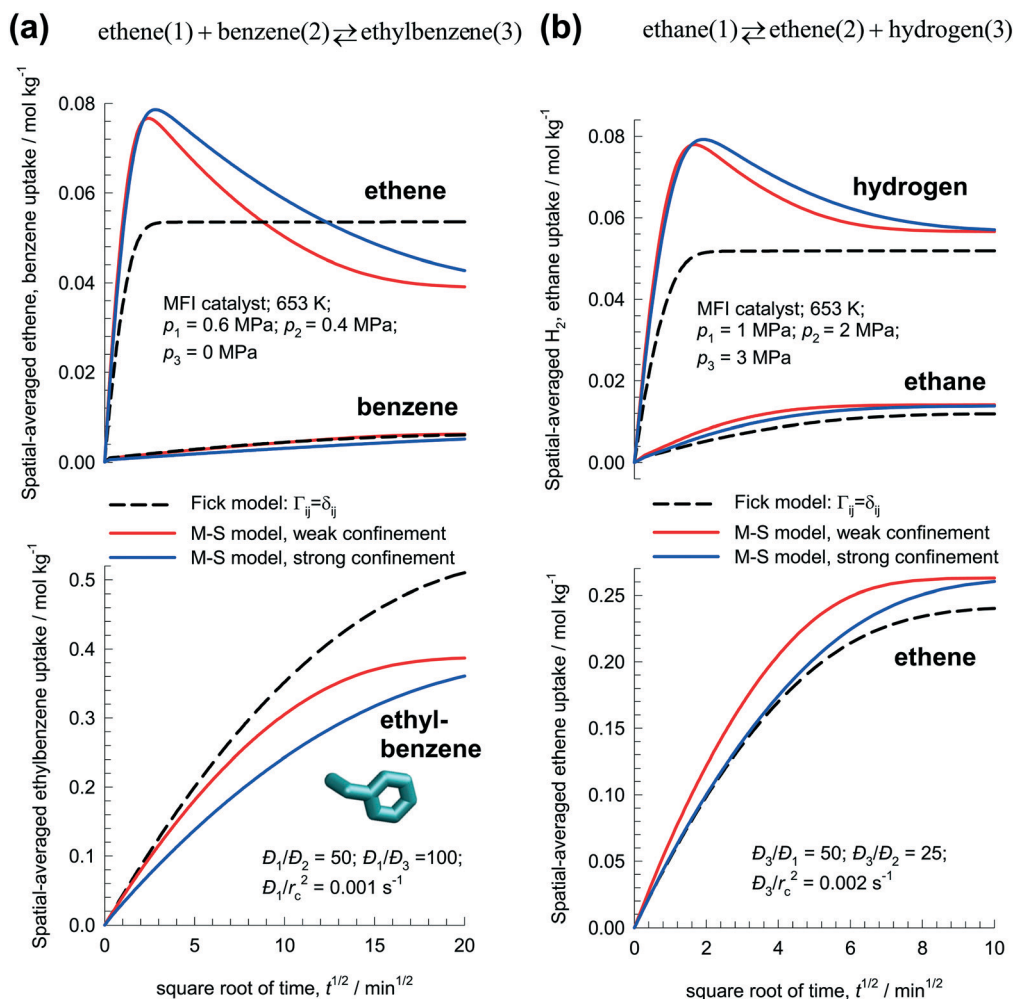
This journal is © The Royal Society of Chemistry 2017

React. Chem. Eng., 2017, **2**, 324–336 | 331

Fig. 7 Transient uptake inside MFI catalyst with: (a) ethene(1) + benzene(2) ↔ ethylbenzene(3), and (b) ethane(1) ↔ ethene(2) + hydrogen(3) reaction. The spatial-averaged loadings are calculated using eqn (17). The continuous solid lines represent uptake simulations include thermodynamic coupling using eqn (8). The dashed lines represent uptake simulations ignoring thermodynamic coupling and use uncoupled flux eqn (9). All calculation details and data inputs are provided in the ESI.† Video animations of the spatio-temporal variations of the component loadings within the catalyst are available as ESI.†

computational procedures are required for solving the set of eqn (22); these are outlined in the ESI.†

Fig. 8a presents the transient breakthrough simulations for fixed bed 2MP/22DMB isomerization reactor with MFI. The plot shows the molar concentrations in the gas phase as a function of the dimensionless time, $\tau = tv/L$, obtained by dividing the actual time, t, by the characteristic time, L/v. The continuous solid lines represent breakthrough simulations using eqn (8), along with the weak confinement scenario. The dashed lines represent breakthrough simulations using the uncoupled Fickian eqn (9). The transient breakthroughs are predicted to be sharper in the M–S model implementation. 22DMB with purities exceeding 90% can be recovered during the earlier stages of transient breakthrough as indicated in Fig. 8b; at steady-state, the product exiting the reactor contains 70% 22DMB. Baur and Krishna[56] present a detailed analysis of transient operations of SMB reactors for optimal 2MP/22DMB isomerization performance, obviating the need for a subsequent separation step to recover 22DMB.

The use of zeolite SMB reactors for alkane isomerization has been patented by Universal Oil Products (UOP).[57–59]

At steady-state, the gas phase concentrations of 2MP, and 22DMB long the dimensionless length of the fixed bed reactor are shown in Fig. 9a. Using the M–S model, the rate of production of 22DMB is 1.81×10^{-4} mol kg catalyst^{-1} s^{-1}; this value is significantly higher than the rate of production of 22DMB predicted by the Fick model: 1.14×10^{-4} mol kg catalyst^{-1} s^{-1}. The use of the conventional Fick model will severely under-predict 22DMB productivity.

The conclusion that the Fick model predicts diminished productivity of the desired product is not, however, a general one. Fig. 9b shows the shows the steady-state gas phase molar concentrations of o-xylene and p-xylene along the length of the reactor bed for o-xylene(1) ⇌ p-xylene(2) isomerization reaction. For the M–S model, assuming the strong confinement scenario, the rate of production of p-xylene is 5.7×10^{-6} mol kg catalyst^{-1} s^{-1}; this value is significantly lower than the rate of production of p-xylene predicted by

332 | *React. Chem. Eng.*, 2017, **2**, 324–336

This journal is © The Royal Society of Chemistry 2017
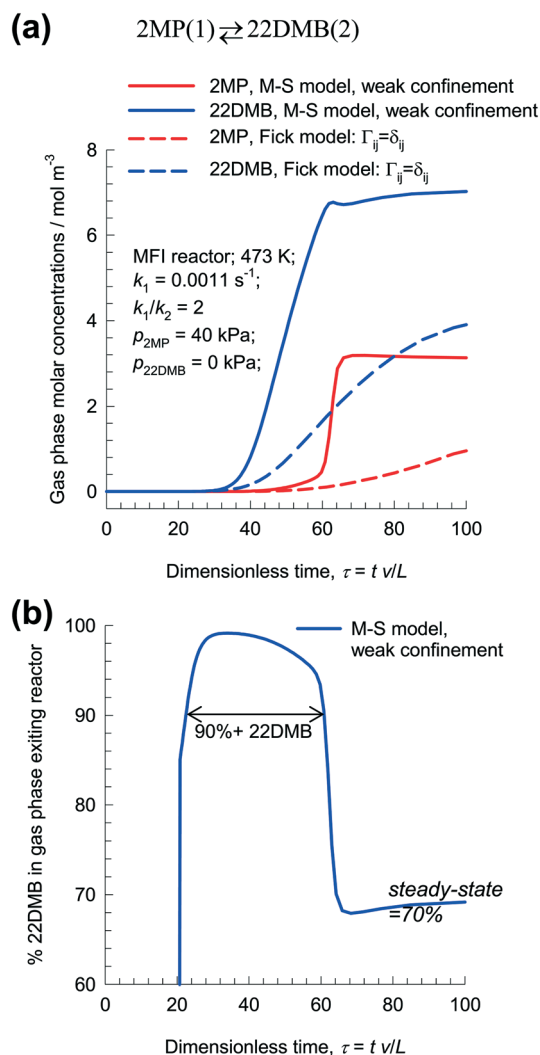
(a) $2MP(1) \rightleftarrows 22DMB(2)$

(b)

Fig. 8 (a) Transient breakthrough simulations for fixed bed with MFI extrudates, carrying out the isomerization reaction 2MP(1) $\rightleftarrows$ 22DMB(2). The partial pressures of the components in the bulk gas phase at the reactor inlet are $p_1 = 40$ kPa, $p_2 = 0$ kPa. The continuous solid lines represent simulations using eqn (8), along with the weak confinement scenario. The dashed lines represent breakthrough simulations ignoring thermodynamic coupling and using uncoupled flux eqn (9). (b) The plot shows the % 22DMB in the gas phase as a function of the dimensionless time, $\tau = tv/L$, obtained by dividing the actual time, t, by the characteristic time, L/v. All calculation details and data inputs are provided in the ESI.†

(a) $2MP(1) \rightleftarrows 22DMB(2)$

(b) $o - xylene(1) \rightleftarrows p - xylene(2)$

Fig. 9 Steady-state molar concentrations of (a) 2MP/22DMB, and (b) o-xylene/p-xylene along the dimensionless length of fixed bed isomerization reactor with MFI catalyst. All calculation details and data inputs are provided in the ESI.†

the Fick model calculations that ignores thermodynamic coupling: 7.2×10^{-6} mol kg catalyst^{-1} s^{-1}. Use of the Fick model to predict reactor performance will be overly optimistic in this case; this conclusion is opposite to that for the 2MP(1) $\rightleftarrows$ 22DMB(2) reaction. The differences in the two foregoing examples are rationalized as follows. For 2MP/22DMB, the desired product is the tardier species; for o-xylene/p-xylene, the desired isomerization product is the more mobile species.

Whether the simple Fickian model over-predicts or under-predicts the productivity of the desired species also depends on the hierarchy of adsorption strengths. To illustrate this,

we consider n-hexane isomerization using two different catalysts: MFI, and MOR. Fig. 10a shows the steady-state molar concentrations of 22DMB along the dimensionless length of fixed bed nC6(1) $\rightleftarrows$ 3MP(2) $\rightleftarrows$ 22DMB(3) isomerization reactor with MFI catalyst; the hierarchy of adsorption strengths is nC6 > 3MP > 22DMB. In this case, the Fickian model predicts a 22DMB productivity of 7.82×10^{-5} mol kg catalyst^{-1} s^{-1}; this value is lower than either of the two different implementations of the M–S model. For the weak confinement scenario, the rate of production of 22DMB is 3.4×10^{-4} mol kg catalyst^{-1} s^{-1}. For the strong confinement scenario, the rate of production of 22DMB is 2.74×10^{-4} mol kg catalyst^{-1} s^{-1}.

This journal is © The Royal Society of Chemistry 2017

React. Chem. Eng., 2017, **2**, 324–336 | 333

Fig. 10b shows the steady-state molar concentrations of 22DMB along the dimensionless length of fixed bed nC6(1) $\rightleftharpoons$ 2MP(2) $\rightleftharpoons$ 22DMB(3) isomerization reactor with MOR catalyst. As explained earlier, entropy effects in MOR lead to the reverse adsorption hierarchy nC6 < 2MP < 22DMB. For the Fickian model that ignores thermodynamic coupling, the productivity of 22DMB is 9.9×10^{-4} mol kg catalyst^{-1} s^{-1}; this value is higher than that predicted by either of the two M–S model implementations: weak confinement: 8.7×10^{-4} mol kg catalyst^{-1} s^{-1}; strong confinement: 4.72×10^{-4} mol kg catalyst^{-1} s^{-1}.

For the ethylation reaction ethene(1) + benzene(2) $\rightleftharpoons$ ethylbenzene(3), the desired product ethylbenzene is least mobile but most strongly adsorbed. Fig. 11a compares the ethylbenzene concentrations in the gas phase along the length of the fixed zeolite bed at steady-state using the Fick and M–S models. The Fick model predicts the productivity of ethylbenzene as: 1.6×10^{-3} mol kg catalyst^{-1} s^{-1}; this value is significantly higher than that predicted by either of the two M–S model implementations. For weak confinement, the productivity is: 1.36×10^{-3} mol kg catalyst^{-1} s^{-1}; for strong confinement, the productivity is: 7.9×10^{-4} mol kg catalyst^{-1} s^{-1}.

Clearly, if diffusional influences are minor in nature, the differences between Fick and M–S models will be
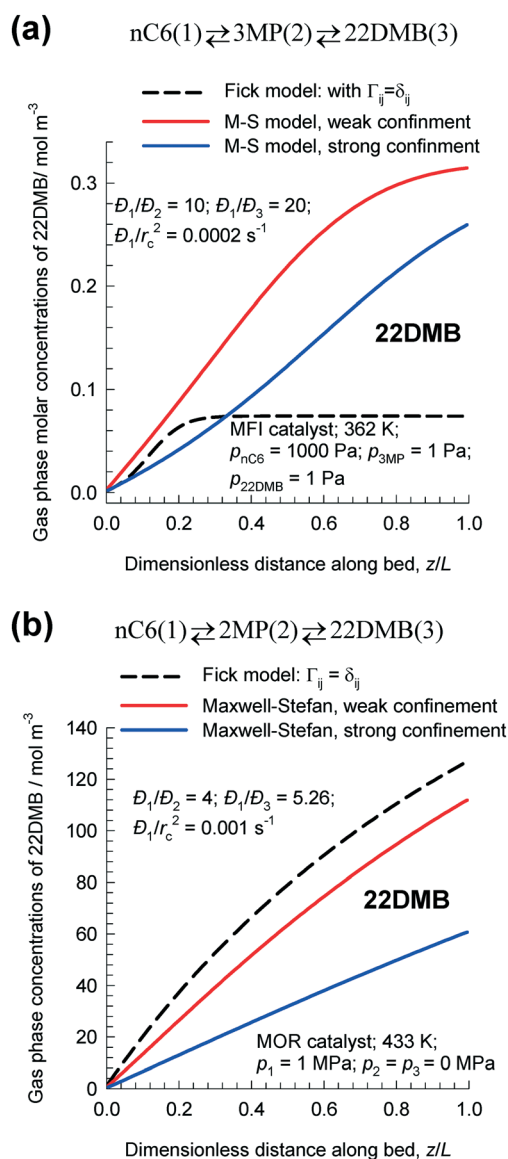
Fig. 10 Steady-state molar concentrations of the desired product 22DMB along the dimensionless length of fixed bed carrying out *n*-hexane isomerization reactions: (a) MFI nC6(1) $\rightleftharpoons$ 3MP(2) $\rightleftharpoons$ 22DMB(3) with MFI catalyst, and (b) nC6(1) $\rightleftharpoons$ 2MP(2) $\rightleftharpoons$ 22DMB(3) with MOR catalyst. All calculation details and data inputs are provided in the ESI.†
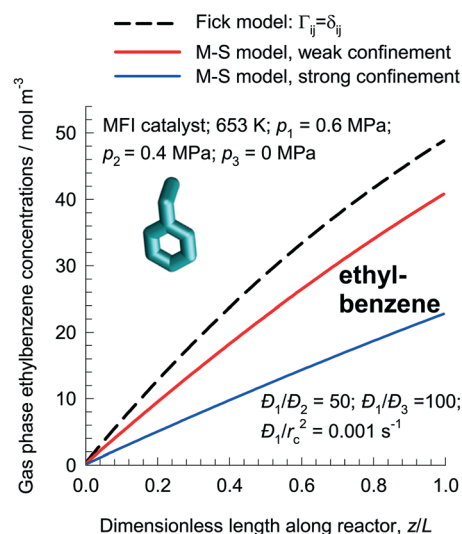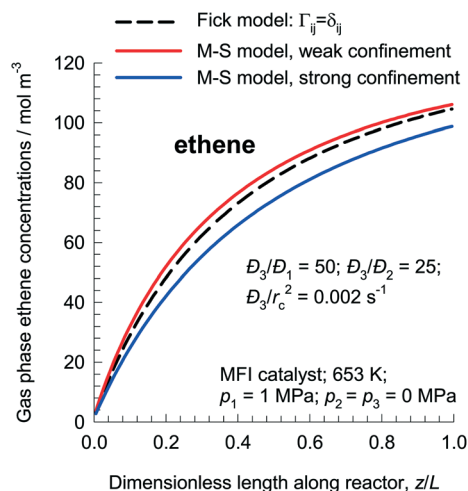
Fig. 11 Steady-state simulations of fixed bed reactor packed with MFI catalyst carrying out: (a) ethene(1) + benzene(2) $\rightleftharpoons$ ethylbenzene(3), and (b) ethane(1) $\rightleftharpoons$ ethene(2) + hydrogen(3) reactions. The plots show the molar concentrations of the desired products (a) ethylbenzene, and (b) ethene in the gas phase along the dimensionless length of the fixed bed, *z/L*. All calculation details and data inputs are provided in the ESI.†

334 | *React. Chem. Eng.*, 2017, **2**, 324–336

This journal is © The Royal Society of Chemistry 2017

insignificant. This is evidenced in the dehydrogenation reaction ethane(1) $\rightleftharpoons$ ethene(2) + hydrogen(3) with MFI catalyst. Fig. 11b compares the ethene concentrations in the gas phase along the length of the fixed zeolite bed at steady-state using the Fick and M–S models. For the Fick model that ignores thermodynamic coupling, the rate of production of ethene is predicted to be 5.4×10^{-4} mol kg catalyst^{-1} s^{-1}. The predictions of the M–S model, with either weak or strong confinement, are different by about 10%. Diffusional effects are of lesser importance for small molecules such as H_2, C_2H_4, and C_2H_6; therefore there is no great penalty for using the simple Fick model for intra-particle transport.

5. Conclusions

The influence of intra-crystalline diffusion on zeolite catalyzed reactions has been examined by combining the Maxwell–Stefan diffusion formulation with Langmuir–Hinshelwood kinetics. The following major conclusions emergence from our study of five different reversible reaction systems.

1. Unlike the classical η–ϕ inter-relationship based on Fick's law, the effectiveness factor for zeolite catalyzed reactions is also dependent on the occupancy of the guest molecules within the zeolite pores. Broadly speaking, the higher the total occupancy, the lower the catalyst effectiveness.

2. Thermodynamic coupling effects are of significant importance in the calculation of transient equilibration trajectories for uptake within single zeolite crystals. In all the reaction systems investigated, the more mobile component in the mixture exhibits an overshoot in the uptake. This may imply that supra-equilibrium conversions are achievable during the initial transience. Such overshoots are not realized by use of the Fick model that ignores thermodynamic coupling, *i.e.* $\Gamma_{ij} \rightarrow \delta_{ij}$. The equilibration trajectories predicted the Fick and M–S model follow significantly different paths; see Fig. 4 and 5; these differences could have a significant bearing on the selectivity of complex reaction systems.

3. Thermodynamic coupling effects have a significant influence on the conversion and productivity in fixed bed reactors and predictions of the M–S model are at significant variance with that of the Fickian model that ignores coupling. Whether the Fickian model over-predicts, or under-predicts, the productivity of the desired product depends on a variety of factors including the hierarchy of mobilities and adsorption strengths.

4. Transient operations of fixed bed reactors could be exploited to obtain near-pure products during earlier stages of the transience, as illustrated in Fig. 8.

6. Notation

b_i Langmuir constant for species i, Pa^{-1}
$Đ_i$ M–S diffusivity for molecule–wall interaction, m^2 s^{-1}
$Đ_{ij}$ M–S exchange coefficient for n-component mixture, m^2 s^{-1}
$Đ_i(0)$ Zero-loading M–S diffusivity for molecule–wall interaction, m^2 s^{-1}

k_1 Forward reaction rate constant, s^{-1}
k_2 Backward reaction rate constant, s^{-1}
L Length of packed bed reactor, m
n Number of species in the mixture, dimensionless
n_{sites} Number of adsorption sites, dimensionless
N_i Molar flux of species i with respect to framework, mol m^{-2} s^{-1}
p_i Partial pressure of species i in mixture, Pa
q_i Component molar loading of species i, mol kg^{-1}
$q_{i,sat}$ Molar loading of species i at saturation, mol kg^{-1}
q_t Total molar loading in mixture, mol kg^{-1}
$\bar{q}_i(t)$ Spatial-averaged component uptake of species i, mol kg^{-1}
r Radial direction coordinate, m
r_c Radius of crystallite, m
R Gas constant, 8.314 J mol^{-1} K^{-1}
R_{kg} Rate of chemical reaction, mol kg catalyst^{-1} s^{-1}
t Time, s
T Absolute temperature, K
v Interstitial gas velocity in packed bed, m s^{-1}
x_i Mole fraction of species i in adsorbed phase, dimensionless
z Distance coordinate, m

Greek letters

Γ_{ij} Thermodynamic factors, dimensionless
δ Thickness of microporous membrane, m
δ_{ij} Kronecker delta, dimensionless
ε Voidage of packed bed, dimensionless
η Effectiveness factor, dimensionless
θ_i Fractional occupancy of component i, dimensionless
θ_V Fractional vacancy, dimensionless
θ_{is} Fractional occupancy at catalyst surface, dimensionless
θ_{i0} Fractional occupancy at center of catalyst, dimensionless
μ_i Molar chemical potential of component i, J mol^{-1}
ν_i Stoichiometric reaction coefficient, dimensionless
ξ Dimensionless radial coordinate, dimensionless
ρ Framework density, kg m^{-3}
τ Dimensionless time, dimensionless
ϕ Classic Thiele modulus, dimensionless

Subscripts

b   Referring to backward reaction
c   Referring to crystallite
f   Referring to forward reaction
i Referring to component i
j Referring to component j
t   Referring to total mixture
0   Referring to position, $\xi = 0$.
1   Referring to species 1
2   Referring to species 2
s   Referring to position $\xi = 1$.
sat   Referring to saturation conditions
V   Vacancy

This journal is © The Royal Society of Chemistry 2017

React. Chem. Eng., 2017, **2**, 324–336 | 335

References

1 C. Baerlocher, W. M. Meier and D. H. Olson, *Atlas of Zeolite Framework Types*, Elsevier, Amsterdam, 5th edn, 2002.

2 T. F. Degnan, *J. Catal.*, 2003, **216**, 32–46.

3 C. Marcilly, *J. Catal.*, 2003, **216**, 47–62.

4 A. Corma, *J. Catal.*, 2003, **216**, 298–312.

5 J. Čejka, A. Corma and S. Zones, *Zeolites and Catalysis: Synthesis, Reactions and Applications*, Wiley-VCH, Weinheim, 2010.

6 W. Vermeiren and J.-P. Gilson, *Top. Catal.*, 2009, **52**, 1131–1161.

7 B. Yilmaz and U. Müller, *Top. Catal.*, 2009, **52**, 888–895.

8 A. Primo and H. Garcia, *Chem. Soc. Rev.*, 2014, **43**, 7548–7561.

9 O. P. Keipert, D. Wolf, P. Schulz and M. Baerns, *Appl. Catal., A*, 1995, **131**, 347–365.

10 *Zeolites in Industrial Separation and Catalysis*, ed. S. Kulprathipanja, Wiley-VCH, Weinheim, 2010.

11 A. Bhan and M. Tsapatsis, *Curr. Opin. Chem. Eng.*, 2013, **2**, 320–324.

12 J. Wei, *Ind. Eng. Chem. Res.*, 1994, **33**, 2467–2472.

13 M. E. Davis, *Ind. Eng. Chem. Res.*, 1991, **30**, 1675–1683.

14 M. E. Davis, *Nature*, 2002, **417**, 813–821.

15 R. Aris, *The mathematical theory of diffusion and reaction in permeable catalysts*, Clarendon Press, Oxford, 1975.

16 G. F. Froment, K. B. Bischoff and J. De Wilde, *Chemical Reactor – Analysis and Design*, John Wiley & Sons, New York, 3rd edn, 2011.

17 O. Levenspiel, *Chemical Reaction Engineering*, John Wiley, New York, 3rd edn, 1999.

18 R. Jackson, *Transport in Porous Catalysts*, Elsevier, Amsterdam, 1977.

19 R. Krishna, *J. Phys. Chem. C*, 2009, **113**, 19756–19781.

20 R. Krishna, *Chem. Soc. Rev.*, 2012, **41**, 3099–3118.

21 J. Kärger, D. M. Ruthven and D. N. Theodorou, *Diffusion in Nanoporous Materials*, Wiley-VCH, Weinheim, 2012.

22 N. Y. Chen, T. F. Degnan and C. M. Smith, *Molecular transport and reaction in zeolites. Design and application of shape selective catalysts*, VCH Publishers, New York, 1994.

23 J. R. Xiao and J. Wei, *Chem. Eng. Sci.*, 1992, **47**, 1123–1141.

24 J. R. Xiao and J. Wei, *Chem. Eng. Sci.*, 1992, **47**, 1143–1159.

25 G. Mirth, J. Cejka and J. Lercher, *J. Catal.*, 1993, **139**, 24–33.

26 N. Hansen, R. Krishna, J. M. van Baten, A. T. Bell and F. J. Keil, *J. Phys. Chem. C*, 2009, **113**, 235–246.

27 R. Krishna and J. M. van Baten, *J. Phys. Chem. C*, 2012, **116**, 23556–23568.

28 R. Krishna and J. M. van Baten, *Phys. Chem. Chem. Phys.*, 2013, **15**, 7994–8016.

29 R. Krishna, *Microporous Mesoporous Mater.*, 2014, **185**, 30–50.

30 R. Krishna, *Phys. Chem. Chem. Phys.*, 2016, **18**, 15482–15495.

31 N. Hansen and F. J. Keil, *Soft Mater.*, 2012, **10**, 179–201.

32 F. Keil, *Diffusion und Chemische Reaktionen in der Gas/Festoff-Katalyse*, Springer Verlag Berlin Heidelberg New York, 1999.

33 R. Krishna, *Ind. Eng. Chem. Res.*, 2016, **55**, 4749–4759.

34 R. Krishna and R. Baur, *Sep. Purif. Technol.*, 2003, **33**, 213–254.

35 R. Krishna and J. M. van Baten, *Chem. Eng. Sci.*, 2008, **63**, 3120–3140.

36 T. Titze, C. Chmelik, J. Kärger, J. M. van Baten and R. Krishna, *J. Phys. Chem. C*, 2014, **118**, 2660–2665.

37 R. Krishna and J. M. van Baten, *J. Membr. Sci.*, 2013, **430**, 113–128.

38 R. Krishna and J. M. van Baten, *Microporous Mesoporous Mater.*, 2008, **109**, 91–108.

39 R. Krishna and J. M. van Baten, *Microporous Mesoporous Mater.*, 2008, **107**, 296–298.

40 J. M. van Baten and R. Krishna, *Microporous Mesoporous Mater.*, 2005, **84**, 179–191.

41 R. Baur and R. Krishna, *Chem. Eng. J.*, 2004, **99**, 105–116.

42 R. Baur and R. Krishna, *Catal. Today*, 2005, **105**, 173–179.

43 D. Wang, F. Li and X. Zhao, *Chem. Eng. Sci.*, 2004, **59**, 5615–5622.

44 S. V. Nayak, P. A. Ramachandran and M. P. Dudukovic, *Ind. Eng. Chem. Res.*, 2012, **51**, 1570–1578.

45 S. van Donk, A. Broersma, O. L. J. Gijzeman, J. A. van Bokhoven, J. H. Bitter and K. P. de Jong, *J. Catal.*, 2001, **204**, 272–280.

46 R. Krishna, *Chem. Soc. Rev.*, 2015, **44**, 2812–2836.

47 R. Krishna, *Curr. Opin. Chem. Eng.*, 2016, **12**, 106–119.

48 E. Jolimaître, M. Tayakout-Fayolle, C. Jallut and K. Ragil, *Ind. Eng. Chem. Res.*, 2001, **40**, 914–926.

49 E. Jolimaître, K. Ragil, M. Tayakout-Fayolle and C. Jallut, *AIChE J.*, 2002, **48**, 1927–1937.

50 H. Ban, J. Gui, L. Duan, X. Zhang, L. Song and Z. Sun, *Fluid Phase Equilib.*, 2005, **232**, 149–158.

51 L. Duan, X. Dong, Y. Wu, H. Li, L. Wang and L. Song, *J. Porous Mater.*, 2013, **20**, 431–440.

52 R. Krishna and R. Baur, *Chem. Eng. Sci.*, 2005, **60**, 1155–1166.

53 Z. R. Herm, B. M. Wiers, J. M. Van Baten, M. R. Hudson, P. Zajdel, C. M. Brown, N. Maschiocchi, R. Krishna and J. R. Long, *Science*, 2013, **340**, 960–964.

54 N. Hansen, R. Krishna, J. M. van Baten, A. T. Bell and F. J. Keil, *Chem. Eng. Sci.*, 2010, **65**, 2472–2480.

55 H. A. Jakobsen, *Chemical Reactor Modeling. Multiphase Reactive Flows*, Springer Verlag, Berlin, Heidelberg, 2008.

56 R. Baur and R. Krishna, *Chem. Eng. J.*, 2005, **109**, 107–113.

57 H. W. Dandekar, G. A. Funk, R. D. Gillespie, H. A. Zinnen, C. P. McGonegal, M. Kojima and S. H. Hobbs, Process for alkane isomerization using reactive chromatography, UOP Inc., USA., *US Pat.*, US5763730, 1998.

58 H. W. Dandekar, G. A. Funk, R. D. Gillespie, H. A. Zinnen, C. P. McGonegal, M. Kojima and S. H. Hobbs, Process for alkane isomerization using reactive chromatography, UOP, Des Plaines, Illinois, USA., *U.S. Pat.*, US5763730, 1999.

59 H. W. Dandekar, G. A. Funk and H. A. Zinnen, Process for separating and recovering multimethyl-branched alkanes, UOP LLC, Des Plaines, Illinois, USA., *U.S. Pat.*, US6069289, 2000.

336 | *React. Chem. Eng.*, 2017, **2**, 324–336

This journal is © The Royal Society of Chemistry 2017

Highlighting Diffusional Coupling Effects in Zeolite Catalyzed Reactions by Combining the Maxwell-Stefan and Langmuir-Hinshelwood Formulations

Rajamani Krishna[a], * Richard Baur[a,b], and Jasper M. van Baten[a,c]

Footnotes

[a] Van 't Hoff Institute for Molecular Sciences, University of Amsterdam, Science Park 904, 1098 XH Amsterdam, The Netherlands;

E-mail: r.krishna@contact.uva.nl
[b] *Current affiliation: Shell Technology Center Amsterdam, Amsterdam, The Netherlands; E-mail: richard.baur@shell.com*
[c] *Current affiliation: AmsterCHEM, Almería, Spain; E-mail: jasper@amsterchem.com*

Table of Contents

1. Preamble

This ESI accompanying the article *Highlighting Diffusional Coupling Effects in Zeolite Catalyzed Reactions by Combining the Maxwell-Stefan and Langmuir-Hinshelwood Formulations* provides:

(i)   Structural data on zeolites

(ii)   Detailed derivations of the Maxwell-Stefan diffusion formulation for intra-crystalline diffusion in microporous zeolites

(iii) Details of the modelling of mixture adsorption in zeolites

(iv)   Details of the Langmuir-Hinshelwood formulation for reaction kinetics

(v)   Simulation methodology for transient-diffusion and reaction inside single crystal

(vi)   Simulation methodology for transient breakthrough in fixed bed reactors

(vii) Input data and detailed simulation results for the following reactions:

$$2MP(1) \rightleftarrows 22DMB(2),$$

$$o-xylene(1) \rightleftarrows p-xylene(2),$$

$$nC6(1) \rightleftarrows 3MP(2) \rightleftarrows 22DMB(3),$$

$$nC6(1) \rightleftarrows 2MP(2) \rightleftarrows 22DMB(3),$$

$$ethene(1) + benzene(2) \rightleftarrows ethylbenzene(3), \text{ and}$$

$$ethane(1) \rightleftarrows ethene(2) + hydrogen(3).$$
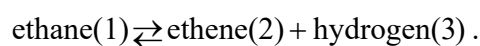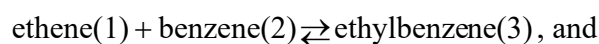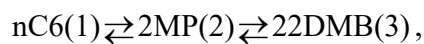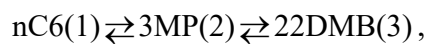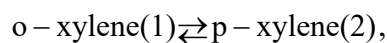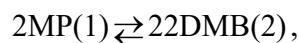
For ease of reading, this ESI is written as a stand-alone document; as a consequence, there is some overlap of material with the main manuscript.

2. List of Video animations uploaded as ESI

The following set of video animations have been uploaded as ESI.

(1) Transient development of loadings of 2MP/22DMB in MFI catalyst carrying out the isomerization reaction $2MP(1) \rightleftarrows 22DMB(2)$. 2MP exhibits spatio-temporal overshoots. The animation is based the M-S model with weak confinement.

(2) Transient development of loadings of o-xylene/p-xylene in MFI catalyst carrying out the isomerization reaction $o-xylene(1) \rightleftarrows p-xylene(2)$. p-xylene exhibits spatio-temporal overshoots. The animation is based the M-S model with strong confinement.

(3) Transient development of loadings of nC6/3MP/22DMB in MFI catalyst carrying out the isomerization reaction $nC6(1) \rightleftarrows 3MP(2) \rightleftarrows 22DMB(3)$ at 362 K. nC6 and 3MP exhibit spatio-temporal overshoots. The animation is based the M-S model with weak confinement.

(4) Transient development of loadings of nC6/3MP/22DMB in BEA catalyst carrying out the isomerization reaction $nC6(1) \rightleftarrows 3MP(2) \rightleftarrows 22DMB(3)$ at 433 K. nC6 and 3MP exhibit spatio-temporal overshoots. The animation is based the M-S model with weak confinement.

(5) Transient development of loadings of nC6/2MP/22DMB in MFI catalyst carrying out the isomerization reaction $nC6(1) \rightleftarrows 2MP(2) \rightleftarrows 22DMB(3)$ at 433 K. nC6 and 2MP exhibit spatio-temporal overshoots. The animation is based the M-S model with weak confinement.

(6) Transient development of loadings of nC6/2MP/22DMB in MOR catalyst carrying out the isomerization reaction $nC6(1) \rightleftarrows 2MP(2) \rightleftarrows 22DMB(3)$. nC6 and 2MP exhibit spatio-temporal overshoots. The animation is based the M-S model with strong confinement.

(7) Transient development of loadings of ethene/benzene/ethylbenzene in MFI catalyst carrying out the reaction $ethene(1) + benzene(2) \rightleftarrows ethylbenzene(3)$. Ethene exhibits spatio-temporal overshoots. The animation is based the M-S model with strong confinement.

(8) Transient development of loadings of ethane/ethene/hydrogen in MFI catalyst carrying out the reaction $ethane(1) \rightleftarrows ethene(2) + hydrogen(3)$. Hydrogen exhibits spatio-temporal overshoots. The animation is based the M-S model with weak confinement.

These animations provide some "feel" of spatio-temporal overshoots of during transient uptake in zeolite catalysts.

3. Structural topology and connectivity of some common zeolites

A number of different channel topologies and connectivities are encountered in zeolite structures; these can be divided into five broad classes;

1. One-dimensional (1D) channels (e.g. LTL, TON, LTL).

2. 1D channels with side pockets (e.g. MOR, FER).

3. Intersecting channels (e.g. MFI, BEA)

4. Cages separated by narrow windows (e.g. LTA, CHA)

5. Cavities with large windows (e.g. FAU).

The crystallographic data are available on the zeolite atlas website of the International Zeolite Association (IZA). [1, 2] The pore topology and structural details of some common zeolites are provided are provided in the accompanying Figures as indicated below:

BEA (see Figures 1, 2)

CHA (see Figures 3, 4)

FAU (see Figures 5, 6)

FER (see Figures 7, 8, 9, 10, 11)

LTA (see Figures 12, 13)

LTL (see Figures 14, 15)

MFI (see Figures 16, 17)

MOR (see Figures 18, 19)

MTW (see Figures 20, 21)

TON (see Figures 22, 23)

Table 1 gives salient information on the variety of a few typical all-silica zeolite structures that are used as catalysts in the process industries. The crystallographic data are available on the zeolite atlas website.[2]. The unit cell dimensions, and pore volumes are summarized in Table 2. Further details on the structure, landscape, pore dimensions of a very wide variety of micro-porous materials are available in the published literature.[3-10]

4. The Maxwell-Stefan relations unary diffusion in micropores

Within microporous crystalline materials, the guest molecules exist in the adsorbed phase. The Gibbs adsorption equation[11] in differential form is

$$Ad\pi = \sum q_i d\mu_i \tag{1}$$

The quantity A on the left side of Equation (1) is the surface area per kg of framework, with units of m^2 per kg of the framework of the crystalline material; q_i is the molar loading of component i in the adsorbed phase with units moles per kg of framework; μ_i is the molar chemical potential of component i. The spreading pressure π has the same units as surface tension, i.e. N m^{-1}; indeed the spreading pressure is the negative of the surface tension.[12]

For describing the *unary* transport of bound moisture in wood, Babbitt[13, 14] suggested the use of the gradient of the spreading pressure $\partial\pi/\partial r$ as the thermodynamically correct driving force. The units of $\partial\pi/\partial r$ are N m^{-2}, and this represents the force acting per m^2 of material surface. The number of moles

of adsorbate per m^2 of surface is $\frac{q_i}{A}$. Therefore the force per mole of adsorbate is

$-\left(\frac{\partial \pi}{\partial r}\right) \Big/ \left(\frac{q_i}{A}\right) = -\frac{\partial \mu_i}{\partial r}$. This force is balanced by friction between the mobile adsorbates and the

surface of the material.

$$-\left(\frac{\partial \pi}{\partial r}\right) \Big/ \left(\frac{q_i}{A}\right) = \frac{RT}{Ð_i} u_i; \quad -\frac{\partial \mu_i}{\partial r} = \frac{RT}{Ð_i} u_i \tag{2}$$

where u_i is the velocity of motion of the adsorbate with respect to the framework material. The quantity

$\frac{RT}{Ð_i}$ in the right member of equation (2) is interpreted as the "drag coefficient". The unary diffusivity

$Ð_i$, with the units m^2 s^{-1}, is to be interpreted as an inverse drag coefficient between the adsorbate and

the surface. If we define N_i as the number of moles of species i transported per m^2 of crystalline material

per second

$$N_i \equiv \rho q_i u_i \tag{3}$$

where ρ is the framework density with units of kg m^{-3}, we obtain the flux relation

$$-\rho \frac{A}{RT} \frac{\partial \pi}{\partial r} = \frac{N_i}{Ð_i} \tag{4}$$

Combining Equation (1) and (4) we get

$$-\rho \frac{q_i}{RT} \frac{\partial \mu_i}{\partial r} = \frac{N_i}{Ð_i} \tag{5}$$

Equation (5) is the familiar form of the Maxwell-Stefan (M-S) formulation[3, 4, 15] for unary diffusion.

The chemical potential gradient can be related to the gradient of the molar loading by defining a

thermodynamic correction factor Γ_i

$$\frac{q_i}{RT} \frac{\partial \mu_i}{\partial r} = \Gamma_i \frac{\partial q_i}{\partial r}; \quad \Gamma_i \equiv \frac{q_i}{p_i} \frac{\partial p_i}{\partial q_i} \tag{6}$$

Combining Equations (5) and (6) we may write

$$N_i = -\rho Ð_i \frac{q_i}{RT} \frac{\partial \mu_i}{\partial r} = -\rho Ð_i \Gamma_i \frac{\partial q_i}{\partial r} \qquad (7)$$

The product of the M-S diffusivity and the thermodynamic correction factor is the Fick diffusivity

$$D_i = Ð_i \Gamma_i \qquad (8)$$

The simplest isotherm model is the single-site Langmuir isotherm

$$q = q_{sat} \frac{bp}{1+b}; \quad \theta = \frac{bp}{1+bp}; \quad bp = \frac{\theta}{1-\theta} \qquad (9)$$

where we define the fractional occupancy of the adsorbate molecules, $\theta = q/q_{sat} = \Theta/\Theta_{sat}$. The single-site Langmuir isotherm can be derived by equating the rate of adsorption with the rate of desorption. The rate of adsorption is proportional to the total number of vacant sites, $Rate_{ads} = k_{ads} p n_{sites} \theta_V = k_{ads} n_{sites} p(1-\theta)$. The rate of desorption is proportional to the number of occupied sites, $Rate_{des} = k_{des} n_{sites} \theta$. At adsorption equilibrium, we have $k_{ads} p N_{sites}(1-\theta) = k_{des} n_{sites} \theta$

$$\frac{k_{ads} p}{k_{des}} = bp = \frac{\theta}{(1-\theta)}.$$

Differentiation of equation (9) yields the following expression for Γ

$$\Gamma = \frac{1}{1-\theta} = \frac{1}{\theta_V}; \quad \text{single - site Langmuir isotherm} \qquad (10)$$

where $\theta_V = (1-\theta)$ is the fractional vacancy.

Figure 24a presents a calculation of the thermodynamic factor Γ, for single-site Langmuir isotherm, plotted as a function of the fractional occupancy, θ. The thermodynamic factor Γ always exceeds unity. At pore saturation, we have $\theta \to 1$; $\Gamma \to \infty$, and it is therefore convenient to calculate the *inverse* thermodynamic factor $1/\Gamma$ which decreases linearly with θ; see Figure 24b.

5. Loading dependence of M-S diffusivities in MFI zeolite

Figure 25 presents Molecular Dynamics (MD) data on the M-S diffusivities of H_2, Ne, Ar, N_2, CH_4 and Kr all-silica MFI zeolite at 300 K; the MD data are culled from our earlier publications.[3-10] For molar loadings < 4 mol kg^{-1}, the M-S diffusivity is practically independent of loading. This scenario has been termed the "weak confinement" scenario by Krishna and Baur.[16]

Preferential location of molecules within the structural framework can cause strong isotherm inflections. Such inflection characteristics require fitting with the dual-site-Langmuir (DSL) model[17, 18]

$$\Theta_i = \Theta_{i,A,sat} \frac{b_{i,A} p_i}{1 + b_{i,A} p_i} + \Theta_{i,B,sat} \frac{b_{i,B} p_i}{1 + b_{i,B} p_i} \tag{11}$$

For example, branched alkanes, benzene, alkyl benzenes, and cyclohexane prefer to locate at the channel intersections of MFI zeolite due to extra "leg-room" and other configurational considerations.[19] There are only 4 intersection sites available per unit cell of MFI. This implies that to obtain loadings higher than $\Theta_i = 4$ molecules per unit cell, an extra "push" will be required to locate the molecules elsewhere within the channels; this leads to isotherm inflection. Due to strong isotherm inflections, the $1/\Gamma_i$ exhibits a cusp-like inflection at a loading of $\Theta_i = 4$, when all the preferred adsorption sites are occupied; is demonstrated in the data on $1/\Gamma_i$ for iso-butane/MFI in Figure 26a. In the range $0 < \Theta_i < 4$, $1/\Gamma_i$ decreases nearly linearly with Θ_i signifying the fact that the vacancy *decreases* almost linearly with loading. For $\Theta_i > 4$, $1/\Gamma_i$ increases with Θ_i because additional sites *within* the MFI channels are created to accommodate more than 4 molecules per unit cell, i.e. the number of available sites *increases* within this loading range. These additional sites must be accommodated within the channels, requiring the additional "push" that caused the inflection.

Figures 26b,c show the experimental data[20] for the loading dependence of n-hexane and n-heptane in MFI zeolite. For both guest molecules, a reasonably good description of the loading dependence of the M-S diffusivity is

$$\mathit{Đ}_i = \mathit{Đ}_i(0)\frac{1}{\Gamma_i} \tag{12}$$

where $\mathit{Đ}_i(0)$ represents the zero-loading M-S diffusivity. If MFI zeolite, for $\Theta_i < 4$, the loading dependence can be further approximated as follows

$$\mathit{Đ}_i = \mathit{Đ}_i(0)(1-\theta_i) = \mathit{Đ}_i(0)\theta_V \tag{13}$$

where $\theta_V = (1-\theta_i)$ is the fractional vacancy. Equation (13) is essentially based on a simple hopping model in which a molecule can jump from one adsorption site to an adjacent one, provided it is not already occupied. The loading dependence portrayed in equation (13) has been termed the "strong confinement" scenario by Krishna and Baur.[16]

6. The Maxwell-Stefan relations for *n*-component diffusion in micropores

The best starting point for developing the Maxwell-Stefan formulation for mixture diffusion is Equation (2), that needs extension. The force acting per mole of adsorbate species i is balanced by (1) friction between i and the pore walls (this is the same term as for unary transport), and (2) friction between species i and species j. We may write

$$-\frac{1}{RT}\frac{\partial \mu_i}{\partial r} = \sum_{\substack{j=1 \\ j \neq i}}^{n} \frac{x_j}{\mathit{Đ}_{ij}}(u_i - u_j) + \frac{1}{\mathit{Đ}_i}(u_i); \quad i = 1,2..n \tag{14}$$

The x_i in equations (14) represent the component mole fractions in the adsorbed phase within the pores

$$x_i = q_i / q_t; \quad q_t = \sum_{i=1}^{n} q_i; \quad i = 1,2,..n \tag{15}$$

The $\mathit{Đ}_i$ have the same significance as for unary diffusion; they are inverse drag coefficients between the species i and the material surface. Indeed, an important persuasive advantage of the M-S equations is that the $\mathit{Đ}_i$ for mixture diffusion often retains the same magnitude and loading dependence as for unary diffusion.[3, 5, 21]

The $Đ_{ij}$ may be interpreted as the inverse drag coefficient between species i and species j. At the molecular level, the $Đ_{ij}$ reflect how the facility for transport of species i *correlates* with that of species j; they are also termed *exchange coefficients*. The multiplication factor x_j has been introduced in the numerator of the first right member of equation (14) because the friction experience by species i with the each of the other species in the adsorbed phase ($j = 2, 3, ..n$) should be proportional to the relative amounts of species j ($= 2, 3, ..n$) in the adsorbed phase. Expressing the velocities u_j in terms of the intra-crystalline diffusion fluxes $u_i = N_i / \rho q_i$

$$-\frac{\rho}{RT}\frac{\partial \mu_i}{\partial r} = \sum_{\substack{j=1 \\ j\neq i}}^{n}\frac{x_j}{Đ_{ij}}\left(\frac{N_i}{q_i} - \frac{N_j}{q_j}\right) + \frac{1}{Đ_i}\left(\frac{N_i}{q_i}\right); \quad i = 1,2...n \tag{16}$$

Multiplying both sides of equation (16) by x_i we get

$$-\rho\frac{x_i}{RT}\frac{\partial \mu_i}{\partial r} = \sum_{\substack{j=1 \\ j\neq i}}^{n}\frac{x_i x_j}{Đ_{ij}}\left(\frac{N_i}{q_i} - \frac{N_j}{q_j}\right) + \frac{1}{Đ_i}\left(\frac{x_i N_i}{q_i}\right); \quad i = 1,2...n \tag{17}$$

In view of the equation (15), we may simplify equation (17) to write

$$-\rho\frac{q_i}{RT}\frac{\partial \mu_i}{\partial r} = \sum_{\substack{j=1 \\ j\neq i}}^{n}\left(\frac{x_j N_i - x_i N_j}{Đ_{ij}}\right) + \frac{N_i}{Đ_i}; \quad i = 1,2...n \tag{18}$$

The Onsager reciprocal relations demand the symmetry constraint

$$Đ_{ij} = Đ_{ji}; \quad i, j = 1,2,...n \tag{19}$$

The ratio ($Đ_i/Đ_{ij}$) is a reflection of the *degree of correlations*. [3-5, 22] We consider correlation effects to be strong when $Đ_1/Đ_{12} > 1$. If correlations are considered to be negligible, i.e. $Đ_i/Đ_{ij} \ll 1$, equation (18) simplifies to yield

$$N_i = -\rho Đ_i \frac{q_i}{RT}\frac{\partial \mu_i}{\partial r}; \quad i = 1,2...n \tag{20}$$

An entirely analogous manner of writing equation (18) is in terms of molar concentrations c_i, in the adsorbed phase, based on the accessible pore volume, V_p ($= m^3$ pore volume per kg framework)

$$c_i = \frac{q_i}{V_p}; \quad c_t = \sum_{i=1}^{n} c_i = \frac{q_t}{V_p} \tag{21}$$

This alternative formulation:

$$-\rho V_p \frac{c_i}{RT} \frac{\partial \mu_i}{\partial r} = \sum_{\substack{j=1 \\ j \neq i}}^{n} \left(\frac{x_j N_i - x_i N_j}{Đ_{ij}} \right) + \frac{N_i}{Đ_i}; \quad i = 1,2...n \tag{22}$$

The quantity ρV_p is the fractional pore volume

$$\rho V_p = \left(\frac{\text{kg framework}}{m^3 \text{ framework}} \right) \left(\frac{m^3 \text{ pore volume}}{\text{kg framework}} \right) = \left(\frac{m^3 \text{ pore volume}}{m^3 \text{ framework}} \right) = \varepsilon \tag{23}$$

So, we re-write equation (22) in the form

$$-\varepsilon \frac{c_i}{RT} \frac{\partial \mu_i}{\partial r} = \sum_{\substack{j=1 \\ j \neq i}}^{n} \left(\frac{x_j N_i - x_i N_j}{Đ_{ij}} \right) + \frac{N_i}{Đ_i}; \quad i = 1,2...n \tag{24}$$

The formulation (24) has been employed to develop a unified theory of mixture diffusion in both micropores and mesopores.[5, 23-25] The fluxes N_i in equation (24), and in this entire article are defined in terms of the moles transported per m^2 of the *total surface of crystal material*. Alternatively, if we just focus on fluxes inside a single pore, it is convenient to define the fluxes N_i in terms of the moles transported per m^2 surface of the pore, then the factor $\varepsilon = \rho V_p$ has to be omitted in the left member of equation (24).

By defining an *n*-dimensional square matrix $[B]$ with elements

$$B_{ii} = \frac{1}{Đ_i} + \sum_{\substack{j=1 \\ j \neq i}}^{n} \frac{x_j}{Đ_{ij}}; \quad B_{ij} = -\frac{x_i}{Đ_{ij}}; \quad i,j = 1,2....n \tag{25}$$

we can recast equation (18)) into the following form

$$-\rho \frac{q_i}{RT} \frac{\partial \mu_i}{\partial r} = \sum_{j=1}^{n} B_{ij} N_j; \quad i = 1, 2, ..n \tag{26}$$

The chemical potential gradients $\dfrac{\partial \mu_i}{\partial r}$ can be related to the gradients of the molar loadings, q_i, by defining thermodynamic correction factors Γ_{ij}

$$\frac{q_i}{RT} \frac{\partial \mu_i}{\partial r} = \sum_{j=1}^{n} \Gamma_{ij} \frac{\partial q_j}{\partial r}; \quad \Gamma_{ij} = \frac{q_i}{p_i} \frac{\partial p_i}{\partial q_j}; \quad i, j = 1, ...n \tag{27}$$

For an ideal gas mixture, the chemical potential gradients can be related to the partial pressure gradients in the bulk gas phase mixture

$$\frac{\partial \mu_i}{\partial r} = RT \frac{\partial \ln p_i}{\partial r} = RT \frac{1}{p_i} \frac{\partial p_i}{\partial r} \tag{28}$$

Let us define the fractional occupancies

$$\theta_i = \frac{q_i}{q_{i,sat}}; \quad i = 1, 2, ..n \tag{29}$$

The fractional *vacancy* θ_V is

$$\theta_V = 1 - \theta_1 - \theta_2 ...... - \theta_n \tag{30}$$

Consider the special case in which each of the pure component adsorption isotherms is described by a single-site Langmuir model $q = \dfrac{q_{sat} b p}{1 + bp}$. The mixed gas Langmuir model for calculation of the component loadings is

$$q_i = \frac{q_{i,sat} b_i p_i}{1 + b_1 p_1 + b_2 p_2 + ... + b_n p_n}; \quad i = 1, 2 ...n \tag{31}$$

Combination of equations (29), (30), and (31) yields the following expression for the fractional vacancy

$$\theta_V = \frac{1}{1 + b_1 p_1 + b_2 p_2 + \dots + b_n p_n} \tag{32}$$

The elements of the matrix of thermodynamic correction factors can be determined by analytic differentiation of equation (31); the resulting expression is[16]

$$\Gamma_{ij} = \delta_{ij} + \left(\frac{q_{i,sat}}{q_{j,sat}}\right)\left(\frac{\theta_i}{\theta_V}\right); \quad i, j = 1, 2 \dots n \tag{33}$$

For binary mixture, the four elements of the matrix of thermodynamic factors are obtained by simplification of equation (33); the result is

$$\begin{bmatrix} \Gamma_{11} & \Gamma_{12} \\ \Gamma_{21} & \Gamma_{22} \end{bmatrix} = \frac{1}{1 - \theta_1 - \theta_2} \begin{bmatrix} 1 - \theta_2 & \dfrac{q_{1,sat}}{q_{2,sat}} \theta_1 \\ \dfrac{q_{2,sat}}{q_{1,sat}} \theta_2 & 1 - \theta_1 \end{bmatrix} \tag{34}$$

where the fractional occupancies, θ_1, are defined by Equation (29).

Equation (26) can be re-written in n-dimensional matrix notation as

$$(N) = -\rho [B]^{-1} [\Gamma] \nabla(q) \tag{35}$$

If correlations are considered to be negligible, i.e. $Đ_i / Đ_{ij} \ll 1$, equation (20) can be combined with equation (27) to yield

$$N_i = -\rho Đ_i \sum_{j=1}^{n} \Gamma_{ij} \frac{\partial q_j}{\partial r}; \quad i = 1, 2 \dots n \tag{36}$$

In the Henry regime of adsorption, when the fractional occupancies are vanishingly small, we have the special case that the matrix of thermodynamic factors reduces to the identity matrix

$$\Gamma_{ij} \to \delta_{ij} \tag{37}$$

If the thermodynamic coupling effects are neglected, and the elements of the matrix of thermodynamic factors Γ_{ij} equals Kronecker delta, $\Gamma_{ij} = \delta_{ij}$ and we obtain the uncoupled form of the flux equations

$$N_i = -\rho Đ_i \frac{\partial q_i}{\partial r}; \quad \text{neglecting thermodynamic coupling} \tag{38}$$

Equation (38) may be considered to be representative of the Fick's law of diffusion for intra-crystalline transport. In implementing the Fickian equation (38), we commonly assume that the M-S diffusivity is independent of loading.

In order to illustrate the influence of thermodynamic coupling, we shall compare the results of implementing equation (36) and (38) as flux expressions.

7. M-S diffusivities of hexane isomers in MOR zeolite

Mordenite (MOR) is used as catalyst in industry for alkane isomerization reactions. Figures 27a,b presents the MD data M-S diffusivity, $Đ_i$, of n-hexane (nC6), (b) 2-methylpentane (2MP), and 2,2 dimethylbutane (22DMB) in MOR zeolite at 433 K. For all three hexane isomers, the $Đ_i$ shows a linear decrease in diffusivity with increased loading, Θ_i, expressed in molecules per unit cell. The linear decrease in M-S diffusivity appears to conform with the strong confinement scenario: Equation (13). As verification, the MD data for nC6 and 2MP are plotted in Figures 28a,b as a function of the fractional occupancy. Also plotted in Figures 28a,b are the values of the M-S diffusivity, $Đ_i$, determined from MD data for 50:50 binary nC6/2MP mixtures. Compared at the mixture occupancy: $\theta_t = \theta_1 + \theta_2$, the $Đ_i$ values are the same for the pure component as for the mixture. This highlights the important advantage of the M-S formulation. The unary and mixture MD data are taken from Van Baten and Krishna.[26] M-S diffusivity of ethene in reacting mixture in MFI zeolite

The strong confinement scenario can be applied to describe the loading dependence of the diffusivity of any species in an adsorbed *reacting mixture*; confirmation of this is available for the alkylation of benzene with ethene using MFI zeolite catalyst (in the acidic form H-ZSM-5) to produce

ethylbenzene.[27] Both benzene (reactant) and ethylbenzene (product) are preferentially located at the intersections of MFI; see Figure 29a. The blocking of intersections causes effective diffusivity of ethene inside the catalyst to reduce five-fold as the total mixture loading approaches 2 molecules per unit cell; see Figure 29.

8. The Ideal Adsorbed Solution Theory (IAST) and the mixed-gas Langmuir models for mixture adsorption

The major assumptions of the Ideal Adsorbed Solution Theory (IAST), developed by Myers and Prausnitz[12] are: (a) the absorbent is thermodynamically inert (the change of the internal energy is negligible), (b) The surface area, A, is temperature invariant (this assumption is not valid for zeolites, MOFs; since the area available depends on the size of the molecules), (c) The Gibbs adsorption isotherm $-Ad\pi + \sum q_i d\mu_i = 0$ applies. The Gibbs free energy is defined by

$$dG = -SdT + Ad\pi + \sum \mu_i dq_i \tag{39}$$

where the term $Ad\pi$ is analogous to the work term in a fluid. For $\pi > 0$ the system does work on the surface during the process of increasing the area of adsorbent. In case of constant T and π, eq (39) simplifies to yield:

$$G = \sum q_i \mu_i \text{ for } T, \pi \text{ constant.} \tag{40}$$

The activity coefficients are related to the excess free Gibbs free energy of mixing:

$$g^m(T, \pi, x_1, ...) = RT \sum x_i \ln(\gamma_i x_i) \text{ for } T, \pi \text{ constant.} \tag{41}$$

Furthermore, we know that any extensive variable, w, can be expressed as

$$w^m(T, \pi, x_1, ...) = w(T, \pi, x_1, ...) - \sum x_i w^0(T, \pi, x_1, ...) \tag{42}$$

where the superscript 0 denotes the property of the pure component. Combining the equations (40) – (42) yields:

$$\mu_i^{ads}(T,\pi,x_1,...) = g_i^0(T,\pi) + RT\ln(\gamma_i x_i) \tag{43}$$

where $g_i^0(T,\pi)$ is the Gibbs free energy of component i when i is adsorbed in absence of other components. $g_i^0(T,\pi)$ has two degree for freedom: temperature and spreading pressure π. Choosing a reference pressure of 1 atm we can reformulate eq (43) and obtain:

$$g_i^0(T,\pi) = g_i^0(T) + RT\ln(P_i^0) \tag{44}$$

Substituting eq(44) in eq(43) yields

$$\mu_i^{ads}(T,\pi,x_1,...) = g_i^0(T) + RT\ln(P_i^0) + RT\ln(\gamma_i x_i) \tag{45}$$

The Gibbs adsorption isotherm is given by eq (15) in Myers and Prausnitz[12]

$$-Ad\pi + \sum q_i d\mu_i = 0 \tag{46}$$

For a pure component, integration of eq (46) results in

$$\frac{\pi A}{RT} = \int_0^{P_i^0} q_i^0(f)d\ln f \tag{47}$$

For a gas phase mixture, the chemical potential is given by $\mu_i^{gas} = g_i^0(T) + RT\ln(p_i)$. Hence at equilibrium we obtain $\mu_i^{gas} = \mu_i^{ads}$, or $P_i^0 \gamma_i x_i = p_i$. If the adsorbed phase is ideal, we get the analogue of Raoult's law for vapor-liquid equilibrium, i.e.

$$P_i^0 x_i = p_i; \quad i = 1,2,...n \tag{48}$$

and P_i^0 is the sorption pressure for every component i, which yields the same spreading pressure, π for each of the pure components, as that for the mixture:

$$\frac{\pi A}{RT} = \int_0^{P_i^0} q_i^0(f)d\ln f = \int_0^{P_n^0} q_n^0(f)d\ln f \tag{49}$$

where R is the gas constant (= 8.314 J mol^{-1} K^{-1}), and $q_i^0(f)$ is the *pure* component adsorption isotherm. The molar loadings $q_i^0(f)$ are expressed in the units of moles adsorbed per kg of framework, i.e. mol kg^{-1}. The units of the spreading pressure π is the same as that for surface tension, i.e. N m^{-1}; indeed the spreading pressure is the negative of the surface tension.[12] The quantity A on the left side of Equation (49) is the surface area per kg of framework, with units of m^2 kg^{-1}. The units of $\dfrac{\pi A}{RT}$, also called the adsorption potential,[28] are mol kg^{-1}.

A key assumption of the IAST is that the enthalpies and surface areas do not change upon mixing, $h^m = 0$ and $a^m = 0$. Hence, applying eq (42) yields $a = \sum a_i^0 x_i^0$. The constraint that there is no change in surface area on adsorption demands the constraint

$$\frac{1}{q_t} = \sum \frac{x_i}{q_i^0} \text{ for } T, \pi \text{ constant.} \tag{50}$$

Considering that the mole fractions in the adsorbed phase are given by

$$x_i = \frac{q_i}{q_1 + q_2 + \ldots + q_n} \tag{51}$$

we can reformulate eq (50) as

$$\frac{1}{q_t} = \frac{1}{q_t} \sum \frac{q_i}{q_i^0} \tag{52}$$

or

$$1 = \sum \frac{q_i}{q_i^0} \tag{53}$$

Equation (53) can cause numerical issues if q_i^0 is small. Hence, it seems better to implement eq (53) in the form of $\prod_i q_i^0 = \sum_i q_i \prod_{j \neq i} q_i^0$. From the foregoing analysis, we obtain a set of equation that has to be solved:

$P_i^0 x_i = p_i$ for i = 1..n-1; $1 = \sum x_i$; $x_i = \dfrac{q_i}{\sum q_i} = \dfrac{\Theta_i}{\sum \Theta_i}$; $\int_0^{P_n^0} q_n^0(f) d\ln f = \int_0^{P_i^0} q_i^0(f) d\ln f$ for i = 1..n-1;

$\dfrac{1}{\sum q_i} = \sum \dfrac{x_i}{q_i^0}$ The set equation contains 2*n* equations and 2*n* unknown. For given partial pressures, the

unknowns are x_i and P_i^0.

Let us consider the special case of the single site Langmuir isotherms are given by

$$q_i^0 = q_{sat} \dfrac{b_i p_i}{1 + b_i p_i} \tag{54}$$

Note, eq (54) assumes that all saturation capacities are equal. Integration of

$\int_0^{P_n^0} q_n^0(f) d\ln f = \int_0^{P_i^0} q_i^0(f) d\ln f$ yields $\dfrac{\pi A}{RT} = \ln(1 + b_i P_i^0) = \ln(1 + b_n P_n^0)$ or $b_i P_i^0 = b_n P_n^0 = \exp\left(\dfrac{\pi A}{RT}\right) - 1$.

The adsorbed phase mole fractions x_i are then determined from $\quad x_i = \dfrac{p_i}{P_i^0}; \quad i = 1,2,...n$. The total

amount adsorbed is calculated from $\quad \dfrac{1}{\sum q_i} = \dfrac{1}{q_t} = \sum \dfrac{x_i}{q_i^0} = \dfrac{x_1}{q_1^0(P_1^0)} + \dfrac{x_2}{q_2^0(P_2^0)} + ... + \dfrac{x_n}{q_n^0(P_n^0)}$ or

$1 = \sum \dfrac{q_i}{q_i^0} = \sum q_i \dfrac{1 + b_i P_i^0}{q_{sat} b_i P_i^0} = \left(1 + \dfrac{1}{b_n P_n^0}\right) \sum \dfrac{q_i}{q_{sat}}$. If we define the fractional occupancies, θ_i, as the ratio of

q_i/q_{sat}, then we obtain $1 = \left(1 + \dfrac{1}{b_n P_n^0}\right) \sum \theta_i = \left(1 + \dfrac{1}{b_n P_n^0}\right) \theta_t$ where θ_t is the total occupancy. In other words

the total occupancy is a function of the pure sorption pressures: $\theta_t = \dfrac{b_n P_n^0}{1 + b_n P_n^0}$ or

$b_n P_n^0 = b_i P_i^0 = \dfrac{\theta_t}{1 - \theta_t} = \dfrac{\theta_t}{\theta_V}$. The equilibrium relation for an ideal solution (γ_i=1) yields $P_i^0 x_i = p_i$ or by

substituting the definition of the mole fraction in the absorbed phase we obtain $P_i^0 q_i = p_i \sum q_i$,

$P_i^0 \theta_i = p_i \theta_t$, $\dfrac{\theta_t}{\theta_V} \theta_i = b_i p_i \theta_t$ or $\theta_i = b_i p_i \theta_V$. Summing over the *n* constituent species, we obtain the total

occupancy $\theta_t = \sum b_i p_i \theta_V$ or $\theta_t = \frac{\sum b_i P_i}{1 + \sum b_i P_i}$. We can back substitute $\theta_t = \frac{\sum b_i P_i}{1 + \sum b_i P_i}$ in $\theta_i = b_i p_i \theta_V$ and

obtain the mixed gas Langmuir isotherm equation $q_i = q_{sat} \frac{b_i p_i}{1 + \sum b_i p_i}$. The sorption pressure for the

pure component can be calculated from $P_i^0 = \frac{1}{b_i} \frac{\theta_t}{\theta_V}$.

9. Entropy effects in adsorption of mixture of hexane isomers in MFI zeolite

The use of the mixed-gas Langmuir expression, equation (31), is strictly valid only when the saturation capacities $q_{i,sat}$ are equal for all species; this point has been emphasized by Sircar.[29-31] When the saturation capacities of the constituent species are significantly different, subtle *entropy* effects come into play in determining mixture loadings in zeolites and metal-organic frameworks.[32-35] For proper description of entropy effects in mixture adsorption, we need to use either the Ideal Adsorbed Solution Theory (IAST)[12] or Real Adsorbed Solution Theory (RAST); for more detailed discussions see Krishna.[35-37] The elements of the matrix of thermodynamic correction factors Γ_{ij} are more precisely determined by numerical differentiation of the IAST and RAST models describing mixture adsorption equilibrium.

As demonstration of entropy effects in mixture adsorption, let us consider sorption of hexane isomers, n-hexane (nC6), 3-methylpentane (3MP) and 2,2 dimethylbutane (22DMB) in MFI zeolite, that consists of a set of straight channels (0.53 nm – 0.56 nm wide), intersecting with zig-zag channels (0.51 nm – 0.55 nm wide). Figures 16, and 17 provide the pore landscape and structural details of MFI zeolite.

Configurational-Bias Monte Carlo (CBMC) simulations of the pure component sorption isotherms of hexane isomers[38, 39] in MFI at 362 K are shown in Fig. 30a. The accuracy of the CBMC calculation techniques have been verified in several publications[4, 38-42] in which comparisons are made with experimental data. The linear nC6 molecule has a chain length that is commensurate with the length of the zig-zag channels (see computational snapshots in Figure 30) and a maximum of 8 molecules per unit

cell can be accommodated. The configuration of di-branched 22DMB is such that these bulky, yet compact, molecules can be located only at the intersections between the straight and zig-zag channels (see computational snapshots in Figure 30) and the saturation loading is restricted to 4 molecules per unit cell. The mono-branched 3MP also prefers to locate at the intersections and only at pressures exceeding 10 kPa can these molecules be pushed into the channel interiors. The saturation capacity of 3MP is 6.3 molecules per unit cell, intermediate in value between that of nC6 and 22DMB. The sorption hierarchy of the pure components in MFI is nC6 > 3MP > 22DMB.

We also note from Figure 30a that the dual-site Langmuir (DSL) isotherm (parameters specified in Table 4):

$$\Theta_i^0(p) \equiv \Theta_{i,A} + \Theta_{i,B} = \frac{\Theta_{i,sat,A} b_{i,A} p}{1 + b_{i,A} p} + \frac{\Theta_{i,sat,B} b_{i,B} p}{1 + b_{i,B} p} \tag{55}$$

provides a good description of the pure component isotherms for all three hexane isomers.

Differences in the saturation capacities of the hexane isomers have a dramatic influence on the component loadings in *mixtures*. For an equimolar ternary mixture of nC6, 3MP and 22DMB both the branched isomers lose out to the linear isomer when the total system pressure exceeds about 500 Pa, at which pressure all the intersection sites are occupied; see Figure 30b. There is considerable amount of experimental evidence to support the accuracy of the CBMC simulations for estimation of mixture adsorption equilibria.[4, 35, 38-42] These data also verify entropy effects in mixture adsorption.[35]

The Ideal Adsorbed Solution Theory (IAST) provides a reasonably good description of the mixture isotherms in zeolites.[33, 35] The component loadings calculated from IAST are shown by the continuous solid lines in Figure 30b. The agreement with the CBMC simulations is found to reasonably good for the whole range of pressures, also for other alkane mixtures.[16, 33, 35, 39]

For the equimolar ternary mixture of nC6, 3MP and 22DMB the calculation of the fractional vacancy θ_V using the IAST are compared in Figure 30c. The IAST calculations are in good agreement with the calculations from CBMC simulations for the whole range of pressures.

The entropy effects in the adsorption of nC6/3MP/22DMB mixtures in MFI zeolite also manifests at other temperatures. Figure 31a shows the unary isotherms, fitted with the dual-site Langmuir-Freundlich model. Figure 31b presents CBMC simulations of component loadings in a ternary equimolar nC6/3MP/22DMB mixture at 433 K as a function of the total hydrocarbons fugacity f_t. The IAST (continuous solids lines) predicts entropy effects in quantitative agreement with CBMC simulations. The plot of the component loading Θ_i as a function of the total mixture loading Θ_t (cf. Figure 31c), demonstrates that configurational entropy effects manifest at $\Theta_t > 4$, causing the hierarchy of component loadings to be nC6 > 3MP > 22DMB. The total mixture loading of $\Theta_t = 4$/uc is attained at a total hydrocarbons fugacity $f_t \approx 0.1$ MPa. This suggests the efficacy of MFI for separating hexane isomers according to the degree of branching; we need to operate at $f_t > 0.1$ MPa.

Entropy effects also manifest for 5-component nC6/2MP/3MP/22DMB/23DMB mixtures in MFI zeolite. The pure component isotherms are shown in Figure 32a; the continuous solid lines are the unary isotherm fits with the dual-site Langmuir-Freundlich model. Figure 32b presents CBMC simulations of component loadings in a 5-component nC6/2MP/3MP/22DMB/23DMB mixture at 433 K as a function of the total hydrocarbons fugacity f_t. The IAST calculations are in good agreement with the CBMC simulations. The plot of the component loading Θ_i as a function of the total mixture loading Θ_t (cf. Figure 32c), demonstrates that configurational entropy effects manifest at $\Theta_t > 4$/uc, causing the hierarchy of component loadings to be nC6 > 2MP > 3MP > 23DMB > 22DMB. The total mixture loading of $\Theta_t = 4$ is attained at a total hydrocarbons fuactity $f_t \approx 0.3$ MPa. This suggests the efficacy of MFI for separating hexane isomers according to the degree of branching; we need to operate at $f_t > 0.3$ MPa.

The adsorption of mixtures of pentane isomers in MFI zeolite are also guided by entropy effects. Figure 33a shows the pure component sorption isotherms for n-pentane (nC5), 2-methylbutane (2MB) and neo-pentane (neo-P) in MFI at 433 K. The symbols represent CBMC simulation data.[34, 38, 39] The continuous lines are the fits using the dual-site Langmuir-Freundlich parameter model. Figure 33b presents CBMC simulations of component loadings in a ternary equimolar nC5/2MB/neo-P mixture at

433 K as a function of the total hydrocarbons fugacity f_t. The IAST (continuous solids lines) predicts entropy effects in quantitative agreement with CBMC simulations. The plot of the component loading Θ_i as a function of the total mixture loading Θ_t (cf. Figure 33c), demonstrates that configurational entropy effects manifest at $\Theta_t > 4$, causing the hierarchy of component loadings to be nC5 > 2MB > neo-P. The total mixture loading of $\Theta_t = 4$/uc is attained at a total hydrocarbons fugacity $f_t \approx 0.05$ MPa. This suggests the efficacy of MFI for separating hexane isomers according to the degree of branching; we need to operate at $f_t > 0.05$ MPa.

For the $nC6(1) \rightleftarrows 2MP(2) \rightleftarrows 22DMB(3)$, and $nC6(1) \rightleftarrows 3MP(2) \rightleftarrows 22DMB(3)$ isomerization reactiona with MFI catalyst, to be considered below, we shall use IAST for calculation of mixture adsorption equilibrium.

10. Entropy effects in adsorption of mixture of hexane isomers in MOR zeolite

Entropy effects also manifest for hexane isomers in MOR zeolite. MOR consists of 12-ring (7.0 Å × 6.5 Å) and 8-ring (5.7 Å × 2.6 Å) channels running along the z-direction (see Figures 18, and 19); detailed crystallographic data are available elsewhere[2].

Let us first consider adsorption of the isomers nC6, 2MP and 22DMB in MOR at 433 K. CBMC simulations of the sorption isotherms are presented in Fig. 34a. The isotherms conform very closely to the dual site Langmuir isotherm

$$\Theta(p) \equiv \Theta_A + \Theta_B; \quad \Theta_A = \frac{\Theta_{sat,A} b_A p}{1 + b_A p}; \quad \Theta_B = \frac{\Theta_{sat,B} b_B p}{1 + b_B p} \tag{56}$$

with fitted DSL model parameters as specified in Table 7. In eq. (56), b_A and b_B represent the DSL model parameters expressed in Pa^{-1} and the subscripts A and B refer to two sorption sites within the zeolite structure, with different sorption capacities and sorption strengths. The $\Theta_{sat,A}$ and $\Theta_{sat,B}$ represent the saturation capacities of sites A and B, respectively. The saturation capacities, $\Theta_{sat} = \Theta_{sat,A} + \Theta_{sat,B}$, of

the hexane isomers increase with the degree of branching. This is due to the increased packing efficiency with increased degree of branching in one-dimensional channels, as has been explained in the published literature. [34, 43] By examination of the snapshots of the location of the molecules within the MOR topology it is clear that the hexane isomers are only adsorbed within the 12-ring channels. Some representative snapshots showing the siting and conformation of the molecules along one of the 12-ring channels, 8 unit cells long, are seen in Fig. 35b,c,d for a pressure $p = 1000$ kPa. Within the same channel length we find five nC6 molecules, seven 2MP molecules and nine 22DMB molecules. The higher loading with increased degree of branching is due to increased degree of compactness of the molecules. The mean length of the hexane isomers are 5.2 Å, 4.3 Å and 3 Å for nC6, 2MP and 22DMB, respectively. The more compact the molecule, the higher the packing efficiency within the one-dimensional channels. This data also explains why the saturation capacity for 22DMB is significantly higher ($\Theta_{sat} = 2.5$), compared to that for 2MP ($\Theta_{sat} = 2.0$) and nC6 ($\Theta_{sat} = 1.95$).

Entropy effects have a pronounced effect on adsorption in mixtures. In order to illustrate this, Fig. 34b presents CBMC simulations for the binary mixture nC6/22DMB in MOR at $T = 433$ K keeping the partial pressures of the two isomers the same, i.e. $p_1 = p_2$. At low pressures, $p = p_1 + p_2 < 500$ kPa, nC6 adsorbs more strongly than 22DMB, but for $p > 500$ kPa, 22DMB adsorbs more strongly than nC6; see Fig. 34b. This reversal of selectivity in favor of 22DMB is caused due to its higher packing efficiency at high loadings.

The continuous solid lines in Figure 34b are the IAST calculations using the unary DSL isotherm fits. The IAST is able to quantitatively predict the entropy effects in MOR zeolite.

For the nC6(1)$\rightleftarrows$2MP(2)$\rightleftarrows$22DMB(3) isomerization reaction with MOR catalyst, to be considered later, we shall use IAST for calculation of mixture adsorption equilibrium.

11. The Langmuir-Hinshelwood formulation of reaction kinetics

Within the micropores of zeolite catalysts, the appropriate expression for the reaction kinetics needs to be set up in terms of the component loadings in the adsorbed phase, q_i. Equilibrium thermodynamics

tells us that the Gibbs free energy should be at a minimum.[44, 45] The change in the Gibbs free energy is given by eq(39). For a reacting mixture we obtain

$$dG = -SdT + Ad\pi + \sum \mu_i \nu_i d\chi \qquad (57)$$

where ν_i is the stoichiometric coefficient and χ the fractional conversion. At constant spreading pressure and temperature, eq (57) simplifies

$$dG = \sum \mu_i \nu_i d\chi \qquad (58)$$

In order to reach a minimum of the Gibbs free energy we have to satisfy the relation

$$\left(\frac{\partial g}{\partial \chi}\right)_{\pi,T} = \sum \nu_i \mu_i = 0$$

Substituting the chemical potential in the adsorbed phase (see eq(45)) results in

$$\sum \nu_i \left(g_i^0(T) + RT \ln(P_i^0) + RT \ln(\gamma_i x_i)\right) = 0 \qquad (59)$$

$$\exp\left(\sum \nu_i \frac{g_i^0(T)}{RT}\right) = \Pi\left(P_i^0 \gamma_i x_i\right)^{\nu_i} \qquad (60)$$

The left hand side describes the equilibrium constant

$$\exp\left(\sum \nu_i \frac{g_i^0(T)}{RT}\right) = \exp\left(\frac{\Delta G^\circ}{RT}\right) = K_{eq} \qquad (61)$$

Therefore, for an ideal adsorbed solution we obtain:

$$K_{eq} = \Pi\left(P_i^0 x_i\right)^{\nu_i} \qquad (62)$$

At thermodynamic equilibrium we know that the chemical potentials in the gas and adsorbed phase are equal, $\mu^{gas} = \mu^{ads}$. Therefore, $P_i^0 x_i = p_i$ applies and therefore

$$K_{eq} = \Pi\left(P_i^0 x_i\right)^{\nu_i} = \Pi(p_i)^{\nu_i} \qquad (63)$$

Consider an isomerization reaction: A↔B.

$$K_{eq} = \frac{P_2^0 x_2}{P_1^0 x_1} = \frac{P_2^0 q_2}{P_1^0 q_1} = \frac{p_2}{p_1} \tag{64}$$

Equation (64) is general and holds for IAST theory as well as the mixed gas Langmuir model.

Let us assume that the mixed-gas Langmuir model for mixture adsorption equilibrium relates the fractional occupancies, θ_i, molar loadings, q_i, of components 1 (= A$_1$) and 2 (= A$_2$) to the partial pressures p_1 and p_2 in the bulk gas phase surrounding the zeolite catalyst:

$$\theta_1 = \frac{q_1}{q_{1,sat}} = \frac{b_1 p_1}{1 + b_1 p_1 + b_2 p_2} = b_1 p_1 \theta_V ; \quad \theta_2 = \frac{q_2}{q_{2,sat}} = \frac{b_2 p_2}{1 + b_1 p_1 + b_2 p_2} = b_2 p_2 \theta_V \tag{65}$$

The Langmuir-Hinshelwood (L-H) kinetic expression relates the reaction rate to the fractional occupancies θ_i. The expression for the net forward reaction rate, expressed in terms of moles per kg catalyst per second, is

$$R_{kg} = k_1^\theta \theta_1 - k_2^\theta \theta_2 = k_1 q_1 - k_2 q_2$$
$$k_1^\theta \equiv q_{1,sat} k_1 ; \quad k_2^\theta \equiv q_{2,sat} k_2 \tag{66}$$

Combination of equations (66) and (65) allows the L-H expression to be expressed in terms of the partial pressures

$$R_{kg} = k_1^\theta \theta_1 - k_2^\theta \theta_2 = \frac{k_1 q_{1,sat} b_1 p_1 - k_2 q_{2,sat} b_2 p_2}{1 + b_1 p_1 + b_2 p_2} = \left(k_1 q_{1,sat} b_1 p_1 - k_2 q_{2,sat} b_2 p_2 \right) \theta_V = \left(k_1^p p_1 - k_2^p p_2 \right) \theta_V$$
$$k_1^p \equiv k_1 q_{1,sat} b_1 ; \quad k_2^p \equiv k_2 q_{2,sat} b_2 \tag{67}$$

We conclude that the L-H expression (67) is consistent with the mixed-gas Langmuir model for describing mixture adsorption. More generally, we may use the rate expression (66), wherein the component loadings q_1, and q_2 are determined using say the IAST or RAST.

In the foregoing, the L-H expression has been expressed in three different, but entirely equivalent, ways; in each case, the reaction rate constants have different units. In equation (66), the reaction rate constants k_1, k_2 have the units: s^{-1}; the reaction rate constants k_1^θ, k_2^θ have the units: mol kg^{-1} s^{-1}. In equation (67), the reaction rate constants k_1^p, k_2^p have the units: mol kg^{-1} Pa^{-1} s^{-1}. In the calculations and

simulations presented in this article, we choose the rate expression in terms of the molar loadings,

$R_{kg} = k_1 q_1 - k_2 q_2$.

12. Simulation methodology for transient diffusion-reaction in microporous crystal

For most crystal geometries, representation as an equivalent sphere is an acceptable approximation.[11] Indeed, most researchers report their uptake diffusivities in terms of a model that assumes uptake within a single spherical crystalline particle. The values thus obtained for the diffusivities within a spherical crystal can be translated to other crystal geometries by comparing values at the same characteristic dimension, defined as the ratio of the crystal volume to its external suface area. For a spherical shaped crystal of radius r_c, the ratio of the volume to the external surface area is $\dfrac{\left(\dfrac{4}{3}\pi r_c^3\right)}{4\pi r_c^2} = \dfrac{r_c}{3}$.

The radial distribution of molar loadings, q_i, within a spherical crystallite, of radius r_c, is obtained from a solution of a set of differential equations describing the uptake

$$\rho \frac{\partial q_i(r,t)}{\partial t} = -\frac{1}{r^2}\frac{\partial}{\partial r}\left(r^2 N_i\right) + \rho \nu_i R_{kg} \qquad (68)$$

where ν_i is the reaction stoichiometric coefficient; negative for reactants and positive for products; R_{kg} represents the reaction rate expressed as moles per kg catalyst per second. The reaction rate is commonly formulated using the Langmuir-Hinshelwood (L-H) expression such as equation (67).[43] The fluxes N_i, in turn, are related to the radial gradients in the molar loadings by Equation (35), simplified in the form of Equation (36) or Equation (38).

At time $t = 0$, i.e. the initial conditions, the molar loadings $q_i(r,0)$ at all locations r within the crystal are uniform (zero loadings). For all times $t \geq 0$, the exterior of the crystal is brought into contact with a bulk gas mixture at partial pressures $p_i(r_c,t)$ that is maintained constant till the crystal reaches thermodynamic equilibrium with the surrounding gas mixture.

$$t \geq 0; \quad q_i(r_c,t) \text{ in equilibrium with the initial values } p_i(r_c,t) \tag{69}$$

At any time t, during the transient approach to thermodynamic equilibrium, the spatial-averaged component loading within the crystallites of radius r_c is calculated using

$$\overline{q_i}(t) = \frac{3}{r_c^3} \int_0^{r_c} q_i(r,t) r^2 dr \tag{70}$$

The set of Equations (35), (68), (69), and (70) need to be solved numerically using robust computational techniques. Equations (68) are first subjected to finite volume discretization. One of two strategies can be adopted: (a) equi-volume discretization, or (b) equi-distant discretization; see Figure 36. The choice of the discretization scheme used is crucially important in obtaining accurate, converged results. The choice of equi-volume slices is needed when the gradients of the loadings are particularly steep nearer to $r = r_c$. For either strategy, about $100 – 400$ slices are employed, depending on the guest/host combination. Combination of the discretized partial differential equations (68) along with algebraic equations describing mixture adsorption equilibrium, results in a set of differential-algebraic equations (DAEs), which are solved using BESIRK.[46] BESIRK is a sparse matrix solver, based on the semi-implicit Runge-Kutta method originally developed by Michelsen,[47] and extended with the Bulirsch-Stoer extrapolation method.[48] Use of BESIRK improves the numerical solution efficiency in solving the set of DAEs. The evaluation of the sparse Jacobian required in the numerical algorithm is largely based on analytic expressions.[16] Further details of the numerical procedures used in this work, are provided by Krishna and co-workers;[16-18, 49] interested readers are referred to our website that contains the numerical details.[49]

13. Simulation methodology for transient breakthrough in fixed bed reactors

Fixed bed and moving bed reactors are commonly used in industry for carrying out zeolite catalyzed reactions. In moving bed reactors, the operations are essentially *transient* in nature; see schematic in Figure 37. Assuming plug flow of an *n*-component gas mixture through a fixed bed maintained under

isothermal conditions, the partial pressures in the gas phase at any position and instant of time are obtained by solving the following set of partial differential equations for each of the species i in the gas mixture.[11, 16, 50-54]

$$\frac{1}{RT}\frac{\partial p_i(t,z)}{\partial t} = -\frac{1}{RT}\frac{\partial(v(t,z)p_i(t,z))}{\partial z} - \frac{(1-\varepsilon)}{\varepsilon}\frac{3}{r_c}\left(N_i\big|_{r=r_c}\right); \quad i = 1,2,...n \tag{71}$$

In equation (71), t is the time, z is the distance along the reactor, ρ is the framework density, ε is the bed voidage, v is the interstitial gas velocity, and $N_i\big|_{r=r_c}$ is the molar flux loading at the position $r = r_c$, monitored at position z, and at time t, determined by use of Equation (36) or Equation (38), as appropriate.

Summing equation (70) over all n species in the mixture allows calculation of the *total average* molar loading of the mixture within the crystallite

$$\overline{q}_t(t,z) = \sum_{i=1}^{n}\overline{q}_i(t,z) \tag{72}$$

Assuming that the crystallites in the reactor bed are initially free of adsorbates, i.e. we have the initial condition

$$t = 0; \quad q_i(0,z) = 0 \tag{73}$$

At time, $t = 0$, the inlet to the reactor, $z = 0$, is subjected to a step input of the n-component gas mixture and this step input is maintained till steady-state conditions are reached.

$$t \geq 0; \quad p_i(0,t) = p_{i0}; \quad v(0,t) = v_0 \tag{74}$$

where v_0 is the interstitial gas velocity at the inlet to the reactor.

For convenience, the set of equations describing the fixed bed reactor are summarized in Figure 38. Typically, the reactor length is divided into 100 – 200 slices. Combination of the discretized partial differential equations (PDEs) along with the algebraic IAST or RAST equilibrium model, results in a set

of differential-algebraic equations (DAEs), which are solved using BESIRK.[46] Interested readers are referred to our website that contains the numerical details.[49]

Besides, the breakthrough simulations with a step-input (74), we also carried out simulations for a packed bed adsorber with injection of a short duration pulse of the mixture of reactants. Figure 39 presents a schematic of a packed bed reactor with pulse input of feed gas mixture. For simulation of pulse chromatographic reactors, we use the corresponding set of inlet conditions

$$0 \le t \le t_0; \quad p_i(0,t) = p_{i0}; \quad u(0,t) = u_0 \tag{75}$$

where the time for duration of the pulse is t_0.

14. Effectiveness factor for zeolite catalyzed isomerization reaction

The analysis of diffusion and chemical reaction within catalysts particles is extensively treated in standard textbooks.[55-57] The derivation of analytic expressions for the effectiveness factor are largely restricted to the use of the Fickian equation (38).

Consider the reversible isomerization reaction $A_1 \leftrightarrow A_2$; such isomerization reactions are of great significance to the petroleum industry.[43, 58-63] Let us consider the specific example of isomerization of 2-methylpentane (2MP) to its di-branched isomer 2,2 dimethyl-butane (22DMB) in a packed bed reactor using extrudates of MFI zeolite as catalyst. Figures 16, and 17 provide the pore landscape and structural details of MFI zeolite. The process conditions correspond to those described by Jolimaître et al.,[64, 65] that are summarized in Table 8.

The rate of chemical reaction, $2MP(1) \rightleftarrows 22DMB(2)$, expressed as moles per kg catalyst per second, R_{kg}, is written as $R_{kg} = k_1 q_1 - k_2 q_2$. The rate of chemical reaction per m^3 of catalyst, R_{m3}, is $R_{m3} = \rho R_{kg}$.

The reaction rate constants, taken from Baur and Krishna.[61, 62] are $k_1 = 0.0011$ s^{-1}, $k_2 = 0.00055$ s^{-1}.

Under steady-state conditions we have

$$\frac{1}{r^2}\frac{\partial}{\partial r}\left(r^2 N_i\right) = \rho \nu_i R_{kg}; \quad \text{steady - state} \tag{76}$$

where ν_i is the reaction stoichiometric coefficient; $\nu_1 = -1$ for reactant 2MP; $\nu_2 = 1$ for product 22DMB.

After insertion of the appropriate rate expressions for the chemical reaction rate, R_{kg}, the flux equations for N_i, the equation (76) can be solved to obtain the steady-state distribution of the loadings of the components along the crystal radius, r.

$$\eta = \frac{\int_0^1 R_{kg}\, \xi^2 d\xi}{R_{kg}\Big|_{r=r_c} \int_0^1 \xi^2 d\xi} \tag{77}$$

where $\xi = r / r_c$ is the dimensionless radial coordinate. The chemical reaction rate R_{kg}, varies with loading and is ξ-dependent. The effectiveness factor, η, quantifies the influence of intra-crystalline diffusion on the effective rate of chemical reaction. In the absence of any diffusional limitations, $\eta = 1$, and the chemical reaction rate can be calculated using the loadings at the external surface, $R_{kg}\Big|_{r=r_c}$.

Baur and Krishna.[61, 62] have presented analytic solutions to equation (76) for a variety of scenarios.

(1) Classical scenario: the diffusivities are independent of loading (called the weak confinement scenario), and thermodynamic coupling effects are ignored, $\Gamma_{ij} = \delta_{ij}$. Also ignored are the correlation effects, i.e. $Đ_1/Đ_{12} \to 0$; $Đ_2/Đ_{12} \to 0$. In this article, this Scenario 1 is also referred to as "Fick model, with $\Gamma_{ij} = \delta_{ij}$".

(2) "Weak" confinement scenario for the diffusivities; in this scenario the M-S diffusivities $Đ_1, Đ_2$ are assumed to be loading independent. Also ignored are the correlation effects, i.e. $Đ_1/Đ_{12} \to 0$; $Đ_2/Đ_{12} \to 0$. Thermodynamic coupling effects are accounted for using the mixed-gas Langmuir isotherm model. In this article, this Scenario 2 is also referred to as "M-S model, weak confinement, with Γ_{ij}".

(3) Strong confinement scenario for the diffusivities in which the diffusivities are related to the zero-loading diffusivities by $Đ_i = Đ_i(0)\theta_V = Đ_i(0)(1 - \theta_1 - \theta_2)$. Also ignored are the correlation effects, i.e. $Đ_1/Đ_{12} \to 0; \quad Đ_2/Đ_{12} \to 0$. Thermodynamic coupling effects are accounted for using the mixed-gas Langmuir isotherm model. In this article, this Scenario is also referred to as "M-S model, strong confinement, with Γ_{ij}".

(4) "Weak" confinement scenario for the diffusivities; in this scenario the M-S diffusivities $Đ_1, Đ_2$ are assumed to be loading independent. Thermodynamic coupling effects are accounted for using the mixed-gas Langmuir isotherm model. Correlation effects are accounted for with finite values of $Đ_1/Đ_{12}; \quad Đ_2/Đ_{12}$. Calculations using Scenario 4 are not presented in this article; the reader is referred to Baur and Krishna, [61, 62] and Krishna and van Baten.[4, 7, 66]

(5) Strong confinement scenario for the diffusivities in which the diffusivities are related to the zero-loading diffusivities by $Đ_i = Đ_i(0)\theta_V = Đ_i(0)(1 - \theta_1 - \theta_2)$. Thermodynamic coupling effects are accounted for using the mixed-gas Langmuir isotherm model. Correlation effects are accounted for with finite values of $Đ_1/Đ_{12}; \quad Đ_2/Đ_{12}$. Calculations using Scenario 5 are not presented in this article; the reader is referred to Baur and Krishna, [61, 62] and Krishna and van Baten.[4, 7, 66]

For the classical scenario (1), the effectiveness factor is given by

$$\eta = \frac{1}{\phi}\left(\frac{1}{\tanh(3\phi)} - \frac{1}{3\phi}\right) \tag{78}$$

where the Thiele modulus is calculated from

$$\phi \equiv \frac{r_c}{3}\sqrt{\frac{k_1}{Đ_1(0)} + \frac{k_2}{Đ_2(0)}} \tag{79}$$

Analytical solutions are derived for the other four scenarios by Baur and Krishna.[61, 62]

The expressions for the effectiveness factor are expressed as

$$\eta = \frac{1}{\Phi}\left(\frac{1}{\tanh(3\Phi)} - \frac{1}{3\Phi}\right); \quad \text{General scenario} \tag{80}$$

where the generalized Thiele modulus Φ is obtained by multiplying the classical Thiele modulus ϕ by various "correction factors" as listed in Table 3.[61]

The solutions for the vacancy profile $\theta_V(\xi)$ for spherical geometry is

$$\frac{\theta_V}{\theta_{Vs}} = \frac{1}{\Psi^2} + \left(\frac{\Psi^2 - 1}{\Psi^2}\right)\frac{\sinh(3\Phi\xi)}{\xi\sinh(3\Phi)}; \quad \text{sphere} \tag{81}$$

We draw the readers' attention to the typographical error in the vacancy profile for a spherical catalyst in equation (27) of Baur and Krishna;[61] equation (81) is the corrected version.

The fractional occupancies of the individual components can be obtained from

$$\begin{aligned}
\theta_1 &= \frac{\Lambda}{(\Lambda - 1)} - \frac{\Lambda\theta_{Vs} + \theta_{1s} + \Lambda\theta_{2s}}{(\Lambda - 1)}\frac{\theta_V}{\theta_{Vs}} \\
\theta_2 &= \frac{1}{(1 - \Lambda)} - \frac{\Lambda\theta_{2s} + \theta_{Vs} + \theta_{1s}}{(1 - \Lambda)}\frac{\theta_V}{\theta_{Vs}}
\end{aligned} \tag{82}$$

As illustration, Figure 40a presents calculations of the (steady-state) effectiveness factor, η, for uptake inside MFI catalyst exposed to a gas phase 2MP(1)/22DMB(2) mixture at 473 K, carrying out the isomerization reaction $2MP(1) \rightleftarrows 22DMB(2)$. The partial pressures of the components in the bulk gas phase are $p_1 = p_2 = 10$ kPa. The ratio of rate constants $k_1/k_2 = 2$. The values of the rate constant k_1 are varied. The zero-loading diffusivities $Đ_1(0) = 2\times10^{-14}$ m^2 s^{-1}; $Đ_1(0) = 2.5\times10^{-16}$ m^2 s^{-1}. The radius of the crystal $r_c = 2$ μm. The x-axis in Figure 40a is the classical Thiele modulus calculated using equation (79). For 2MP/22DMB mixtures, correlation effects are not important as established by the experiments of Jolimaître et al.;[64, 65] see also detailed analysis of Krishna.[4, 22] We therefore ignore the scenarios (4) and (5) that include correlation effects. The calculations using the three different scenarios 1, 2 and 3 are based on the analytical solutions provided by Baur and Krishna.[61] The highest effectiveness factors are obtained with Scenario 1 in which thermodynamic coupling effects are ignored, by taking $\Gamma_{ij} = \delta_{ij}$. As is to be expected, diffusion effects are strongest for the scenarios in which the M-S diffusivities are linearly related to the vacancy, $Đ_i = Đ_i(0)\theta_V$.

The most important feature of the Maxwell-Stefan diffusion formulation is the proper accounting of the adsorption mixture thermodynamics. In order to stress the direct influence of adsorption thermodynamics, Figure 40b presents calculations of the effectiveness factor, η, for a MFI catalyst that is exposed to an equimolar gas 2MP/22DMB gas mixture; the total pressure $p_1 + p_2$ is varied in the range 0 to 40 kPa. The reaction and diffusion parameters are chosen as: $k_1 = 0.0011$ s^{-1}; $k_1/k_2 = 2$, $\phi = 1.0011$. Increasing the bulk gas pressure increases the fractional occupancy at the catalyst surface, $\theta_{1s} + \theta_{2s}$. The classical effectiveness factor is a constant, independent of $\theta_{1s} + \theta_{2s}$. By proper accounting of the mixture adsorption thermodynamics, we note that the effectiveness factor for Scenarios 2 (weak confinement), and 3 (strong confinement) decreases when the $\theta_{1s} + \theta_{2s}$ increases.

Figure 41a presents the calculations of the (steady-state) effectiveness factor, η, for uptake inside MFI catalyst exposed a gas phase o-xylene(1)/p-xylene(2) mixture at 433 K, carrying out the isomerization reaction $o-\text{xylene}(1) \rightleftarrows p-\text{xylene}(2)$. The partial pressures of the components in the bulk gas phase are $p_1 = p_2 = 1$ MPa. The zero-loading diffusivities $Ð_1(0) = 1\times10^{-16}$ m^2 s^{-1}; $Ð_1(0) = 1\times10^{-14}$ m^2 s^{-1}. The ratio of rate constants $k_1/k_2 = 2$. The values of the rate constant k_1 are varied. The radius of the crystal r_c = 10 μm. The classical Thiele modulus is calculated from Equation (78). The calculations using the three different scenarios are based on the analytical solutions provided by Baur and Krishna.[61] The lowest effectiveness factor is realized for Scenario 3; in this scenario both M-S diffusivities are reduced following $Ð_i = Ð_i(0)\theta_V = Ð_i(0)(1 - \theta_1 - \theta_2)$.

Figure 41b presents calculation of the effectiveness factor, η, for $o-\text{xylene}(1) \rightleftarrows p-\text{xylene}(2)$ reaction in MFI catalyst exposed a gas phase equimolar o-xylene(1)/p-xylene(2) mixture at 433 K and total pressures varying in the range 0 to 3 MPa. The x-axis is the fractional occupancy at the catalyst surface, $\theta_{1s} + \theta_{2s}$. The reaction rate constant $k_1 = 1\times10^{-4}$ s^{-1}; the ratio of rate constants $k_1/k_2 = 2$. In this case, we note that the effectiveness factor for Scenario 2 is slightly higher than the classical effectiveness factor. For Scenario 3 (strong confinement), there is a significant reduction in the

effectiveness factor with increased occupancy due to the reduction in the M-S diffusivities following

$$Đ_i = Đ_i(0)\theta_V = Đ_i(0)(1 - \theta_1 - \theta_2).$$

In all the transient diffusion-reaction simulations presented in this article, we assume negligible correlation effects and use either Equation (36) or Equation (38) to describe the intra-crystalline fluxes.

15. $2MP(1) \rightleftarrows 22DMB(2)$ **reaction in MFI catalyst**

We now demonstrate the possibility of transient overshoots within microporous zeolite catalysts. As illustration, we consider the reversible isomerization reaction $2MP(1) \rightleftarrows 22DMB(2)$ using extrudates of MFI zeolite as catalyst. The adsorption and diffusion data are taken from the works of Jolimaître et al.;[64, 65] these are summarized in Table 8. For 2MP/22DMB mixtures, correlation effects are not important as established by the experiments of Jolimaître et al.;[64, 65] see also detailed analysis of Krishna.[4, 22] We therefore ignore the scenarios (4) and (5) that include correlation effects.

The mixed-gas Langmuir model for mixture adsorption equilibrium, equation (65), relates the molar loadings of components 1 (= 2MP) and 2 (= 22DMB) to the partial pressures p_1 and p_2 in the bulk gas phase surrounding the MFI catalyst. The rate of chemical reaction, expressed as moles per kg of catalyst per second is written as $R_{kg} = k_1 q_1 - k_2 q_2$. The reaction rate constants, taken from Baur and Krishna,[61] are $k_1 = 0.0011$ s^{-1}, $k_2 = 0.00055$ s^{-1}.

Consider first the transient uptake with chemical reaction within MFI extrudates exposed to a gas phase 2MP/22DMB mixture at 473 K. The partial pressures of the components in the bulk gas phase are $p_1 = p_2 = 10$ kPa. The continuous solid lines in Figure 42a represent the transient simulations that include thermodynamic coupling using the flux relations equation (36). Both the weak and strong confinement scenarios predict a pronounced overshoot in the uptake of 2MP. The 2MP overshoot signifies the phenomena of uphill diffusion.[15, 22, 67] The dashed lines in Figure 42a represent uptake simulations ignoring thermodynamic coupling and use uncoupled Fick model (38); no overshoot in 2MP

uptake is observed. This leads us to conclude that thermodynamic coupling is the origin of the transient overshoot in the 2MP uptake.

Figure 42b compares the transient equilibration trajectories in composition space, using three different model implementations (Fick model, M-S model, with weak and strong confinements). Both the M-S model implementations (weak and strong confinement) predict the 2MP overshoot and the trajectories in composition space are significantly different from that anticipated by the Fick model.

Figure 43 presents the equilibration trajectories within the catalyst in ternary occupancy space, with coordinates, θ_1 (2MP), θ_2 (22DMB), θ_V (MFI zeolite vacancy).

In order to demonstrate the 2MP occupancy overshoots persist for other bulk gas phase mixture compositions, Figure 44 presents simulations of the equilibration trajectories for different choices of the bulk gas phase mixture compositions, keeping the total pressure $p_1 + p_2 = 20$ kPa. We note that the 2MP overshoot manifests for all compositions examined.

Figure 45 compares the steady-state radial distribution of component loadings inside MFI catalyst for the specific case in which the reaction and diffusion parameters are chosen as: $k_1 = 0.0011$ s^{-1}; $k_1/k_2 = 2$, $\phi = 1.0011$. The continuous solid lines represent simulations include thermodynamic coupling using equation (36), with weak and strong confinement scenarios. The dashed lines represent simulations ignoring thermodynamic coupling and use uncoupled flux equation (38). The M-S and Fick models yield significantly different loading profiles. The spatial-averaged loading of the desired 22DMB product is predicted to be higher in the M-S model than for the Fick model.

In order to highlight the influence of thermodynamic coupling effects on the performance of fixed bed reactors, Figure 46a presents the transient breakthrough simulations for fixed bed 2MP/22DMB isomerization reactor with MFI extrudates. The continuous solid lines represent uptake simulations include thermodynamic coupling using equation (36). The dashed lines represent breakthrough simulations ignoring thermodynamic coupling and using uncoupled flux equation (38). The reactor performance is significantly different in the two diffusion model implementations. Baur and Krishna,[63]

present a detailed analysis of transient operations of simulated moving bed reactors for optimal 2MP/22DMB isomerization performance.

At steady-state, the gas phase concentrations in the fixed bed reaction, calculated using the two model implementations, are shown in Figures 46b,c. For the M-S model calculations with the weak confinement, the rate of production of 22DMB is 1.81×10^{-4} mol (kg catalyst)$^{-1}$ s^{-1}; this value is significantly higher than the rate of production of 22DMB predicted by the Fick model calculations that ignores thermodynamic coupling: 1.14×10^{-4} mol (kg catalyst)$^{-1}$ s^{-1}. The rate of the production of 22DMB in the M-S model with strong confinement is 1.21×10^{-4} mol (kg catalyst)$^{-1}$ s^{-1}. The use of proper models to describe reactor conversion is vitally important. On the basis of the re-analysis of transient adsorption breakthrough experiments of Jolimaître et al.[64, 65] it has been established that the proper model to describe intra-crystalline diffusion is the M-S model with the weak confinement scenario for M-S diffusivities.[4, 22]

16. $o-xylene(1) \rightleftarrows p-xylene(2)$ **reaction in MFI catalyst**

Para-xylene is an important feedstock in the petrochemical industry.[35] The largest use of p-xylene is in its oxidation to make terephthalic acid, that is used in turn to make polymers such as polyethylene terephthalate (PET) and polybutylene terephthalate (PBT). PET is one of the largest volume polymers in the world, and is used to produce fibers, resins, films, and blown beverage bottles. Isomerization of xylenes with MFI catalyst is of importance.

As illustration, we consider the isomerization of o-xylene to p-xylene: $o-xylene(1) \rightleftarrows p-xylene(2)$.

The rate of chemical reaction, expressed as moles per kg of catalyst per second is written as $R_{kg} = k_1 q_1 - k_2 q_2$. The rate constants are taken as: $k_1 = 1 \times 10^{-4}$ s^{-1}, $k_2 = 5 \times 10^{-5}$ s^{-1}. Para-xylene has a higher diffusivity than o-xylene due to configurational considerations. Following the work of Mirth et al.,[68] we assume that the diffusivity of p-xylene is 100 times that of o-xylene.

Figure 47a shows the transient uptake inside MFI catalyst exposed to a gas phase o-xylene(1)/p-xylene(2) mixture at 433 K. The partial pressures of the components in the bulk gas phase are $p_1 = 5$ MPa; $p_2 = 5$ MPa. The continuous solid lines represent uptake simulations include thermodynamic coupling using equation (36). In this scenario, we note that p-xylene shows a pronounced overshoot in the uptake; this overshoot signifies the phenomena of uphill diffusion.[15, 22, 67] The dashed lines represent uptake simulations ignoring thermodynamic coupling and use uncoupled flux equation (38); in this scenario no p-xylene overshoot is observed.

Figure 47b compares the transient equilibration trajectories in 3D composition space, using three different model implementations (Fick model, M-S model (with weak and strong confinements)). Both the M-S model implementations (weak and strong confinement) predict the p-xylene overshoot and the trajectories in composition space are significantly different from that anticipated by the Fick model.

Figure 48 plots the equilibration trajectories in ternary occupancy space, with coordinates, θ_1 (o-xylene), θ_2 (p-xylene), θ_V (MFI zeolite vacancy). The diffusivity and kinetics data are the same as in Figure 47.

In order to demonstrate the p-xylene occupancy overshoots persist for other bulk gas phase mixture compositions, Figure 49 presents simulations of the equilibration trajectories for different choices of the bulk gas phase mixture compositions, keeping the total pressure $p_1 + p_2 = 10$ MPa as constant. We note that the p-xylene overshoot gets shallower with increasing partial pressure of o-xylene; For the choices $p_1 = 9$ MPa, $p_2 = 1$ MPa, and $p_1 = 10$ MPa, $p_2 = 0$ MPa, there is no overshoot of p-xylene occupancy.

Though there is no reliable published experimental data on the loading dependence of xylenes in MFI, the experimental data of Ban et al.[69] and Duan et al.[70] on the loading dependence of the diffusivity of benzene in MFI suggests that the strong confinement scenario is the appropriate one to use.

Figure 50 compares the steady-state radial distribution of component loadings in inside MFI catalyst for scenarios 1 and 2 for the specific case $k_1 = 1 \times 10^{-4}$ s^{-1}; $\phi = 3.34$. The continuous solid lines represent simulations include thermodynamic coupling using equation (36), along with the strong confinement

scenario. The dashed lines represent simulations ignoring thermodynamic coupling and use uncoupled flux equation (38). The two scenarios yield significantly different loading profiles.

In order to highlight the influence of the flux model on the performance of fixed bed reactors, we performed steady-state simulations for a fixed zeolite bed reactor with a o-xylene(1)/p-xylene(2) mixture at 433 K. The partial pressures in the inlet mixture are $p_1 = 10$ MPa; $p_2 = 0$ MPa. Figure 51 shows the gas phase molar concentrations of o-xylene and p-xylene along the length of the reactor bed. The continuous solid lines represent simulations include thermodynamic coupling using equation (36), along with the strong confinement scenario. The dashed lines represent simulations ignoring thermodynamic coupling and use uncoupled flux equation (38). For the M-S model calculations with the strong confinement, the rate of production of p-xylene is 5.7×10^{-6} mol (kg catalyst)$^{-1}$ s^{-1}; this value is significantly lower than the rate of production of p-xylene predicted by the Fick model calculations that ignores thermodynamic coupling: 7.2×10^{-6} mol (kg catalyst)$^{-1}$ s^{-1}. Use of the Fick model to predict reactor performance will be overly optimistic.

The overshoot in the p-xylene uptake, experienced in Figure 47 can be exploited by carrying out the xylene isomerization reaction in a pulsed chromatographic reactor. Figure 52 presents the transient breakthrough in a reactor feed with a pulse injection of 200 s duration. The continuous solid lines represent breakthrough simulations using equation (36) with strong confinement. We note that the exiting gas mixture initially consists of pure o-xylene. Pure p-xylene can be recovered towards the end of the pulse cycle.

17. $nC6(1) \rightleftarrows 3MP(2) \rightleftarrows 22DMB(3)$ **reaction with MFI catalyst**

Consider uptake within MFI catalyst carrying out the isomerization of nC6 to produce a product containing mono-branched 3-methylpentane (3MP) and di-branched 22DMB. We restrict our analysis to the simplified reaction scheme $nC6(1) \rightleftarrows 3MP(2) \rightleftarrows 22DMB(3)$ where the Langmuir-Hinshelwood (L-H) reaction rate expressions for the two constituent reversible reactions, expressed as mol (kg catalyst)$^{-1}$

s^{-1} are $R_{kg,1} = \left(k_{f1}q_1 - k_{b1}q_2 \right)$; $R_{kg,2} = \left(k_{f2}q_2 - k_{b2}q_3 \right)$. The subscripts f and b refer to the forward and reverse reactions, and the subscripts 1 and 2 refer to the first and second isomerization reaction steps. Using our earlier publication as guidelines,[43] we take $k_{f1} = k_{f2} = 0.01$ s^{-1} and $k_{b1} = k_{b2} = 0.001$ s^{-1}. The catalyst radius is taken to be $r_c = 1$ mm.

Figure 53a presents simulations of transient uptake inside MFI catalyst exposed to a gas phase nC6(1)/3MP(2)/22DMB(3) mixture at 362 K. The partial pressures of the components in the bulk gas phase are $p_1 = 1000$ Pa; $p_2 = 1$ Pa, $p_3 = 1$ Pa. The mixture adsorption equilibrium is determined using the IAST. The zero-loading M-S diffusivities are chosen as $Đ_1(0)/r_c^2 = 2\times10^{-4}$ s^{-1}; $Đ_2(0)/r_c^2 = 2\times10^{-5}$ s^{-1}; $Đ_3(0)/r_c^2 = 1\times10^{-5}$ s^{-1}; the choice of these diffusivities is based on earlier works.[4, 22, 42, 71] The continuous solid lines represent uptake simulations with the M-S equation (36). We note that the most mobile nC6 displays an overshoot during transient uptake. 3-methylpentane (3MP), with intermediate mobility, also exhibits a slight overshoot. The dashed lines represent uptake simulations with uncoupled Fickian flux equations (38); in this scenario, all three components approach equilibrium in a monotonous manner.

Figure 53b compares the transient equilibration trajectories in 3D composition space, using three different flux calculation scenarios; the followed trajectories are significantly different.

The important conclusion to be drawn from the uptake simulations in Figure 53 is that the average molar loading of 22DMB is predicted to be higher for the model that includes thermodynamic coupling in the proper manner.

In order to confirm that this conclusion also holds for fixed bed reactors of finite length, steady-state simulations were performed for a fixed bed reactor. The gas phase molar concentrations as function of the dimensionless length of the fixed bed, z/L are shown in Figures **54**a,b. For the Fick model that ignores thermodynamic coupling the rate of production of 22DMB is 7.82×10^{-5} mol (kg catalyst)$^{-1}$ s^{-1}; this value is lower than either of the two different implementations of the M-S model. For the weak

confinement scenario, the rate of production of 22DMB is 3.4×10^{-4} mol (kg catalyst)$^{-1}$ s^{-1}. For the strong confinement scenario, the rate of production of 22DMB is 2.74×10^{-4} mol (kg catalyst)$^{-1}$ s^{-1}.

The choice of the proper model is important in reactor modelling. In the transient uptake experiments of Titze et al. [42], the M-S model, including thermodynamic coupling, has been established to be a good representation of the uptake of n-hexane/2-methylpentane mixtures in MFI zeolite.

The difference between the Fick and M-S model formulations become more prominent in transient operations. To demonstrate this, we carried out transient fixed reactor simulations for the same set of input conditions as in Figure 54. Figure 55 shows the molar concentrations in the gas phase exiting the reactor, plotted as a function of the dimensionless time, $\tau = \dfrac{tv}{L}$. The continuous solid lines represent simulations with the M-S model, Equation (36), for the weak confinement scenario. The dashed lines represent simulations ignoring thermodynamic coupling and use uncoupled flux equation (38). For the M-S model the breakthrough of 22DMB occurs earlier and there is a period of time within which nearly pure 22DMB may be recovered as product. The exploitation of transient operation is best carried out in simulated moving bed reactor configurations, as discussed in detail by Krishna and Baur.[43]

18. $nC6(1) \rightleftarrows 3MP(2) \rightleftarrows 22DMB(3)$ **reaction with BEA catalyst**

Consider uptake within BEA catalyst carrying out the isomerization of nC6 to produce a product containing mono-branched 3-methylpentane (3MP) and di-branched 22DMB at 433 K. We restrict our analysis to the simplified reaction scheme $nC6(1) \rightleftarrows 3MP(2) \rightleftarrows 22DMB(3)$ where the Langmuir-Hinshelwood (L-H) reaction rate expressions for the two constituent reversible reactions, expressed as mol (kg catalyst)$^{-1}$ s^{-1} are $R_{kg,1} = \left(k_{f1} q_1 - k_{b1} q_2 \right); \quad R_{kg,2} = \left(k_{f2} q_2 - k_{b2} q_3 \right)$. The subscripts f and b refer to the forward and reverse reactions, and the subscripts 1 and 2 refer to the first and second isomerization reaction steps. In our simulations we assume $k_{f1} = k_{f2} = 0.005$ s^{-1} and $k_{b1} = k_{b2} = 0.001$ s^{-1}. The catalyst radius is taken to be $r_c = 0.1$ mm.

Figure 56a presents simulations of transient uptake inside BEA catalyst exposed to a gas phase nC6(1)/3MP(2)/22DMB(3) mixture at 433 K. The partial pressures of the components in the bulk gas phase are p_1 =1000 Pa; p_2 = 1 Pa, p_3 = 1 Pa. The mixture adsorption equilibrium is determined using the IAST. The zero-loading M-S diffusivities are $Đ_1(0)/r_c^2 = 0.01$ s^{-1}; $Đ_2(0)/r_c^2 = 0.005$ s^{-1}; $Đ_3(0)/r_c^2 = 1\times10^{-3}$ s^{-1}. The continuous solid lines represent uptake simulations with the M-S equation (36). We note that the most mobile nC6 displays an overshoot during transient uptake. 3-methylpentane (3MP), with intermediate mobility, also exhibits a slight overshoot. The dashed lines represent uptake simulations with uncoupled Fickian flux equations (38); in this scenario, all three components approach equilibrium in a monotonous manner.

Figure 56b compares the transient equilibration trajectories in 3D composition space, using three different flux calculation scenarios; the followed trajectories are significantly different.

19. nC6(1)$\rightleftarrows$2MP(2)$\rightleftarrows$22DMB(3) **reaction with MFI catalyst**

Consider uptake within MFI catalyst carrying out the isomerization of nC6 to produce a product containing mono-branched 2-methylpentane (2MP) and di-branched 22DMB. We restrict our analysis to the simplified reaction scheme nC6(1)$\rightleftarrows$2MP(2)$\rightleftarrows$22DMB(3) where the Langmuir-Hinshelwood (L-H) reaction rate expressions for the two constituent reversible reactions, expressed as mol (kg catalyst)$^{-1}$ s^{-1} are $R_{kg,1} = (k_{f1}q_1 - k_{b1}q_2)$; $R_{kg,2} = (k_{f2}q_2 - k_{b2}q_3)$. The subscripts f and b refer to the forward and reverse reactions, and the subscripts 1 and 2 refer to the first and second isomerization reaction steps. We assume $k_{f1} = k_{f2} = 0.01$ s^{-1} and $k_{b1} = k_{b2} = 0.001$ s^{-1}. The catalyst radius is taken to be $r_c = 0.2$ mm.

Figure 57a presents simulations of transient uptake inside MFI catalyst exposed to a gas phase nC6(1)/2MP(2)/22DMB(3) mixture at 433 K. The partial pressures of the components in the bulk gas phase are p_1 = 50 kPa; p_2 = 25 kPa, p_3 =25 kPa. The mixture adsorption equilibrium is determined using the IAST. The zero-loading M-S diffusivities are chosen as The zero-loading M-S diffusivities are $Đ_1(0)/r_c^2 = 0.0125$ s^{-1}; $Đ_2(0)/r_c^2 = 0.0025$ s^{-1}; $Đ_3(0)/r_c^2 = 5\times10^{-4}$ s^{-1}; the choice of these diffusivities is

based on earlier works.[4, 22, 42, 71] The continuous solid lines represent uptake simulations with the M-S equation (36). We note that the most mobile nC6 displays an overshoot during transient uptake. 2-methylpentane (2MP), with intermediate mobility, also exhibits a slight overshoot. The dashed lines represent uptake simulations with uncoupled Fickian flux equations (38); in this scenario, all three components approach equilibrium in a monotonous manner.

Figure 57b compares the transient equilibration trajectories in 3D composition space, using three different flux calculation scenarios; the followed trajectories are significantly different.

In order to confirm that this conclusion also holds for fixed bed reactors of finite length, steady-state simulations were performed for a fixed bed reactor. The gas phase molar concentrations as function of the dimensionless length of the fixed bed, z/L are shown in Figure 58a,b. For the Fick model that ignores thermodynamic coupling the rate of production of 22DMB is 1.17×10^{-3} mol (kg catalyst)$^{-1}$ s^{-1}; this value is lower than either of the two different implementations of the M-S model. For the weak confinement scenario, the rate of production of 22DMB is 2.13×10^{-3} mol (kg catalyst)$^{-1}$ s^{-1}. For the strong confinement scenario, the rate of production of 22DMB is 9.17×10^{-4} mol (kg catalyst)$^{-1}$ s^{-1}.

The choice of the proper model is important in reactor modelling. In the transient uptake experiments of Titze et al. [42], the M-S model including thermodynamic coupling has been established to be a good representation of the uptake of n-hexane/2-methylpentane mixtures in MFI zeolite.

The difference between the Fick and M-S model formulations become more prominent in transient operations. To demonstrate this, we carried out transient fixed reactor simulations for the same set of input conditions as in Figure 58. Figure 59 shows the molar concentrations in the gas phase exiting the reactor, plotted as a function of the dimensionless time, $\tau = \dfrac{tv}{L}$. The continuous solid lines represent simulations with the M-S model, Equation (36), for the weak confinement scenario. The dashed lines represent simulations ignoring thermodynamic coupling and use uncoupled flux equation (38). For the M-S model the breakthrough of 22DMB occurs earlier and there is a period of time within which nearly

pure 22DMB may be recovered as product. The exploitation of transient operation is best carried out in simulated moving bed reactor configurations, as discussed in detail by Krishna and Baur. [43]

20. $nC6(1) \rightleftarrows 2MP(2) \rightleftarrows 22DMB(3)$ **reaction with MOR catalyst**

Consider uptake within MOR catalyst carrying out the isomerization of nC6 to produce a product containing mono-branched 2-methylpentane (2MP) and di-branched 22DMB. We restrict our analysis to the simplified reaction scheme $nC6(1) \rightleftarrows 2MP(2) \rightleftarrows 22DMB(3)$ where the Langmuir-Hinshelwood (L-H) reaction rate expressions for the two constituent reversible reactions, expressed as mol (kg catalyst)$^{-1}$ s^{-1} are $R_{kg,1} = \left(k_{f1}q_1 - k_{b1}q_2\right)$; $R_{kg,2} = \left(k_{f2}q_2 - k_{b2}q_3\right)$. The subscripts f and b refer to the forward and reverse reactions, and the subscripts 1 and 2 refer to the first and second isomerization reaction steps. In absence of reliable kinetic data assume the reaction rate constants to be the same as with MFI catalyst: $k_{f1} = k_{f2} = 0.01$ s^{-1} and $k_{b1} = k_{b2} = 0.001$ s^{-1}. The catalyst radius is taken to be $r_c = 1$ mm.

Figure 60a presents simulations of transient uptake inside MOR catalyst exposed to a gas phase nC6(1)/2MP(2)/22DMB(3) mixture at 433 K, carrying out the isomerization reaction $nC6(1) \rightleftarrows 2MP(2) \rightleftarrows 22DMB(3)$. The partial pressures of the components in the bulk gas phase are $p_1 = p_2 = p_3 = 40$ kPa. The zero-loading M-S diffusivities are $Ð_1(0)/r_c^2 = 1 \times 10^{-3}$ s^{-1}; $Ð_2(0)/r_c^2 = 2.5 \times 10^{-4}$ s^{-1}; $Ð_3(0)/r_c^2 = 1.9 \times 10^{-4}$ s^{-1}; these diffusivities are based on MD simulation results of Van Baten and Krishna;[26] see Figures 27 and 28. The reaction rate constants are $k_{f1} = 0.01$ s^{-1}, $k_{b1} = 0.001$ s^{-1}; $k_{f2} = 0.01$ s^{-1}, $k_{b2} = 0.001$ s^{-1}. The continuous solid lines represent uptake simulations include thermodynamic coupling using equation (36). We note that the most mobile nC6 displays an overshoot during transient uptake. 2-methylpentane (2MP), with intermediate mobility, also exhibits a slight overshoot. The dashed lines represent uptake simulations ignoring thermodynamic coupling and use uncoupled flux equation (38); in this scenario, both nC6 and 2MP approach equilibrium in a monotonous manner.

Figure 60b compares the transient equilibration trajectories in 3D composition space, using three different flux calculation scenarios; the followed trajectories are significantly different.

At steady-state, the gas phase concentrations of 22DMB along the length of a fixed zeolite bed reactor, calculated using three different flux calculation scenarios, are shown in Figure 61. For the Fick model that ignores thermodynamic coupling, the productivity of 22DMB is 9.9×10^{-4} mol (kg catalyst)$^{-1}$ s^{-1}; this value is higher than that predicted by the M-S model (weak confinement): 8.7×10^{-4} mol (kg catalyst)$^{-1}$ s^{-1}, and the M-S model (strong confinement): 4.72×10^{-4} mol (kg catalyst)$^{-1}$ s^{-1},

From the MD simulation data of Van Baten and Krishna,[26] it can be established that the M-S model with the strong confinement scenario is the appropriate one to use; see Figures 27 and 28.

21. $\text{ethene}(1) + \text{benzene}(2) \rightleftarrows \text{ethylbenzene}(3)$ **reaction with MFI catalyst**

H-ZSM-5, which has the MFI topology, is used as a catalyst for carrying out the ethylation of benzene to produce ethylbenzene $\text{ethene}(1) + \text{benzene}(2) \rightleftarrows \text{ethylbenzene}(3)$; for background on process and reaction kinetics, see Hansen et al.[27, 72] In our simulations we use the Langmuir-Hinshelwood rate expression $R_{kg} = k_f q_1 q_2 - k_b q_3$. The forward and reverse reaction rate constants are taken to be $k_f =$ 0.05 mol^{-1} kg s^{-1} and k_b= 0.05 s^{-1}.

Figure 62a presents the simulation results for transient uptake inside MFI catalyst exposed to a gas phase ethene(1)/benzene(2)/ethylbenzene(3) mixture at 653 K; the partial pressures of the components in the bulk gas phase are p_1 = 0.6 MPa; p_2 = 0.4 MPa; p_3 = 0 MPa. Based on MD simulation data,[27]   the zero-loading M-S diffusivities are taken to be $Đ_1(0)/r_c^2 = 1 \times 10^{-3}$ s^{-1}, $Đ_2(0)/r_c^2 = 2 \times 10^{-5}$ s^{-1}; $Đ_3(0)/r_c^2 =$ 1×10^{-5} s^{-1}. The continuous solid lines represent uptake simulations include thermodynamic coupling using equation (36). We note that the most mobile species ethene displays an overshoot during equilibration. The dashed lines represent uptake simulations ignoring thermodynamic coupling and use uncoupled flux equation (38); in this scenario, no ethene overshoot is observed.

Figure 62b compares the transient equilibration trajectories in 3D composition space, using three different model implementations (Fick model, M-S model with weak and strong confinements). Both the M-S model implementations (weak and strong confinement) predict the ethene overshoot and the trajectories in composition space are significantly different from that anticipated by the Fick model.

The MD simulation data[27] indicate that the M-S model with strong confinement is the appropriate model to use.

In order to highlight the influence of thermodynamic coupling on conversion in fixed bed reactors, we undertook steady-state simulations of fixed bed reactor packed with MFI catalyst exposed to a gas phase ethene(1)/benzene(2)/ethylbenzene(3) mixture at 653 K. The continuous solid lines represent simulations include thermodynamic coupling using Equation (36), with the strong confinement scenario. The dashed lines represent simulations ignoring thermodynamic coupling and use uncoupled flux equation (38). Figures 63a,b shows the molar concentrations in the gas phase along the reactor length. The Fick model predicts the productivity of ethylbenzene to be: 1.6×10^{-3} mol (kg catalyst)$^{-1}$ s^{-1}; this value is significantly higher than that predicted by either of the two M-S model implementations. For weak the productivity is: 1.36×10^{-3} mol (kg catalyst)$^{-1}$ s^{-1}; for strong confinement: 7.9×10^{-4} mol (kg catalyst)$^{-1}$ s^{-1}.

22. $\text{ethane}(1) \rightleftarrows \text{ethene}(2) + \text{hydrogen}(3)$ reaction with MFI catalyst

Hansen et al.[72] describe the use of MFI catalyst for the dehydrogenation of ethane to produce ethene: $\text{ethane}(1) \rightleftarrows \text{ethene}(2) + \text{hydrogen}(3)$. The reaction rate R_{kg} expressed as mol (kg catalyst)$^{-1}$ s^{-1} is

$R_{kg} = k_f q_1 - k_b q_2 q_3$. For our simulations we take k_f = 10 s^{-1} and k_b= 0.005 mol^{-1} kg s^{-1}.

Figure 64a presents the simulation results for transient uptake inside MFI catalyst exposed to a gas phase ethane(1)/ethene(2)/hydrogen(3) mixture at 653 K. The partial pressures of the components in the bulk gas phase are p_1 = 1.0 MPa; p_2 = 2 MPa, p_3 = 3 MPa. The zero-loading M-S diffusivities, based on MD simulations,[27, 72] are taken as $Đ_1/r_c^2$ = 4×10^{-5} s^{-1}; $Đ_2/r_c^2$ = 8×10^{-5} s^{-1}; $Đ_3/r_c^2$ = 2×10^{-3} s^{-1}. The

continuous solid lines represent uptake simulations include thermodynamic coupling using equation (36). We note that more mobile species hydrogen displays a slight overshoot during equilibration. The dashed lines represent uptake simulations ignoring thermodynamic coupling and use uncoupled Fickian equation (38); in this scenario, no hydrogen overshoot is observed.

Figure 64b compares the transient equilibration trajectories in 3D composition space, using three different model implementations (Fick model, M-S model, with weak and strong confinements). Both the M-S model implementations (weak and strong confinement) predict the hydrogen overshoot and the trajectories in composition space are significantly different from that anticipated by the Fick model.

To examine the influence of thermodynamic coupling on conversion in fixed bed reactors, steady-state simulations were performed, using three different flux calculation scenarios. Figure 65 shows the molar concentrations of ethene in the gas phase along the reactor length. For the Fickian model that ignores thermodynamic coupling, the rate of production of ethene is predicted to be 5.4×10^{-4} mol (kg catalyst)$^{-1}$ s^{-1}. The predictions of the M-S model, with either weak or strong confinement, are only different by about 10%. Diffusional effects are of lesser importance for small molecules such as H_2, C_2H_4, and C_2H_6; therefore there is no great penalty for using the simple Fick model for flux calculations.

23. Notation

A	surface area per kg of framework, $m^2\ kg^{-1}$
b_i	Langmuir-Freundlich constant for species i, $Pa^{-\nu}$
c_i	molar concentration, $mol\ m^{-3}$
c_t	total pore concentration in mixture, $mol\ m^{-3}$
d_p	pore diameter, m
$Đ_i$	M-S diffusivity for molecule-wall interaction, $m^2\ s^{-1}$
$Đ_{ij}$	M-S exchange coefficient for n-component mixture, $m^2\ s^{-1}$
$Đ_i(0)$	zero-loading M-S diffusivity for molecule-wall interaction, $m^2\ s^{-1}$
f_i	partial fugacity of species i, Pa
f_t	total fugacity of bulk fluid mixture, Pa
n	number of species in the mixture, dimensionless
k_1	forward reaction rate constant, s^{-1}
k_2	backward reaction rate constant, s^{-1}
L	length of packed bed reactor, m
n	number of species in the mixture, dimensionless
n_{sites}	number of adsorption sites, dimensionless
N_i	molar flux of species i with respect to framework, $mol\ m^{-2}\ s^{-1}$
p_i	partial pressure of species i in mixture, Pa
P_i^0	sorption pressure, Pa
q_i	component molar loading of species i, $mol\ kg^{-1}$
$q_{i,sat}$	molar loading of species i at saturation, $mol\ kg^{-1}$
q_t	total molar loading in mixture, $mol\ kg^{-1}$
$\overline{q}_i(t)$	spatial-averaged component uptake of species i, $mol\ kg^{-1}$
r	radial direction coordinate, m
r_c	radius of crystallite, m
R	gas constant, 8.314 $J\ mol^{-1}\ K^{-1}$

R_{kg} rate of chemical reaction, mol (kg catalyst)$^{-1}$ s^{-1}

t time, s

T absolute temperature, K

u_i velocity of motion of adsorbate species i with respect to the framework material, m s^{-1}

v interstitial gas velocity in packed bed, m s^{-1}

V_p pore volume, m^3 kg^{-1}

x_i mole fraction of species i in adsorbed phase, dimensionless

z distance coordinate, m

Greek letters

β dimensionless parameter, $\beta \equiv \sqrt{\dfrac{\dfrac{\DJ_2(0)}{\DJ_1(0)}\left(\Lambda\dfrac{k_1}{k_2}+1\right)}{\Lambda\left(\dfrac{\DJ_2(0)}{\DJ_1(0)}\dfrac{k_1}{k_2}+1\right)}}$

γ confinement parameter, $\gamma = 0$ for weak , $\gamma = 1$ for strong, dimensionless

Γ_{ij} thermodynamic factors, dimensionless

$[\Gamma]$ matrix of thermodynamic factors, dimensionless

δ thickness of microporous membrane, m

δ_{ij} Kronecker delta, dimensionless

ε fractional pore volume of particle, dimensionless

ε voidage of packed bed, dimensionless

η effectiveness factor, dimensionless

θ_i fractional occupancy of component i, dimensionless

θ_V fractional vacancy, dimensionless

θ_{is} fractional occupancy at catalyst surface, dimensionless

θ_{i0} fractional occupancy at centre of catalyst, dimensionless

Θ dimensionless parameter, $\Theta \equiv \dfrac{\sqrt{2\left(1-1/\Psi^2-2\ln(\Psi)/\Psi^2\right)}}{\left|1-1/\Psi^2\right|}$

Θ_i loading of species i, molecules per unit cell

$\Theta_{i,sat}$	saturation loading of species i, molecules per unit cell
Θ_t	total molar loading of mixture, molecules per unit cell
Λ	dimensionless diffusivity ratio, $\Lambda \equiv \dfrac{D_2(0)}{D_1(0)} \dfrac{\left(1 + (\theta_{1s} + \theta_{2s})\dfrac{D_1(0)}{D_{12}(0)}\right)}{\left(1 + (\theta_{1s} + \theta_{2s})\dfrac{D_2(0)}{D_{12}(0)}\right)}$
μ_i	molar chemical potential of component i, J mol^{-1}
μ_i^0	molar chemical potential of component i at standard state, J mol^{-1}
ν_i	stoichiometric reaction coefficient, dimensionless
ν	Freundlich exponent, dimensionless
ξ	dimensionless radial coordinate, r/r_c, dimensionless
Ξ	$\Xi \equiv \sqrt{\dfrac{1}{\theta_{Vs}^{\gamma}}\left(1 + (\theta_{1s} + \theta_{2s})\dfrac{D_1(0)}{D_{12}(0)}\right)}$
π	spreading pressure, N m^{-1}
ρ	framework density, kg m^{-3}
τ	dimensionless time, dimensionless
ϕ	Thiele modulus, $\phi \equiv \dfrac{r_c}{3}\sqrt{\dfrac{k_1}{D_1(0)} + \dfrac{k_2}{D_2(0)}}$, dimensionless
Φ	modified Thiele modulus; see Table 3, dimensionless
Ψ	dimensionless parameter, $\Psi \equiv \sqrt{\dfrac{(\Lambda + (1-\Lambda)\theta_{1s})k_1 + (1 + (\Lambda - 1)\theta_{2s})k_2}{(\Lambda k_1 + k_2)}}$

Subscripts

b	referring to backward reaction
c	referring to crystallite
f	referring to forward reaction
i	referring to component i
j	referring to component j

n   referring to component n

t   referring to total mixture

0   referring to position, $\xi = 0$.

1   referring to species 1

2   referring to species 2

s   referring to position $\xi = 1$.

sat   referring to saturation conditions

V   vacancy

24. Tabulated data on zeolite structural parameters, along with input data on isotherms, diffusivities, and reaction rate constants

Table 1. Salient information on zeolite structures.

Zeolite	Channel or window size/ Å
MFI	10-ring intersecting channels of 5.1 Å – 5.5 Å and 5.3 Å – 5.6 Å size
FAU	11.4 Å size cages separated by 7.4 Å size windows. The sodalite cages are blocked in simulations and are not accessible to guest molecules. Cage size is calculated on the basis of the equivalent sphere volume.
CHA	8.4 Å size cages separated by 3.8 Å size windows.
LTA	11.2 Å size cages separated by 4.1 Å size windows. The sodalite cages are blocked in simulations and are not accessible to guest molecules.
BEA	Intersecting channels of two sizes: 12-ring of 7.1 Å - 7.3 Å and 10-ring of 5.6 – 5.6 Å
LTL	12-ring 1D channels of 7.1 Å size
MOR	12-ring 1D main channels of 6.5 Å -7 Å size, connected with 8-ring side pockets of 2.6 Å -5.7 Å size
TON	10-ring 1D channels of 4.6 Å -5.7 Å size
MTW	12-ring 1D channels of 5.6 Å -6 Å size
FER	10-ring 1D main channels of 4.2 Å -5.4 Å size, connected with 8-ring side pockets of 3.5 Å -4.8 Å size

Table 2. Unit cell dimensions, unit cell volumes, pore volumes of various all-silica zeolites. Also indicated are the framework density, ρ, (expressed as kg per m^3 framework), the factor to convert from molecules per unit cell to kmol/m^3 of accessible pore volume.

Structure	a / Å	b / Å	c / Å	Unit cell volume/ Å^3	Pore volume per unit cell/ Å^3	Fractional pore volume	Pore volume/ cm^3/g	Framework density/ kg/m^3	Conversion factor
MFI	20.02	19.90	13.38	5332.03	1584.94	0.297	0.165	1796.39	1.0477
BEA	12.66	12.66	26.41	4232.91	1728.05	0.408	0.271	1508.56	0.9609
LTL	31.98	18.47	7.48	4415.45	1221.27	0.277	0.170	1626.97	1.3597
MOR	18.09	20.52	7.52	2793.03	795.41	0.285	0.166	1714.69	2.0877
FER	19.16	14.13	7.49	2026.65	573.24	0.283	0.160	1772.33	2.8968
TON	13.86	17.42	5.04	1216.29	231.39	0.190	0.097	1968.76	7.1763
MTW	24.86	5.01	24.33	2887.49	620.55	0.215	0.111	1935.03	2.6759
FAU	24.28	24.28	24.28	14313.51	6285.60	0.439	0.328	1338.37	0.2642
CHA	15.08	23.91	13.80	4974.57	1898.40	0.382	0.264	1444.10	0.8747
LTA	24.61	24.61	24.61	14905.10	5944.38	0.399	0.310	1285.25	0.2794

Table 3. Calculation of modified Thiele modulus for various scenarios. Adapted from Baur and Krishna.[61]

Scenario	Formula for modified Thiele Modulus	Remarks about analytic solution
Equal diffusivities: $Đ_1(0) = Đ_2(0)$	$\Phi = \phi\, \Xi$	Exact for facile exchange. For finite exchange, a very good approximation.
Strong confinement	$\Phi = \phi\, \beta\, \Xi\Psi$	Exact for facile exchange. For finite exchange, a very good approximation.
Weak confinement	$\Phi = \dfrac{\phi\, \beta\,\Xi\Psi}{\Theta}$	Exact for facile exchange in the limiting cases $\phi \to \infty$ and $\phi \to 0$. For all other cases, including that for finite exchange, a very good approximation.

(1) Classical scenario: $\Phi = \phi$.

(2) Weak confinement scenario for the diffusivities. Also ignored are the correlation effects, i.e. $Đ_1/Đ_{12} \to 0;\quad Đ_2/Đ_{12} \to 0$. Thermodynamic coupling effects are accounted for using the mixed-gas Langmuir isotherm model. $\Phi = \dfrac{\phi\, \beta\,\Xi\Psi}{\Theta}$

(3) Strong confinement scenario for the diffusivities in which the diffusivities are related to the zero-loading diffusivities by $Đ_i = Đ_i(0)\theta_V$. Also ignored are the correlation effects, i.e. $Đ_1/Đ_{12} \to 0;\quad Đ_2/Đ_{12} \to 0$. Thermodynamic coupling effects are accounted for using the mixed-gas Langmuir isotherm model. $\Phi = \phi\, \beta\, \Xi\Psi$

(4) Weak confinement scenario for the diffusivities. Thermodynamic coupling effects are accounted for using the mixed-gas Langmuir isotherm model. Correlation effects are accounted for with finite values of $Đ_1/Đ_{12};\quad Đ_2/Đ_{12}$.

$\Phi = \dfrac{\phi\, \beta\,\Xi\Psi}{\Theta}$

(5) Strong confinement scenario for the diffusivities in which the diffusivities are related to the zero-loading diffusivities by $Đ_i = Đ_i(0)\theta_V$. Thermodynamic coupling effects are accounted for using the mixed-gas Langmuir isotherm model. Correlation effects are accounted for with finite values of $Đ_1/Đ_{12};\quad Đ_2/Đ_{12}$. $\Phi = \phi\, \beta\, \Xi\Psi$

Table 4. Dual-site Langmuir parameters for hexane isomers in MFI at 362 K. The fits correspond to CBMC simulations. [16, 38, 39] Note that the saturation capacities are specified in molecules per unit cell. Multiply these by 0.17337 to obtain the loading values in mol per kg framework.

$$\Theta_i^0(p) \equiv \Theta_{i,A} + \Theta_{i,B} = \frac{\Theta_{i,sat,A} b_{i,A} p}{1+b_{i,A} p} + \frac{\Theta_{i,sat,B} b_{i,B} p}{1+b_{i,B} p}$$

Component	Dual Langmuir Parameters			
	Site A		Site B	
	$b_{i,A}$ /Pa^{-1}	$\Theta_{i,sat,A}$ /molecules uc^{-1}	$b_{i,B}$ /Pa^{-1}	$\Theta_{i,sat,B}$ /molecules uc^{-1}
nC$_6$	6.32×10^{-2}	4.0	1.7×10^{-3}	4.0
3MP	4.75×10^{-2}	4.0	2.27×10^{-5}	2.3
2DMB	1.085×10^{-2}	4.0	2.27×10^{-5}	0.0

The zero-loading M-S diffusivities are $Ð_1(0)/r_c^2 = 2\times10^{-4}$ s^{-1}; $Ð_2(0)/r_c^2 = 2\times10^{-5}$ s^{-1}; $Ð_3(0)/r_c^2 = 1\times10^{-5}$ s^{-1}. The Langmuir-Hinshelwood (L-H) reaction rate expressions for the two constituent reversible reactions, expressed as mol (kg catalyst)$^{-1}$ s^{-1} are $R_{kg,1} = (k_{f1}q_1 - k_{b1}q_2)$; $R_{kg,2} = (k_{f2}q_2 - k_{b2}q_3)$. The reaction rate constants are k_{f1} = 0.01 s^{-1}, k_{b1} = 0.001 s^{-1}; k_{f2} = 0.01 s^{-1}, k_{b2} = 0.001 s^{-1}.

Table 5. Dual-site Langmuir-Freundlich parameters for pure component hexane isomers at 433 K in BEA zeolite. The parameters are obtained by re-fitting the isotherm data of Bárcia et al.,[73] measured at three different temperatures, 423 K, 473 K, and 523 K. The data were fitted with T-dependent parameters. The tabulated values below are interpolated from the T-dependent parameters, for $T = 433$ K.

$$q_i = q_{i,A,sat} \frac{b_{i,A} p_i^{\nu_{i,A}}}{1 + b_{i,A} p_i^{\nu_{i,A}}} + q_{i,B,sat} \frac{b_{i,B} p_i^{\nu_{i,B}}}{1 + b_{i,B} p_i^{\nu_{i,B}}}$$

	Site A			Site B		
	$q_{i,A,sat}$ mol kg^{-1}	$b_{i,A}$ Pa$^{-\nu_A}$	$\nu_{i,A}$ dimensionless	$q_{i,B,sat}$ mol kg^{-1}	$b_{i,B}$ Pa$^{-\nu_B}$	$\nu_{i,B}$ dimensionless
nC6	0.32	2.43×10^{-6}	1.36	0.6	1.04×10^{-2}	0.8
3MP	0.44	6.97×10^{-5}	1	0.51	1.13×10^{-3}	1
22DMB	0.31	6.18×10^{-4}	0.85	0.67	2.63×10^{-5}	1.13

The zero-loading M-S diffusivities are $Đ_1(0)/r_c^2 = 0.01$ s^{-1}; $Đ_2(0)/r_c^2 = 0.005$ s^{-1}; $Đ_3(0)/r_c^2 = 1 \times 10^{-3}$ s^{-1}.

The Langmuir-Hinshelwood (L-H) reaction rate expressions for the two constituent reversible reactions, expressed as mol (kg catalyst)$^{-1}$ s^{-1} are $R_{kg,1} = \left(k_{f1} q_1 - k_{b1} q_2 \right)$; $R_{kg,2} = \left(k_{f2} q_2 - k_{b2} q_3 \right)$. The reaction rate constants are $k_{f1} = 0.005$ s^{-1}, $k_{b1} = 0.001$ s^{-1}; $k_{f2} = 0.005$ s^{-1}, $k_{b2} = 0.001$ s^{-1}.

Table 6. Dual-site Langmuir-Freundlich parameters for pure component pentane and hexane isomers at 433 K in MFI zeolite. The fits correspond to CBMC simulations.[16, 38, 39] Note that the saturation capacities are specified in molecules per unit cell. Multiply these by 0.17337 to obtain the loading values in mol per kg framework.

$$\Theta_i \equiv \Theta_{i,A} + \Theta_{i,B} = \frac{\Theta_{i,sat,A} b_{i,A} p^{\nu_A}}{1 + b_{i,A} p^{\nu_A}} + \frac{\Theta_{i,sat,B} b_{i,B} p^{\nu_B}}{1 + b_{i,B} p^{\nu_B}}$$

	Site A			Site B		
	$\Theta_{i,A,sat}$	$b_{i,A}$	$\nu_{i,A}$	$\Theta_{i,B,sat}$	$b_{i,B}$	$\nu_{i,B}$
	molecules uc^{-1}	Pa$^{-\nu_A}$	dimensionless	molecules uc^{-1}	Pa$^{-\nu_B}$	dimensionless
nC5	4	6.26×10^{-6}	1.12	4	1.94×10^{-4}	1
2MB	4	1.69×10^{-4}	1	2	4.93×10^{-7}	1
Neo-pentane	4	1.24×10^{-4}	1			
nC6	3.2	2.21×10^{-8}	1.6	4.3	7.42×10^{-4}	1
2MP	4	7.85×10^{-4}	1.03			
3MP	4	4.22×10^{-4}	1.02	1	9.88×10^{-7}	1
22DMB	4	2.55×10^{-4}	1.02			
23DMB	4	4.59×10^{-4}	1.02			

The zero-loading M-S diffusivities are $Đ_1(0)/r_c^2 = 0.0125$ s^{-1}; $Đ_2(0)/r_c^2 = 0.0025$ s^{-1}; $Đ_3(0)/r_c^2 = 5 \times 10^{-4}$ s^{-1}. The Langmuir-Hinshelwood (L-H) reaction rate expressions for the two constituent reversible reactions, expressed as mol (kg catalyst)$^{-1}$ s^{-1} are $R_{kg,1} = (k_{f1} q_1 - k_{b1} q_2)$; $R_{kg,2} = (k_{f2} q_2 - k_{b2} q_3)$. The reaction rate constants are $k_{f1} = 0.01$ s^{-1}, $k_{b1} = 0.001$ s^{-1}; $k_{f2} = 0.01$ s^{-1}, $k_{b2} = 0.001$ s^{-1}.

Table 7. Dual-site Langmuir parameters for hexane isomers in MOR at 433 K. The fits correspond to CBMC simulations. Note that the saturation capacities are specified in molecules per unit cell. Multiply these by 0.34673 to obtain the loading values in mol per kg framework.

$$\Theta_i \equiv \Theta_{i,A} + \Theta_{i,B} = \frac{\Theta_{i,sat,A} b_{i,A} p}{1 + b_{i,A} p} + \frac{\Theta_{i,sat,B} b_{i,B} p}{1 + b_{i,B} p}$$

Component	Dual Langmuir Parameters			
	Site A		Site B	
	$b_{i,A}$ /Pa^{-1}	$\Theta_{i,sat,A}$ /molecules uc^{-1}	$b_{i,B}$ /Pa^{-1}	$\Theta_{i,sat,B}$ /molecules uc^{-1}
nC$_6$	4.27×10^{-4}	1.5	8.78×10^{-8}	0.45
2MP	6.77×10^{-4}	1.5	6.34×10^{-6}	0.5
2DMB	3.06×10^{-4}	1.96	2.05×10^{-7}	0.54

The zero-loading M-S diffusivities are $Đ_1(0)/r_c^2 = 1 \times 10^{-3}$ s^{-1}; $Đ_2(0)/r_c^2 = 2.5 \times 10^{-4}$ s^{-1}; $Đ_3(0)/r_c^2 = 1.9 \times 10^{-4}$ s^{-1}. The Langmuir-Hinshelwood (L-H) reaction rate expressions for the two constituent reversible reactions, expressed as mol (kg catalyst)$^{-1}$ s^{-1} are $R_{kg,1} = (k_{f1}q_1 - k_{b1}q_2)$; $R_{kg,2} = (k_{f2}q_2 - k_{b2}q_3)$. The reaction rate constants are $k_{f1} = 0.01$ s^{-1}, $k_{b1} = 0.001$ s^{-1}; $k_{f2} = 0.01$ s^{-1}, $k_{b2} = 0.001$ s^{-1}.

Table 8. Single-site Langmuir parameters, and M-S diffusivities $Đ_i/r_c^2$, for pure component 2MB, 2MP, and 22DMB at 473 K in MFI zeolite. The parameters are based on the experimental data of Jolimaître et al.[64, 65] All simulations of the breakthrough experiments of Jolimaître et al.[65] were performed for extrudate 2; bed voidage, $\varepsilon = 0.4$; density of extrudate 2, $\rho = 620.8$ kg m^{-3}; The interstitial velocity v varied with each run and were taken from Table 6 of Jolimaître et al.[65] The partial pressures of each of the components 2MB, 2MP, and 22DMB at the inlet to the reactor are specified using the data provided in Table 6 of Jolimaître et al.[65] Note that the saturation capacities are specified in molecules per unit cell. Multiply these by 0.17337 to obtain the loading values in mol per kg framework.

$\Theta_i = \dfrac{\Theta_{i,sat}b_i p}{1+b_{i,}p}$	$\Theta_{i,sat}$ molecules uc^{-1}	b_i Pa^{-1}	$Đ_i/r_c^2$ s^{-1}
2MB	4	4.12×10^{-5}	0.0075
2MP	4	1.27×10^{-4}	0.005
22DMB	4	7.12×10^{-5}	0.0000625

The zero-loading M-S diffusivities are $Đ_1(0)/r_c^2 = 5\times10^{-3}$ s^{-1}; $Đ_2(0)/r_c^2 = 6.25\times10^{-5}$ s^{-1}. The rate of chemical reaction, $2MP(1) \rightleftarrows 22DMB(2)$, expressed as moles per kg catalyst per second, R_{kg}, is written as $R_{kg} = k_1 q_1 - k_2 q_2$. The reaction rate constants are $k_1 = 0.0011$ s^{-1}, $k_2 = 0.00055$ s^{-1}; these rate constants are taken from Baur and Krishna.[61]

Table 9. Single-site Langmuir fit parameters of the isotherms for o-xylene, m-xylene and p-xylene in MFI zeolite at 433 K. The pure component isotherms are obtained from the molecular simulation data of Torres-Knoop et al.,[74] as reported on page S61 of the Supplementary material of their paper. The simulation data are for orthorhombic MFI zeolite using the van Koningsveld structural framework parameters. Note that the saturation capacities are specified in molecules per unit cell. Multiply these by 0.17337 to obtain the loading values in mol per kg framework.

$\Theta_i = \dfrac{\Theta_{i,sat} b_i p}{1 + b_{i,} p}$	$\Theta_{i,sat}$	b_i
	molecules uc^{-1}	Pa^{-1}
o-xylene	4	9×10^{-7}
m-xylene	4	5×10^{-6}
p-xylene	4	5.7×10^{-7}

The zero-loading diffusivities are $Ð_1(0)/r_c^2 = 1 \times 10^{-6}$ s^{-1}; $Ð_2(0)/r_c^2 = 1 \times 10^{-4}$ s^{-1}. The rate of chemical reaction, expressed as moles per kg of catalyst per second is written as $R_{kg} = k_1 q_1 - k_2 q_2$. The rate constants are taken as: $k_1 = 1 \times 10^{-4}$ s^{-1}, $k_2 = 5 \times 10^{-5}$ s^{-1}.

Table 10. Single-site Langmuir fit parameters of the isotherms for ethene (1), benzene (2), and ethylbenzene (3) in MFI zeolite at 653 K. The pure component isotherms are obtained from the molecular simulation data of Hansen et al.[27, 72] for the range of pressure up to 1 MPa. Hansen provides the isotherm fit parameters for a 3-site Langmuir fit. For our purposes in this article the simpler single site $\Theta_i = \dfrac{\Theta_{i,sat} b_i p}{1 + b_{i,} p}$ is of sufficient accuracy for total mixture loadings below 4 molecules per unit cell.

Note that the saturation capacities are specified in molecules per unit cell. Multiply these by 0.17337 to obtain the loading values in mol per kg framework.
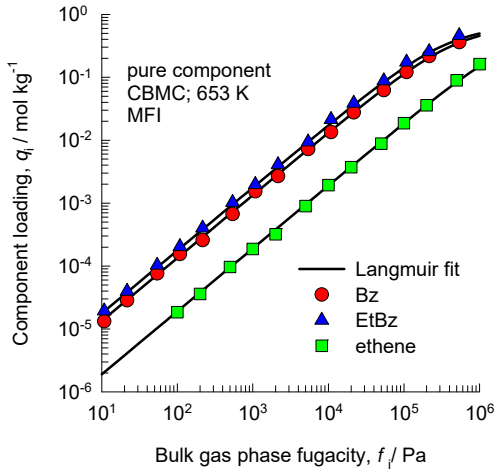
$\Theta_i = \dfrac{\Theta_{i,sat} b_i p}{1 + b_{i,} p}$	$\Theta_{i,sat}$	b_i
	molecules uc^{-1}	Pa^{-1}
ethene	4	2.75×10^{-7}
benzene	4	1.93×10^{-6}
ethylbenzene	4	2.55×10^{-6}

The zero-loading M-S diffusivities are taken to be $Đ_1(0)/r_c^2 = 1\times10^{-3}$ s^{-1}, $Đ_2(0)/r_c^2 = 2\times10^{-5}$ s^{-1}; $Đ_3(0)/r_c^2 = 1\times10^{-5}$ s^{-1}. In our simulations we use the Langmuir-Hinshelwood rate expression $R_{kg} = k_f q_1 q_2 - k_b q_3$. The forward and reverse reaction rate constants are taken to be $k_f = 0.05$ mol^{-1} kg s^{-1} and $k_b = 0.05$ s^{-1}.

Table 11. Single-site Langmuir fit parameters of the isotherms for ethane (1), ethene(2), hydrogen (3) e

in MFI zeolite at 653 K. The pure component isotherms are obtained from the molecular simulation data

of Hansen et al.[27, 72] for the range of pressure up to 1 MPa. Hansen provides the isotherm fit parameters

for a 3-site Langmuir fit. For our purposes in this article the simpler single site $\Theta_i = \dfrac{\Theta_{i,sat} b_i p}{1 + b_{i,p}}$ is of

sufficient accuracy for total mixture loadings below 4 molecules per unit cell. Note that the saturation

capacities are specified in molecules per unit cell. Multiply these by 0.17337 to obtain the loading

values in mol per kg framework.
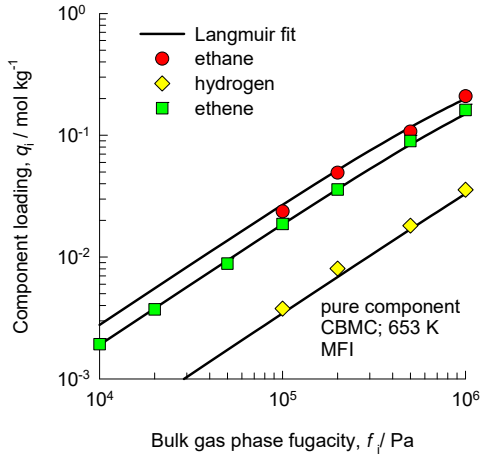
$\Theta_i = \dfrac{\Theta_{i,sat} b_i p}{1 + b_{i,p}}$	$\Theta_{i,sat}$	b_i
	molecules uc^{-1}	Pa^{-1}
hydrogen	4	5×10^{-8}
ethene	4	2.75×10^{-7}
ethane	4	4.03×10^{-7}

The zero-loading M-S diffusivities are $Đ_1(0)/r_c^2 = 4 \times 10^{-5}$ s^{-1}; $Đ_2(0)/r_c^2 = 8 \times 10^{-5}$ s^{-1}; $Đ_3(0)/r_c^2 =$

2×10^{-3} s^{-1}. The reaction rate R_{kg} expressed as mol (kg catalyst)$^{-1}$ s^{-1} is

$R_{kg} = k_f q_1 - k_b q_2 q_3$. For our simulations we take $k_f = 10$ s^{-1} and $k_b = 0.005$ mol^{-1} kg s^{-1}.

25.　References

(1) Baerlocher, C.; Meier, W. M.; Olson, D. H. *Atlas of Zeolite Framework Types*; 5th Edition, Elsevier: Amsterdam, 2002.

(2) Baerlocher, C.; McCusker, L. B. Database of Zeolite Structures. http://www.iza-structure.org/databases/, International Zeolite Association, 10 January 2002.

(3) Krishna, R. Diffusion in Porous Crystalline Materials. *Chem. Soc. Rev.* **2012**, *41*, 3099-3118.

(4) Krishna, R. The Maxwell-Stefan Description of Mixture Diffusion in Nanoporous Crystalline Materials. *Microporous Mesoporous Mater.* **2014**, *185*, 30-50.

(5) Krishna, R. Describing the Diffusion of Guest Molecules inside Porous Structures. *J. Phys. Chem. C* **2009**, *113*, 19756-19781.

(6) Krishna, R.; van Baten, J. M. Investigating the Relative Influences of Molecular Dimensions and Binding Energies on Diffusivities of Guest Species Inside Nanoporous Crystalline Materials *J. Phys. Chem. C* **2012**, *116*, 23556-23568.

(7) Krishna, R.; van Baten, J. M. Investigating the Influence of Diffusional Coupling on Mixture Permeation across Porous Membranes *J. Membr. Sci.* **2013**, *430*, 113-128.

(8) Krishna, R.; van Baten, J. M. Influence of Adsorption Thermodynamics on Guest Diffusivities in Nanoporous Crystalline Materials. *Phys. Chem. Chem. Phys.* **2013**, *15*, 7994-8016.

(9) Krishna, R.; van Baten, J. M. Insights into diffusion of gases in zeolites gained from molecular dynamics simulations. *Microporous Mesoporous Mater.* **2008**, *109*, 91-108.

(10) Krishna, R.; van Baten, J. M. Diffusion of alkane mixtures in MFI zeolite. *Microporous Mesoporous Mater.* **2008**, *107*, 296-298.

(11) Ruthven, D. M. *Principles of Adsorption and Adsorption Processes*; John Wiley: New York, 1984.

(12) Myers, A. L.; Prausnitz, J. M. Thermodynamics of Mixed Gas Adsorption. *A.I.Ch.E.J.* **1965**, *11*, 121-130.

(13) Babbitt, J. D. On the Differential Equations of Diffusion. *Canad. J. Res.* **1950**, *28 A*, 449-474.

(14) Babbitt, J. D. A Unified Picture of Diffusion. *Canad. J. Phys.* **1951**, *29*, 427-436.

(15) Krishna, R. Uphill Diffusion in Multicomponent Mixtures. *Chem. Soc. Rev.* **2015**, *44*, 2812-2836.

(16) Krishna, R.; Baur, R. Modelling Issues in Zeolite Based Separation Processes. *Sep. Purif. Technol.* **2003**, *33*, 213-254.

(17) He, Y.; Krishna, R.; Chen, B. Metal-Organic Frameworks with Potential for Energy-Efficient Adsorptive Separation of Light Hydrocarbons. *Energy Environ. Sci.* **2012**, *5*, 9107-9120.

(18) Krishna, R.; van Baten, J. M. Investigating the potential of MgMOF-74 membranes for CO_2 capture. *J. Membr. Sci.* **2011**, *377*, 249-260.

(19) Gupta, A.; Clark, L. A.; Snurr, R. Q. Grand canonical Monte Carlo simulations of nonrigid molecules: Siting and segregation in silicalite zeolite. *Langmuir* **2000**, *16*, 3910-3919.

(20) Jobic, H.; Laloué, C.; Laroche, C.; van Baten, J. M.; Krishna, R. Influence of isotherm inflection on the loading dependence of the diffusivities of n-hexane and n-heptane in MFI zeolite. Quasi-Elastic Neutron Scattering experiments supplemented by molecular simulations. *J. Phys. Chem. B* **2006**, *110*, 2195-2201.

(21) Krishna, R.; van Baten, J. M. Onsager coefficients for binary mixture diffusion in nanopores. *Chem. Eng. Sci.* **2008**, *63*, 3120-3140.

(22) Krishna, R. Tracing the Origins of Transient Overshoots for Binary Mixture Diffusion in Microporous Crystalline Materials. *Phys. Chem. Chem. Phys.* **2016**, *18*, 15482-15495.

(23) Krishna, R.; van Baten, J. M. An Investigation of the Characteristics of Maxwell-Stefan Diffusivities of Binary Mixtures in Silica Nanopores. *Chem. Eng. Sci.* **2009**, *64*, 870-882.

(24) Krishna, R.; van Baten, J. M. Unified Maxwell-Stefan Description of Binary Mixture Diffusion in Micro- and Meso- Porous Materials. *Chem. Eng. Sci.* **2009**, *64*, 3159-3178.

(25) Krishna, R.; van Baten, J. M. Describing Mixture Diffusion in Microporous Materials under Conditions of Pore Saturation. *J. Phys. Chem. C* **2010**, *114*, 11557-11563.

(26) van Baten, J. M.; Krishna, R. Entropy effects in adsorption and diffusion of alkane isomers in mordenite: An investigation using CBMC and MD simulations. *Microporous Mesoporous Mater.* **2005**, *84*, 179-191.

(27) Hansen, N.; Krishna, R.; van Baten, J. M.; Bell, A. T.; Keil, F. J. Analysis of Diffusion Limitation in the Alkylation of Benzene over H-ZSM-5 by Combining Quantum Chemical Calculations, Molecular Simulations, and a Continuum Approach. *J. Phys. Chem. C* **2009**, *113*, 235-246.

(28) Siperstein, F. R.; Myers, A. L. Mixed-Gas Adsorption. *A.I.Ch.E.J.* **2001**, *47*, 1141-1159.

(29) Sircar, S. Influence of Adsorbate Size and Adsorbent Heterogeneity on IAST. *A.I.Ch.E.J.* **1995**, *41*, 1135-1145.

(30) Sircar, S.; Rao, M. B. Effect of adsorbate size on adsorption of gas mixtures on homogeneous adsorbents. *A.I.Ch.E.J.* **1999**, *45*, 2657-2661.

(31) Rao, M. B.; Sircar, S. Thermodynamic consistency for binary gas adsorption equilibria. *Langmuir* **1999**, *15*, 7258-7267.

(32) Kapteijn, F.; Moulijn, J. A.; Krishna, R. The generalized Maxwell-Stefan model for diffusion in zeolites: sorbate molecules with different saturation loadings. *Chem. Eng. Sci.* **2000**, *55*, 2923-2930.

(33) Krishna, R.; Calero, S.; Smit, B. Investigation of Entropy effects during Sorption of Mixtures of Alkanes in MFI zeolite. *Chem. Eng. J.* **2002**, *88*, 81-94.

(34) Krishna, R.; Smit, B.; Calero, S. Entropy effects during sorption of alkanes in zeolites. *Chem. Soc. Rev.* **2002**, *31*, 185-194.

(35) Krishna, R. Separating Mixtures by Exploiting Molecular Packing Effects in Microporous Materials. *Phys. Chem. Chem. Phys.* **2015**, *17*, 39-59.

(36) Gutierrez-Sevillano, J. J.; Calero, S.; Krishna, R. Selective Adsorption of Water from Mixtures with 1-Alcohols by Exploitation of Molecular Packing Effects in CuBTC. *J. Phys. Chem. C* **2015**, *119*, 3658-3666.

(37) Gutierrez-Sevillano, J. J.; Calero, S.; Krishna, R. Separation of Benzene from Mixtures with Water, Methanol, Ethanol, and Acetone: Highlighting Hydrogen Bonding and Molecular Clustering Influences in CuBTC. *Phys. Chem. Chem. Phys.* **2015**, *17*, 20114-20124.

(38) Calero, S.; Smit, B.; Krishna, R. Configurational entropy effects during sorption of hexane isomers in silicalite. *J. Catal.* **2001**, *202*, 395-401.

(39) Schenk, M.; Vidal, S. L.; Vlugt, T. J. H.; Smit, B.; Krishna, R. Separation of alkane isomers by exploiting entropy effects during adsorption on silicalite-1: A configurational-bias Monte Carlo simulation study. *Langmuir* **2001**, *17*, 1558-1570.

(40) Dubbeldam, D.; Calero, S.; Vlugt, T. J. H.; Krishna, R.; Maesen, T. L. M.; Smit, B. United Atom Forcefield for Alkanes in Nanoporous Materials. *J. Phys. Chem. B* **2004**, *108*, 12301-12313.

(41) Vlugt, T. J. H.; Krishna, R.; Smit, B. Molecular Simulations of Adsorption Isotherms for Linear and Branched Alkanes and Their Mixtures in Silicalite. *J. Phys. Chem. B* **1999**, *103*, 1102-1118.

(42) Titze, T.; Chmelik, C.; Kärger, J.; van Baten, J. M.; Krishna, R. Uncommon Synergy Between Adsorption and Diffusion of Hexane Isomer Mixtures in MFI Zeolite Induced by Configurational Entropy Effects *J. Phys. Chem. C* **2014**, *118*, 2660-2665.

(43) Krishna, R.; Baur, R. On the Langmuir-Hinshelwood formulation for zeolite catalysed reactions. *Chem. Eng. Sci.* **2005**, *60*, 1155 - 1166.

(44) Tester, J. W.; Modell, M. *Thermodynamics and its Applications*; 3rd Edition, Prentice Hall, Inc.: Upper Saddle River, NJ, USA, 1997.

(45) Sandler, S. I. *Chemical, Biochemical, and Engineering Thermodynamics*; 3rd Edition, John Wiley: New York, 1999.

(46) Kooijman, H. A.; Taylor, R. A dynamic nonequilibrium model of tray distillation columns. *A.I.Ch.E.J.* **1995**, *41*, 1852-1863.

(47) Michelsen, M. An efficient general purpose method of integration of stiff ordinary differential equations. *A.I.Ch.E.J.* **1976**, *22*, 594-597.

(48) Bulirsch, R.; Stoer, J. Numerical treatment of ordinary differential equations by extrapolation methods. *Numer. Math.* **1966**, *8*, 1-14.

(49) Krishna, R.; Baur, R. Diffusion, Adsorption and Reaction in Zeolites: Modelling and Numerical Issues. http://krishna.amsterchem.com/zeolite/, University of Amsterdam, Amsterdam, 1 January 2015.

(50) Ruthven, D. M.; Farooq, S.; Knaebel, K. S. *Pressure swing adsorption*; VCH Publishers: New York, 1994.

(51) Yang, R. T. *Gas separation by adsorption processes*; Butterworth: Boston, 1987.

(52) Do, D. D. *Adsorption analysis: Equilibria and kinetics*; Imperial College Press: London, 1998.

(53) van den Broeke, L. J. P.; Krishna, R. Experimental Verification of the Maxwell-Stefan Theory for Micropore Diffusion. *Chem. Eng. Sci.* **1995**, *50*, 2507-2522.

(54) Walton, K. S.; LeVan, M. D. Consistency of Energy and Material Balances for Bidisperse Particles in Fixed-Bed Adsorption and Related Applications. *Ind. Eng. Chem. Res.* **2003**, *42*, 6938-6948.

(55) Aris, R. *The mathematical theory of diffusion and reaction in permeable catalysts*; Clarendon Press: Oxford, 1975.

(56) Froment, G. F.; Bischoff, K. B.; De Wilde, J. *Chemical Reactor - Analysis and Design*; 3rd Edition, John Wiley & Sons: New York, 2011.

(57) Levenspiel, O. *Chemical Reaction Engineering*; 3rd Edition, John Wiley: New York, 1999.

(58) Corma, A. State of the Art and Future Challenges of Zeolites as Catalysts. *J. Catal.* **2003**, *216*, 298-312.

(59) Degnan, T. F. The Implications of the Fundamentals of Shape Selectivity for the Development of Catalysts for the Petroleum and Petrochemical Industries. *J. Catal.* **2003**, *216*, 32-46.

(60) Marcilly, C. Present status and future trends in catalysis for refining and petrochemicals. *J. Catal.* **2003**, *216*, 47-62.

(61) Baur, R.; Krishna, R. Effectiveness factor for zeolite catalysed isomerization reactions. *Chem. Eng. J.* **2004**, *99*, 105-116.

(62) Baur, R.; Krishna, R. The effectiveness factor for zeolite catalysed reactions. *Catal. Today* **2005**, *105*, 173-179.

(63) Baur, R.; Krishna, R. A moving bed reactor concept for alkane isomerization. *Chem. Eng. J.* **2005**, *109*, 107-113.

(64) Jolimaître, E.; Tayakout-Fayolle, M.; Jallut, C.; Ragil, K. Determination of mass transfer and thermodynamic properties of branched paraffins in silicalite by inverse chromatography technique. *Ind. Eng. Chem. Res.* **2001**, *40*, 914-926.

(65) Jolimaître, E.; Ragil, K.; Tayakout-Fayolle, M.; Jallut, C. Separation of Mono- and Dibranched Hydrocarbons on Silicalite. *A.I.Ch.E.J.* **2002**, *48*, 1927-1937.

(66) Krishna, R.; van Baten, J. M. Maxwell-Stefan modeling of slowing-down effects in mixed gas permeation across porous membranes. *J. Membr. Sci.* **2011**, *383*, 289-300.

(67) Krishna, R. Diffusing Uphill with James Clerk Maxwell and Josef Stefan. *Curr. Opin. Chem. Eng.* **2016**, *12*, 106-119.

(68) Mirth, G.; Cejka, J.; Lercher, J. Transport and Isomerization of Xylenes over HZSM-5 Zeolites. *J. Catal.* **1993**, *139*, 24-33.

(69) Ban, H.; Gui, J.; Duan, L.; Zhang, X.; Song, L.; Sun, Z. Sorption of hydrocarbons in silicalite-1 studied by intelligent gravimetry. *Fluid Phase Equilib.* **2005**, *232*, 149-158.

(70) Duan, L.; Dong, X.; Wu, Y.; Li, H.; Wang, L.; Song, L. Adsorption and diffusion properties of xylene isomers and ethylbenzene in metal–organic framework MIL-53(Al). *J. Porous Mater.* **2013**, *20*, 431-440.

(71) Herm, Z. R.; Wiers, B. M.; Van Baten, J. M.; Hudson, M. R.; Zajdel, P.; Brown, C. M.; Maschiocchi, N.; Krishna, R.; Long, J. R. Separation of Hexane Isomers in a Metal-Organic Framework with Triangular Channels *Science* **2013**, *340*, 960-964.

(72) Hansen, N.; Krishna, R.; van Baten, J. M.; Bell, A. T.; Keil, F. J. Reactor simulation of benzene ethylation and ethane dehydrogenation catalyzed by ZSM-5: A multiscale approach. *Chem. Eng. Sci.* **2010**, *65*, 2472-2480.

(73) Bárcia, P. S.; Silva, J. A. C.; Rodrigues, A. E. Separation by fixed-bed adsorption of hexane isomers in zeolite BETA pellets. *Ind. Eng. Chem. Res.* **2006**, *45*, 4316-4328.

(74) Torres-Knoop, A.; Krishna, R.; Dubbeldam, D. Separating Xylene Isomers by Commensurate Stacking of p-Xylene within Channels of MAF-X8. *Angew. Chem. Int. Ed.* **2014**, *53*, 7774-7778.

(75) Chmelik, C.; Heinke, L.; Kärger, J.; Shah, D. B.; Schmidt, W.; van Baten, J. M.; Krishna, R. Inflection in the Loading Dependence of the Maxwell-Stefan Diffusivity of Iso-butane in MFI Zeolite. *Chem. Phys. Lett.* **2008**, *459*, 141-145.

26.   Caption for Figures

Figure 1. Pore landscape of all-silica BEA zeolite.

Figure 2. Structural details for BEA zeolite.

Figure 3. Pore landscape of all-silica CHA zeolite.

Figure 4. Structural details for CHA zeolite.

Figure 5. Pore landscape of all-silica FAU zeolite.

Figure 6. Structural details for FAU zeolite.

Figure 7, Figure 8, Figure 9, and Figure 10. Pore landscape of all-silica FER zeolite.

Figure 11. Structural details for FER zeolite.

Figure 12. Pore landscape of all-silica LTA zeolite.

Figure 13. Structural details for LTAzeolite.

Figure 14. Pore landscape of all-silica LTL zeolite.

Figure 15. Structural details for LTL zeolite.

Figure 16. Pore landscape for MFI zeolite.

Figure 17. Structural details for MFI zeolite.

Figure 18. Pore landscape of all-silica MOR zeolite.

Figure 19. Structural details for MOR zeolite.

Figure 20. Pore landscape of all-silica MTW zeolite.

Figure 21. Structural details for MTW zeolite.

Figure 22. Pore landscape of all-silica TON zeolite.

Figure 23. Structural details for TON zeolite.

Figure 24. (a) Thermodynamic factor Γ for single-site Langmuir isotherm, plotted as a function of the fractional occupancy. (b) Inverse thermodynamic factor $1/\Gamma$, plotted as a function of the fractional occupancy.

Figure 25. MD data[3-10] on the loading dependence of the M-S diffusivities of various guest molecules in all-silica MFI zeolite at 300 K.

Figure 26. Experimental data on the M-S diffusivity, $Đ_i$, of (a) iso-butane (iC4),[75] (b) n-hexane (nC6),[20] and (c) n-heptane (nC7)[20] in MFI zeolite as a function of the loading, compared with the corresponding dependence of the inverse thermodynamic factor $1/\Gamma_i$.

Figure 27. Molecular Dynamics (MD) simulation data for the M-S diffusivity, $Đ_i$, of (a) n-hexane (nC6), (b) 2-methylpentane (2MP), and 2,2 dimethylbutane (22DMB) in MOR zeolite at 433 K plotted as a function of the loading, expressed in molecules per unit cell. The MD data are taken from Figure 5a of Van Baten and Krishna.[26]

Figure 28. Comparing the M-S diffusivity, $Đ_i$, of (a) n-hexane (nC6), (b) 2-methylpentane (2MP), at 433 K determined from unary MD with those determined from MD data for 50:50 binary nC6/2MP mixtures. The x-axis is the fractional occupancy $\theta_t = \theta_1 + \theta_2$. The unary and mixture MD data are taken from Van Baten and Krishna.[26]

Figure 29. (a) Snapshot showing the location of reactants and products in the alkylation of benzene with ethene to produce ethylbenzene within the intersecting channel topology of MFI catalyst. (b) Effective diffusivity of ethene within MFI catalyst as a function of the mixture loading.[27]

Figure 30. (a) Pure component sorption isotherms for nC6, 3MP and 22DMB in MFI at 362 K. The symbols represent CBMC simulation data.[34, 38, 39] The continuous lines are the dual site Langmuir fits using the parameters as specified in Table 4. (b) CBMC simulations (denoted by symbols), of loadings in MFI zeolite at 362 K for equimolar ternary nC6/3MP/22DMB mixture. The continuous solid lines are calculations using IAST, with the DSL parameter inputs as specified in Table 4. (c) Fractional vacancy for equimolar ternary mixture of C6, 3MP and 22DMB as a function of the total pressure. The continuous solid line represents calculations of θ_V using IAST, with the DSL parameter inputs as specified in Table 4.

Figure 31. (a) Pure component sorption isotherms for nC6, 3MP and 22DMB in MFI at 433 K. The symbols represent CBMC simulation data.[34, 38, 39] The continuous lines are the fits using the dual-site Langmuir-Freundlich model; the parameter values are specified in Table 6. (b, c) CBMC simulations (denoted by symbols), of loadings in MFI zeolite at 433 K for equimolar ternary nC6/3MP/22DMB mixture. The continuous solid lines are calculations using IAST, with parameter values specified in Table 6.

Figure 32. (a) Pure component sorption isotherms for nC6, 2MP, 3MP, 22DMB and 23DMB in MFI at 433 K. The symbols represent CBMC simulation data.[34, 38, 39] The continuous lines are the fits using the dual-site Langmuir-Freundlich model; the parameter values are specified in Table 6. (b, c) CBMC simulations (denoted by symbols), of loadings in MFI zeolite at 433 K for equimolar 5-component

nC6/2MP/3MP/22DMB/23DMB mixture. The continuous solid lines are calculations using IAST, with parameter values specified in Table 6.

Figure 33. (a) Pure component sorption isotherms for nC5, 2MB and neo-pentane in MFI at 433 K. The symbols represent CBMC simulation data.[34, 38, 39] The continuous lines are fits using the dual-site Langmuir-Freundlich model; the parameter values are specified in Table 6. (b, c) CBMC simulations (denoted by symbols), of loadings in MFI zeolite at 433 K for equimolar ternary nC5/2MB/neo-pentane mixture. The continuous solid lines are calculations using IAST, with parameter values specified in Table 6.

Figure 34. (a) CBMC simulations (open symbols) of the sorption isotherms for pure hexane isomers nC6, 2MP, 22DMB in MOR at 433 K. The continuous solid lines in represent the dual-site Langmuir fits of the isotherms with the parameter values specified in Table 7. (b) CBMC simulations for binary mixture nC6(1)/22DMB(2), with $p_1 = p_2$, in MOR at $T = 433$ K. The continuous solid lines are IAST calculations.

Figure 35. (a) One 12- ring channel of MOR, [100] view. (b,c,d) Snapshots of the conformation and siting of siting of nC6, 2MP, and 22DMB.

Figure 36. Discretization schemes for a single spherical crystallite.

Figure 37. Schematic of a packed bed reactor with step input of feed gas mixture.

Figure 38. Summary of model equations describing packed bed adsorber, along with discretization scheme.

Figure 39. Schematic of a packed bed reactor with pulse input of feed gas mixture.

Figure 40. (a) Calculation of the effectiveness factor, η, for uptake inside MFI catalyst exposed to a gas phase 2MP(1)/22DMB(2) mixture at 473 K, carrying out the isomerization reaction 2MP(1) $\rightleftarrows$ 22DMB(2). The partial pressures of the components in the bulk gas phase are $p_1 = p_2 = 10$ kPa. The ratio of rate constants $k_1/k_2 = 2$. The values of the rate constant k_1 are varied. The zero-loading diffusivities $Đ_1(0) = 2 \times 10^{-14}$ m^2 s^{-1}; $Đ_2(0) = 2.5 \times 10^{-16}$ m^2 s^{-1}. The radius of the crystal $r_c = 2$ μm. The classical Thiele modulus plotted on the x-axis is $\phi \equiv \dfrac{r_c}{3} \sqrt{\dfrac{k_1}{Đ_1(0)} + \dfrac{k_2}{Đ_2(0)}}$. (b) The effectiveness factor as a function of the fractional occupancy at the catalyst surface, $\theta_{1s} + \theta_{2s}$. The partial pressures of the components in the bulk gas phase are $p_1 = p_2$. The total pressure $p_1 + p_2$ is varied in the range 0 to 40 kPa. The x-axis is the fractional occupancy at the catalyst surface, $\theta_{1s} + \theta_{2s}$. The reaction rate constant $k_1 = 0.0011$ s^{-1}; the ratio of rate constants $k_1/k_2 = 2$; $\phi = 1.0011$. The calculations using the three different scenarios are based on the analytical solutions provided by Baur and Krishna.[61]

Figure 41. (a) Calculation of the effectiveness factor, η, for uptake inside MFI catalyst exposed a gas phase o-xylene(1)/p-xylene(2) mixture at 433 K, carrying out the isomerization reaction $o-\text{xylene}(1) \rightleftarrows p-\text{xylene}(2)$. The partial pressures of the components in the bulk gas phase are $p_1 = 1$ MPa; $p_2 = 1$ MPa. The zero-loading diffusivities $Đ_1(0) = 1 \times 10^{-16}$ m² s⁻¹; $Đ_2(0) = 1 \times 10^{-14}$ m² s⁻¹. The radius of the crystal $r_c = 10$ μm. The ratio of rate constants $k_1/k_2 = 2$. The values of the rate constant k_1 are varied. The classical Thiele modulus plotted on the x-axis is $\phi \equiv \dfrac{r_c}{3}\sqrt{\dfrac{k_1}{Đ_1(0)} + \dfrac{k_2}{Đ_2(0)}}$. (b) The effectiveness factor as a function of the fractional occupancy at the catalyst surface, $\theta_{1s} + \theta_{2s}$. The partial pressures of the components in the bulk gas phase are $p_1 = p_2$. The total pressure $p_1 + p_2$ is varied in the range 0 to 3 MPa. The x-axis is the fractional occupancy at the catalyst surface, $\theta_{1s} + \theta_{2s}$. The reaction rate constant $k_1 = 1 \times 10^{-4}$ s⁻¹; the ratio of rate constants $k_1/k_2 = 2$; $\phi = 3.34$. The calculations using the three different scenarios are based on the analytical solutions provided by Baur and Krishna.[61]

Figure 42. (a) Transient uptake inside MFI catalyst exposed to a gas phase 2MP(1)/22DMB(2) mixture at 473 K, carrying out the isomerization reaction $2\text{MP}(1) \rightleftarrows 22\text{DMB}(2)$. The partial pressures of the components in the bulk gas phase are $p_1 = p_2 = 10$ kPa. The input data for isotherms, diffusivities, and reaction rate constants are provided in Table 8. The continuous solid lines represent uptake simulations include thermodynamic coupling using the M-S equation (36). The dashed lines represent uptake simulations use uncoupled flux equation (38). (b) Transient equilibration trajectories of the component loadings plotted in composition space.

Figure 43. Equilibration trajectories for $2MP(1) \rightleftarrows 22DMB(2)$ plotted in ternary occupancy space, with coordinates, θ_1 (2MP), θ_2 (22DMB), θ_V (MFI zeolite vacancy). The input data are the same as in Figure 42.

Figure 44. Equilibration trajectories for $2MP(1) \rightleftarrows 22DMB(2)$ plotted in ternary occupancy space, with coordinates, θ_1 (2MP), θ_2 (22DMB), θ_V (MFI zeolite vacancy). The bulk gas phase partial pressures are varied as indicated. The diffusivity and kinetics data are the same as in Figure 42.

Figure 45. Steady-state radial distribution of component loadings for uptake inside MFI catalyst exposed to a gas phase 2MP(1)/22DMB(2) mixture at 473 K, carrying out the isomerization reaction $2MP(1) \rightleftarrows 22DMB(2)$. The partial pressures of the components in the bulk gas phase are $p_1 = p_2 = 10$ kPa. The reaction rate constant $k_1 = 0.0011$ s^{-1}; $k_1/k_2 = 2$; $\phi = 1.0011$. Other parameters are the same as in the legend to Figure 42. The continuous solid lines represent uptake simulations include thermodynamic coupling using equation (36). The dashed lines represent uptake simulations ignoring thermodynamic coupling and use uncoupled flux equation (38).

Figure 46. (a) Transient breakthrough simulations for fixed bed 2MP(1)/22DMB(2) isomerization reactor with MFI extrudates, carrying out the isomerization reaction $2MP(1) \rightleftarrows 22DMB(2)$. The partial pressures of the components in the bulk gas phase at the reactor inlet are $p_1 = 40$ kPa, $p_2 = 0$ kPa. The parameter values are: $L = 0.795$ m; voidage of bed, $\varepsilon = 0.4$; interstitial gas velocity, $v = 0.019$ m/s. The continuous solid lines represent simulations using equation (36), along with the weak confinement scenario. The dashed lines represent breakthrough simulations ignoring thermodynamic coupling and using uncoupled flux equation (38). The input data are provided in Table 8. The plot show the molar concentrations in the gas phase as a function of the dimensionless time, $\tau = tv/L$, obtained by dividing the actual time, t, by the characteristic time, L/v. (b) The plot shows the molar concentrations in the gas phase along the dimensionless length of the fixed bed, z/L, at steady-state. (c) Steady-state molar concentrations of 22DMB along the length of the fixed bed for three different flux calculation scenarios.

Figure 47. (a) Transient uptake inside MFI catalyst exposed to a gas phase o-xylene(1)/p-xylene(2) mixture at 303 K, carrying out the isomerization reaction $o - xylene(1) \rightleftarrows p - xylene(2)$. The partial pressures of the components in the bulk gas phase are $p_1 = p_2 = 5$ MPa. The input data for isotherms, diffusivities, and reaction rate constants are provided in Table 9. The continuous solid lines represent uptake simulations include thermodynamic coupling using equation (36). The dashed lines represent uptake simulations ignoring thermodynamic coupling and use uncoupled flux equation (38). (b) Transient equilibration trajectories of the component loadings plotted in composition space.

Figure 48. Equilibration trajectories for $o-xylene(1) \rightleftarrows p-xylene(2)$ plotted in ternary occupancy space, with coordinates, θ_1 (o-xylene), θ_2 (p-xylene), θ_V (MFI zeolite vacancy). The input data are the same as in Figure 47.

Figure 49. Equilibration trajectories for $o-xylene(1) \rightleftarrows p-xylene(2)$ plotted in ternary occupancy space, with coordinates, θ_1 (o-xylene), θ_2 (p-xylene), θ_V (MFI zeolite vacancy). The bulk gas phase partial pressures are varied as indicated. The input data for isotherms, diffusivities, and reaction rate constants are the same as in Figure 47. The input data for isotherms, diffusivities, and reaction rate constants are provided in Table 9.

Figure 50. Steady-state radial distribution of component loadings for uptake inside MFI catalyst exposed to a gas phase o-xylene(1)/p-xylene(2) mixture at 433 K, carrying out the isomerization reaction $o-xylene(1) \rightleftarrows p-xylene(2)$. The partial pressures of the components in the bulk gas phase are $p_1 = p_2 = 5$ MPa. The input data for isotherms, diffusivities, and reaction rate constants are the same as in Figure 47. The continuous solid lines represent simulations using equation (36), along with the strong confinement scenario. The dashed lines represent uptake simulations ignoring thermodynamic coupling and use uncoupled flux equation (38).

Figure 51. Steady-state simulations for fixed bed reactor, carrying out the isomerization reaction $o-xylene(1) \rightleftarrows p-xylene(2)$ with MFI catalyst. The partial pressures of the components in the bulk gas phase at the reactor inlet are $p_1 = 10$ MPa, $p_2 = 0$ MPa. The parameter values are: $L = 1$ m; voidage of bed, $\varepsilon = 0.4$; interstitial gas velocity, $v = 0.00001$ m/s. The reaction rate constant $k_1 = 1 \times 10^{-4}$ s^{-1}; $k_1/k_2 = 2$; $\phi = 3.34$. The input data for isotherms, diffusivities, and reaction rate constants are the same as in Figure 47. The plot shows the molar concentrations in the gas phase along the dimensionless length of the fixed bed, z/L, at steady-state. The continuous solid lines represent simulations using equation (36), and the strong confinement scenario. The dashed lines represent simulations ignoring thermodynamic coupling and using uncoupled flux equation (38).

Figure 52. Transient simulations for pulsed chromatographic reactor, carrying out the isomerization reaction $o-xylene(1) \rightleftarrows p-xylene(2)$ with MFI catalyst. The feed to the reactor is a pulse, of 200 s duration; the partial pressures of the components in the bulk gas phase at the reactor inlet are $p_1 = p_2 = 5$ MPa. The parameter values are: $L = 1$ m; voidage of bed, $\varepsilon = 0.4$; interstitial gas velocity, $v = 0.0001$ m s^{-1}. The reaction rate constant $k_1 = 1 \times 10^{-4}$ s^{-1}; $k_1/k_2 = 2$; $\phi = 3.34$. The input data for isotherms, diffusivities, and reaction rate constants are the same as in Figure 47. The plots show the molar concentrations in the gas phase as a function of the dimensionless time, $\tau = tv/L$, obtained by dividing the actual time, t, by the characteristic time, L/v. The continuous solid lines represent simulations using equation (36), and the strong confinement scenario.

Figure 53. (a) Transient uptake inside MFI catalyst exposed to a gas phase nC6(1)/3MP(2)/22DMB(3) mixture at 362 K, carrying out the isomerization reaction $nC6(1) \rightleftarrows 3MP(2) \rightleftarrows 22DMB(3)$. The partial pressures of the components in the bulk gas phase are p_1 = 1000 Pa; p_2 = 1 Pa, p_3 = 1 Pa. The input data for isotherms, diffusivities, and reaction rate constants are provided in Table 4. The continuous solid lines represent uptake simulations include thermodynamic coupling using equation (36). The dashed lines represent uptake simulations ignoring thermodynamic coupling and use uncoupled flux equation (38). (b) Transient equilibration trajectories of the component loadings plotted in composition space.

Figure 54. (a, b) Steady-state simulations of fixed bed reactor packed with MFI catalyst exposed to a gas phase nC6(1)/3MP(2)/22DMB(3) mixture at 362 K, carrying out the isomerization reaction $nC6(1) \rightleftarrows 3MP(2) \rightleftarrows 22DMB(3)$. The partial pressures of the components in the bulk gas phase at the reactor inlet are p_1 = 1000 Pa; p_2 = 1 Pa, p_3 = 1 Pa. The total length of fixed bed, L = 0.35 m; the bed porosity, ε = 0.4, the interstitial velocity at the inlet v = 1 m s^{-1}. The input data for isotherms, diffusivities, and reaction rate constants are the same as in Figure 53. The continuous solid lines represent simulations using equation (36), and the weak and strong confinement scenarios. The dashed lines represent uptake simulations ignoring thermodynamic coupling and use uncoupled flux equation (38). The plot shows the molar concentrations in the gas phase along the dimensionless length of the fixed bed, z/L, at steady-state. In (b) the gas phase 22DMB profiles are compared for the three different flux calculation scenarios.

Figure 55. Transient simulations of fixed bed reactor packed with MFI catalyst exposed to a gas phase nC6(1)/3MP(2)/22DMB(3) mixture at 362 K, carrying out the isomerization reaction $nC6(1) \rightleftarrows 3MP(2) \rightleftarrows 22DMB(3)$. The partial pressures of the components in the bulk gas phase at the reactor inlet are p_1 = 1000 Pa; p_2 = 1 Pa, p_3 = 1 Pa. The total length of fixed bed, L = 0.35 m; the bed porosity, ε = 0.4, the interstitial velocity at the inlet v = 1 m s^{-1}. The input data for isotherms, diffusivities, and reaction rate constants are the same as in Figure 53. The continuous solid lines represent simulations using equation (36), and the weak confinement scenario. The dashed lines represent uptake simulations ignoring thermodynamic coupling and use uncoupled flux equation (38). The plot show the molar concentrations in the gas phase as a function of the dimensionless time, $\tau = tv/L$, obtained by dividing the actual time, t, by the characteristic time, L/v.

Figure 56. (a) Transient uptake inside BEA catalyst exposed to a gas phase nC6(1)/3MP(2)/22DMB(3) mixture at 433 K, carrying out the isomerization reaction $nC6(1) \rightleftarrows 3MP(2) \rightleftarrows 22DMB(3)$. The partial pressures of the components in the bulk gas phase are $p_1 = p_2 = p_3$ =20 kPa. The input data for isotherms, diffusivities, and reaction rate constants are provided in Table 5. The continuous solid lines represent uptake simulations include thermodynamic coupling using equation (36). The dashed lines represent uptake simulations ignoring thermodynamic coupling and use uncoupled flux equation (38). (b) Transient equilibration trajectories of the component loadings plotted in composition space.

Figure 57. (a) Transient uptake inside MFI catalyst exposed to a gas phase nC6(1)/2MP(2)/22DMB(3) mixture at 433 K, carrying out the isomerization reaction $nC6(1) \rightleftarrows 2MP(2) \rightleftarrows 22DMB(3)$. The partial

pressures of the components in the bulk gas phase are p_1 = 50 kPa; p_2 = 25 kPa, p_3 =25 kPa. The input data for isotherms, diffusivities, and reaction rate constants are provided in Table 6. The continuous solid lines represent uptake simulations include thermodynamic coupling using equation (36). The dashed lines represent uptake simulations ignoring thermodynamic coupling and use uncoupled flux equation (38). (b) Transient equilibration trajectories of the component loadings plotted in composition space.

Figure 58. (a, b) Steady-state simulations of fixed bed reactor packed with MFI catalyst exposed to a gas phase nC6(1)/2MP(2)/22DMB(3) mixture at 433 K, carrying out the isomerization reaction nC6(1)$\rightleftarrows$2MP(2)$\rightleftarrows$22DMB(3). The partial pressures of the components in the bulk gas phase at the reactor inlet are p_1 = 90 Pa; p_2 = 5 kPa, p_3 = 5 kPa. The input data for isotherms, diffusivities, and reaction rate constants are provided in Table 6. The input data for isotherms, diffusivities, and reaction rate constants are the same as in Figure 57. The total length of fixed bed, L = 0.3 m; the bed porosity, ε = 0.4, the interstitial velocity at the inlet v = 0.1 m s^{-1}. The continuous solid lines represent simulations using equation (36), and the weak and strong confinement scenarios. The dashed lines represent uptake simulations ignoring thermodynamic coupling and use uncoupled flux equation (38). The plot shows the molar concentrations in the gas phase along the dimensionless length of the fixed bed, z/L, at steady-state. In (b) the gas phase 22DMB profiles are compared for the three different flux calculation scenarios.

Figure 59. Transient simulations of fixed bed reactor packed with MFI catalyst exposed to a gas phase nC6(1)/2MP(2)/22DMB(3) mixture at 433 K, carrying out the isomerization

reaction $nC6(1) \rightleftarrows 2MP(2) \rightleftarrows 22DMB(3)$. The partial pressures of the components in the bulk gas phase at the reactor inlet are $p_1 = 90$ kPa; $p_2 = 5$ kPa, $p_3 = 5$ kPa. The input data for isotherms, diffusivities, and reaction rate constants are the same as in Figure 57. The total length of fixed bed, $L = 0.3$ m; the bed porosity, $\varepsilon = 0.4$, the interstitial velocity at the inlet $v = 0.1$ m s^{-1}. The continuous solid lines represent simulations using equation (36), and the weak confinement scenario. The dashed lines represent uptake simulations ignoring thermodynamic coupling and use uncoupled flux equation (38). The plot show the molar concentrations in the gas phase as a function of the dimensionless time, $\tau = tv/L$, obtained by dividing the actual time, t, by the characteristic time, L/v.

Figure 60. (a) Transient uptake inside MOR catalyst exposed to a gas phase nC6(1)/2MP(2)/22DMB(3) mixture at 433 K, carrying out the isomerization reaction $nC6(1) \rightleftarrows 2MP(2) \rightleftarrows 22DMB(3)$. The partial pressures of the components in the bulk gas phase are $p_1 = p_2 = p_3 = 40$ kPa. The continuous solid lines represent uptake simulations include thermodynamic coupling using equation (36). The dashed lines represent uptake simulations ignoring thermodynamic coupling and use uncoupled flux equation (38). The input data for isotherms, diffusivities, and reaction rate constants are provided in Table 7. (b) Transient equilibration trajectories of the component loadings plotted in composition space.

Figure 61. Steady-state simulations of fixed bed reactor packed with MOR catalyst exposed to a gas phase nC6(1)/2MP(2)/22DMB(3) mixture at 433 K, carrying out the isomerization reaction $nC6(1) \rightleftarrows 2MP(2) \rightleftarrows 22DMB(3)$. The plot shows the molar concentrations of the desired product 22DMB in the gas phase along the dimensionless length of the fixed bed, z/L, at steady-state. The partial

pressures of the components in the bulk gas phase at the reactor inlet are p_1 = 1 MPa; $p_2 = p_3$ = 0 MPa. The input data for isotherms, diffusivities, and reaction rate constants are provided in Table 7. The total length of fixed bed, L = 1 m; the bed porosity, ε = 0.4, the interstitial velocity at the inlet v = 0.02 m s^{-1}. The input data are the same as in Figure 60. The continuous solid lines represent simulations include thermodynamic coupling using equation (36). The dashed lines represent simulations ignoring thermodynamic coupling and use uncoupled flux equation (38).

Figure 62. (a) Transient uptake inside MFI catalyst exposed to a gas phase ethene(1)/benzene(2)/ethylbenzene(3) mixture at 653 K, carrying out the ethylation reaction $\text{ethene}(1) + \text{benzene}(2) \rightleftarrows \text{ethylbenzene}(3)$. The partial pressures of the components in the bulk gas phase are p_1 = 0.6 MPa; p_2 = 0.4 MPa, p_3 = 0.0 MPa. The input data for isotherms, diffusivities, and reaction rate constants are provided in Table 10. The continuous solid lines represent uptake simulations include thermodynamic coupling using Equation (36). The dashed lines represent uptake simulations ignoring thermodynamic coupling and use uncoupled flux equation (38). (b) Transient equilibration trajectories of the component loadings plotted in composition space.

Figure 63. Steady-state simulations of fixed bed reactor packed with MFI catalyst exposed to a gas phase ethene(1)/benzene(2)/ethylbenzene(3) mixture at 653 K, carrying out the ethylation reaction $\text{ethene}(1) + \text{benzene}(2) \rightleftarrows \text{ethylbenzene}(3)$. The partial pressures of the components in the bulk gas phase at the reactor inlet are p_1 = 0.6 MPa; p_2 = 0.4 MPa, p_3 = 0 MPa. The total length of fixed bed, L = 1 m; the bed porosity, ε = 0.4, the interstitial velocity at the inlet v = 0.1 m s^{-1}. The input data for isotherms, diffusivities, and reaction rate constants are the same as in Figure 62. The plot show the molar concentrations in the gas phase phase along the dimensionless length of the fixed bed, z/L. The

continuous solid lines represent simulations using Equation (36), with the strong confinement scenario. The dashed lines represent simulations ignoring thermodynamic coupling, equation (38). In (b) the ethylbenzene concentrations in the gas phase are compared for three different model implementations.

Figure 64. (a) Transient uptake inside MFI catalyst exposed to a gas phase ethane(1)/ethene(2)/hydrogen(3) mixture at 653 K, carrying out the dehydrogenation reaction $ethane(1) \rightleftarrows ethene(2) + hydrogen(3)$. The partial pressures of the components in the bulk gas phase are $p_1 = 1$ MPa; $p_2 = 2$ MPa, $p_3 = 3$ MPa. The continuous solid lines represent uptake simulations include thermodynamic coupling using Equation (36). The dashed lines represent uptake simulations ignoring thermodynamic coupling and using uncoupled flux equation (38). The input data for isotherms, diffusivities, and reaction rate constants are provided in Table 11. (b) Transient equilibration trajectories of the component loadings plotted in composition space.

Figure 65. Steady-state simulations of fixed bed reactor packed with MFI catalyst exposed to a gas phase ethane(1)/ethene(2)/hydrogen(3) mixture at 653 K, carrying out the dehydrogenation reaction $ethane(1) \rightleftarrows ethene(2) + hydrogen(3)$. The partial pressures of the components in the bulk gas phase at the reactor inlet are $p_1 = 1$ MPa; $p_2 = p_3 = 0$ MPa. The total length of fixed bed, $L = 1$ m; the bed porosity, $\varepsilon = 0.4$, the interstitial velocity at the inlet $v = 0.01$ m s^{-1}. The input data for isotherms, diffusivities, and reaction rate constants are the same as in Figure 64. The plot show the molar concentrations of ethene in the gas phase along the dimensionless length of the fixed bed, z/L. The input data for isotherms, diffusivities, and reaction rate constants are provided in Table 11. The continuous

solid lines represent simulations using Equation (36). The dashed lines represent simulations ignoring thermodynamic coupling, equation (38).

BEA pore landscape
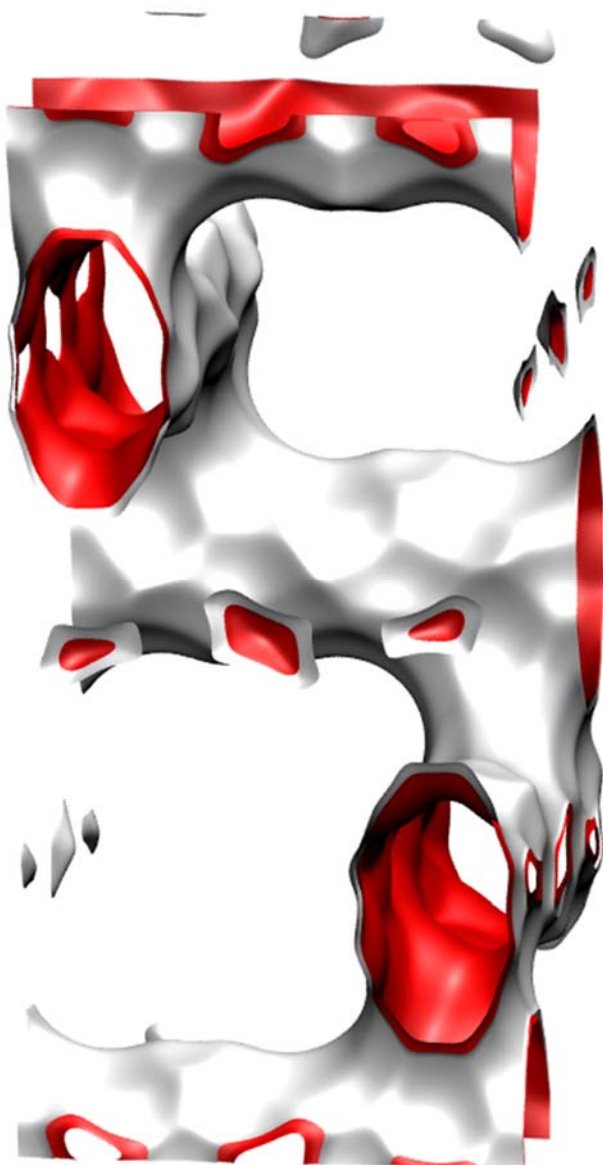
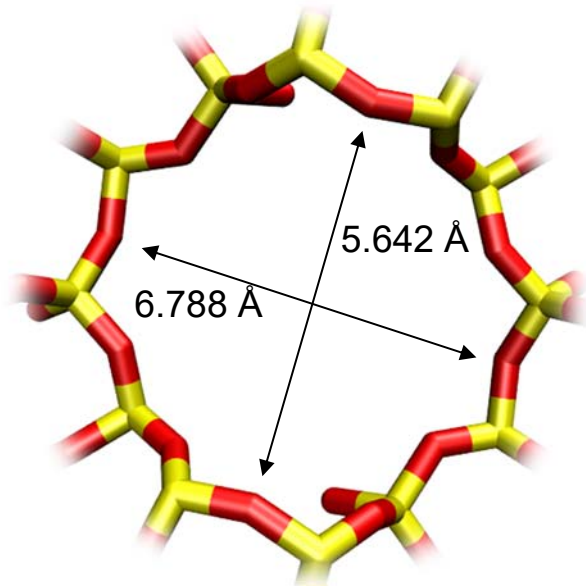|	BEA
a /Å	12.661
b /Å	12.661
c /Å	26.406
Cell volume / Å^3	4232.906
conversion factor for [molec/uc] to [mol per kg Framework]	0.2600
conversion factor for [molec/uc] to [kmol/m^3]	0.9609
ρ [kg/m3]	1508.558
MW unit cell [g/mol(framework)]	3845.427
ϕ, fractional pore volume	0.408
open space / Å^3/uc	1728.1
Pore volume / cm^3/g	0.271
Surface area /m^2/g	923.0
DeLaunay diameter /Å	5.87

BEA pore dimensions

This plot of surface area versus pore dimension is determined using a combination of the DeLaunay triangulation method for pore dimension determination, and the procedure of Düren for determination of the surface area.

BEA

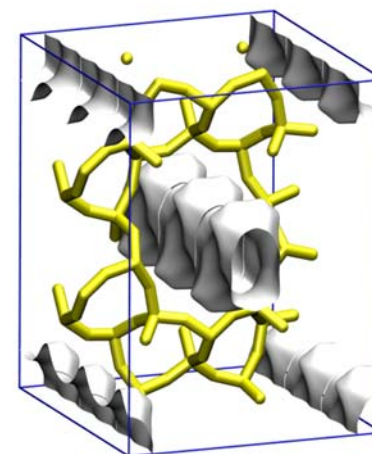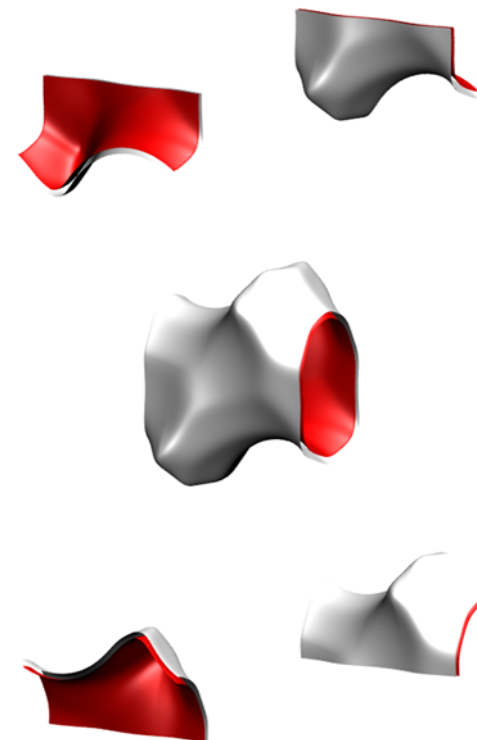Surface area / m² g⁻¹ vs Pore dimension / Å

6.148 Å

6.830 Å

BEA [1 0 0]

6.724 Å   5.604 Å

5.604 Å
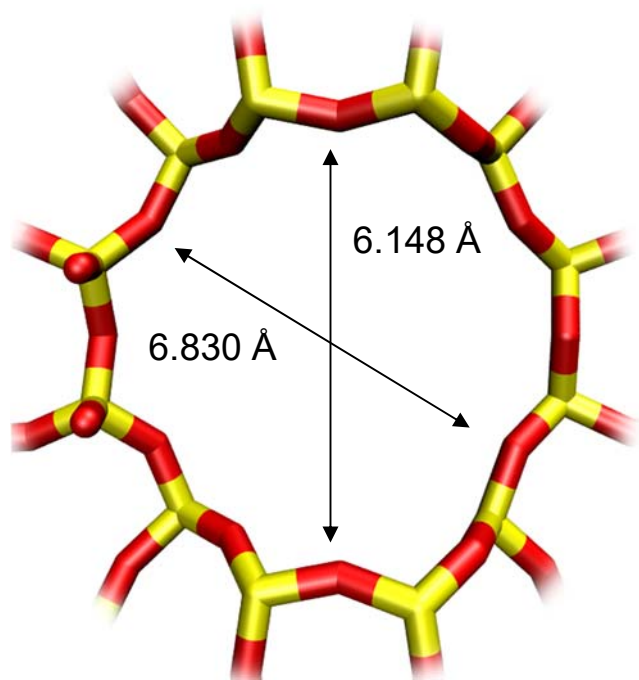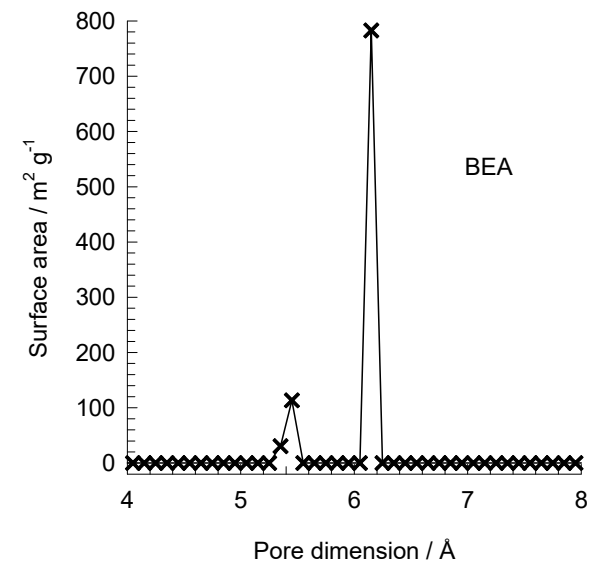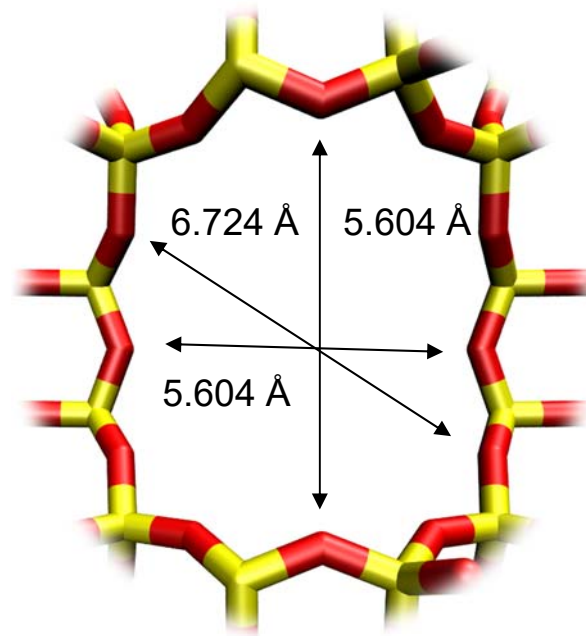
BEA [0 0 1]

CHA landscape
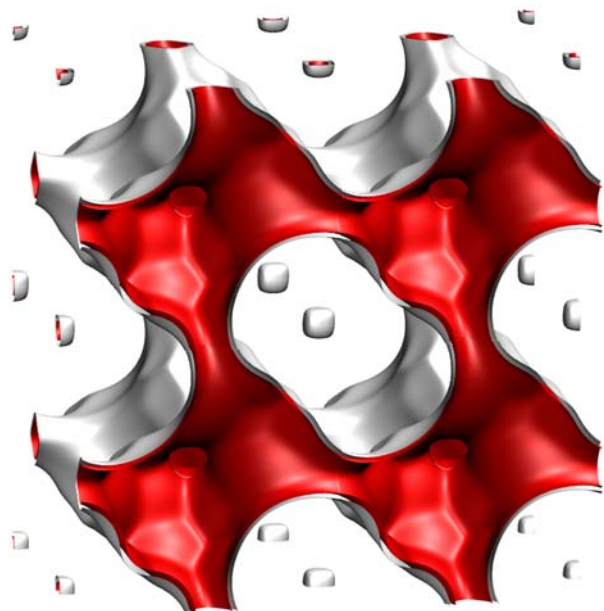
There are 6 cages per unit cell. The volume of one CHA cage is 316.4 Å^3, slightly larger than that of a single cage of DDR (278 Å^3), but significantly lower than FAU (786 Å^3).
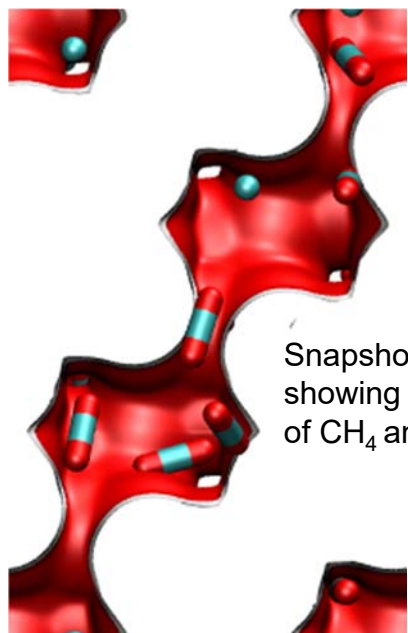
Snapshots showing location of CH$_4$ and CO$_2$
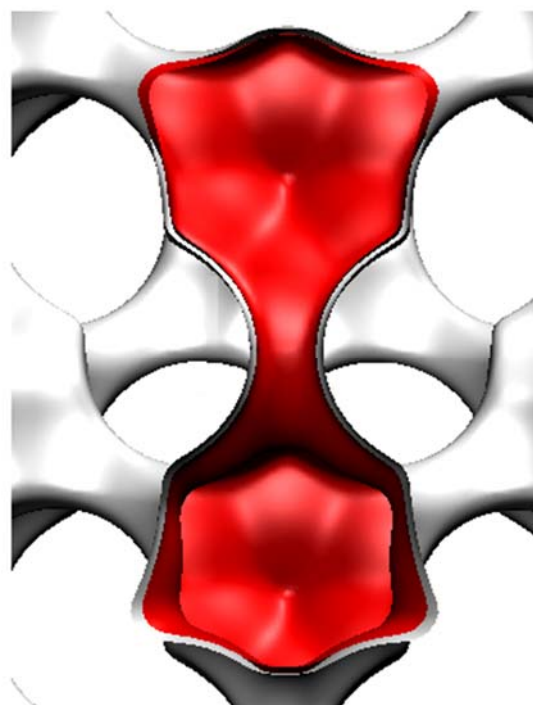
Snapshots showing location of CH$_4$

Structural information from: C. Baerlocher, L.B. McCusker, Database of Zeolite Structures, International Zeolite Association, http://www.iza-structure.org/databases/
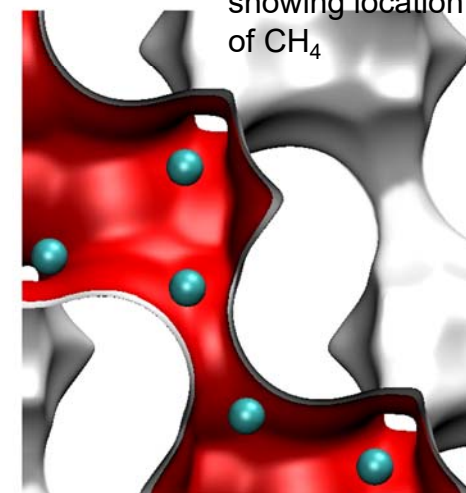
CHA window and pore dimensions

4.23 Å

3.77 Å
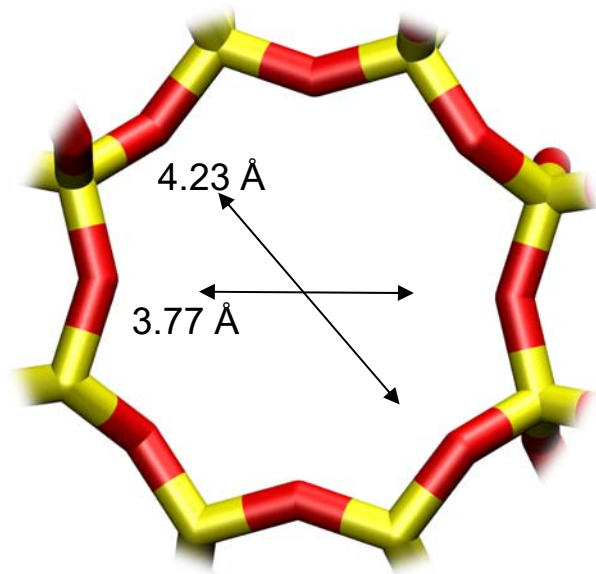
CHA

The window dimensions calculated using the van der Waals diameter of framework atoms = 2.7 Å are indicated above by the arrows.

This plot of surface area versus pore dimension is determined using a combination of the DeLaunay triangulation method for pore dimension determination, and the procedure of Düren for determination of the surface area.
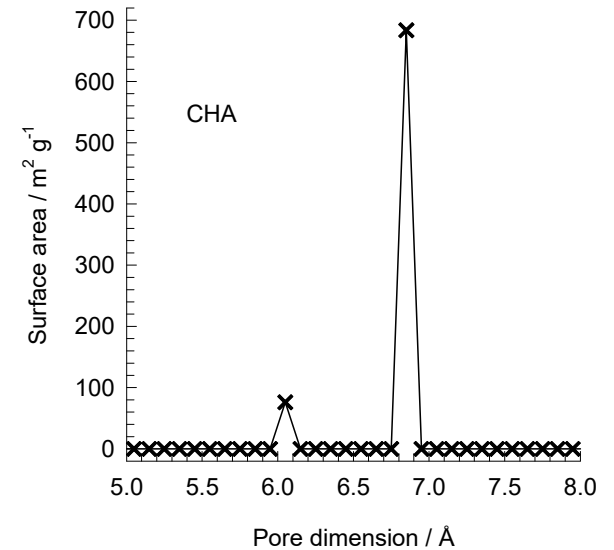

	CHA
a /Å	15.075
b /Å	23.907
c /Å	13.803
Cell volume / Å^3	4974.574
conversion factor for [molec/uc] to [mol per kg Framework]	0.2312
conversion factor for [molec/uc] to [kmol/m^3]	0.8747
ρ [kg/m3]	1444.1
MW unit cell [g/mol(framework)]	4326.106
ϕ, fractional pore volume	0.382
open space / Å^3/uc	1898.4
Pore volume / cm^3/g	0.264
Surface area /m^2/g	758.0
DeLaunay diameter /Å	3.77

FAU-Si pore landscape

The sodalite cages are blocked in simulations and are not accessible to guest molecules; these are excluded for pore volume determination.
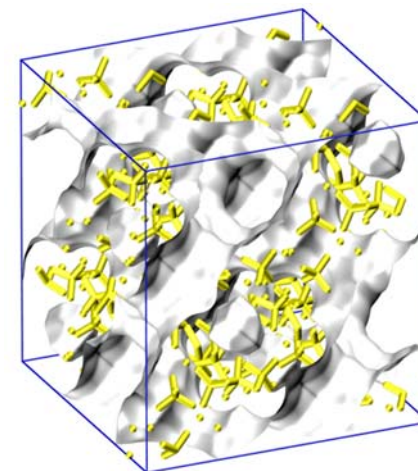
12-ring
window of FAU

There are 8 cages per unit cell. The volume of one FAU cage is 786 Å^3, larger in size than that of LTA (743 Å^3) and DDR (278 Å^3).

Structural information from: C. Baerlocher, L.B. McCusker, Database of Zeolite Structures, International Zeolite Association, http://www.iza-structure.org/databases/

FAU-Si window and pore dimensions

This plot of surface area versus pore dimension is determined using a combination of the DeLaunay triangulation method for pore dimension determination, and the procedure of Düren for determination of the surface area.

7.25 Å

7.25 Å
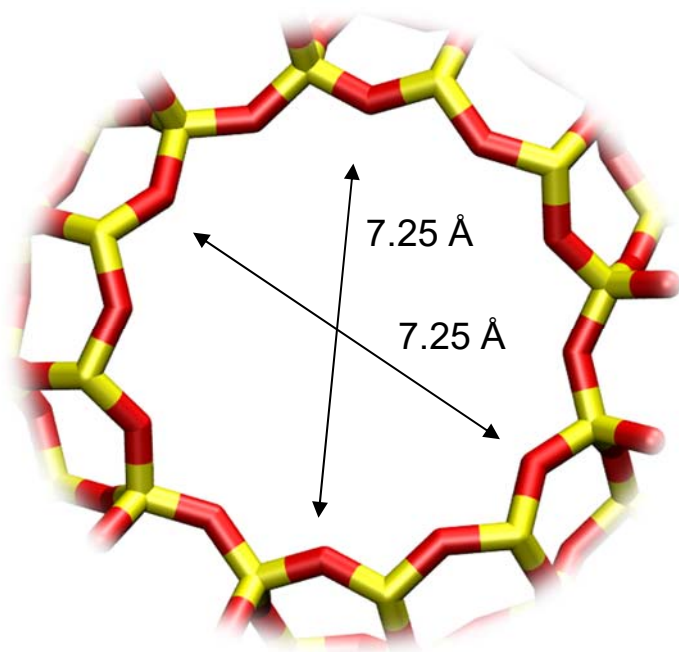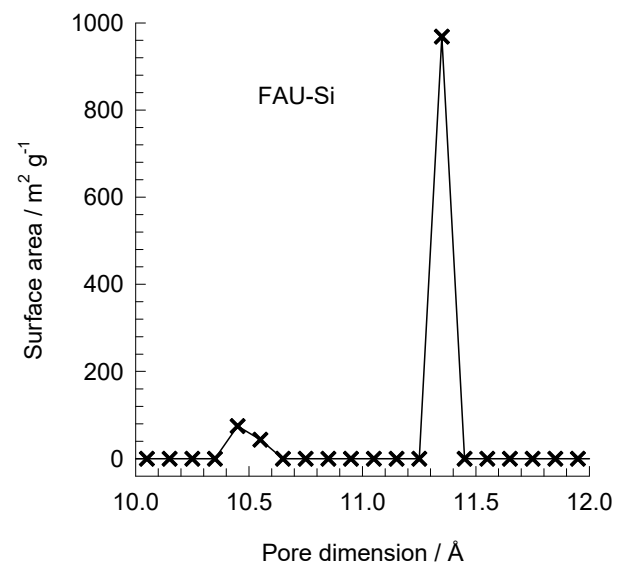
	FAU-Si
a /Å	24.28
b /Å	24.28
c /Å	24.28
Cell volume / Å^3	14313.51
conversion factor for [molec/uc] to [mol per kg Framework]	0.0867
conversion factor for [molec/uc] to [kmol/m^3]	0.2642
ρ [kg/m3]	1338.369
MW unit cell [g/mol (framework)]	11536.28
ϕ, fractional pore volume	0.439
open space / Å^3/uc	6285.6
Pore volume / cm^3/g	0.328
Surface area /m^2/g	1086.0
DeLaunay diameter /Å	7.37

FER pore dimensions

FER channel [0 0 1]
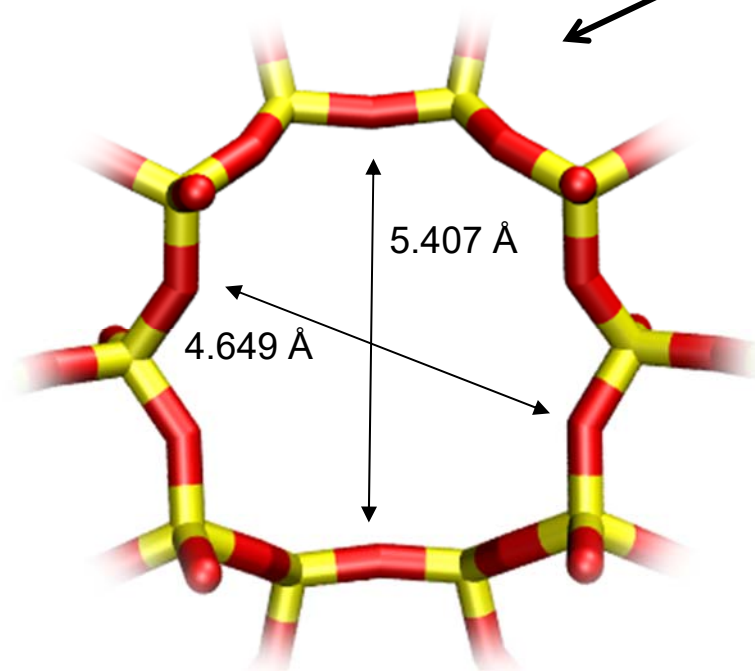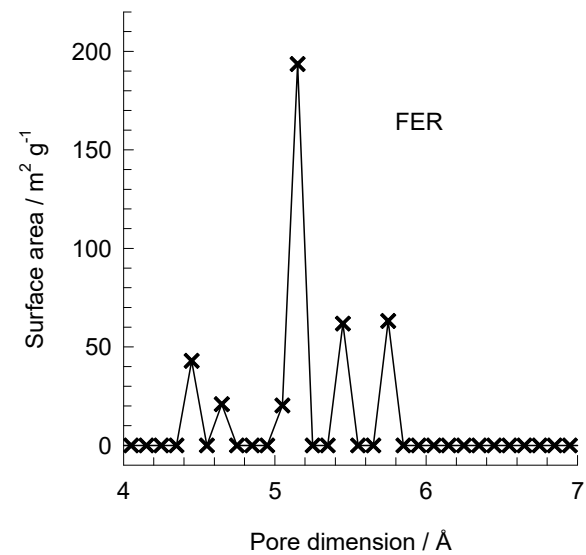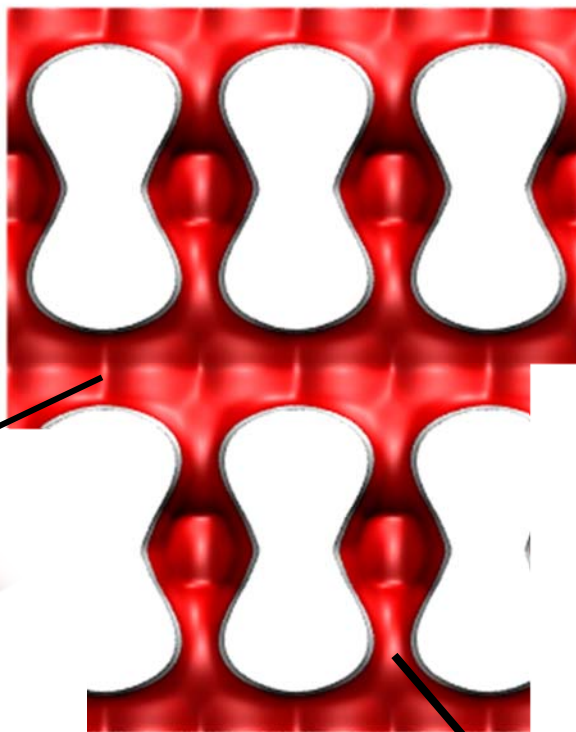
FER [0 1 0]
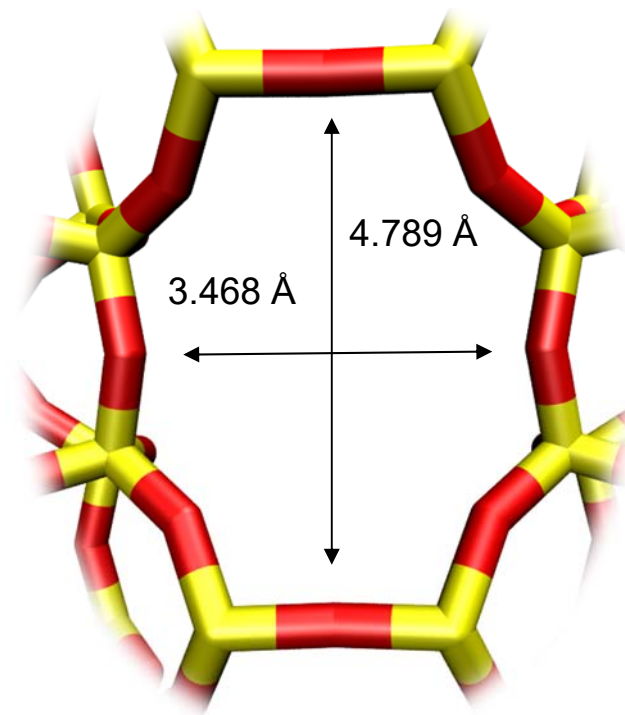
FER pore landscape

8-ring channels
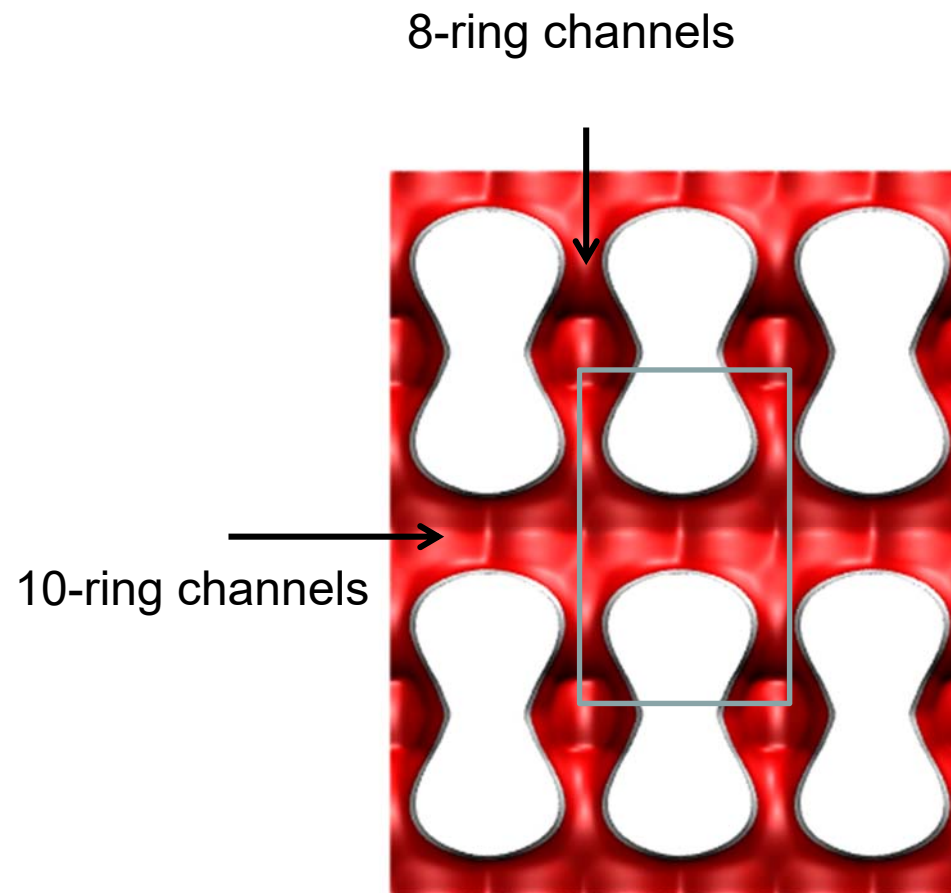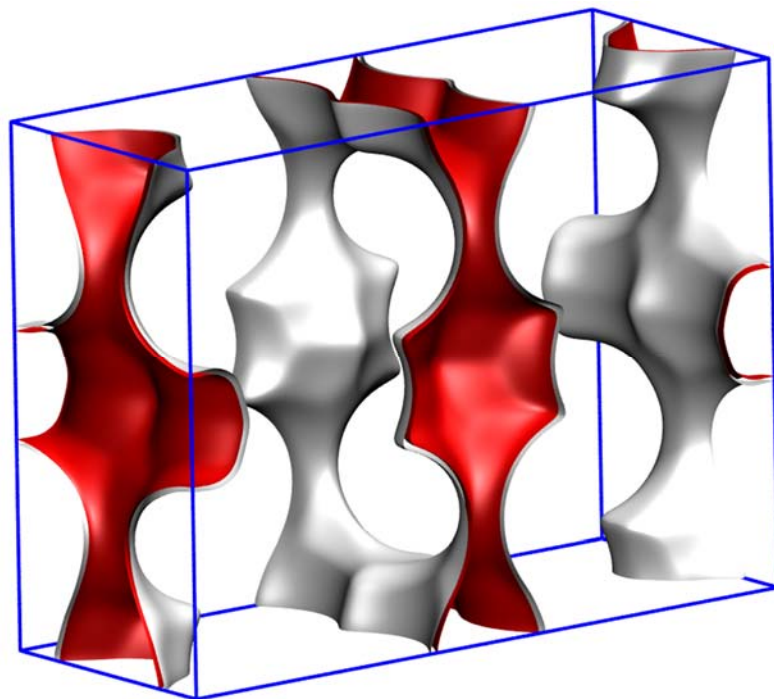
10-ring channels

This is one unit cell

There are two 10-ring channels
There are two 8-ring channels

FER pore landscape

8-ring channels

10-ring channels
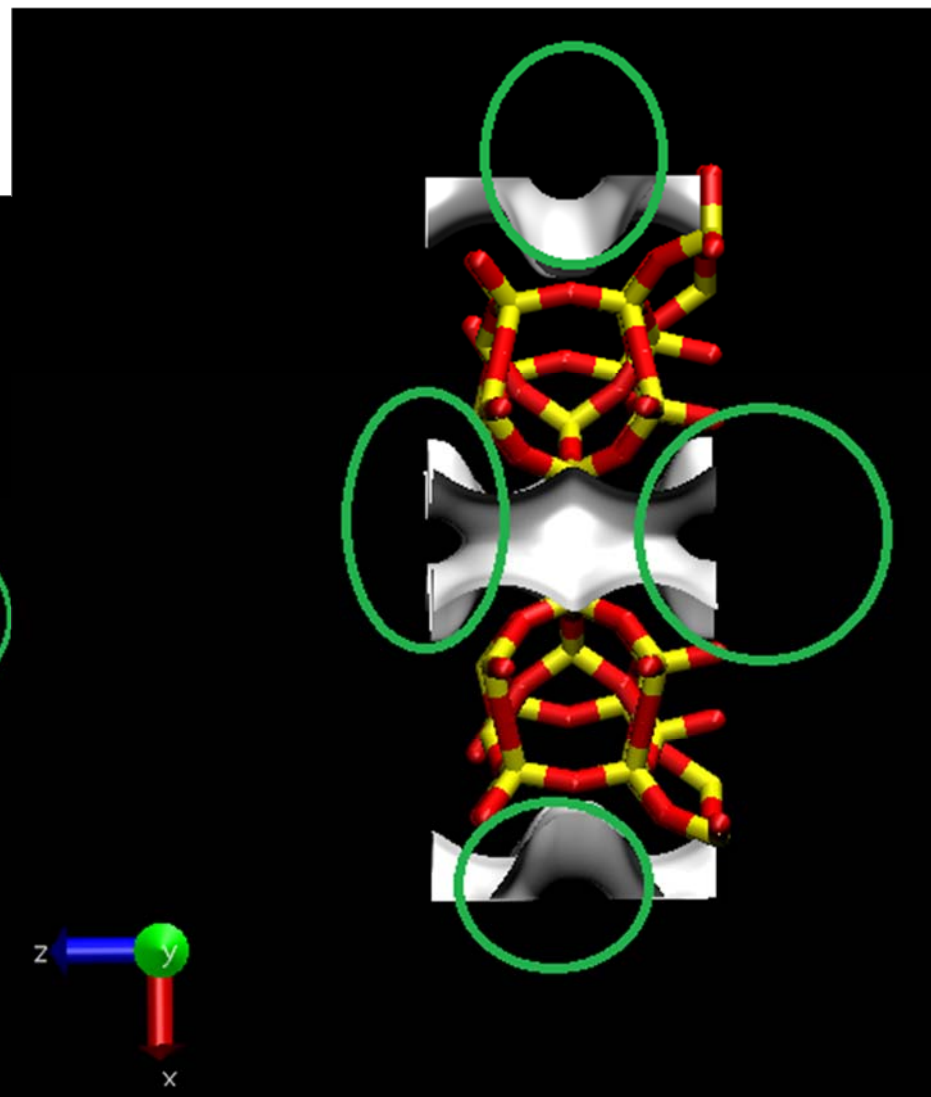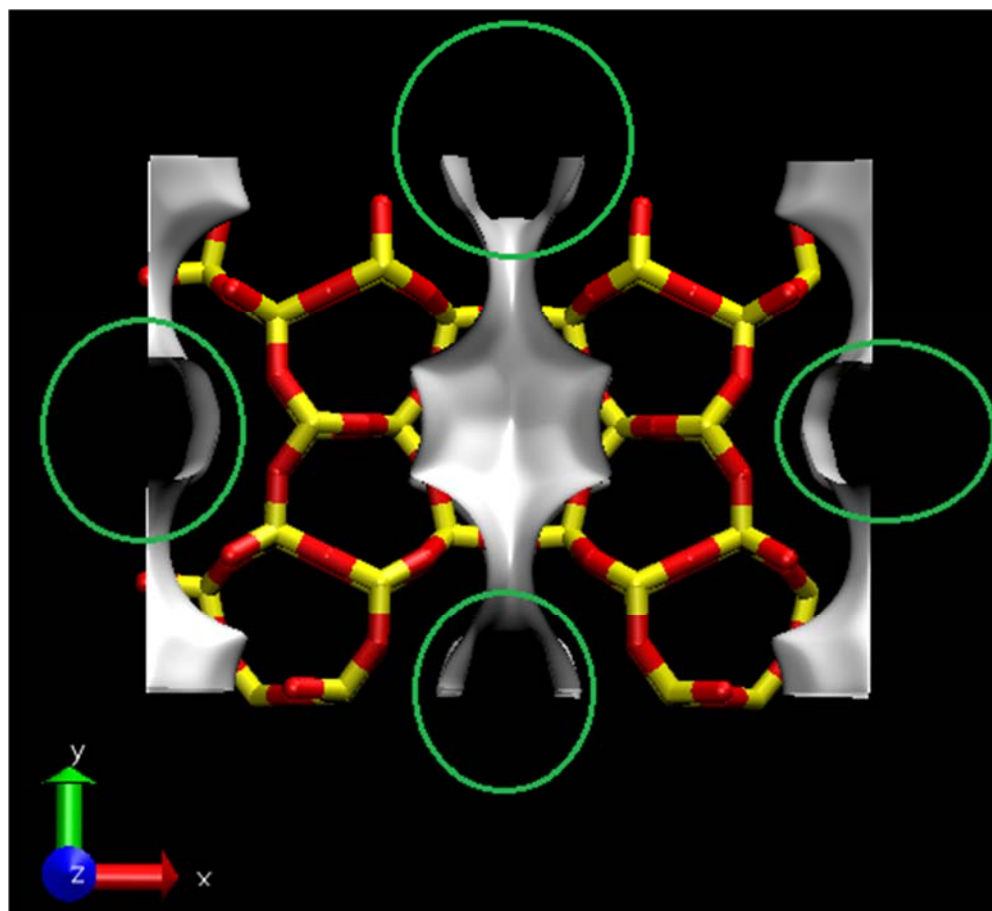
FER pore dimensions
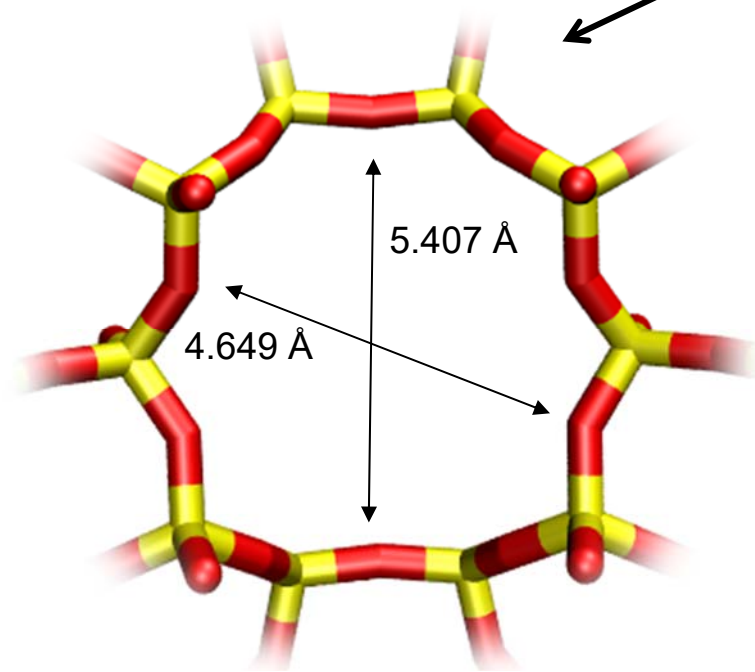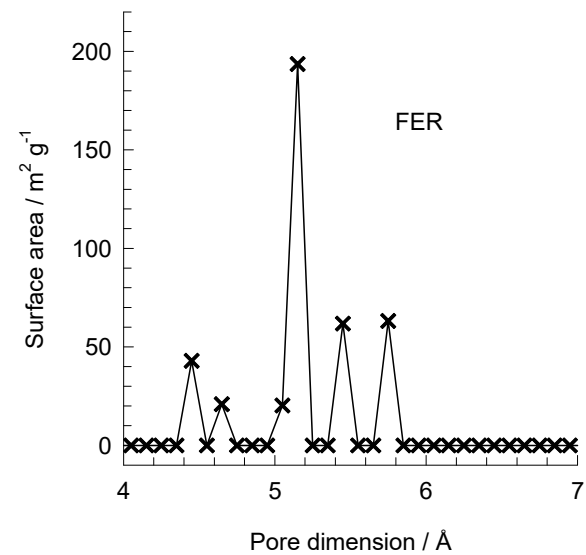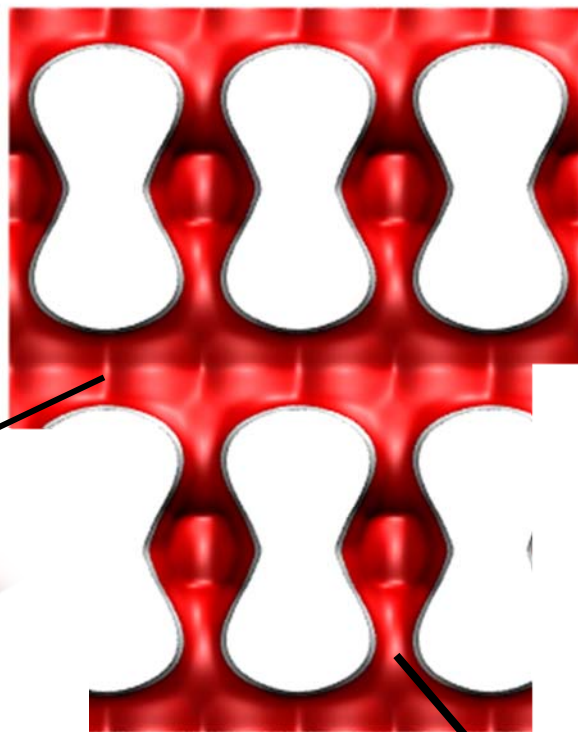
FER channel [0 0 1]
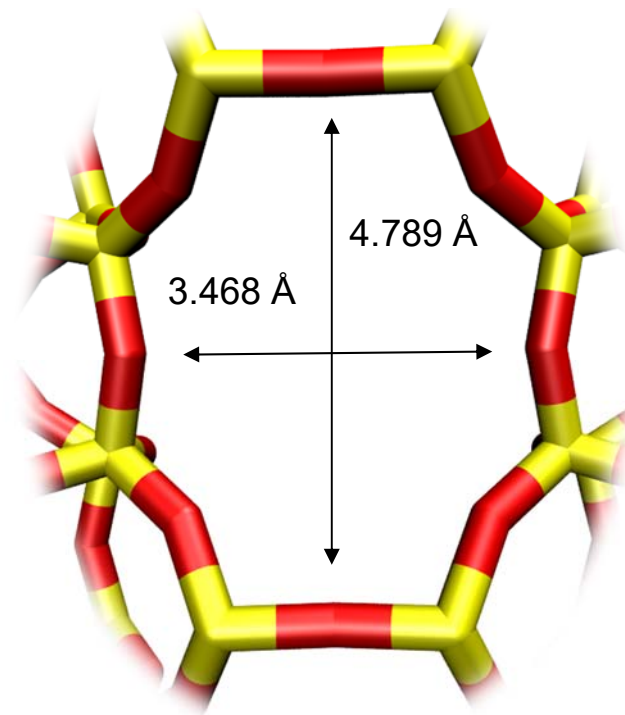
FER [0 1 0]

FER pore landscape
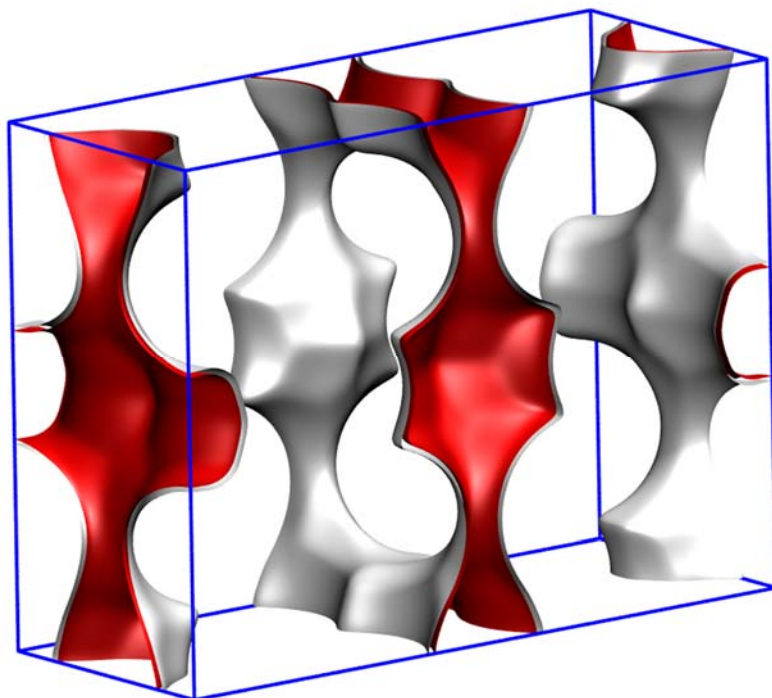
	FER
a /Å	19.156
b /Å	14.127
c /Å	7.489
Cell volume / Å^3	2026.649
conversion factor for [molec/uc] to [mol per kg Framework]	0.4623
conversion factor for [molec/uc] to [kmol/m^3]	2.8968
ρ [kg/m3]	1772.33
MW unit cell [g/mol (framework)]	2163.053
ϕ, fractional pore volume	0.283
open space / Å^3/uc	573.2
Pore volume / cm^3/g	0.160
Surface area /m^2/g	403.0
DeLaunay diameter /Å	4.65

LTA-Si landscapes
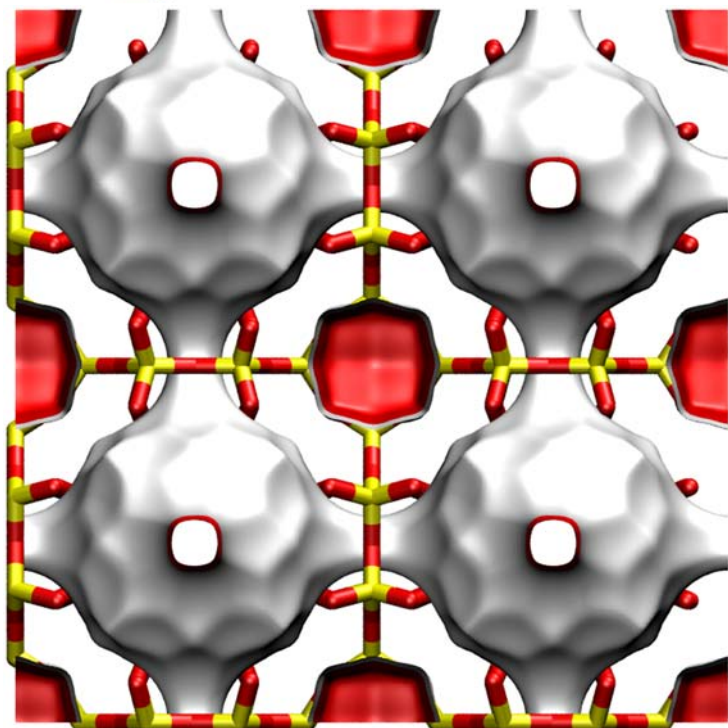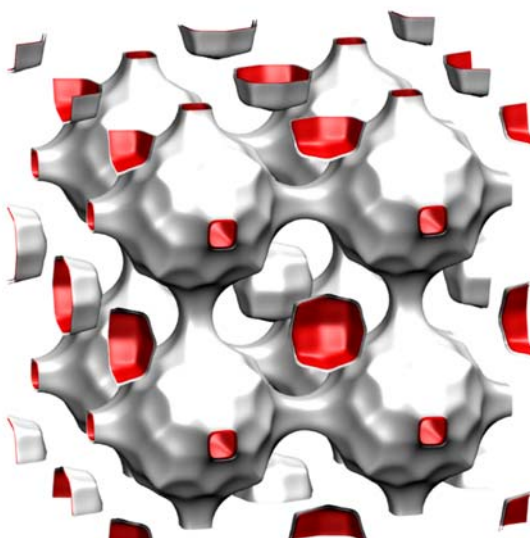
This is a *hypothetical* structure constructed from dealuminized LTA-5A structure

There are 8 cages per unit cell. The volume of one LTA cage is 743 $Å^3$, intermediate in size between a single cage of ZIF-8 (1168 $Å^3$) and of DDR (278 $Å^3$).

Inaccessible sodalite cages

4.1 Å windows

278 $Å^3$ cages
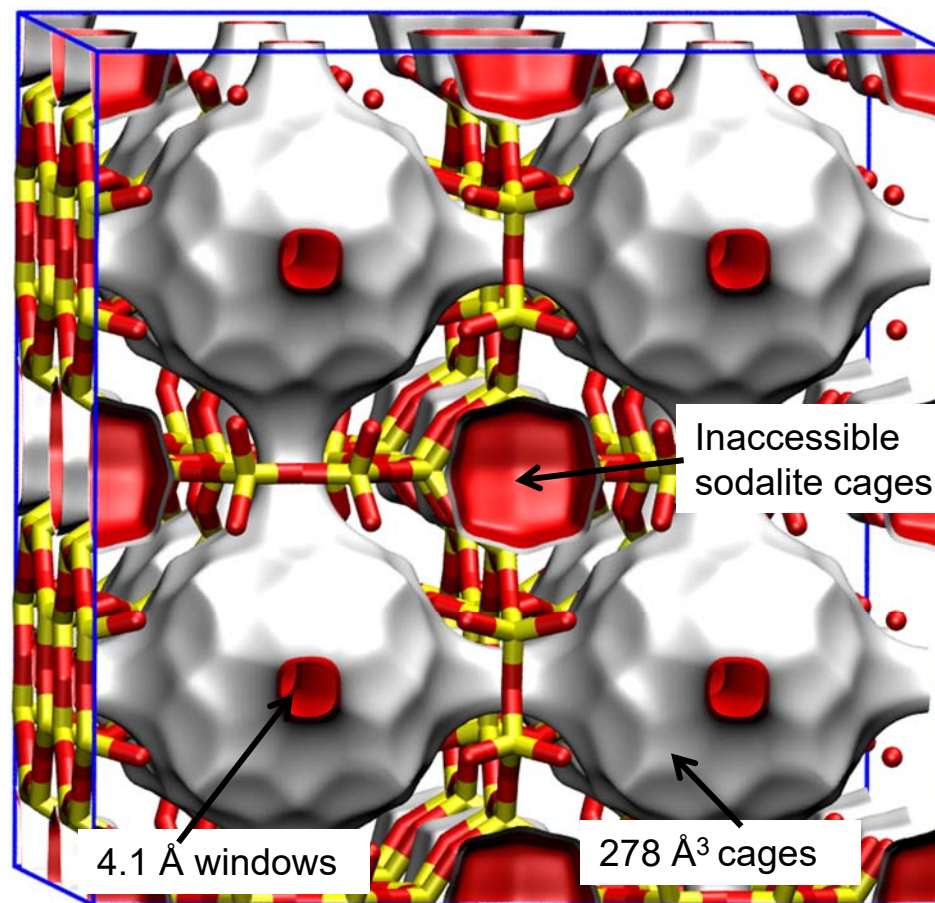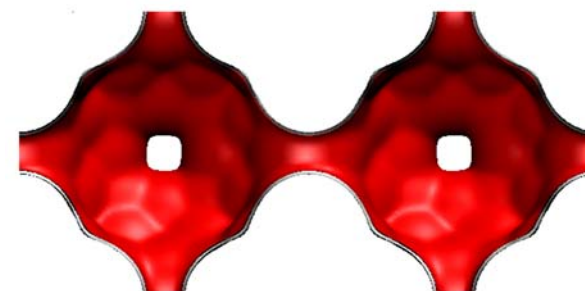
LTA-Si window and pore dimensions

8-ring window of LTA

4.47 Å

4.11 Å
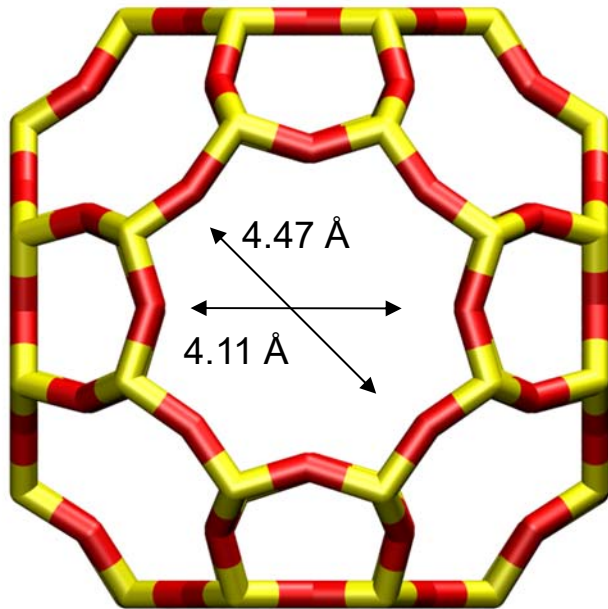
The window dimension calculated using the van der Waals diameter of framework atoms = 2.7 Å is indicated above by the arrows.

This plot of surface area versus pore dimension is determined using a combination of the DeLaunay triangulation method for pore dimension determination, and the procedure of Düren for determination of the surface area.
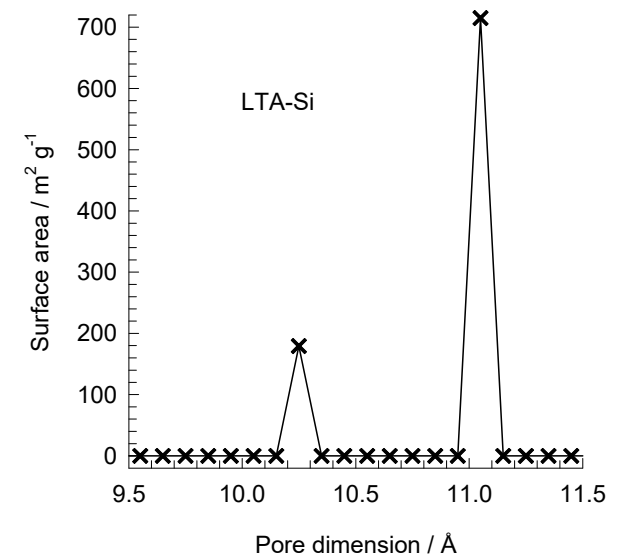
	LTA-Si
a /Å	24.61
b /Å	24.61
c /Å	24.61
Cell volume / Å^3	14905.1
conversion factor for [molec/uc] to [mol per kg Framework]	0.0867
conversion factor for [molec/uc] to [kmol/m^3]	0.2794
ρ [kg/m3]	1285.248
MW unit cell [g/mol(framework)]	11536.28
ϕ, fractional pore volume	0.399
open space / Å^3/uc	5944.4
Pore volume / cm^3/g	0.310
Surface area /m^2/g	896.0
DeLaunay diameter /Å	4.10

LTL pore landscapes
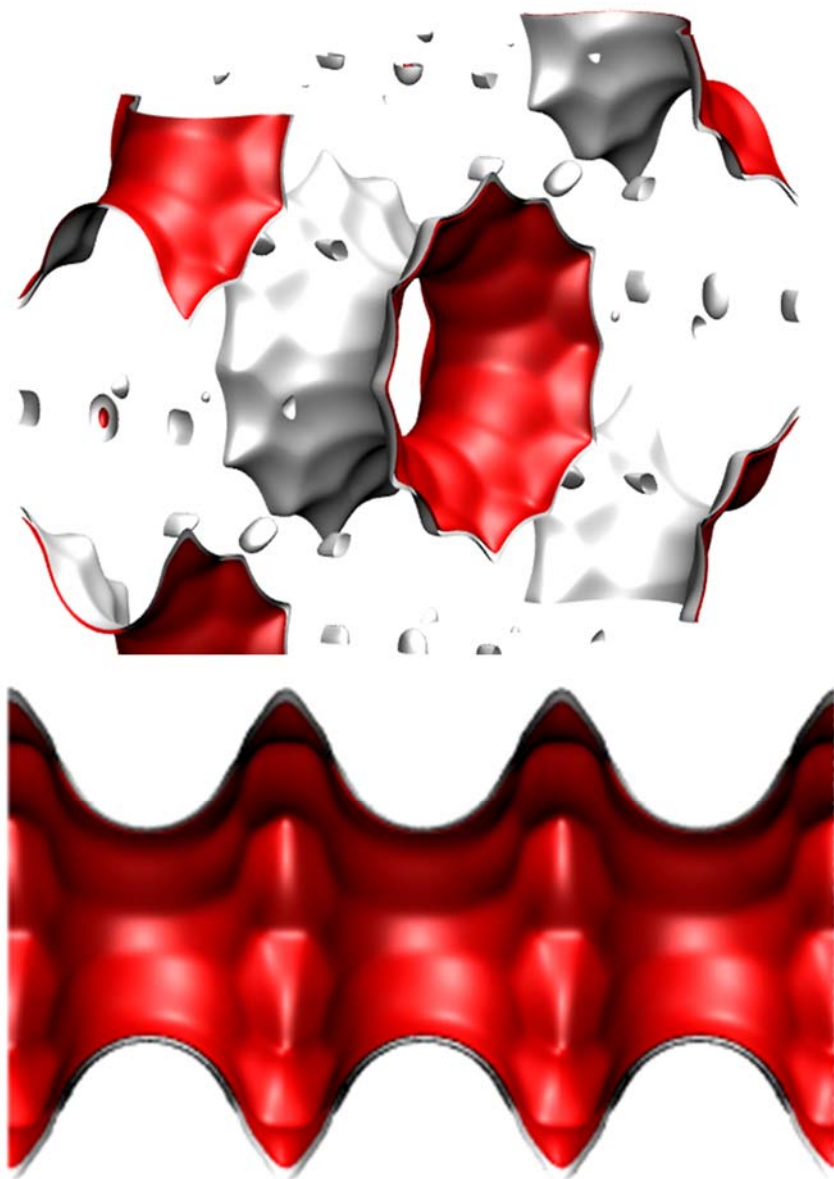
LTL pore dimensions
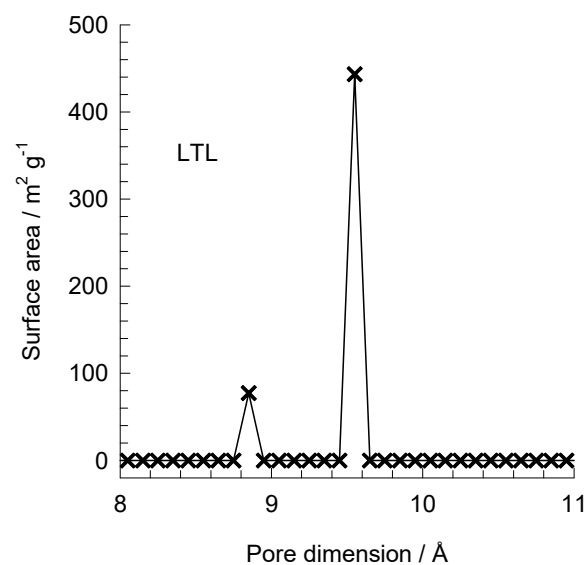
LTL

This plot of surface area versus pore dimension is determined using a combination of the DeLaunay triangulation method for pore dimension determination, and the procedure of Düren for determination of the surface area.

	LTL
a /Å	31.984
b /Å	18.466
c /Å	7.476
Cell volume / Å^3	4415.449
conversion factor for [molec/uc] to [mol per kg Framework]	0.2312
conversion factor for [molec/uc] to [kmol/m^3]	1.3597
ρ [kg/m3]	1626.965
MW unit cell [g/mol(framework)]	4326.106
ϕ, fractional pore volume	0.277
open space / Å^3/uc	1221.3
Pore volume / cm^3/g	0.170
Surface area /m^2/g	521.0
DeLaunay diameter /Å	7.47

MFI pore landscape

	MFI
a /Å	20.022
b /Å	19.899
c /Å	13.383
Cell volume / Å³	5332.025
conversion factor for [molec/uc] to [mol per kg Framework]	0.1734
conversion factor for [molec/uc] to [kmol/m³]	1.0477
ρ [kg/m3]	1796.386
MW unit cell [g/mol(framework)]	5768.141
ϕ, fractional pore volume	0.297
open space / Å³/uc	1584.9
Pore volume / cm³/g	0.165
Surface area /m²/g	487.0
DeLaunay diameter /Å	5.16
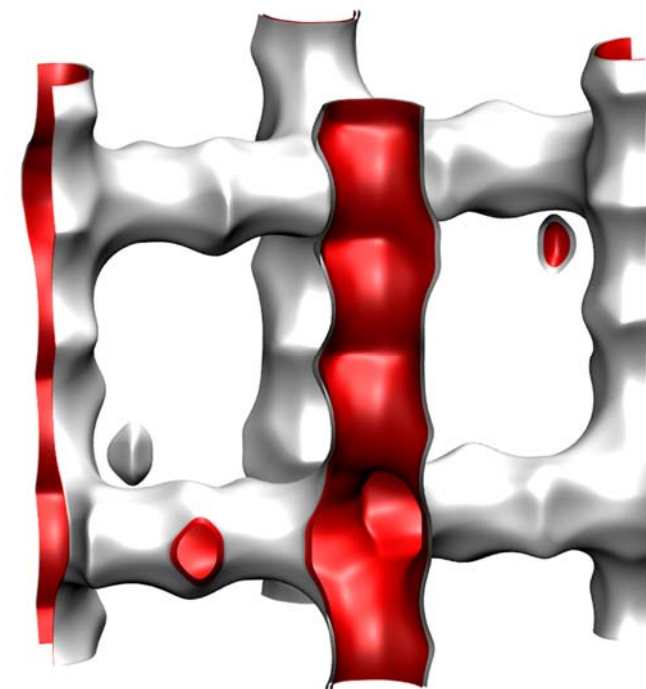
Structural information from: C. Baerlocher, L.B. McCusker,
Database of Zeolite Structures, International Zeolite Association,
http://www.iza-structure.org/databases/

MFI pore dimensions

10 ring channel of MFI viewed along [100]

5.4 Å

5.6 Å
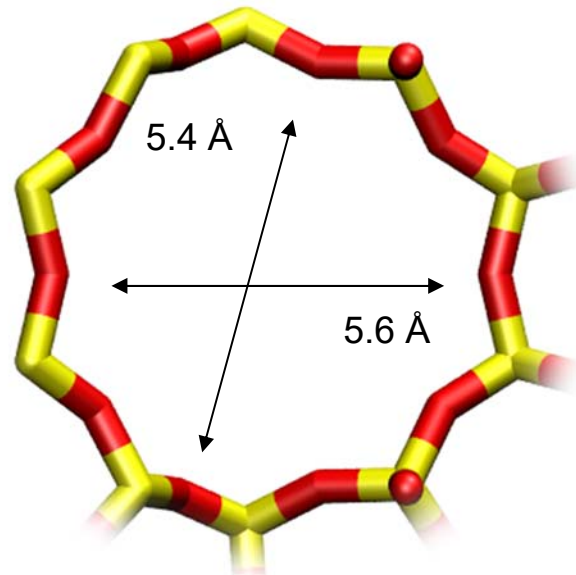
10 ring channel of MFI viewed along [010]

5.4 Å

5.5 Å

MFI

MOR point landscape
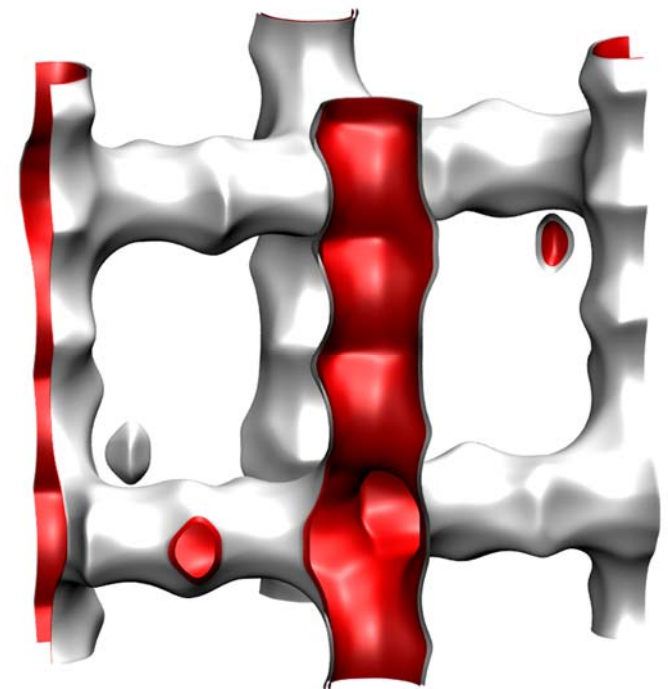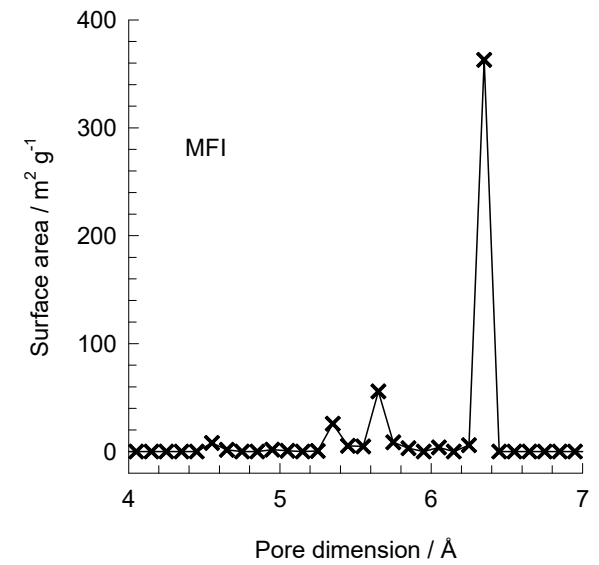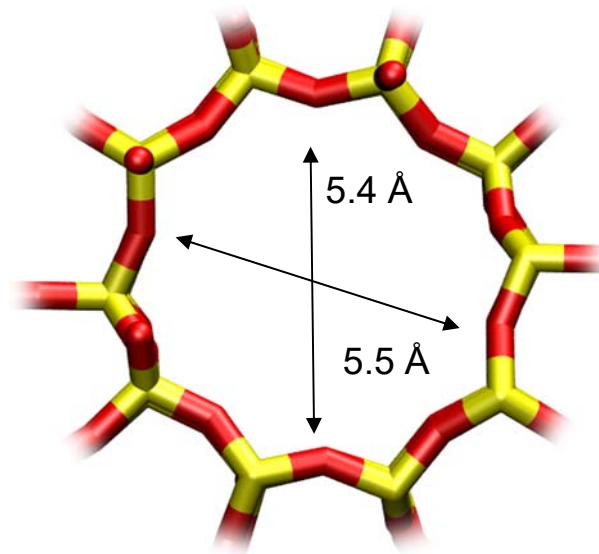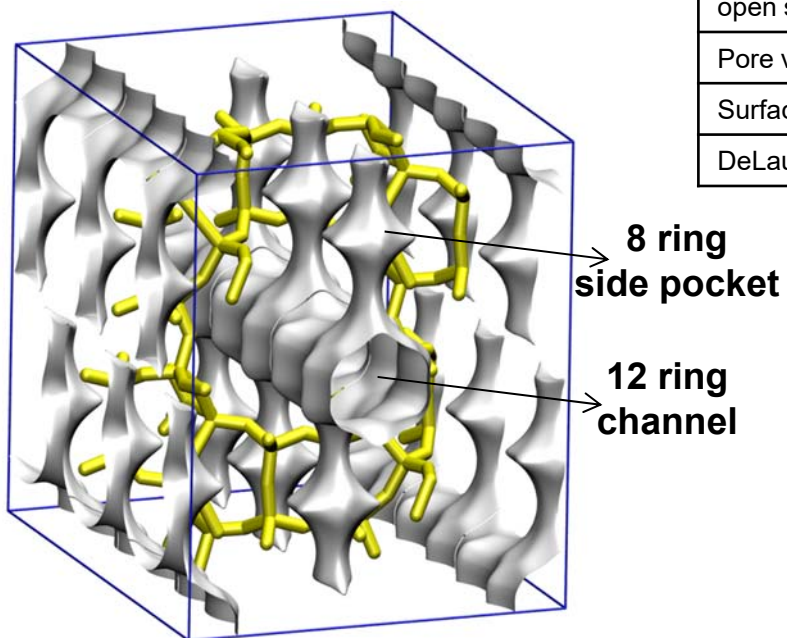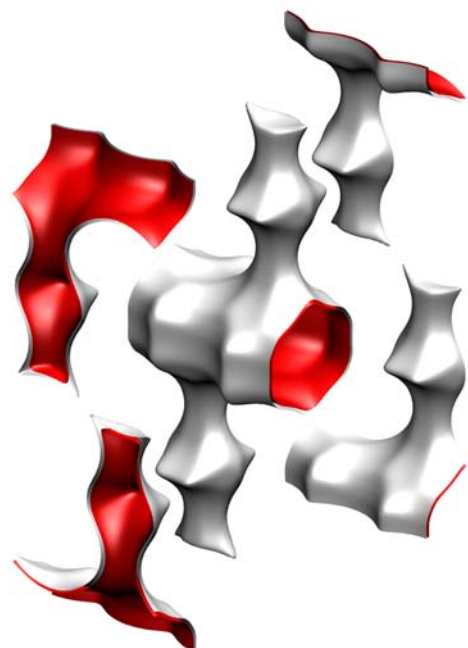
	MOR
a /Å	18.094
b /Å	20.516
c /Å	7.524
Cell volume / Å^3	2793.033
conversion factor for [molec/uc] to [mol per kg Framework]	0.3467
conversion factor for [molec/uc] to [kmol/m^3]	2.0877
ρ [kg/m3]	1714.691
MW unit cell [g/mol(framework)]	2884.07
ϕ, fractional pore volume	0.285
open space / Å^3/uc	795.4
Pore volume / cm^3/g	0.166
Surface area /m^2/g	417.0
DeLaunay diameter /Å	6.44

8 ring side pocket

12 ring channel

MOR pore dimensions
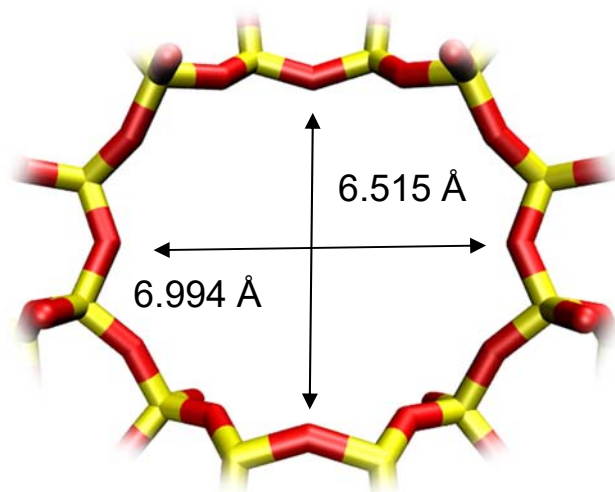
8 ring side pocket
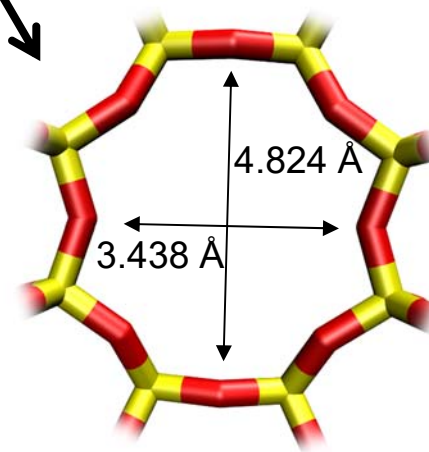
12-ring main channels

6.515 Å

6.994 Å

MOR Channel [1 0 0]

8 ring side pocket

MOR
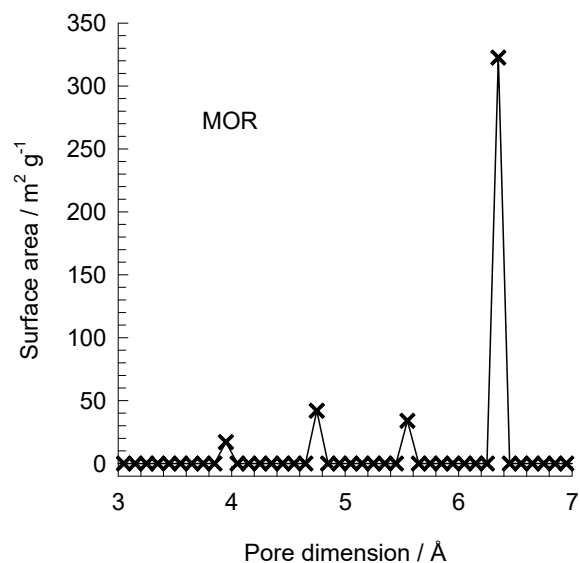
This plot of surface area versus pore dimension is determined using a combination of the DeLaunay triangulation method for pore dimension determination, and the procedure of Düren for determination of the surface area.

4.824 Å

3.438 Å

MOR [0 1 0]

MTW pore landscape

MTW has 1D, 12-ring channels
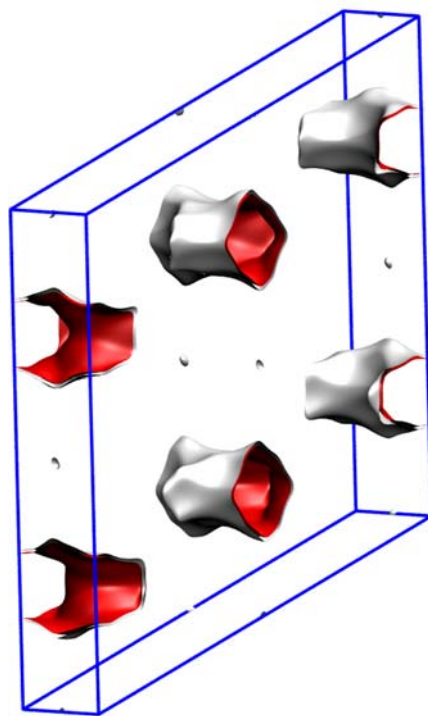
MTW pore dimensions

This plot of surface area versus pore dimension is determined using a combination of the DeLaunay triangulation method for pore dimension determination, and the procedure of Düren for determination of the surface area.
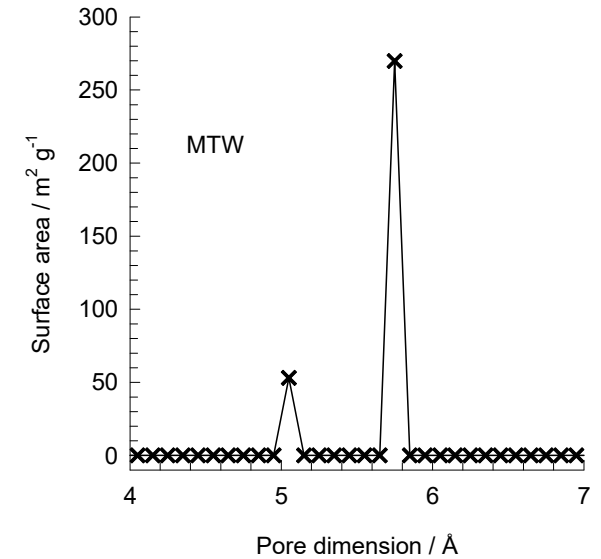
MTW has 1D, 12-ring channels

	MTW
a /Å	24.863
b /Å	5.012
c /Å	24.326
Cell volume / Å^3	2887.491
conversion factor for [molec/uc] to [mol per kg Framework]	0.2972
conversion factor for [molec/uc] to [kmol/m^3]	2.6759
ρ [kg/m3]	1935.031
MW unit cell [g/mol(framework)]	3364.749
ϕ, fractional pore volume	0.215
open space / Å^3/uc	620.6
Pore volume / cm^3/g	0.111
Surface area /m^2/g	323.0
DeLaunay diameter /Å	5.69

TON pore landscape

10-ring channel of TON

TON pore dimensions

This plot of surface area versus pore dimension is determined using a combination of the DeLaunay triangulation method for pore dimension determination, and the procedure of Düren for determination of the surface area.

10-ring channel of TON

5.586 Å

5.323 Å
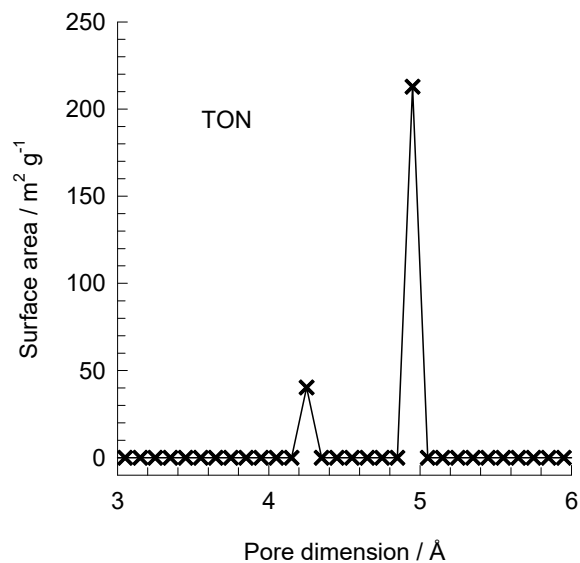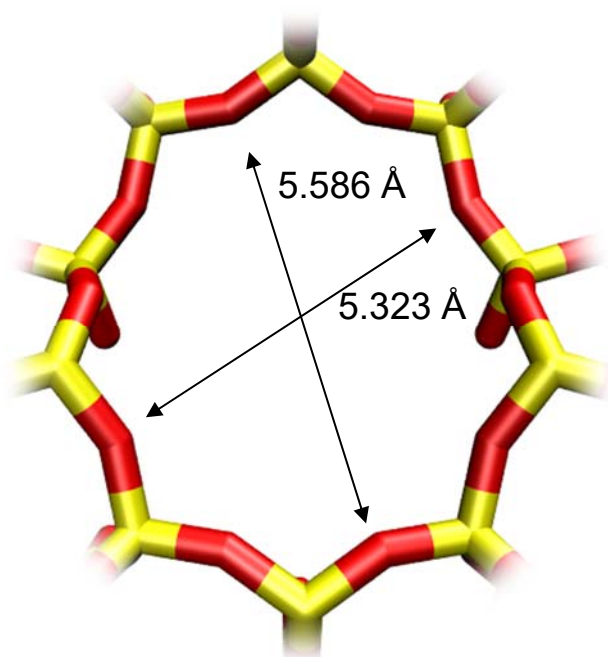
	TON
a /Å	13.859
b /Å	17.42
c /Å	5.038
Cell volume / Å^3	1216.293
conversion factor for [molec/uc] to [mol per kg Framework]	0.6935
conversion factor for [molec/uc] to [kmol/m^3]	7.1763
ρ [kg/m3]	1968.764
MW unit cell [g/mol(framework)]	1442.035
ϕ, fractional pore volume	0.190
open space / Å^3/uc	231.4
Pore volume / cm^3/g	0.097
Surface area /m^2/g	253.0
DeLaunay diameter /Å	4.88

Thermodynamic Factor: unary adsorption

(a)

(b)
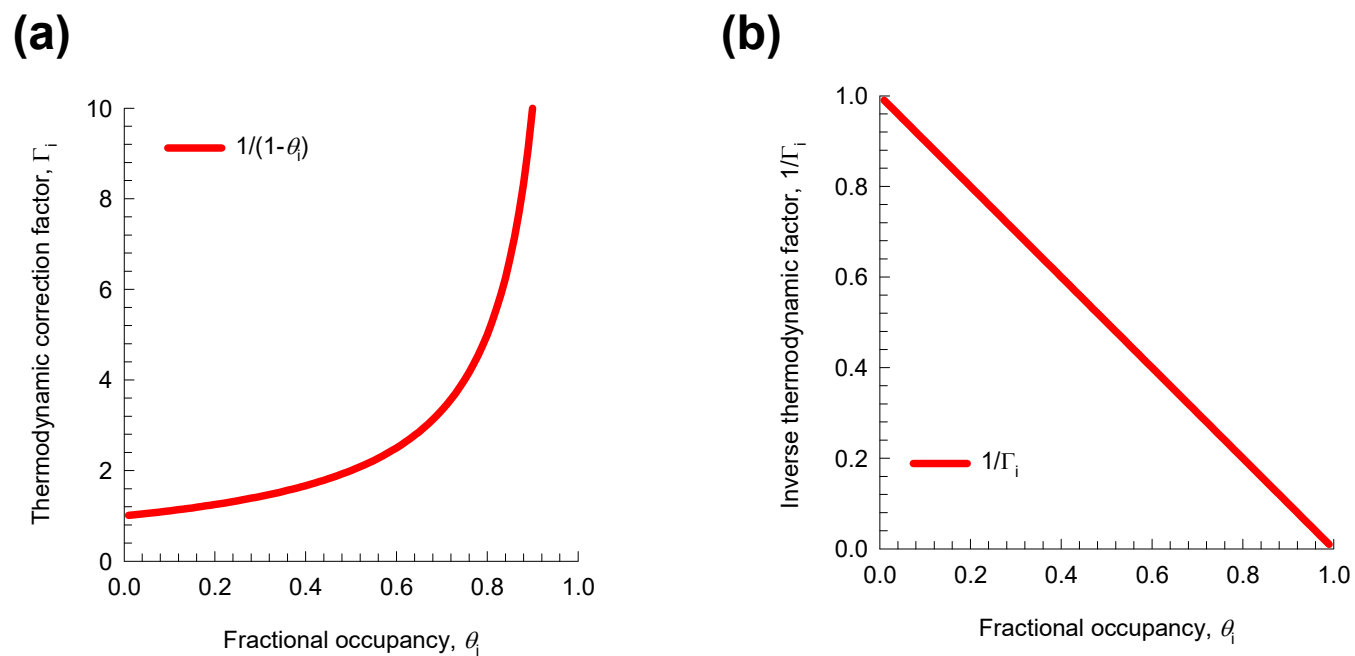
Unary diffusivities in MFI zeolite:
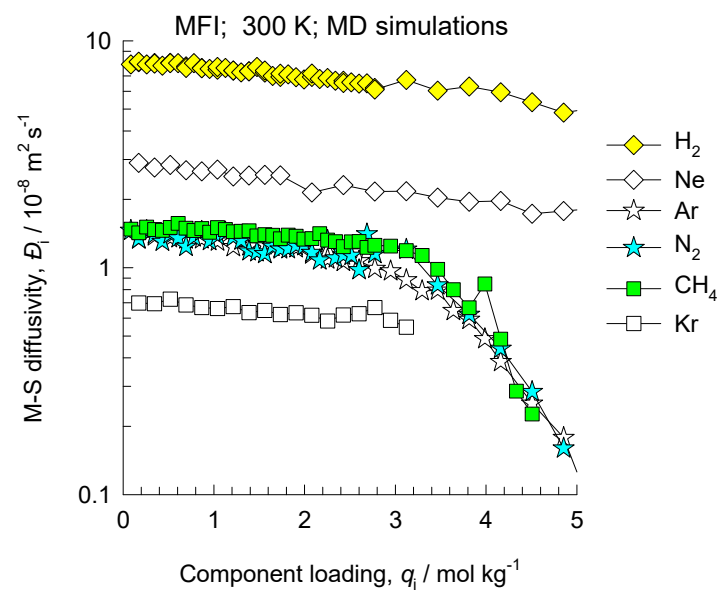
Weak confinement

Unary diffusivities in MFI zeolite: strong confinement
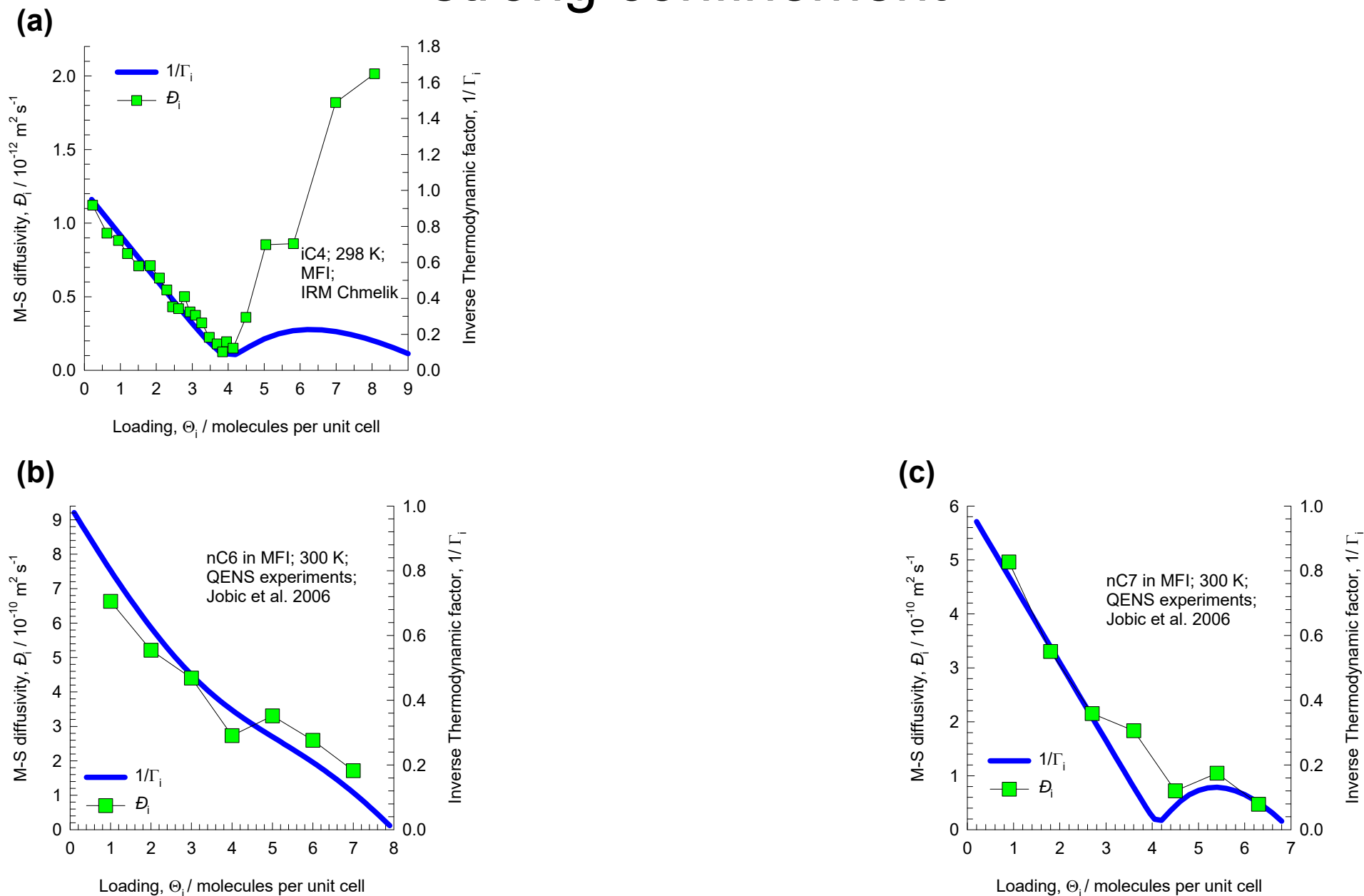
Unary M-S diffusivities in MOR zeolite

(a)

MOR; 433 K

pure nC6

Maxwell-Stefan diffusivity, $Đ_i$ / 10^{-8} m^2 s^{-1}

Loading, Θ_i / molecules per unit cell

(b)

MOR; 433 K

pure 2MP
22DMB

Maxwell-Stefan diffusivity, $Đ_i$ / 10^{-8} m^2 s^{-1}

Loading, Θ_i / molecules per unit cell

M-S diffusivities in MOR zeolite:

Binary Mixtures

(a) nC6/2MP mixture; MOR; 433 K. Maxwell-Stefan diffusivity, $Ð_1$ / 10^{-8} m^2 s^{-1} vs. Fractional occupancy in mixture, $\theta = \theta_1 + \theta_2$. pure nC6; 50-50 mix.

(b) nC6/2MP mixture; MOR; 433 K. Maxwell-Stefan diffusivity, $Ð_2$ / 10^{-8} m^2 s^{-1} vs. Fractional occupancy in mixture, $\theta = \theta_1 + \theta_2$. pure 2MP; 50-50 mix.
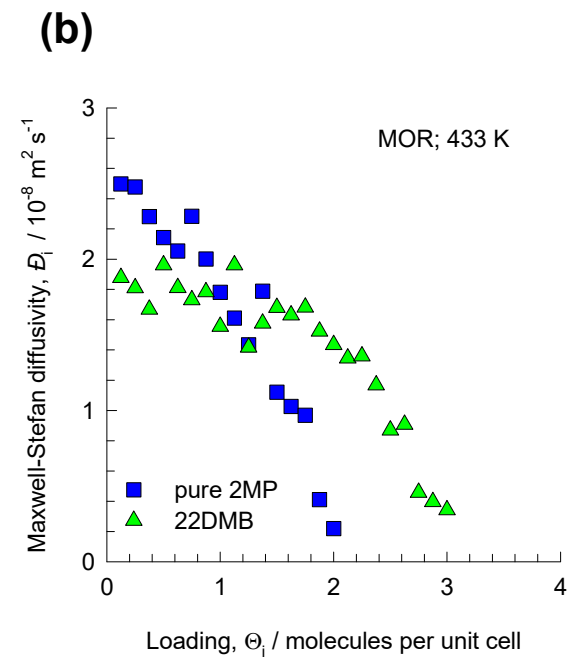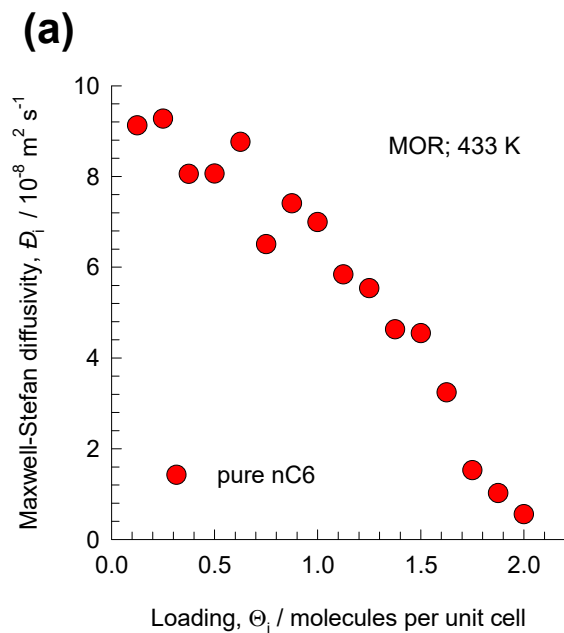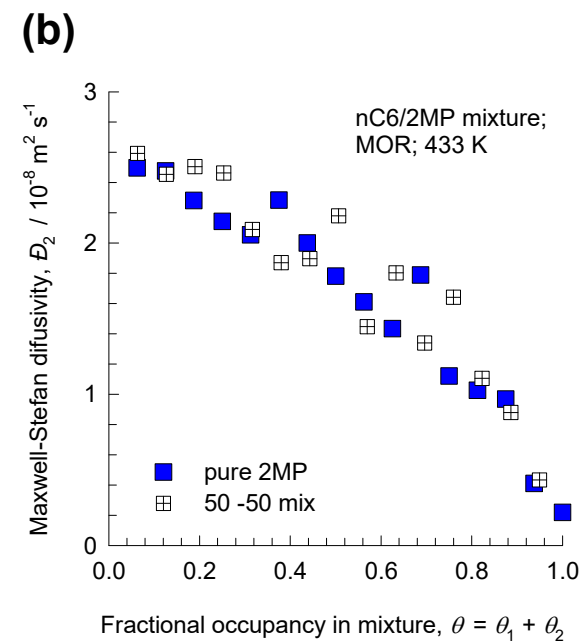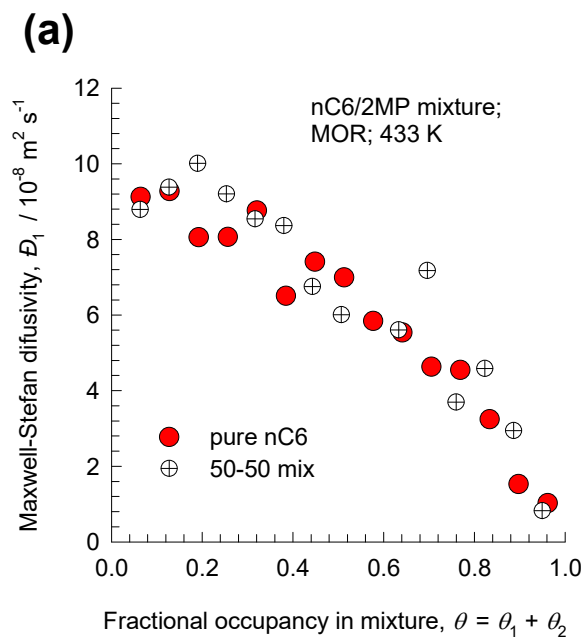
Effectiveness diffusivity in mixture

(a)

ethene

EtBz

Bz

(b)

ethene/benzene/ethylbenze
mixture; H-ZSM-5 catalyst; 653K

Effective diffusivity of ethene / 10^{-12} m^2 s^{-1}

Total loading of mixture / molecules per unit cell

(a) pure component isotherms; $T = 362$ K

Component loading / molecules per unit cell — Pressure / Pa

nC6
3MP
22DMB

— DSL
● nC6, CBMC
■ 3MP, CBMC
▲ 22DMB, CBMC

(b) equimolar mixture nC6-3MP-22DMB; $T = 362$ K

Component loading / molecules per unit cell — Total system pressure / Pa

● nC6
■ 3MP
▲ 22DMB
— IAST

(c) Figure S30

Fractional vacancy $\theta_V = 1 - \theta_1 - \theta_2 - \theta_3$ — Total system pressure / Pa

equimolar mixture nC6-3MP-22DMB; $T = 362$ K

— IAST
● CBMC

Adsorption of hexane isomers in MFI zeolite: CBMC vs IAST

nC6   3MP   22DMB

The linear molecule nC6 can locate along the straight and zig-zag channels.

(a) Unary fits
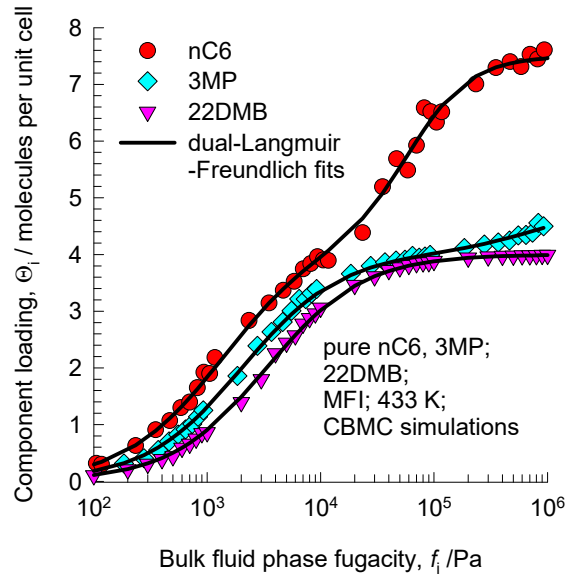
(b) CBMC mixture vs IAST

(c) CBMC mixture

Figure S31

nC6-3MP-22DMB mixture; $f_1=f_2=f_3$; MFI; 433 K; CBMC simulations

pure nC6, 3MP; 22DMB; MFI; 433 K; CBMC simulations

- nC6
- 3MP
- 22DMB
- dual-Langmuir-Freundlich fits

- nC6
- 3MP
- 22DMB
- IAST

- nC6
- 3MP
- 22DMB

Bulk fluid phase fugacity, f_i /Pa

Total fluid phase fugacity, f_t/ Pa

Total mixture loading, Θ_t / molecules per unit cell

Component loading, Θ_i / molecules per unit cell
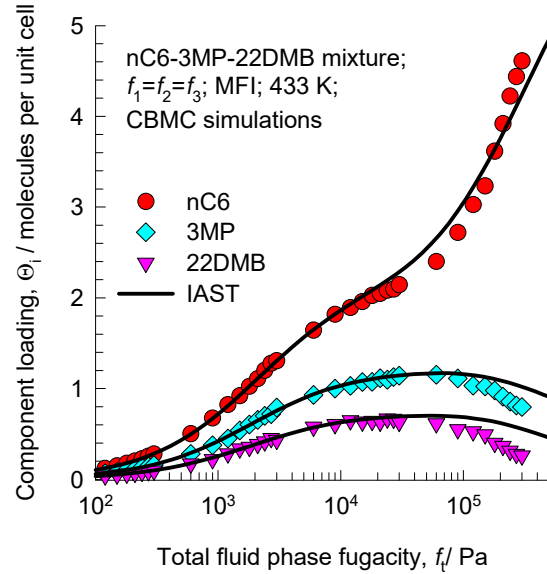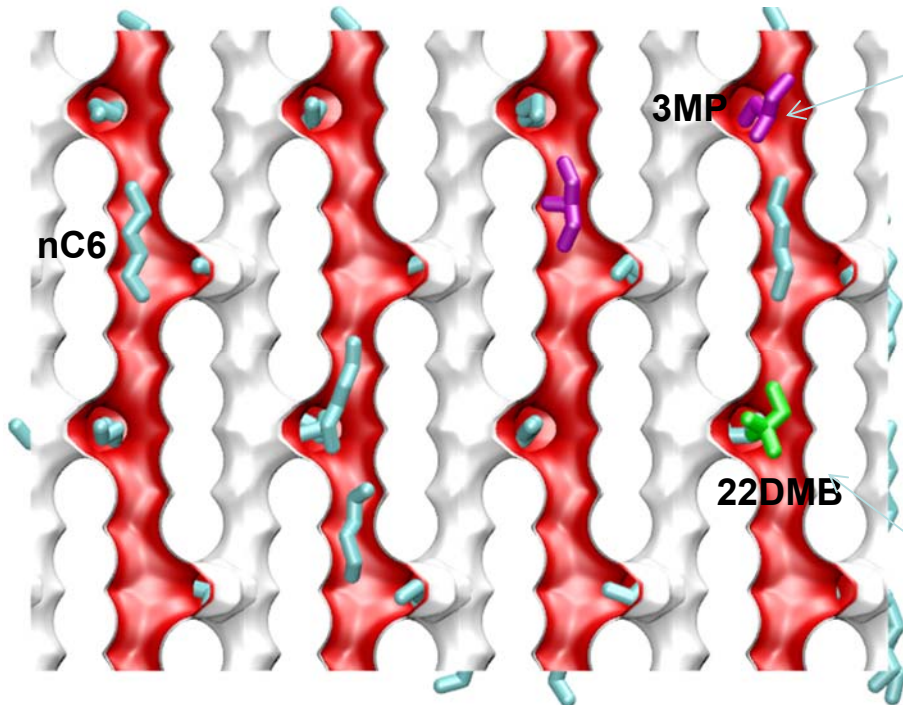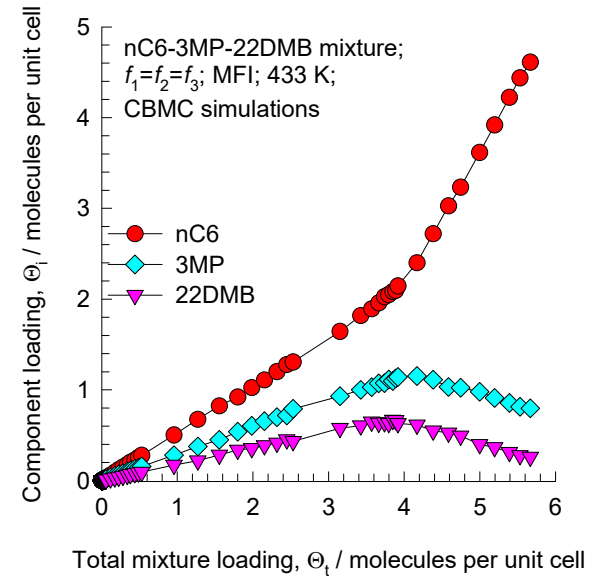
3MP prefers to locate at the intersections

3MP

nC6

22DMB

The di-branched 22DMB can only locate at the intersections

Adsorption of hexane isomers in MFI zeolite: CBMC vs IAST

Adsorption of hexane isomers in MFI zeolite: CBMC vs IAST

(a) Unary fits
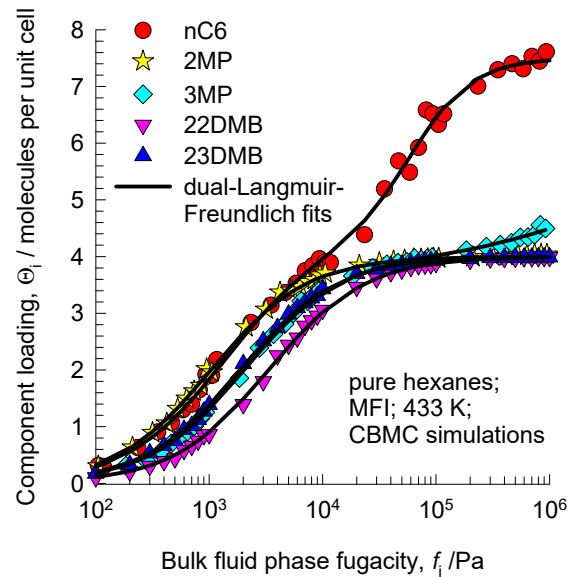
(b) CBMC mixture

(c) CBMC mixture vs IAST
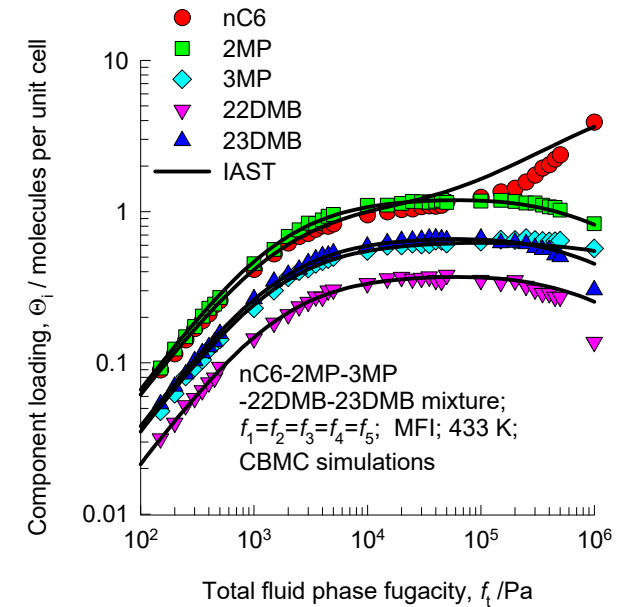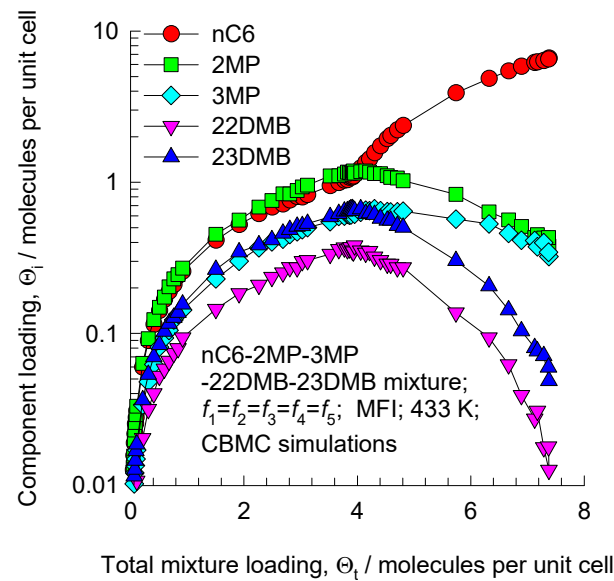
Adsorption of pentane isomers in MFI zeolite: CBMC vs IAST

(a) Unary fits
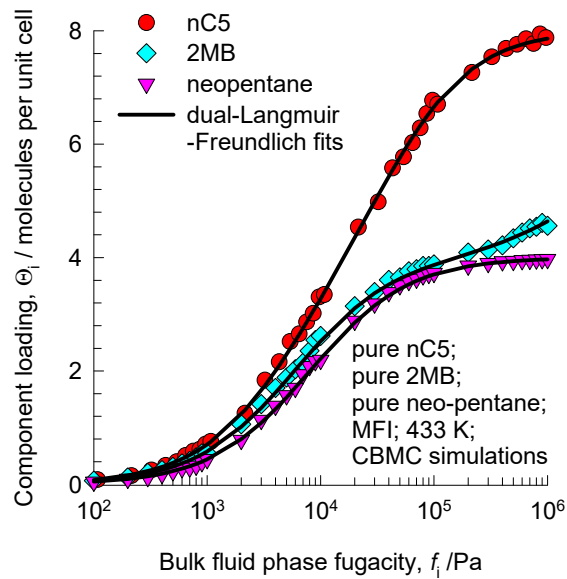
(b) CBMC mixture vs IAST
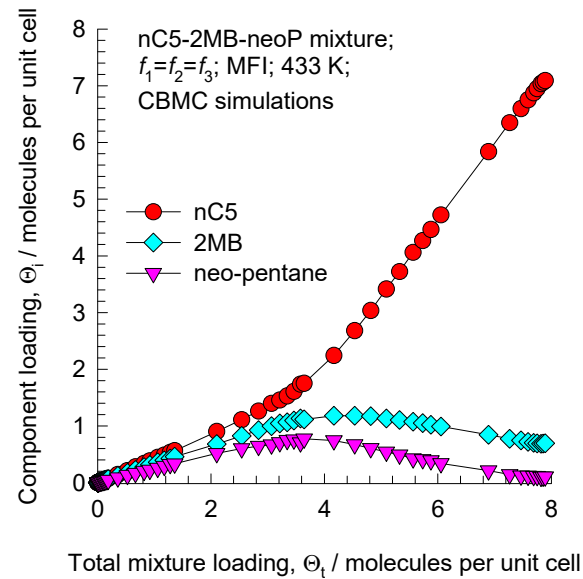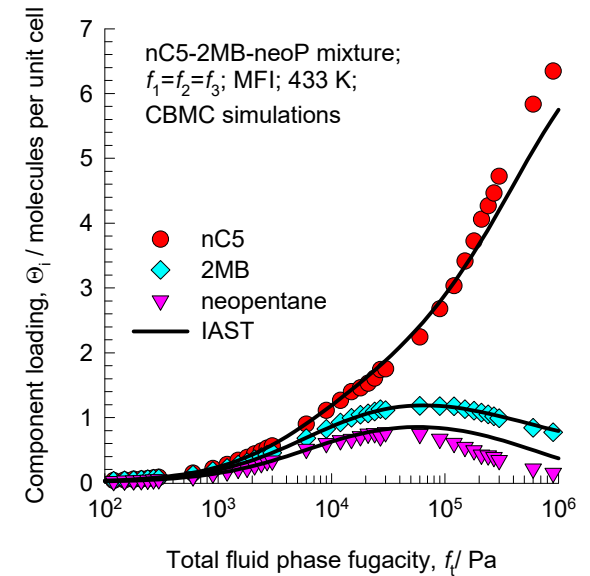
Adsorption of hexane isomers in MOR zeolite
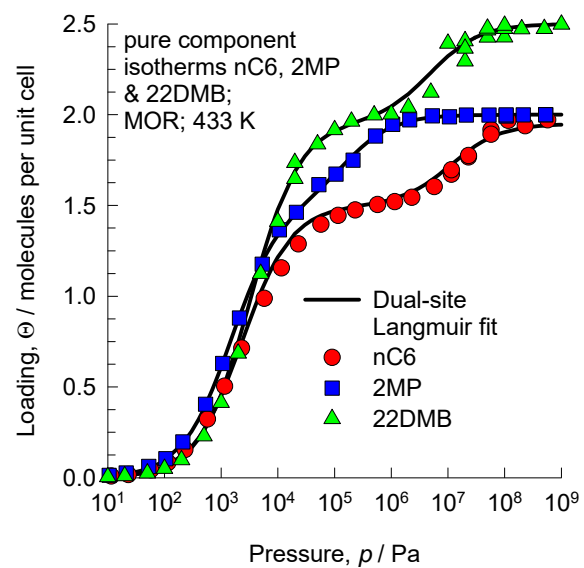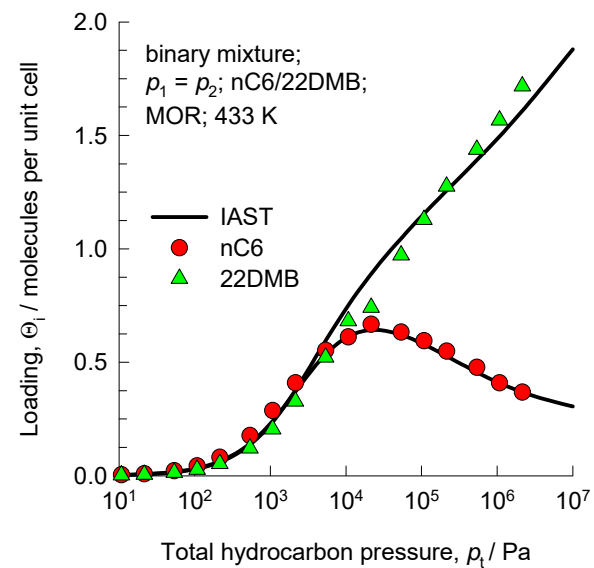
Packing of hexane isomers in MOR channel

(a) 12-ring channel of MOR, 8 unit cells long; [100] view
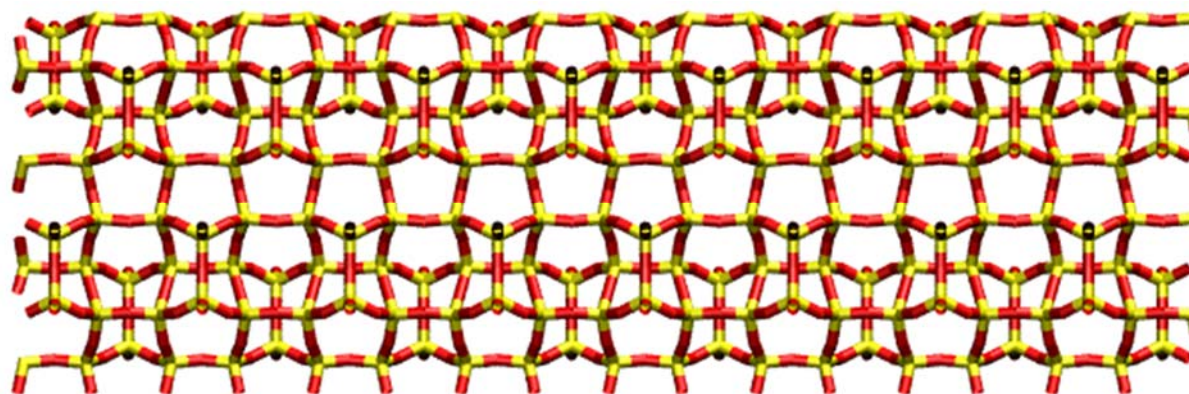
(b) nC6

(c) 2MP

(d) 22DMB

Discretization strategies
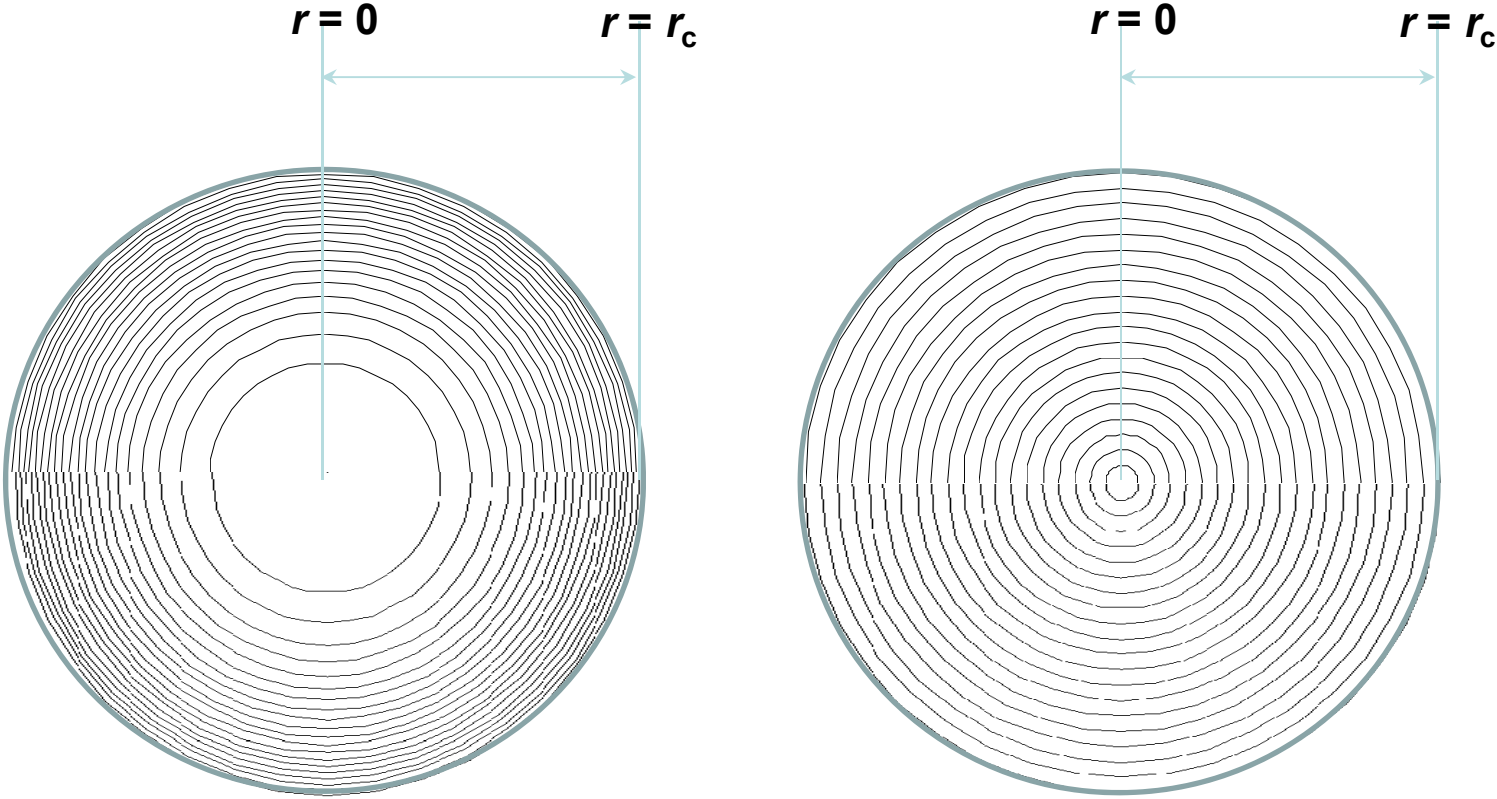
(a) Equi-volume slices   **(b) Equi-distant slices**

Figure S37

Fixed bed reactor with step input
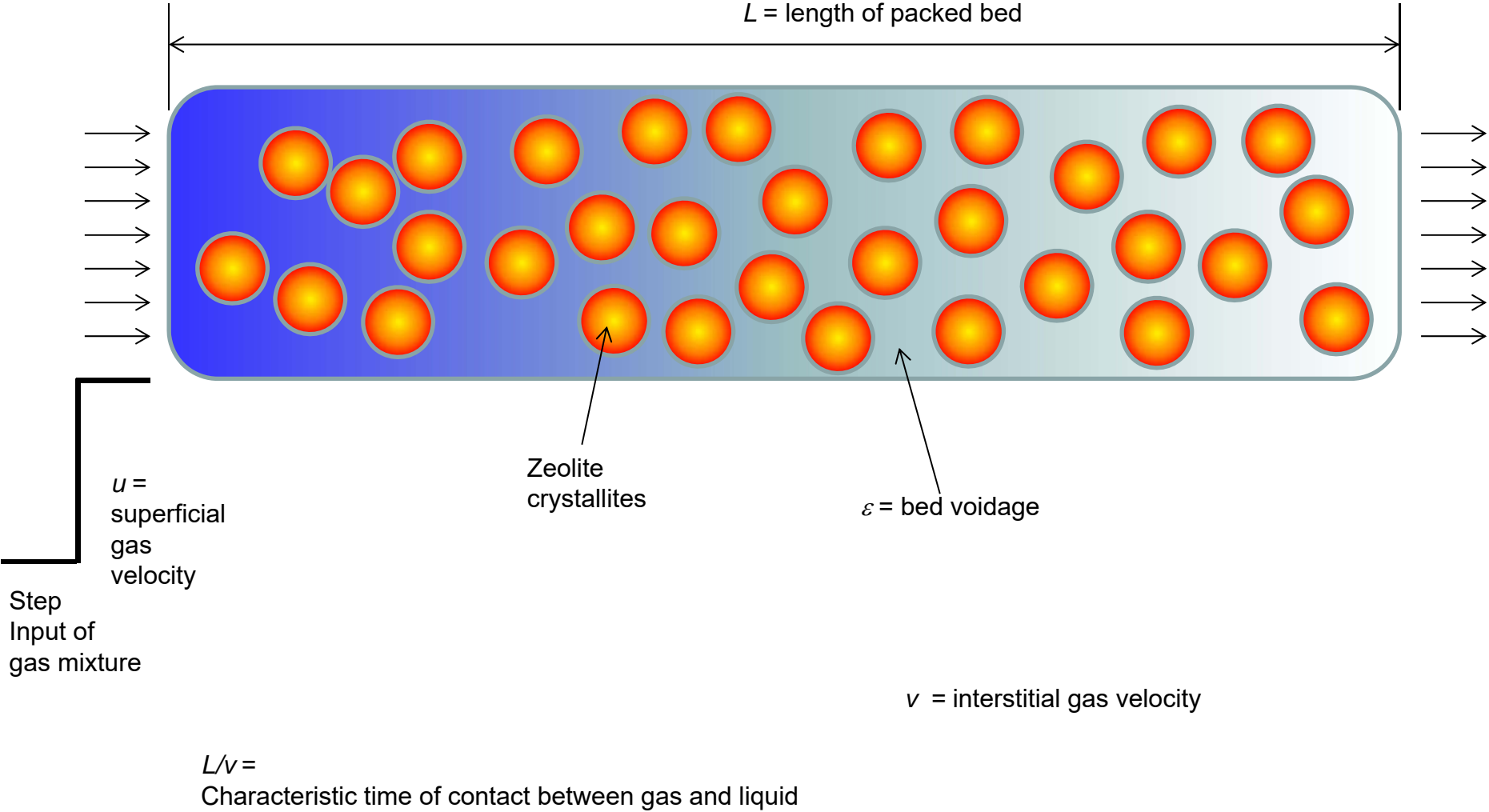
Fixed bed breakthrough model

Component balance

$$\frac{1}{RT}\frac{\partial p_i(t,z)}{\partial t} = -\frac{1}{RT}\frac{\partial(v(t,z)p_i(t,z))}{\partial z} - \frac{(1-\varepsilon)}{\varepsilon}\frac{3}{r_c}\left(N_i\big|_{r=r_c}\right); \quad i=1,2,...n$$

Molar flux at catalyst surface

L = length of packed bed

100-200 slices
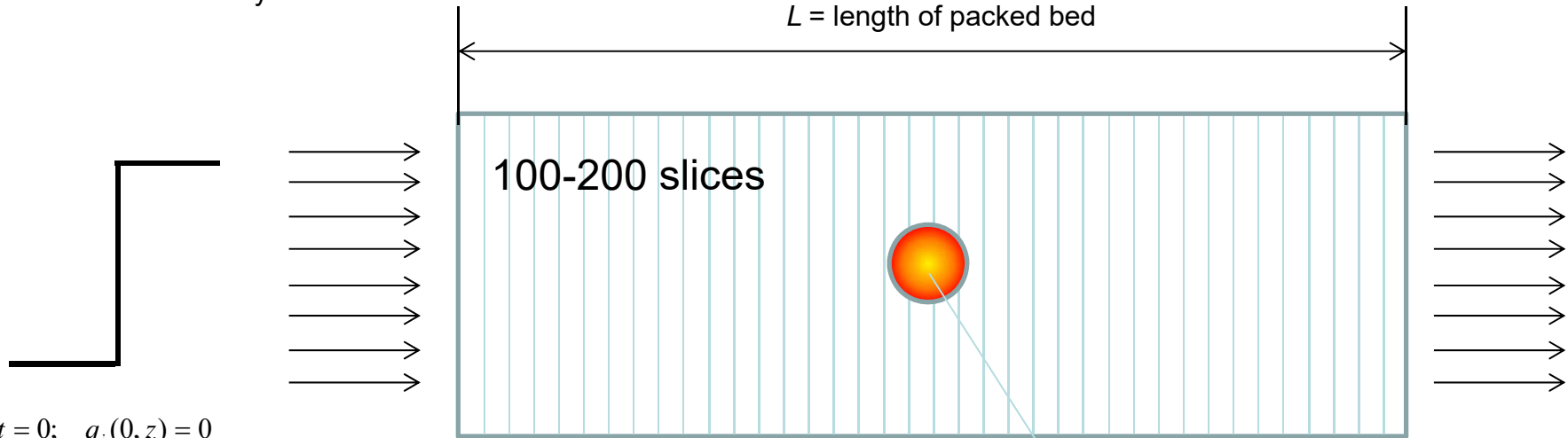
$t=0; \quad q_i(0,z)=0$

$t \geq 0; \quad p_i(0,t)=p_{i0}; \quad u(0,t)=u_0$

Uptake within crystal

$$\rho\frac{\partial q_i(r,t)}{\partial t} = -\frac{1}{r^2}\frac{\partial}{\partial r}\left(r^2 N_i\right) + \rho v_i Rate_{kg}$$

Equi-volume grid within crystal
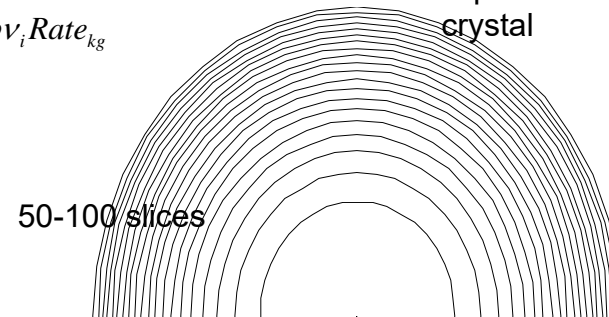
Maxwell-Stefan equations

$$-\rho\frac{q_i}{RT}\nabla\mu_i = \sum_{\substack{j=1 \\ j\neq i}}^{n}\frac{x_j N_i - x_i N_j}{D_{ij}} + \frac{N_i}{D_i}; \quad i=1,2,..n$$

50-100 slices

Figure S39

Fixed bed reactor with pulse input

Pulse Input of gas mixture

t_0
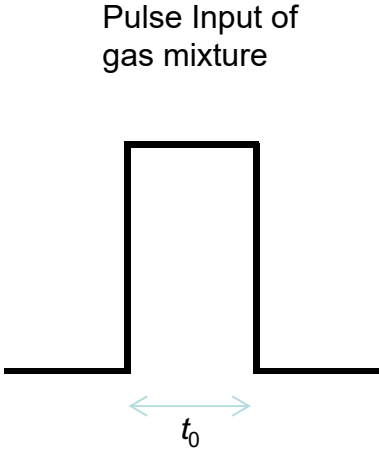
$t = 0; \quad q_i(0, z) = 0$

$0 \leq t \leq t_0; \quad p_i(0, t) = p_{i0}; \quad u(0, t) = u_0$

L = length of packed bed

Zeolite crystallites

ε = bed voidage
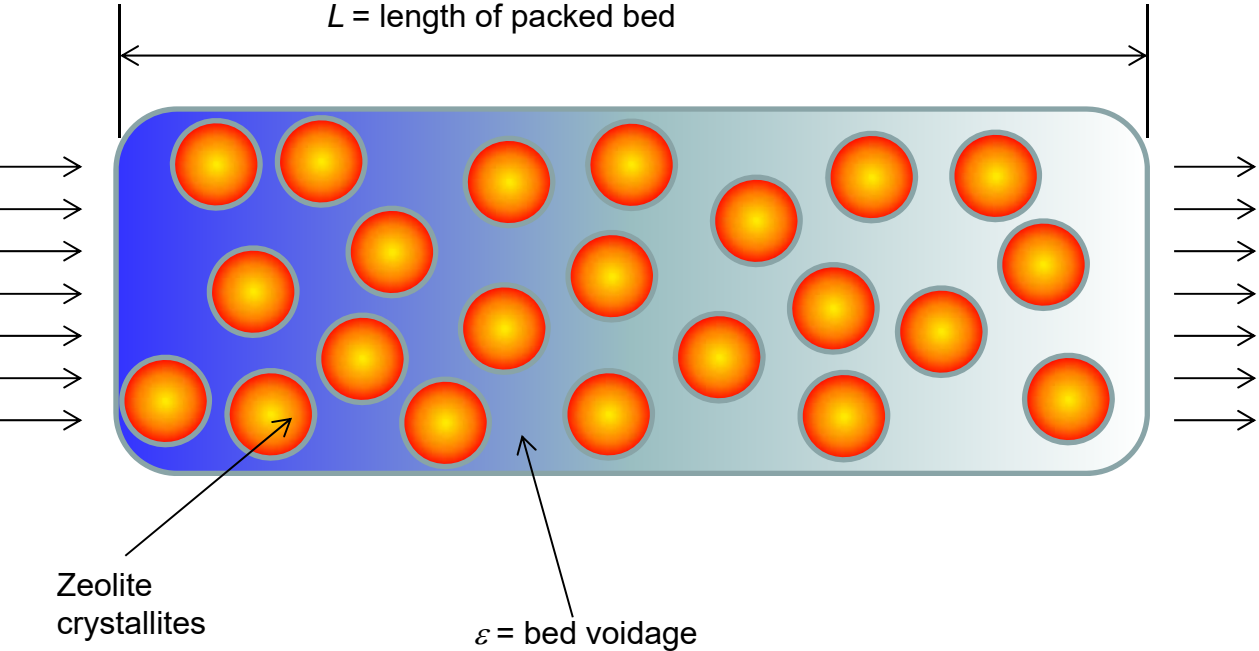
v = interstitial gas velocity

Effectiveness factor for alkane isomerization in MFI catalyst

$$2MP(1) \rightleftarrows 22DMB(2)$$

(a) Effectiveness factor vs ϕ

(b) Effectiveness factor vs $\theta_{1s}+\theta_{2s}$

MFI catalyst; 473 K;
$k_1/k_2 = 2$;
$Đ_1(0)/Đ_2(0)=80$;
$p_1 = p_2 = 10$ kPa;

Fick model,
with $\Gamma_{ij}=\delta_{ij}$

M-S model:
weak confinement

M-S model:
Strong confinement

Effectiveness factor, η

Classic Thiele modulus, ϕ

MFI catalyst; 473 K;
$k_1= 0.0011$ s^{-1}; $k_1/k_2 = 2$;
$Đ_1(0)/Đ_2(0)=80$; $\phi = 1.0011$; $p_1 = p_2$

Fick model,
with $\Gamma_{ij}=\delta_{ij}$

M-S model:
weak confinement

M-S model:
Strong confinement
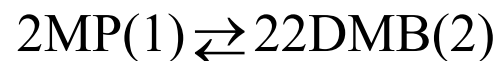
Effectiveness factor, η
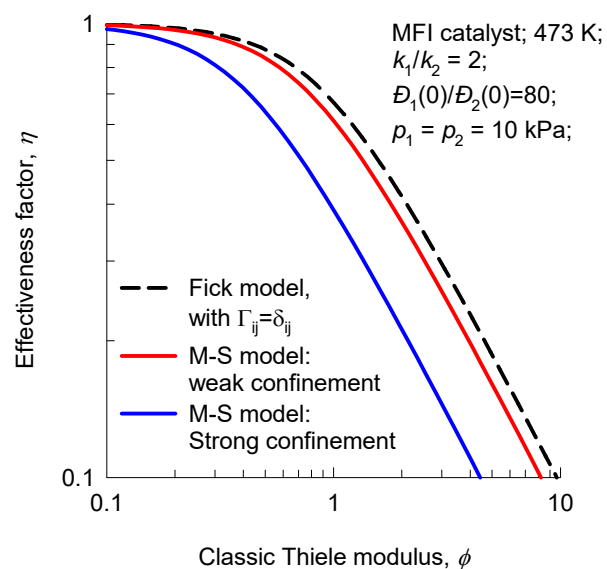
Fractional occupancy, $\theta_{1s}+\theta_{2s}$
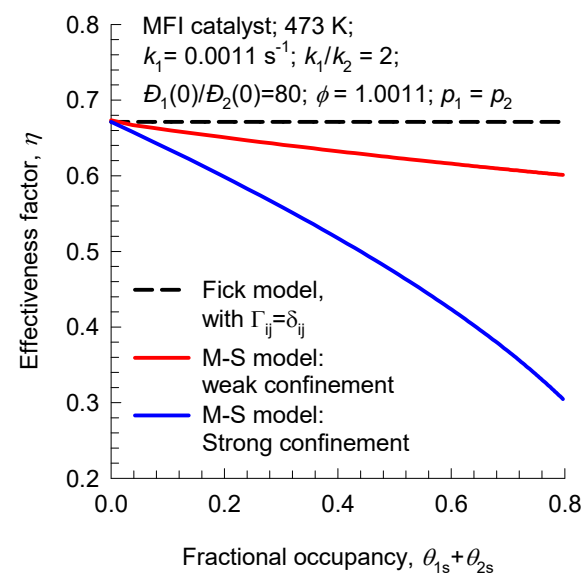
Effectiveness factor for xylene isomerization in MFI catalyst

$$o - xylene(1) \rightleftarrows p - xylene(2)$$

(a) Effectiveness factor vs ϕ

MFI catalyst; 433 K;
$k_1/k_2 = 2$;
$Đ_2(0)/Đ_1(0)=100$;
$p_1 = p_2 = 1$ MPa

Effectiveness factor, η

- – – Fick model: with $\Gamma_{ij}=\delta_{ij}$
- —— M-S model: weak confinement
- —— M-S model: Strong confinement

Classic Thiele modulus, ϕ

(b) Effectiveness factor vs $\theta_{1s}+\theta_{2s}$

MFI catalyst; 433 K;
$k_1/k_2 = 2$;
$Đ_2(0)/Đ_1(0)=100$;
$p_1 = p_2 = 1$ MPa

Effectiveness factor, η

- – – Fick model: with $\Gamma_{ij}=\delta_{ij}$
- —— M-S model: weak confinement
- —— M-S model: Strong confinement

Classic Thiele modulus, ϕ
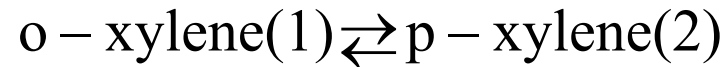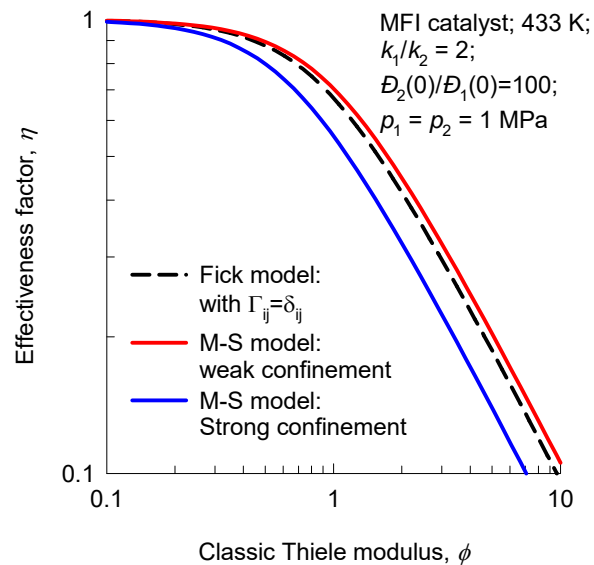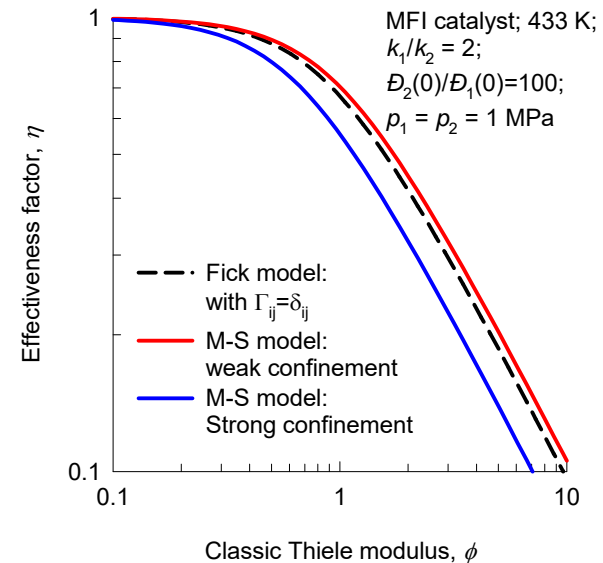
Transient 2MP/22DMB diffusion/reaction in MFI catalyst
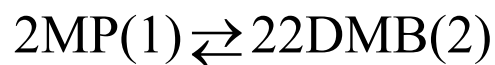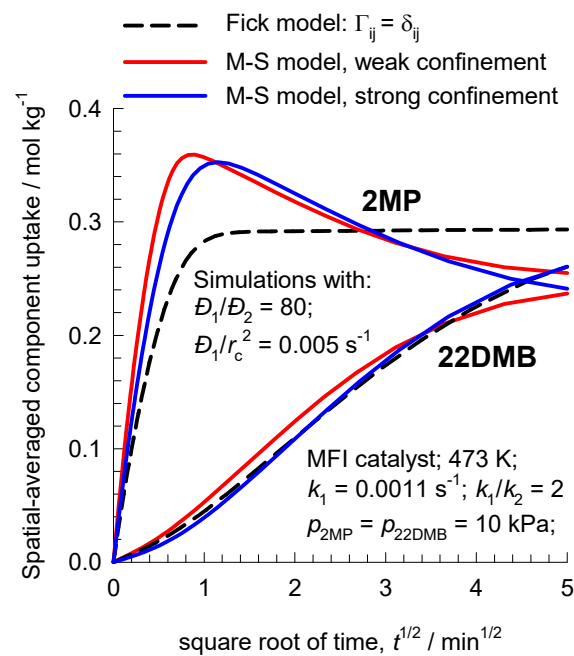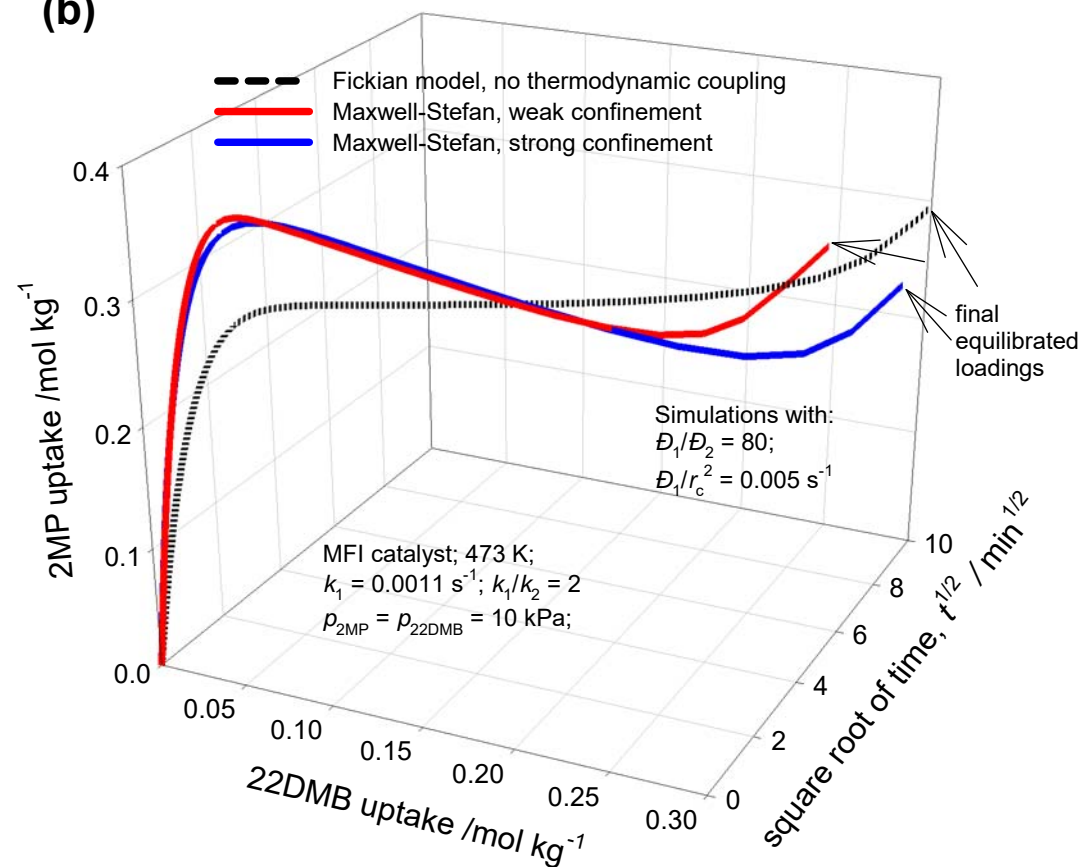
$$2MP(1) \rightleftharpoons 22DMB(2)$$

(a)

(b)

Equilibration Trajectories in Occupancy Space

$$2MP(1) \rightleftarrows 22DMB(2)$$

22DMB

Legend:
- – – – Fickian model, no thermodynamic coupling
- —— Maxwell-Stefan, strong confinement
- —— Maxwell-Stefan, weak confinement
- ······ No diffusion limitation

MFI catalyst; 473 K;
$k_1 = 0.0011$ s^{-1}; $k_1/k_2 = 2$
$p_1 = p_2 = 10$ kPa

Simulations with:
$Đ_1/Đ_2 = 80$;
$Đ_1/r_c^2 = 0.005$ s^{-1}

final equilibrated occupancies

initial occupancy

MFI zeolite vacancy

2MP
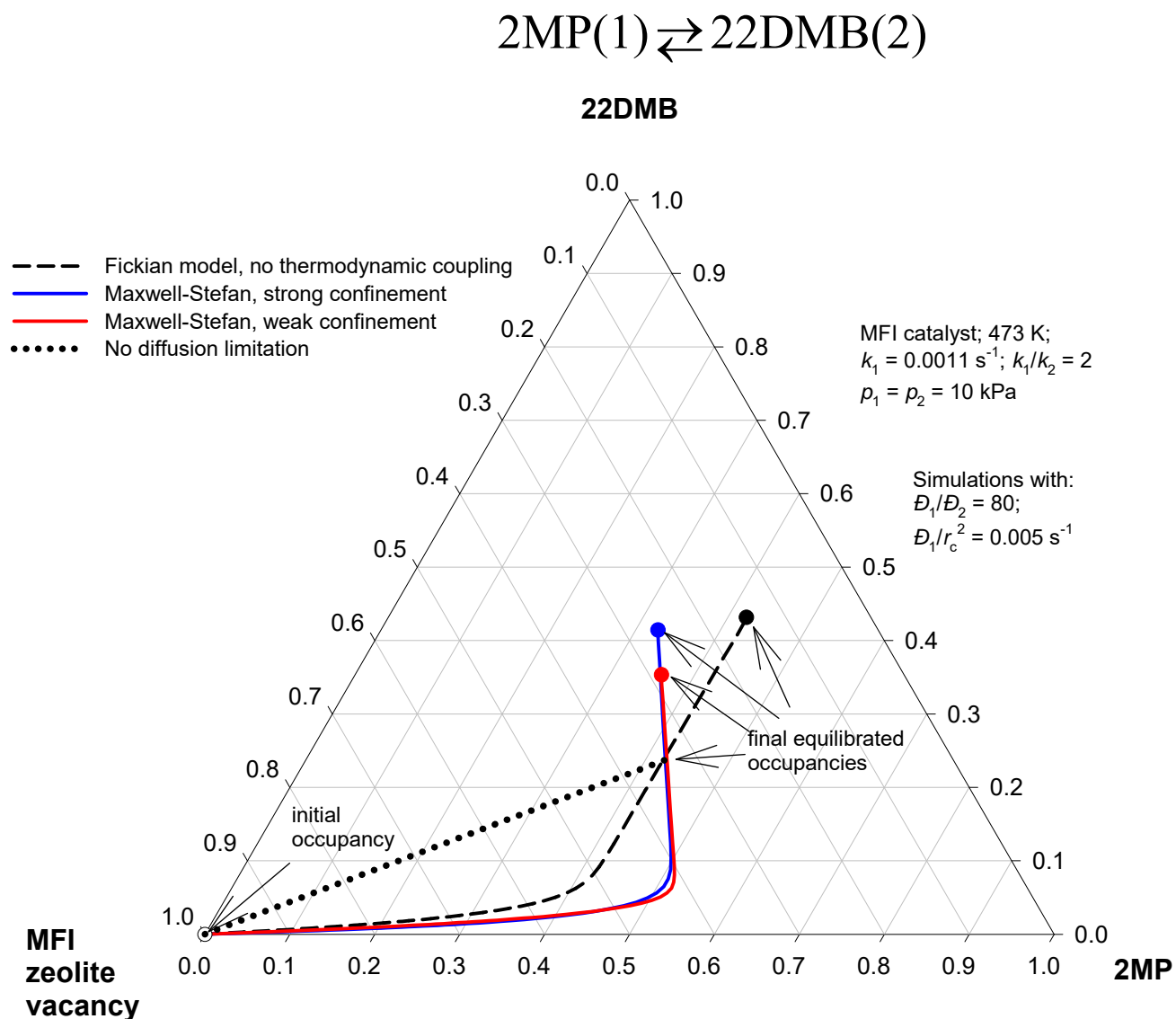
Equilibration Trajectories in Occupancy Space
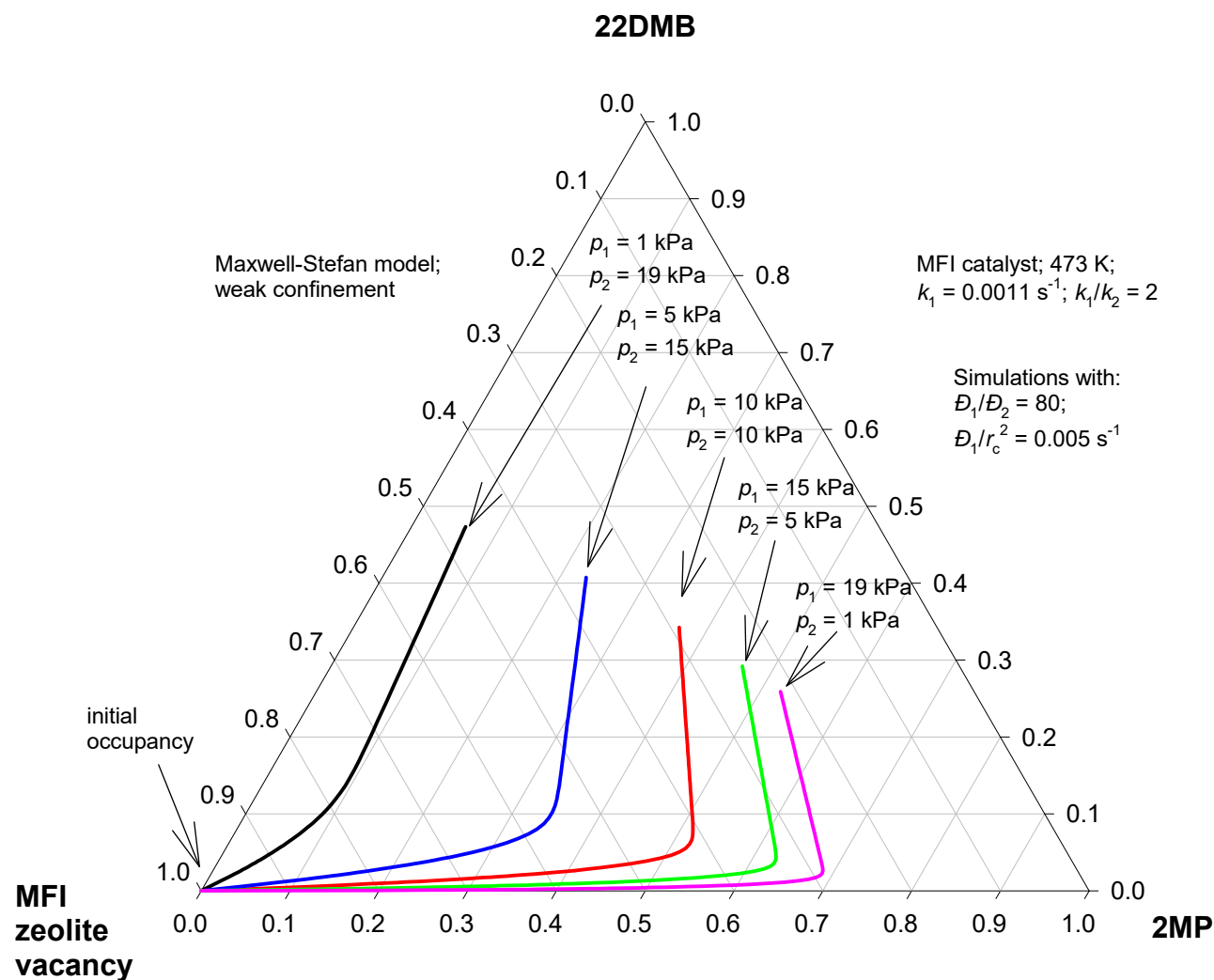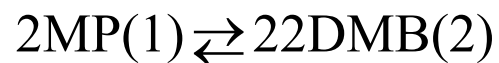
Radial variation of component loadings

$$2MP(1) \rightleftarrows 22DMB(2)$$
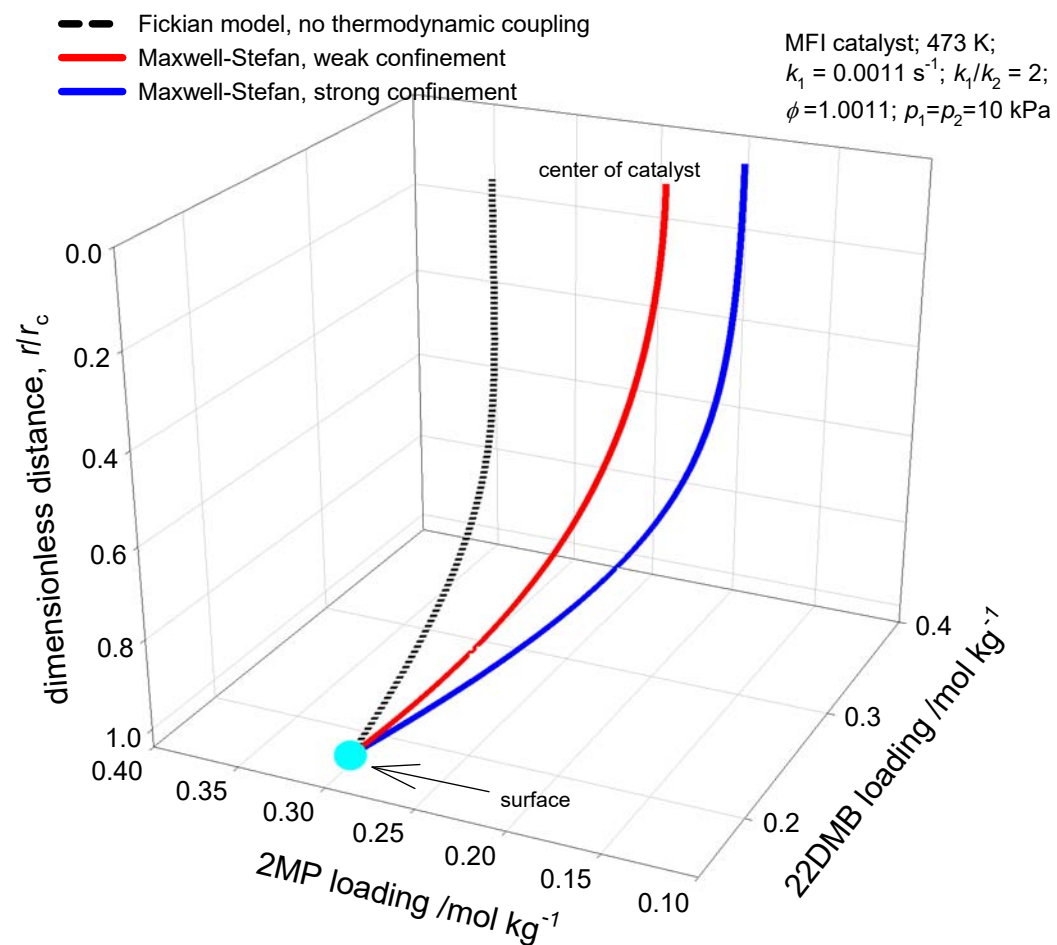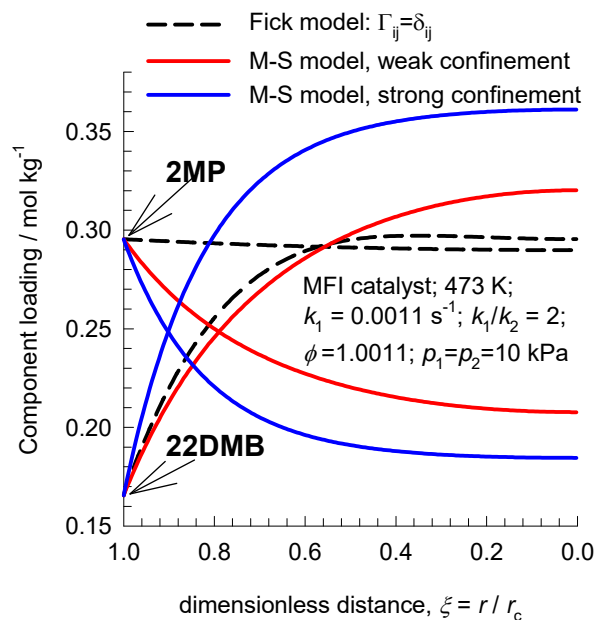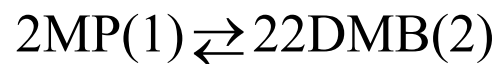
2MP/22DMB breakthrough in fixed bed reactor

(a) Transient breakthrough
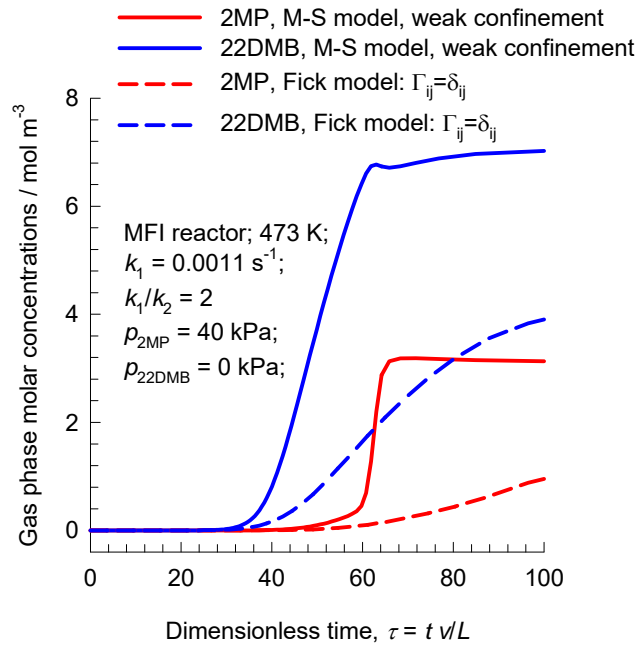
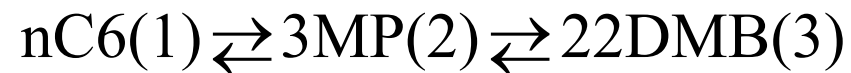**(b) Steady-state profiles along bed**
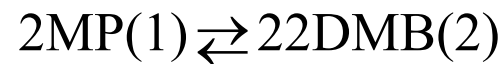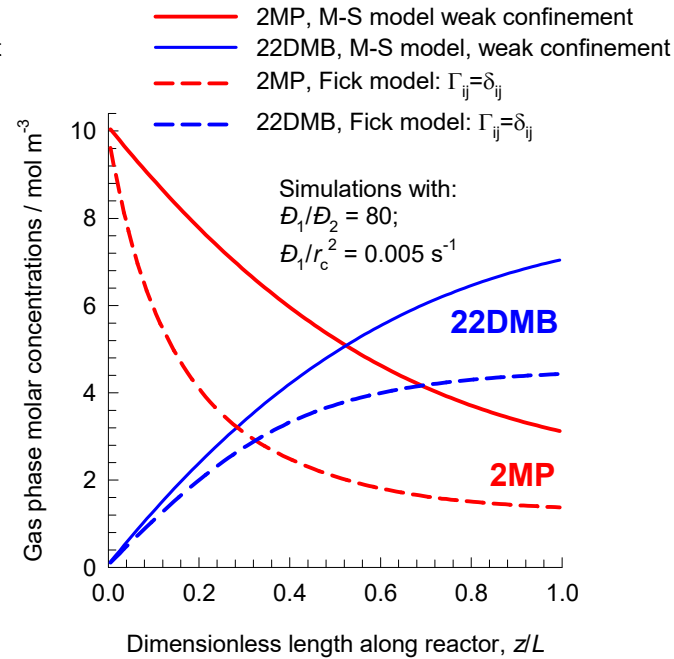
(c) Steady-state 22DMB profiles
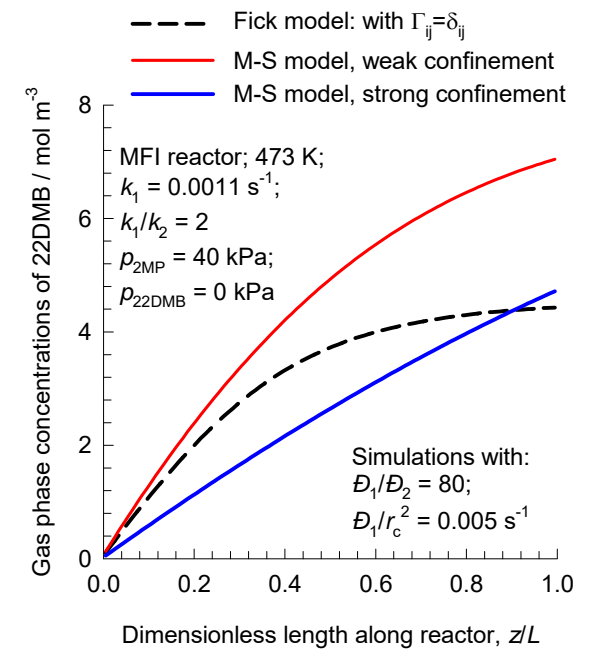
Transient oX/pX diffusion/reaction in MFI catalyst
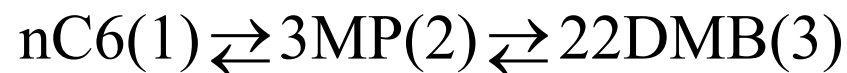
$$o-xylene(1) \rightleftarrows p-xylene(2)$$

(a)

(b)

Equilibration Trajectories in Occupancy Space

$$o-xylene(1) \rightleftarrows p-xylene(2)$$

Equilibration Trajectories in Occupancy Space

$$o-xylene(1) \rightleftarrows p-xylene(2)$$

Radial variation of component loadings

$$o-xylene(1) \rightleftarrows p-xylene(2)$$
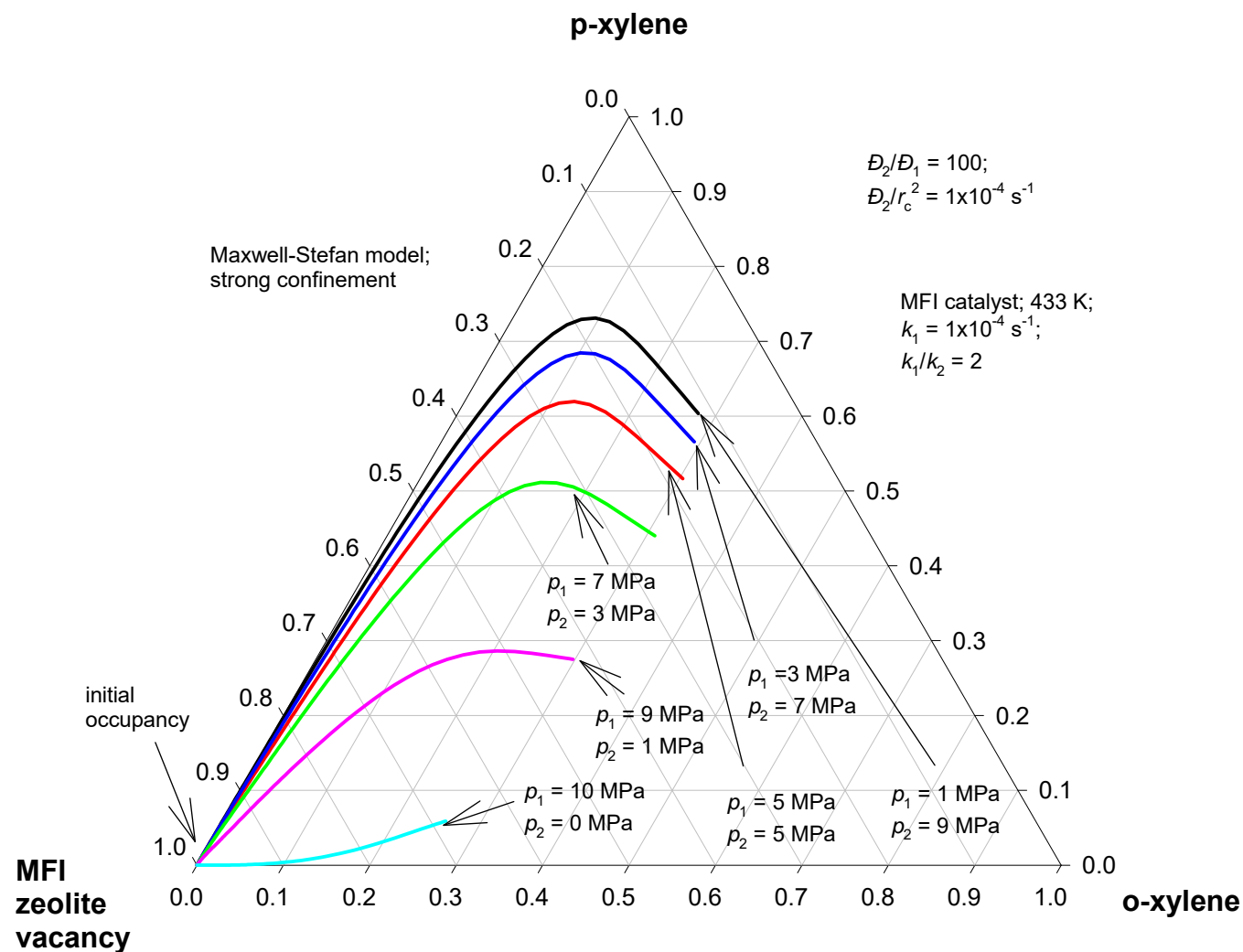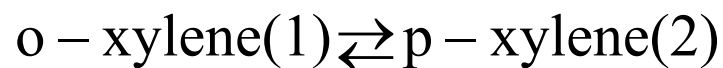
Fixed bed reactor: steady-state

oX, M-S model, strong confinement
pX, M-S model, strong confinement
oX, Fick model: $\Gamma_{ij}=\delta_{ij}$
pX, Fick model: $\Gamma_{ij}=\delta_{ij}$

Simulations with:
$Ð_2/Ð_1 = 10$;
$Ð_2/r_c^2 = 1\times10^{-6}$ s^{-1}

p-xylene

o-xylene

MFI catalyst; 433 K;
$k_1 = 1\times10^{-4}$ s^{-1}; $k_1/k_2 = 2$
$p_1 = 10$ MPa; $p_2 = 0$ MPa

Gas phase molar concentrations / mol m^{-3}

Dimensionless length along reactor, z/L
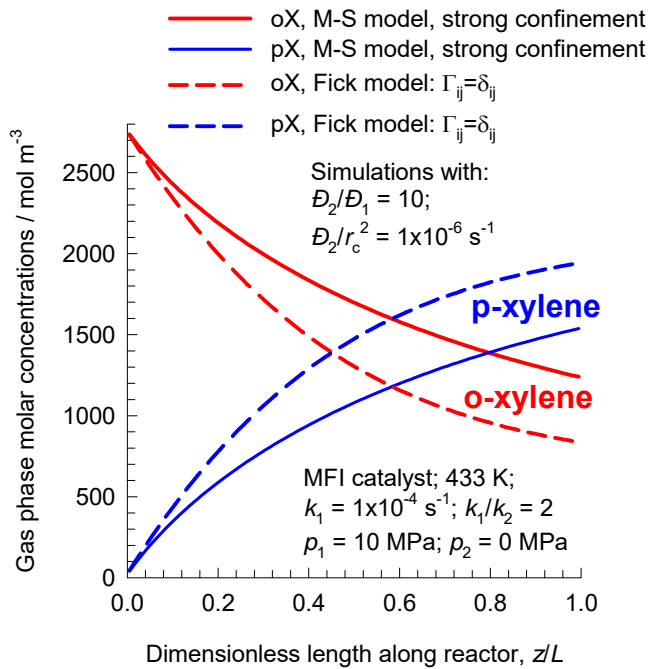
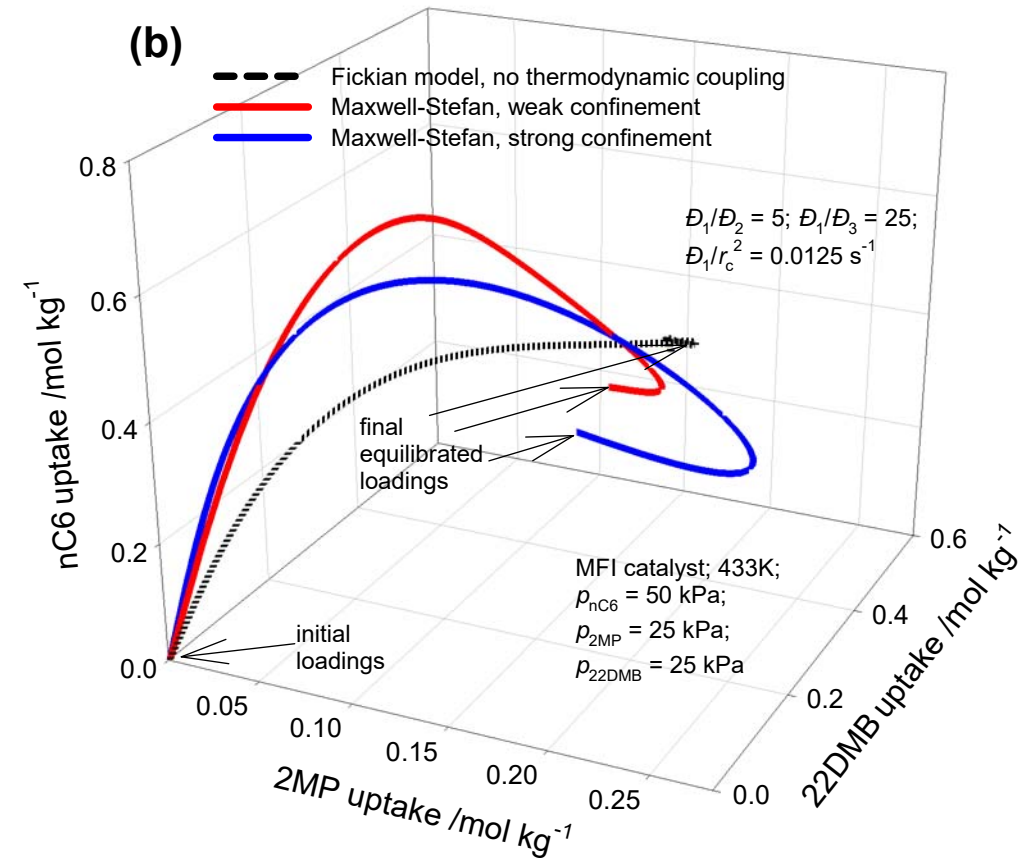# Fixed bed reactor with pulse injection of feed

Transient nC6/3MP/22DMB diffusion/reaction in MFI catalyst

(a)

$nC6(1) \rightleftarrows 3MP(2) \rightleftarrows 22DMB(3)$

Panel (a) axes and labels:
- Top plot: Spatial-averaged nC6 uptake / mol kg^{-1} vs square root of time; curve labeled **nC6**
- $Đ_1/Đ_2 = 10$; $Đ_1/Đ_3 = 20$; $Đ_1/r_c^2 = 0.0002$ s^{-1}
- Legend: Fick model with $\Gamma_{ij}=\delta_{ij}$; M-S model, weak confinement; M-S model, strong confinement
- Bottom plot: Spatial-averaged 3MP, 22DMB uptake / mol kg^{-1}; curves labeled **22DMB**, **3MP**
- MFI catalyst; 362 K; $p_{nC6} = 1000$ Pa; $p_{3MP} = 1$ Pa; $p_{22DMB} = 1$ Pa
- x-axis: square root of time, $t^{1/2}$ / min$^{1/2}$

(b)

Legend:
- Fickian model, no thermodynamic coupling
- Maxwell-Stefan, weak confinement
- Maxwell-Stefan, strong confinement

Panel (b) axes:
- nC6 uptake /mol kg^{-1}
- 3MP uptake /mol kg^{-1}
- 22DMB uptake /mol kg^{-1}
- labels: final equilibrated loadings; initial loadings
- MFI catalyst; 362 K; $p_{nC6} = 1000$ Pa; $p_{3MP} = 1$ Pa; $p_{22DMB} = 1$ Pa; $Đ_1/Đ_2 = 10$; $Đ_1/Đ_3 = 20$; $Đ_1/r_c^2 = 0.0002$ s^{-1}
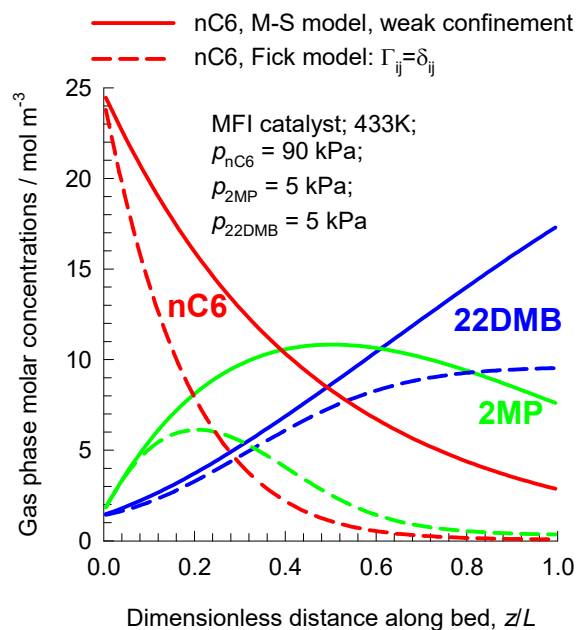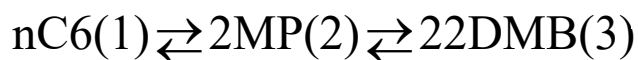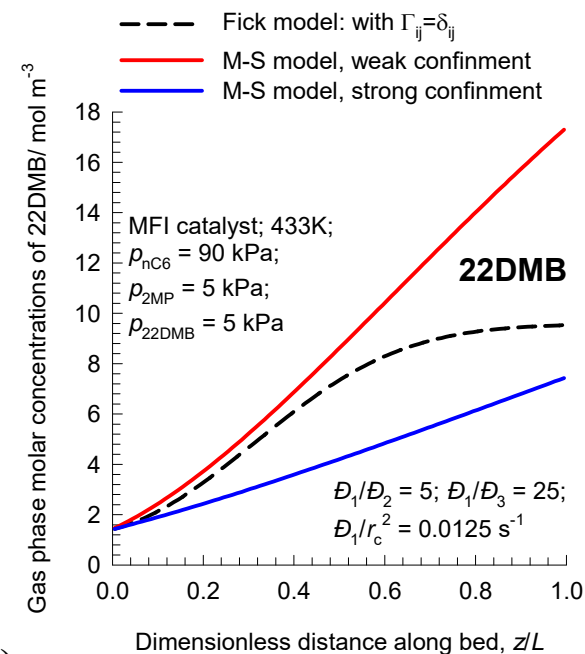
nC6/3MP/22DMB breakthrough in fixed bed reactor with MFI catalyst

(a) Steady-state profiles along bed

MFI catalyst; 362 K;
p_{nC6} = 1000 Pa; p_{3MP} = 1 Pa;
p_{22DMB} = 1 Pa

$Đ_1/Đ_2$ = 10; $Đ_1/Đ_3$ = 20;
$Đ_1/r_c^2$ = 0.0002 s^{-1}

(b) Steady-state 22DMB profiles along bed

$Đ_1/Đ_2$ = 10; $Đ_1/Đ_3$ = 20;
$Đ_1/r_c^2$ = 0.0002 s^{-1}

MFI catalyst; 362 K;
p_{nC6} = 1000 Pa; p_{3MP} = 1 Pa;
p_{22DMB} = 1 Pa

$$nC6(1) \rightleftarrows 3MP(2) \rightleftarrows 22DMB(3)$$

nC6/3MP/22DMB breakthrough in fixed bed reactor with MFI catalyst

Transient breakthrough

$$nC6(1) \rightleftarrows 3MP(2) \rightleftarrows 22DMB(3)$$

Transient nC6/3MP/22DMB diffusion/reaction in BEA catalyst

(a)

$\text{nC6(1)} \rightleftarrows \text{3MP(2)} \rightleftarrows \text{22DMB(3)}$

nC6

$Đ_1/Đ_2 = 2$; $Đ_1/Đ_3 = 10$;
$Đ_1/r_c^2 = 0.01$ s^{-1}

Fick model with $\Gamma_{ij} = \delta_{ij}$
M-S model, weak confinement
M-S model, strong confinement

22DMB

3MP

BEA catalyst; 433K;
$p_{nC6} = p_{3MP} = p_{22DMB} = 20$ kPa

square root of time, $t^{1/2}$ / min$^{1/2}$

Spatial-averaged nC6 uptake / mol kg^{-1}

Spatial-averaged 3MP, 22DMB uptake / mol kg^{-1}

(b)

Fickian model, no thermodynamic coupling
Maxwell-Stefan, weak confinement
Maxwell-Stefan, strong confinement

nC6 uptake /mol kg^{-1}

final equilibrated loadings

initial loadings

$Đ_1/Đ_2 = 2$; $Đ_1/Đ_3 = 10$;
$Đ_1/r_c^2 = 0.01$ s^{-1}

BEA catalyst; 433K;
$p_{nC6} = p_{3MP} = p_{22DMB} = 20$ kPa

3MP uptake /mol kg^{-1}

22DMB uptake /mol kg^{-1}

Transient nC6/2MP/22DMB diffusion/reaction in MFI catalyst

(a)

(b)

$$nC6(1) \rightleftarrows 2MP(2) \rightleftarrows 22DMB(3)$$

nC6/2MP/22DMB breakthrough in fixed bed reactor with MFI catalyst
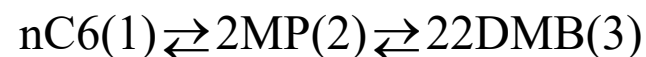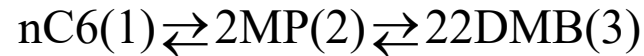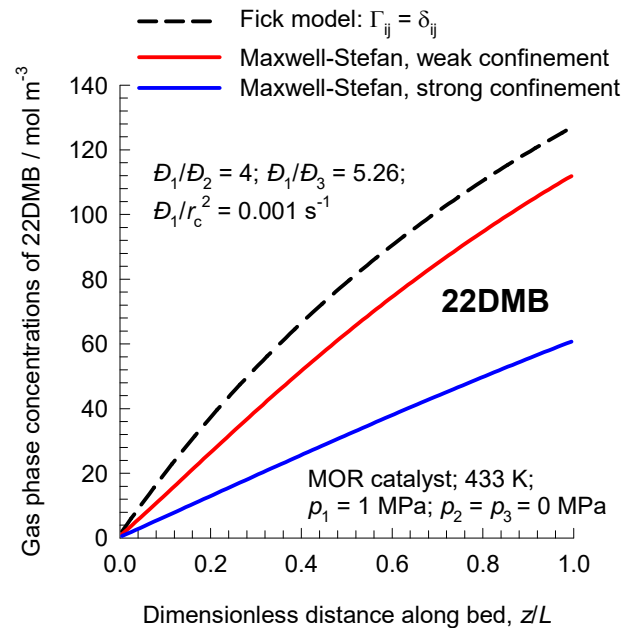
(a) Steady-state profiles along bed

(b) Steady-state 22DMB profiles along bed

$$nC6(1) \rightleftarrows 2MP(2) \rightleftarrows 22DMB(3)$$

nC6/2MP/22DMB breakthrough in fixed bed reactor with MFI catalyst

Transient breakthrough

$$nC6(1) \rightleftarrows 2MP(2) \rightleftarrows 22DMB(3)$$
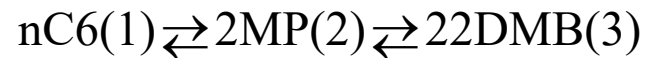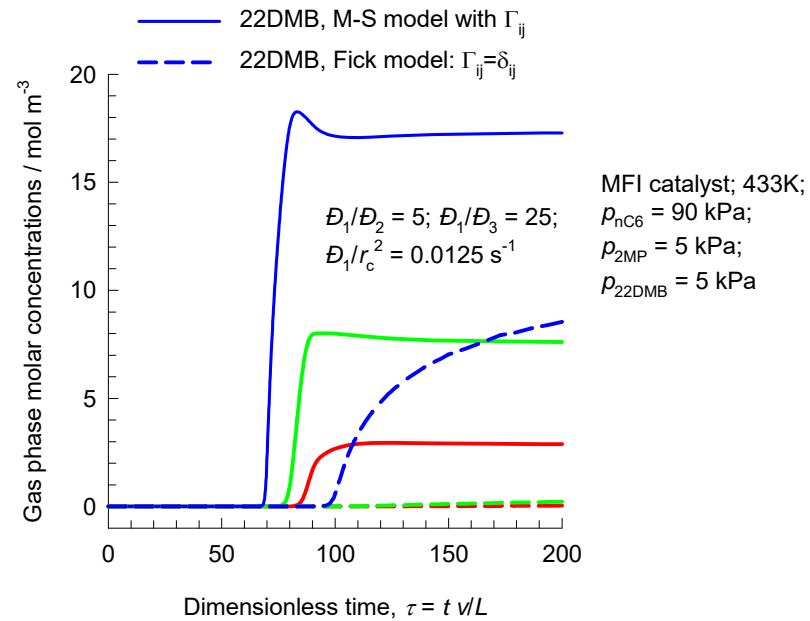
Transient nC6/2MP/22DMB diffusion/reaction in MOR catalyst
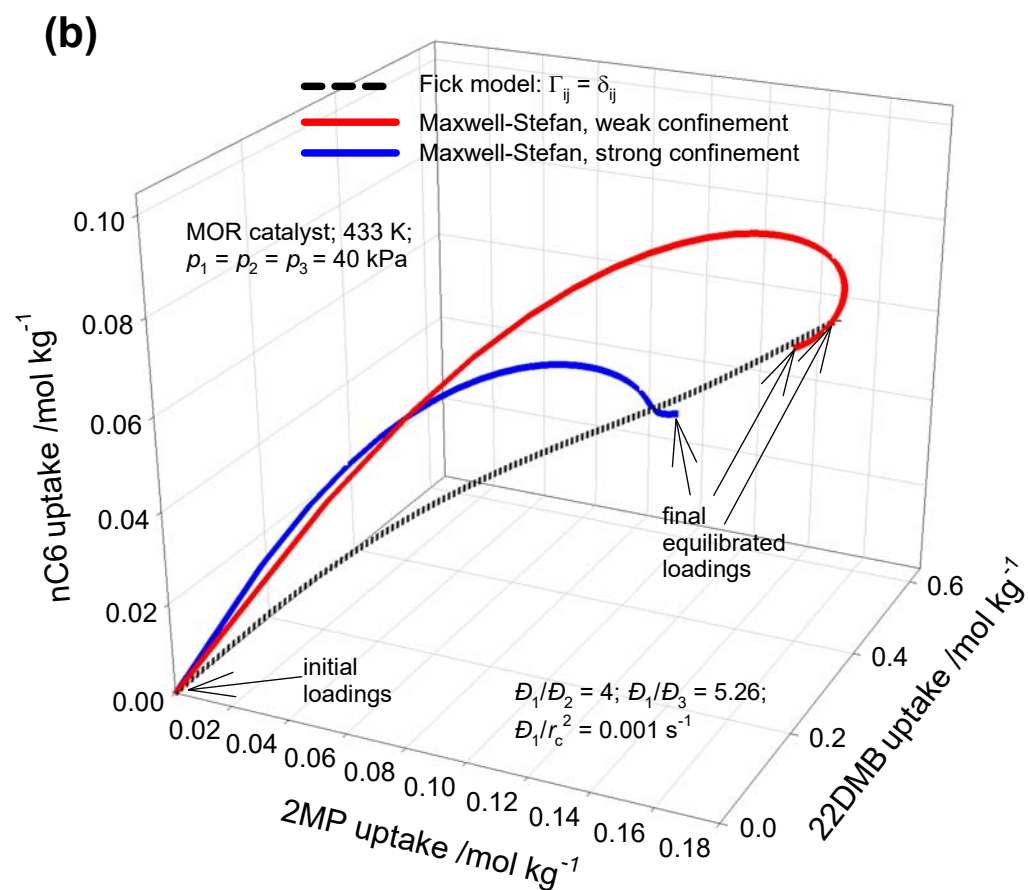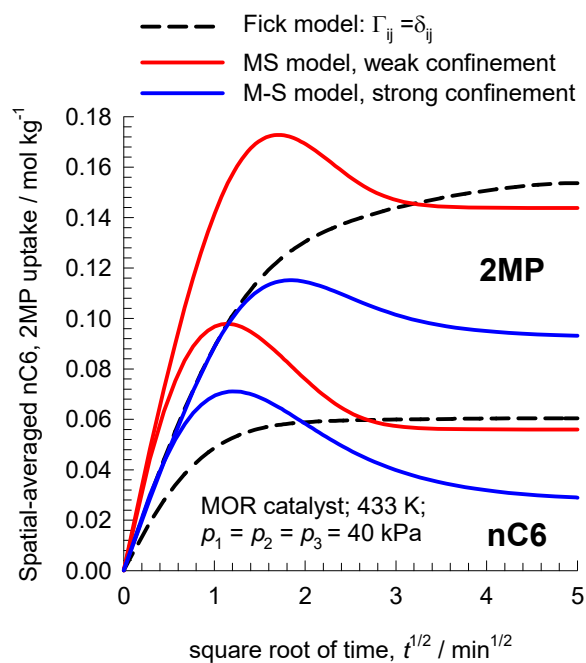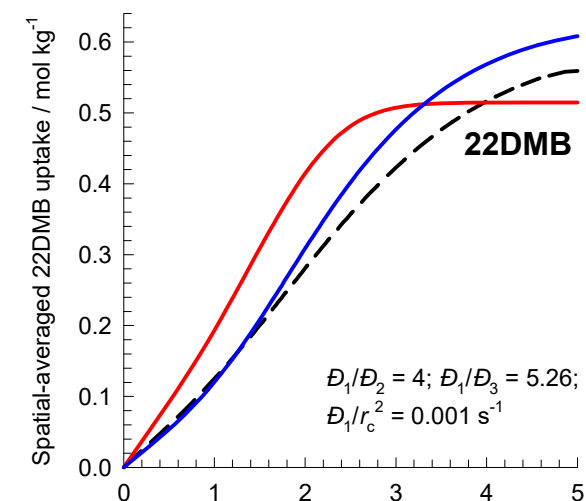
(a)

(b)

nC6/2MP/22DMB breakthrough in fixed bed reactor with MOR catalyst

$$nC6(1) \rightleftarrows 2MP(2) \rightleftarrows 22DMB(3)$$

Steady-state 22DMB profiles along bed

Legend:
- Fick model: $\Gamma_{ij} = \delta_{ij}$
- Maxwell-Stefan, weak confinement
- Maxwell-Stefan, strong confinement

$Đ_1/Đ_2 = 4$; $Đ_1/Đ_3 = 5.26$; $Đ_1/r_c^2 = 0.001 \text{ s}^{-1}$

22DMB

MOR catalyst; 433 K; $p_1 = 1$ MPa; $p_2 = p_3 = 0$ MPa

Y-axis: Gas phase concentrations of 22DMB / mol m^{-3}

X-axis: Dimensionless distance along bed, z/L

Figure S62

Transient ethene/benzene/ethylbenzene diffusion/reaction in MFI catalyst

Steady-state fixed bed reactor

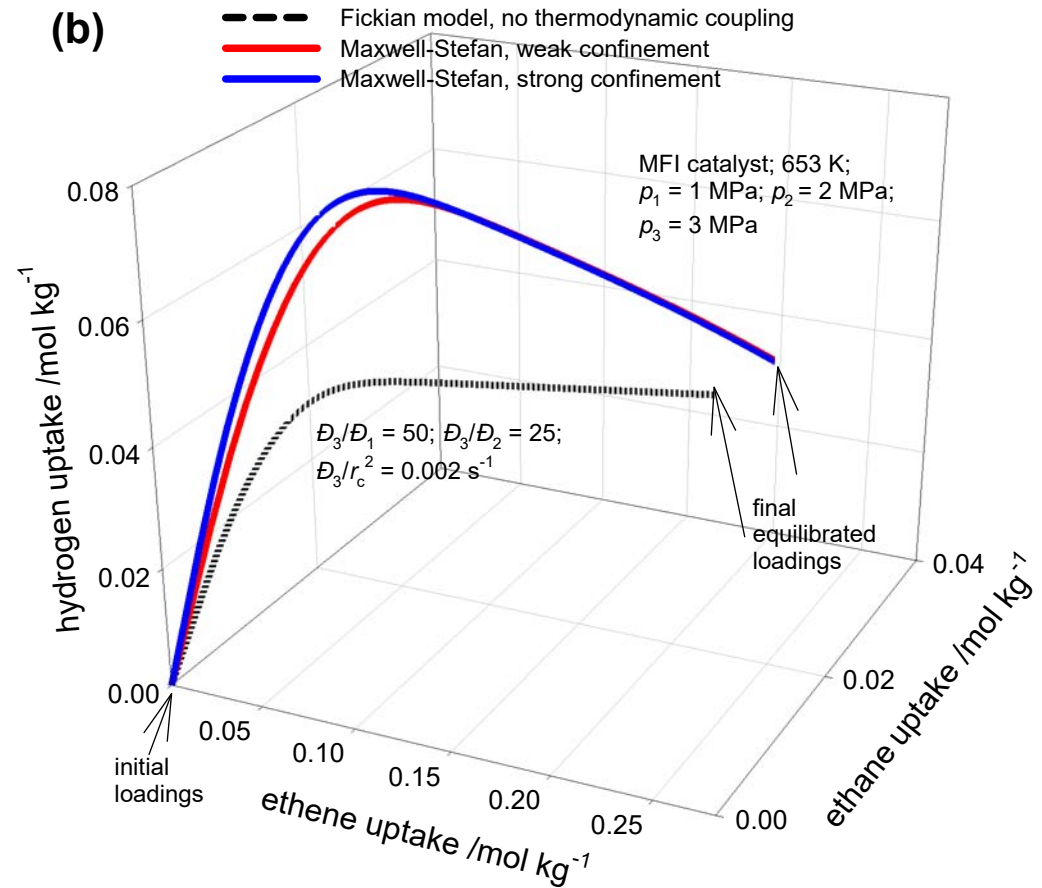$$\text{ethene}(1) + \text{benzene}(2) \rightleftarrows \text{ethylbenzene}(3)$$
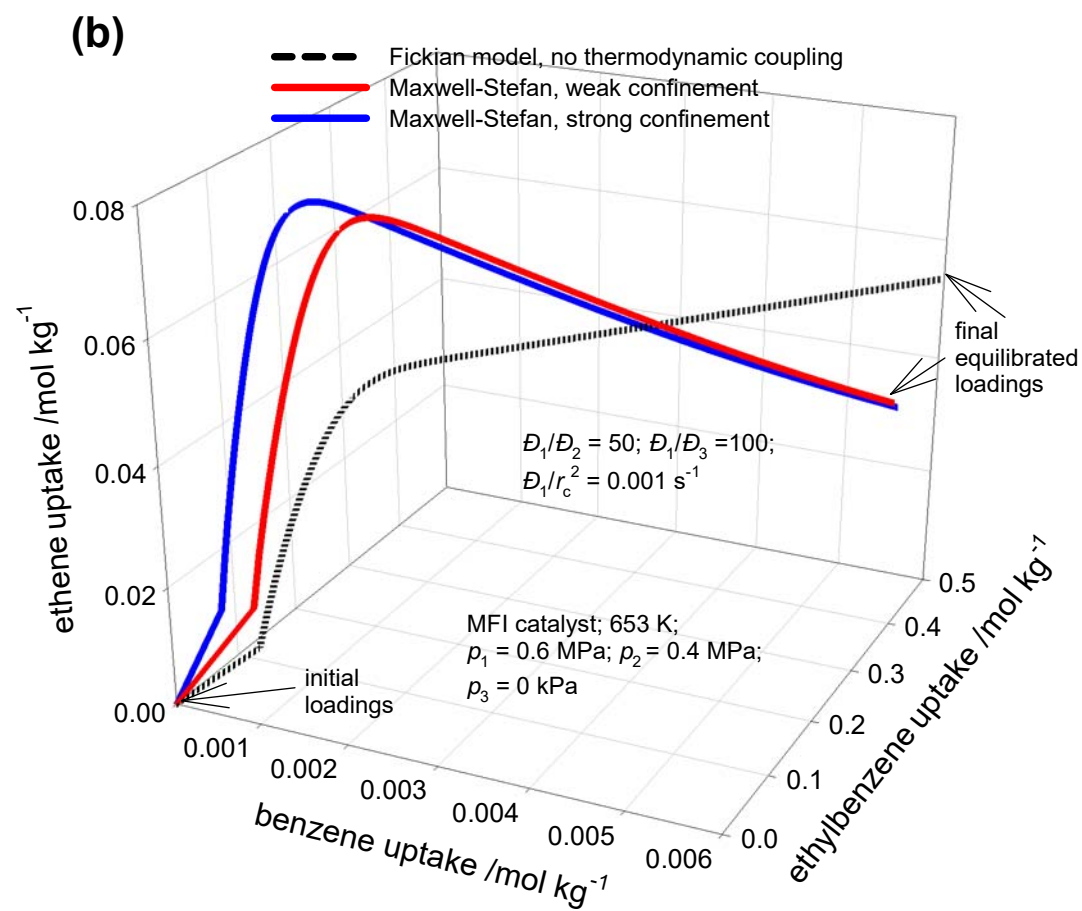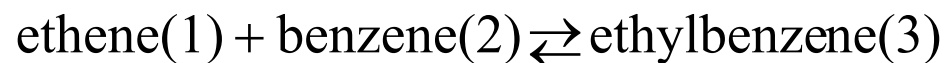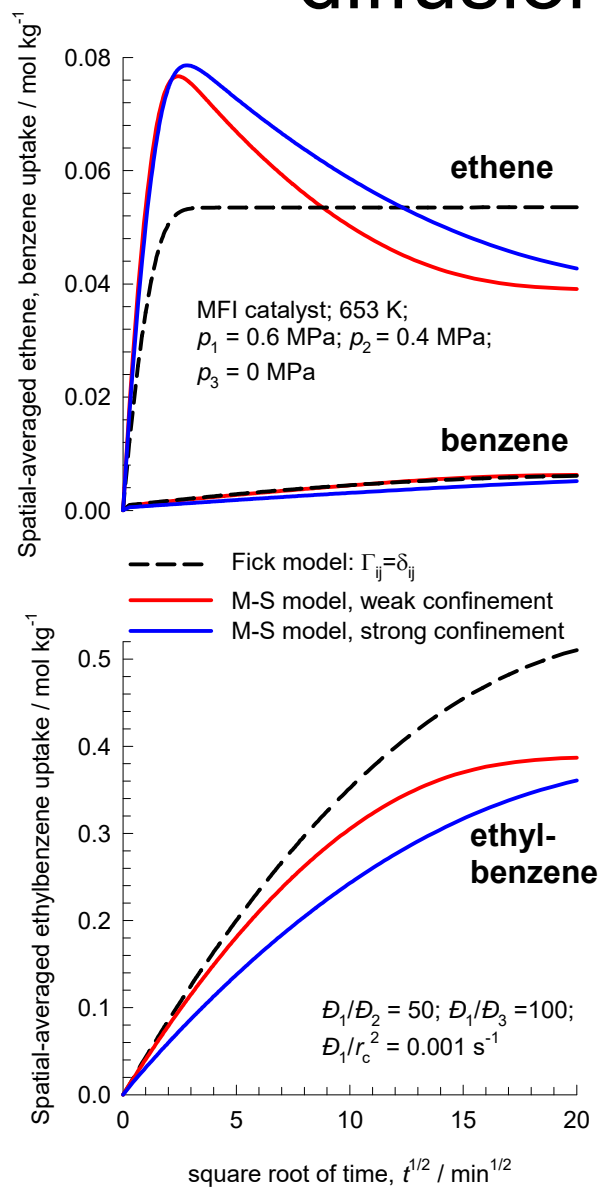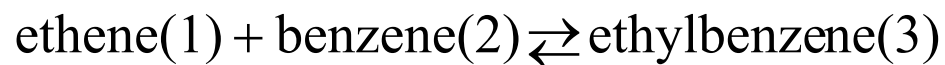
(a)
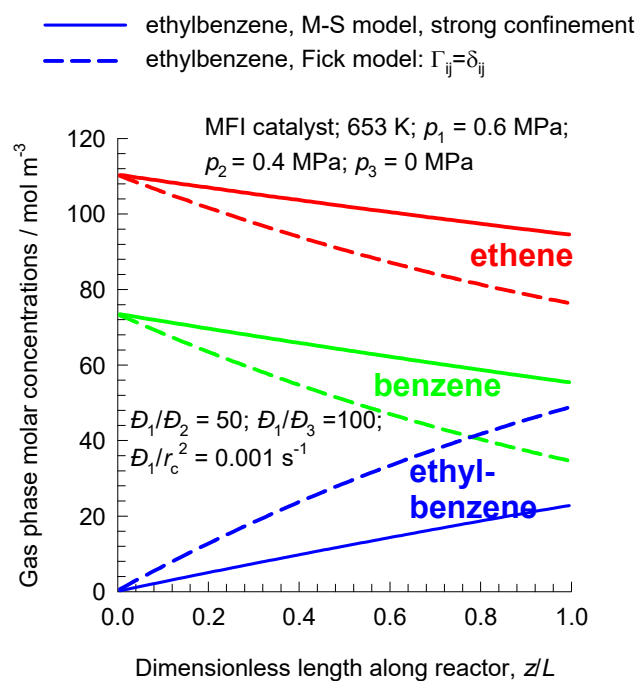
(b)
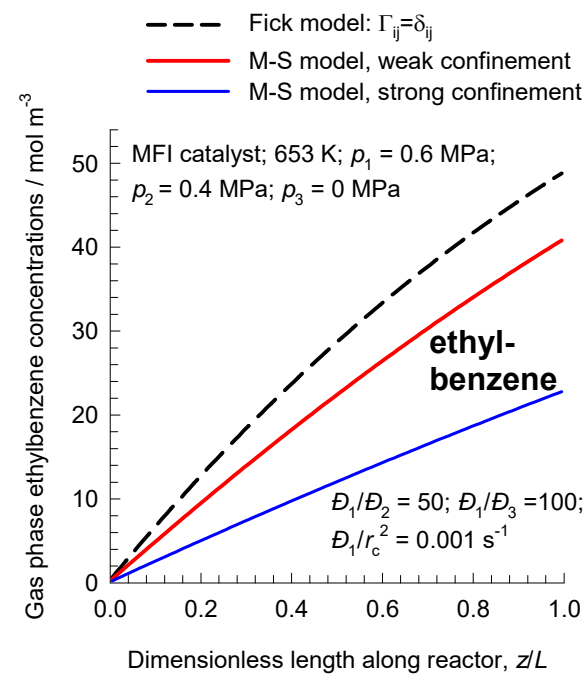
Transient ethane/ethene/hydrogen diffusion/reaction in MFI catalyst

Figure S64

(a)

$$ethane(1) \rightleftarrows ethene(2) + hydrogen(3)$$

(b)

Steady-state fixed bed reactor

$$\text{ethane}(1) \rightleftarrows \text{ethene}(2) + \text{hydrogen}(3)$$